Microscopic characterization of mesoscopic magnetic textures in Fe_3Sn_2

Dissertation

zur Erlangung des akademischen Grades

Dr. rer. nat.

eingereicht an der

Mathematisch-Naturwissenschaftlich-Technischen Fakultät

der Universität Augsburg

von

Markus Fabian Altthaler

Augsburg, Januar 2022

Universität
Augsburg
University

1. Gutachter: Prof. Dr. István Kézsmárki
2. Gutachter: Prof. Dr. Dennis Meier

Tag der mündlichen Prüfung: 22. März 2022

Contents

1 Introduction

Our modern society heavily relies on information and communication technology. The most obvious examples are the trends in digitalization and smart devices, both affecting nearly all segments of our life [1–5]. Improvements in all these devices typically require miniaturization, cost reduction, increased performance of all existing components, and development of new functional units. To date, this challenge has often been met by the scaling down of electronic components, such as transistors, facilitating lower power consumption [6], while simultaneously increasing the performance. This process of downscaling is known and frequently cited as Moore's law [7]. However, in the last years the size reduction has reached fundamental limits [8] as well as technology related limits, such as the diffraction limit of light which is used in the photolithographic processing of wafers to make components like transistors [9–15]. Thus, these challenges have launched widespread research efforts to explore alternative ways of generating functional properties at the nano-scale [16–20].

One particularly exciting solution are spin-transfer electronics, or in short spintronics [21–23], where either individual spins, or emergent spin textures, are used as memory objects. Among such textures, the nanometer sized whirls of spins called topological solitons, have been attracting broad interest. A subgroup of these solitons, magnetic skyrmions, which were originally predicted by A. Bogdanov and D. Yablonskii in 1989 [24] and observed experimentally in 2009 by Mühlbauer et. al. [25], represent a seminal part in novel memory concepts based on spintronics. In addition to skyrmions, magnetic bubble domains have come to a renaissance recently, due to the possibility to stabilize them at room temperature and squeeze them to the nanoscale. Magnetic bubbles and skyrmions have various commonalities and often they are hardly distinguishable. The strong research efforts devoted to the study of these objects can be ascribed to two factors: their technological potential to serve as elementary units in future information technology and the academic excitement about exploring new physics on the nanoscale.

Technologically speaking, there are a number of potential benefits in using these quasi-particles. They can be moved by ultra-low densities of spin polarized currents [26, 27], which is attractive because of the low energy consumption. Moreover, their properties can be sensed by non-local magnetic fields, which is attractive for reading their state [28]. Potential applications include skyrmionic memory and logic devices [29–32], skyrmion magnonic crystals [28, 33], and skyrmion-based radio-frequency devices [34, 35].

Skyrmionics is a fast progressing field, and nowadays there are multiple different ways of generating skyrmions in various different classes of host materials [29]. Skyrmion lattices were first observed in non-centrosymmetric chiral magnets [25, 36] and thin films [37, 38] at low temperature, stabilized by the bulk Dzyaloshinskii-Moriya interaction (DMI). Subsequently, individual skyrmions were stabilized by interfacial DMI in asymmetric magnetic multilayers [39–48]. In addition, skyrmions were observed in axially symmetric polar magnets [49–51] and the frustrated centrosymmetric kagome magnet Fe_3Sn_2 [52]. The latter is of specific interest, because it has been reported to host skyrmions at room temperature [52, 53]. In contrast to the other skyrmion hosts mentioned above [52, 53], Fe_3Sn_2 has a centrosymmetric crystal structure, hence the stabilization of the skyrmions in this compound is caused by the competition between the uniaxial magneticrystalline anisotropy and dipolar interactions, rather than relying on the DMI [54].

Despite the rapid progress in the field and application oriented visions, a lot of research is still focused on the fundamental material properties and the understanding of individual systems. Although there is a plethora of candidate materials, in many respects Fe_3Sn_2 is an excellent choice for potential applications: It is known to have a room temperature skyrmion phase [52], it is composed of abundant, cheap, and non-toxic elemental metals [55], and the bulk properties have been described in detail in the literature [56–63]. Nonetheless, there are still major questions to be addressed in order to prove the real applicability of this compound. For instance, what is the internal spin structure of skyrmions and bubbles observed in Fe_3Sn_2? To which size can they be scaled down? How can these magnetic textures be manipulated and controlled?

This thesis addresses these questions and others to establish an understanding of the different magnetic textures in Fe_3Sn_2, using a combination of magnetic imaging techniques with nanoscale resolution. The experimental work is complemented by micromagnetic simulations to reveal the three-dimensional spin textures of the magnetic objects. While this is very much in the realm of fundamental science, wherever possible the potential for future device applications will be considered. Along this line, this thesis aims to address the following questions:

i) What magnetic objects emerge in Fe_3Sn_2?

ii) How is the stability of these magnetic objects influenced by geometrical confinement?

iii) How are the magnetic objects affected by external magnetic fields?

iv) Which device geometries can be useful for future applications?

These questions will be addressed using two key microscopy techniques: Magnetic force microscopy (MFM) to image the out-of-plane magnetic stray fields, and Lorentz transmission electron microscopy (LTEM) to study the inplane magnetization. Micromagnetic simulations and simulated transport of intensity equation (TIE) reconstructed induction maps are computational tools used to visualize the three-dimensional magnetic textures. TIE reconstructed induction maps based on LTEM data are used to reconcile the modeled spin textures and the experimental data. Focused ion beam scanning electron microscopes (FIB-SEM) are used to control geometrical confinement, namely the lateral size of specimen and its thickness.

The structure of the thesis is as follows. In the second chapter, the basic concepts of magnetism and magnetic textures are introduced following an approach inspired by Hubert and Schäfer [64], also including a description of topologically non-trivial spin textures. After this theoretical background, the experimental methods used in this work are described in chapter three, focusing on the fundamental procedure and principles of the respective techniques. Specifically, MFM and LTEM are considered for imaging, as well as FIB-SEM for advanced sample preparation. Next, in chapter four a brief overview is given about the material-specific properties of Fe_3Sn_2, the target material of this thesis. Then, the results are discussed in light of the questions raised above, where the main focus is on the creation, stability and control of the magnetic mesoscopic objects and revealing their internal structure. The results section is concluded with a series of prototypical functional objects to illustrate how this work moves the community closer to spintronics applications.

2

Theoretical Background

The first application of magnetism dates back to the ancient world when the compass was introduced [65]. The compass needle was initially made of the naturally occurring mineral magnetite, Fe_3O_4, also known as lodestone [66]. Over time, the compass was constantly improved. Eventually, the needle was made out of precisely formed iron that was magnetized using lodestone, leading to improved accuracy. Cartography and navigation hinged on this naturally occurring ferromagnetic material in the following centuries, enabling global trade, discovery, and progress [65, 67]. However, until the 19th century the physical understanding of magnetic phenomena was lacking.

Ørsted and Ampère linked magnetism to electricity laying the foundation for understanding magnetism and the development of numerous applications [68]. The attractive or repulsive long-ranged force between two permanent magnetic poles is still the most well-known magnetic phenomenon to the layman. Ørsted and Ampère were the first to explain the Lorentz force and the origin of induction. The discovery of induction sparked the development of the generator and the electric motor, thus, placing the foundation for a vast variety of technical applications. Magnetic levitation trains and the shift to E-mobility for personal cars are only the pinnacle of current developments in the transport sector, all hinging on magnetism.

The origin of magnetic fields on the macroscopic scale was quickly linked to a looped current. Almost a century later, these current loops were attributed to the orbital angular momentum, associated with the encircling motion of an electron around the nucleus, and the spin of individual electrons, yielding the fundamental origin of the magnetic field. The spin was discovered experimentally in 1925 [69] and the theoretical framework was postulated soon after [70]. Both contributions are highly influenced by the distinct electronic configuration, hence free atoms or ions, differ vastly from condensed matter in terms of magnetic properties.

The final big leap in the application of magnetic phenomena was the utilization of magnetic materials as storage media [64, 71]. Starting from magnetic tapes to spinning disks in hard drives magnetic storage media have been the backbone of high capacity memory devices in the past decades. With the ever-growing requirements for data storage fueled by the digitalization in all branches of our lives, further improvements of magnetic storage media are required. Limiting the scope to relevant developments of the last two decades alone, a variety of interesting new phenomena have been discovered, including the interfacial Dzyaloshinskii-Moriya interaction [72], spin transport mechanisms in 2D materials [73], supermagnetism phenomena [38], and the discovery of novel topological objects on the nanoscale [74]. The latter motivates the investigation of a broad field of complex nanometric spin textures, their nucleation and modification. Research targeted towards application in storage media, comprises both the application focused engineering aspect and the fundamental characterization.

The first section of this chapter is necessarily inspired by the seminal work of Hubert and Schäfer on magnetic domains [64], as such the interested reader is encouraged to expand this section with reference to their textbook. The subsequent section on topological solitons moves beyond this established textbook knowledge to the cutting edge of the respective research fields, as such it focuses on the latest research articles.

2.1 Magnetism

In this section the theoretical foundation of magnetism is elucidated. Starting from a semi-classical picture, the fundamental building block of magnetic order, the magnetic moment is deduced. Subsequently the interactions of multiple moments are examined. Followed by a short overview of the emergent collective behavior and the micromagnetic textures, the emphasis lies on conveying an intuitive idea of what these interactions do, individually and collectively, whilst also formulating them properly. Finally, the link of the microscopic magnetic texture is made to the macroscopic magnetic phenomena.

2.1.1 Fundamental Origin

The origin of magnetism lies in the microscopic world. On the smallest scale, magnetism is linked to the individual magnetic moments of electrons and nuclei, which can be understood as elementary magnetic dipoles. Hereafter the magnetic moment of the nuclei will be neglected as it is of order 10^{-3} smaller compared to the electrons magnetic moment. The fundamental origin of the magnetic moment of an electron are, the orbital angular momentum and the spin.

The origin of the magnetic moment can be deducted from a semi-classical picture [75]. Any electrical current density $\boldsymbol{j}(\boldsymbol{r})$, occupying the volume V, has an associated magnetic moment [76]

$$\boldsymbol{\mu} = \frac{1}{2} \int_V \boldsymbol{r} \times \boldsymbol{j}(\boldsymbol{r}) \mathrm{d}V. \tag{2.1}$$

For an electron with charge e and velocity v, expression (2.1) yields the magnetic moment for an individual electron:

$$\boldsymbol{\mu} = -\frac{e}{2} \boldsymbol{r}_0 \times \boldsymbol{v}. \tag{2.2}$$

Taking the electron mass, m_e, into account the angular momentum of an individual electron is

$$\boldsymbol{L} = \boldsymbol{r} \times \boldsymbol{p} = \boldsymbol{r}_0 \times m_\mathrm{e}\boldsymbol{v}. \tag{2.3}$$

Comparing the latter two equations the relation of the magnetic moment and the angular momentum can be deduced:

$$\boldsymbol{\mu} = -\frac{e}{2m_\mathrm{e}}\boldsymbol{L} \equiv \gamma\boldsymbol{L}, \tag{2.4}$$

with the gyromagnetic ratio γ [77]. Although the classical analogy often works, the individual magnetic moment is inevitably linked to quantum mechanics as the angular momentum is quantized in integer multiples of $\hbar = h/2\pi$, the reduced Planck constant. Therefore, the classical angular momentum $\boldsymbol{L}$ can be translated to the quantum mechanical operator

$$\mathbf{L} = -i\hbar\mathbf{r} \times \nabla \equiv \hbar\mathbf{l}, \tag{2.5}$$

where i represents the imaginary unit, $\mathbf{r}$ is the position operator, and ∇ the vector differential operator. Inserting the smallest possible value of $\mathbf{L} = \hbar$ into equation (2.4) yields the Bohr magneton:

$$\mu_\mathrm{B} = \frac{e\hbar}{2m_\mathrm{e}}, \tag{2.6}$$

the quantized unit of magnetization. On the level of atomic magnetism, the principle quantum number n, referencing the atomic shell, constrains the orbital angular momentum quantum number ℓ to values of $0 \leq \ell \leq (n-1)$. Within each of the s, p, d, and f orbitals (for $\ell = 0, 1, 2, 3$ respectively) the magnetic quantum number m_ℓ is limited to values of $-\ell \leq m_\ell \leq \ell$. m_ℓ references the orientation in space and thereby divides the subshell into individual orbitals which hold the electrons. Additionally, all electrons have a spin angular momentum of $\mathbf{s} = 1/2$, described by the spin operator

$$\mathbf{S} \equiv \hbar\mathbf{s}. \tag{2.7}$$

For an individual electron, the spin quantum number is constrained to values of $m_s \in \{+1/2, -1/2\}$ termed the spin up and spin down state, respectively. For both the orbital and spin angular momentum operator the expectation values correspond to the respective quantum numbers:

$$\langle \mathbf{l}^2 \rangle = \ell(\ell+1) \qquad \langle l_z \rangle = m_\ell \tag{2.8}$$

$$\langle \mathbf{s}^2 \rangle = s(s+1) \qquad \langle s_z \rangle = m_s \tag{2.9}$$

Taking both the orbital and spin angular momentum into account the total angular momentum operator

$$\mathbf{J} = \mathbf{L} + \mathbf{S} \tag{2.10}$$

is defined as their sum. Subsequently, equation (2.4) can be rewritten in the form

$$\boldsymbol{\mu} \equiv \gamma\mathbf{J} = -\frac{g\mu_\mathrm{B}}{\hbar}\mathbf{J}, \tag{2.11}$$

with the quantized total angular momentum and the g-factor. For the orbital and spin contributions the g-factor is equal to 1 and 2, respectively, whereas for free atoms the g-factor is given by the Landé factor:

$$g = 1 + \frac{J(J+1) + S(S+1) - L(L+1)}{2J(J+1)}. \tag{2.12}$$

Analogous to the angular momentum operator the total magnetic moment of a single electron [78],

$$\boldsymbol{\mu} = \boldsymbol{\mu}_{\mathrm{orbit}} + \boldsymbol{\mu}_{\mathrm{spin}} \tag{2.13}$$

can therefore be expressed as the sum of the two contributions:

$$\boldsymbol{\mu}_{\mathrm{orbit}} = -\frac{e\hbar}{2m_{\mathrm{e}}}\mathbf{l} = -\mu_{\mathrm{B}}\mathbf{l}, \tag{2.14}$$

$$\boldsymbol{\mu}_{\mathrm{spin}} = -\frac{e\hbar}{2m_{\mathrm{e}}}g_{\mathrm{e}}\mathbf{s} = -\mu_{\mathrm{B}}g_{\mathrm{e}}\mathbf{s}. \tag{2.15}$$

With the deduction of the magnetic moment of an individual electron covered, the scheme is now expanded to describe several electrons, e.g. orbiting a single atom or contained in a solid-state body. The current density $\boldsymbol{j}(\boldsymbol{r})$ contained in the volume V is rewritten in the following form:

$$\boldsymbol{j}(\boldsymbol{r}) = \sum_k -e\boldsymbol{v}_k\delta(\boldsymbol{r} - \boldsymbol{r}_k), \tag{2.16}$$

where k indexes all electrons contained. No electron-electron interactions will be considered at this point. Inserting the expanded current density into equation (2.1) yields

$$\boldsymbol{\mu} = -\frac{e}{2}\sum_k \boldsymbol{r}_k \times \boldsymbol{v}_k = -\sum_k \gamma\mathbf{J}_k = \sum_k \boldsymbol{\mu}_k. \tag{2.17}$$

Hence, the overall magnetic moment is the sum of all total magnetic moments contained in the volume V. In solid state physics the magnetic moment is commonly expressed in the form of the magnetization $\boldsymbol{M}$, thus independent of the reference volume. Therefore, the definition of the magnetization is introduced:

$$\boldsymbol{M} = \lim_{V\to p}\frac{1}{V}\sum_k \boldsymbol{\mu}_k. \tag{2.18}$$

The source of the magnetic moments and subsequently the magnetization are microscopic magnetic dipoles. Hence, analogous to the Gauss's law for electric charge, the magnetic charge density,

$$\rho_m = -\nabla\cdot\boldsymbol{M}, \tag{2.19}$$

is defined [76]. Considering this equation isolated yields the risk of misinterpretation in line with the existence of magnetic monopoles. A term coined for quasi-particles realized by complex geometrical arrangements of magnets [79, 80]. These should not be confused with an actual elementary magnetic monopole, which has to obey Gauss's law for magnetism:

$$\nabla\cdot\boldsymbol{B} = 0. \tag{2.20}$$

No such restriction is imposed on the magnetization $\boldsymbol{M}$. Here $\boldsymbol{B}$ is the magnetic flux density:

$$\boldsymbol{B} = \mu_0 \cdot (\boldsymbol{H} + \boldsymbol{M}), \tag{2.21}$$

and μ_0 the vacuum permeability.

One of the most fundamental magnetic properties is the magnetic susceptibility

$$\chi = \frac{|\boldsymbol{M}|}{|\boldsymbol{H}|} = \frac{M}{H}, \tag{2.22}$$

describing the response of the magnetization to an external magnetic field of strength H. Its sign determines whether the response of the system is negative, so called diamagnetic, i.e. works against the external field or positive, termed paramagnetic.

The response to external magnetic field can be understood in the following simple scheme. The degeneracy of the energy levels of an electron of total angular momentum $\mathbf{J}$ are lifted by a magnetic field according to the Zeeman effect (which will be covered in more detail in section 2.1.3). The energy E for each individual level is given by

$$E = -\boldsymbol{\mu} \cdot \boldsymbol{B} = m_J g \mu_\mathrm{B} B, \tag{2.23}$$

yielding a symmetric splitting in m_J levels [81]. Note that the parallel alignment of the magnetic moment with the external field effectively lowers the energy level resulting in an energetically favorable state predominantly occupied by the electrons.

All materials exhibit weak diamagnetism as no net spin or orbital angular momentum is required. In the absence of any other superseding contribution the material is classified as diamagnetic. Materials with unpaired electrons show paramagnetic behavior. Whilst these still exhibit a diamagnetic response, it is generally outweighed by the paramagnetism. Even though both dia- and paramagnets are weak magnetic materials they are often falsely referred to as amagnetic (non-magnetic), due to the common misconception of ferromagnetism being the universal key magnetic phenomenon. Ferromagnetism is generally understood as residual magnetization present even in the absence of external magnetic field. In section 2.1.3 a more rigorous definition of ferromagnetism will be given.

2.1.2 Microscopic Description of Magnetic Order

Beyond the dia- and paramagnetic response of magnetic materials, a multitude of peculiar ordered magnetic states, like ferro- and antiferromagnets have been observed. It is evident, these cannot be considered as a simple ensemble of individual magnetic moments of many electrons, as these states originate from the interaction of magnetic moments. Numerous short-range inter-atomic interactions and long-range cooperative interactions contribute to the formation of magnetic order. In the following sections these interactions and subsequent emergent phenomena will be elucidated.

Micromagnetic theory

Micromagnetic theory rests on the assumption that the spatially and temporally resolved magnetization $\boldsymbol{M}(\boldsymbol{r}, t)$ can be treated as a continuous vector field, thus providing a theoretical description of systems with magnetic phenomena in the mesoscopic scale ($\sim 10^{-6}$ to 10^{-3} m). Fundamental assumptions are made within a material. The material is assumed to be saturated everywhere, i.e. magnetized at maximum strength. Furthermore, this local saturation $M_\mathrm{s}(\boldsymbol{r}, t) \approx M_\mathrm{s}$ is considered to be independent of local and temporal variation and dependent only on the temperature. Hence, the magnetization can be expressed as

$$\boldsymbol{M}(\boldsymbol{r}, t) = |\boldsymbol{M}(\boldsymbol{r}, t)| \cdot \boldsymbol{m}(\boldsymbol{r}, t) = M_\mathrm{s}\boldsymbol{m}(\boldsymbol{r}, t), \tag{2.24}$$

represented by the saturation magnetization, M_s, and a unit vector field, $\boldsymbol{m}(\boldsymbol{r}, t)$, called reduced magnetization. The latter describes the local temporarily resolved orientation of the magnetization. Finally, to account for continuity, the characteristic exchange length, where the inter-atomic forces are considered strong enough to keep the magnetic moments aligned almost parallel, is introduced. Within the exchange length

$$l_\mathrm{ex} = \sqrt{\frac{2A}{\mu_0 M_\mathrm{s}^2}} \gg a, \tag{2.25}$$

that has to exceed the lattice constant a, the magnetization remains almost parallel. Here A is the exchange stiffness which is defined later in equation (2.40). Typically, the exchange length is of the order of a few nanometers in ferromagnetic materials. L. Landau and E. Lifshitz introduced a semi-classical theory to describe micromagnetics. It is based on modeling the competing influences as contributions to an effective magnetic flux density $\boldsymbol{B}_\mathrm{eff}$. By applying the variational principle to the Landau-Lifshitz equation

$$\frac{\mathrm{d}\boldsymbol{m}}{\mathrm{d}t} = \gamma_\mathrm{LL}\frac{1}{1+\alpha^2}\left\{\boldsymbol{m} \times \boldsymbol{B}_\mathrm{eff} + \alpha\left[\boldsymbol{m} \times (\boldsymbol{m} \times \boldsymbol{B}_\mathrm{eff})\right]\right\}, \tag{2.26}$$

where γ_LL and α are the Landau-Lifschitz gyromagnetic ratio and damping coefficient, respectively, the ground state, i.e. the reduced magnetization distribution $\boldsymbol{m}$ of lowest total energy, is calculated. In order to improve the readability, here and going forward, the exact dependencies of $\boldsymbol{m}(\boldsymbol{r}, t)$ are omitted. The effective magnetic flux density, similar to the Hamiltonian in the atomic scale consideration, can be expressed as the sum of contributing flux densities:

$$\boldsymbol{B}_\mathrm{eff} = \boldsymbol{B}_\mathrm{demag} + \boldsymbol{B}_\mathrm{exch} + \boldsymbol{B}_\mathrm{DM} + \boldsymbol{B}_\mathrm{anis} + \boldsymbol{B}_\mathrm{ext}, \tag{2.27}$$

where

- $\boldsymbol{B}_\mathrm{demag}$ represents the demagnetization interaction,
- $\boldsymbol{B}_\mathrm{exch}$ represents the Heisenberg exchange interaction,
- $\boldsymbol{B}_\mathrm{DM}$ represents the Dzyaloshinskii-Moriya interaction,
- $\boldsymbol{B}_\mathrm{anis}$ represents the magnetocrystalline anisotropy interaction,
- $\boldsymbol{B}_\mathrm{ext}$ represents the Zeeman interaction.

Each individual interaction favors a particular orientation of the local magnetization $\boldsymbol{m}(\boldsymbol{r}, t)$ relative to the vicinity. Multiple interactions being simultaneously active gives rise to a complex magnetic texture, potentially developing a uniform long-range order, or highly fragmented domain patterns.

In the 1930s, Bohr and van Leeuwen showed that magnetism in materials is incomprehensible within the framework of an exact classical theory, as it is thermodynamically not stable [82]. The origin of magnetism is strictly rooted in quantum mechanics and thus, the Schrödinger equation

$$(\mathcal{H} - E)\,|\psi\rangle = 0. \tag{2.28}$$

Here $\mathcal{H}$, E, and $|\psi\rangle$ are the Hamiltonian, the energy, and the particle wave function, respectively. Consistent with perturbation theory, the Hamiltonian can be expressed in the form

$$\mathcal{H} = \mathcal{H}_0 + \mathcal{H}', \tag{2.29}$$

separating the unperturbed part $\mathcal{H}_0$ from the perturbations summed in $\mathcal{H}'$. The latter describes various interactions and influences on the electron, which can be represented by an individual Hamiltonian. In section 2.1.3 each interaction is covered individually, both on an atomic level by the respective Hamiltonian $\mathcal{H}$, and in terms of its effective magnetic flux density, $\boldsymbol{B}$. Additionally, the respective energy density, ε, is shown before a brief overview of the emergent magnetic order is given in section 2.1.4.

2.1.3 Magnetic Interactions

Demagnetization interaction

The demagnetization interaction originates from the most basic magnetic interaction, the dipole-dipole interaction [64, 83, 84]. Which describes the influence a magnetic dipole has onto another one in its vicinity and vice versa. On an atomic level, the dipole-dipole interaction between two magnetic moments $\boldsymbol{\mu}_i$ and $\boldsymbol{\mu}_j$ located at positions $\boldsymbol{r}_i$ and $\boldsymbol{r}_j$ can be expressed by the Hamiltonian [83, 84]

$$\mathcal{H}_{\mathrm{dd},ij} = -\frac{\mu_0}{4\pi}\left(\frac{3\,(\boldsymbol{\mu}_i\cdot\boldsymbol{r}_{ij})\,(\boldsymbol{\mu}_j\cdot\boldsymbol{r}_{ij}) - |\boldsymbol{r}_{ij}|^2\boldsymbol{\mu}_i\cdot\boldsymbol{\mu}_j}{|\boldsymbol{r}_{ij}|^5}\right), \tag{2.30}$$

where $\boldsymbol{r}_{ij} = \boldsymbol{r}_i - \boldsymbol{r}_j$, denotes the distance in between them. Intuitively, the interaction can be understood as the mutual reaction to the emergent magnetic field of the respective other moment. Thus, the interaction is only influenced by the relative orientation of the magnetic dipoles and their spatial separation. The energy, $E_{\mathrm{dd},i}$, of an individual magnetic moment, $\boldsymbol{\mu}_i$, located at $\boldsymbol{r}_i$ is determined by the interaction with all other moments and therefore reads [84]

$$\begin{aligned} E_{\mathrm{dd},i} &= -\frac{\mu_0}{4\pi}\sum_j\left(\frac{3\,(\boldsymbol{\mu}_i\cdot\boldsymbol{r}_{ij})\,(\boldsymbol{\mu}_j\cdot\boldsymbol{r}_{ij}) - |\boldsymbol{r}_{ij}|^2\boldsymbol{\mu}_i\cdot\boldsymbol{\mu}_j}{|\boldsymbol{r}_{ij}|^5}\right), \forall j \neq i \\ &= -\boldsymbol{\mu}_i\cdot\boldsymbol{B}_{\mathrm{demag}}(\boldsymbol{r}_i)\,. \end{aligned} \tag{2.31}$$

Here, the sum over all individual interactions is rewritten as the effective demagnetization flux density, $\boldsymbol{B}_{\mathrm{demag}}$, acting on the single moment, yielding the micromagnetic representation. The corresponding energy density is [85]

$$\varepsilon_{\mathrm{demag}} = -\frac{1}{2}M_{\mathrm{s}}\boldsymbol{m}\cdot\boldsymbol{B}_{\mathrm{demag}}. \tag{2.32}$$

The interaction is termed demagnetization interaction due to the orientation of the intrinsic magnetic field in magnetic matter. Suppose a permanent magnetic material in vacuum, thus the only source of the magnetic flux density is the magnetization within the material. The resulting field lines for the induction are closed loops, as shown for an individual magnetic moment in figure 2.1a. Within the material, as shown in figure 2.1b, the magnetic field, $\boldsymbol{H}$, has to oppose the magnetization $\boldsymbol{M}$, and thus it is called demagnetizing field. The orientation of the intrinsic magnetic field is given by $-\boldsymbol{m}$. Outside the material, the dipolar fields are responsible for the long-range stray field.

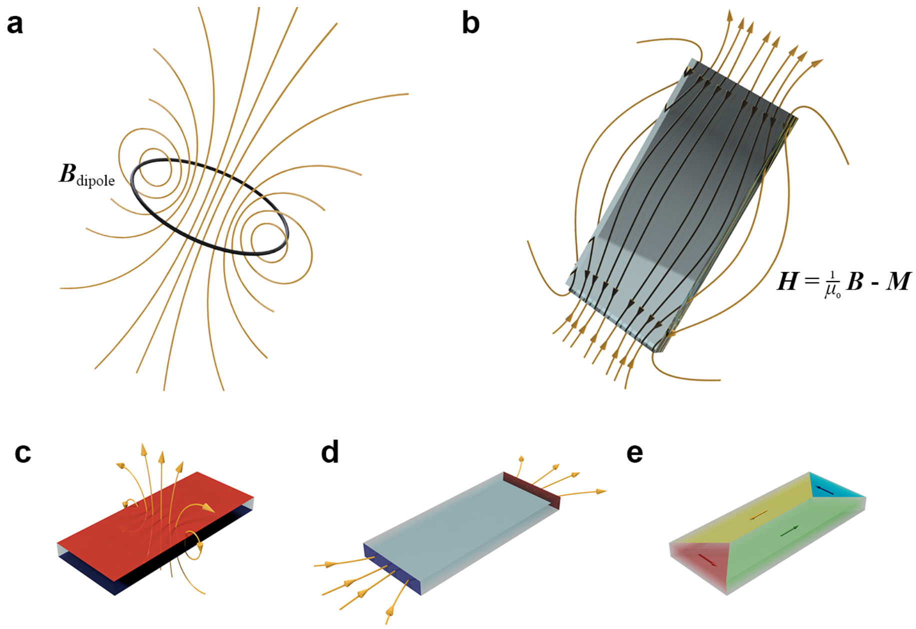

Figure 2.1: Demagnetization interaction. **a**, magnetic flux density $\boldsymbol{B}_{\text{dipole}}$ (yellow lines) emerging from a single dipole represented by the equivalent current loop (black). **b**, magnetic field $\boldsymbol{H}$ for a uniformly magnetized material. Outside the material it accounts for the stray magnetic field $\boldsymbol{H}_{\text{stray}} = 1/\mu_0\boldsymbol{B}$. Whereas within the material it opposes the magnetization $\boldsymbol{M}$, i.e. effectively partially demagnetizing it. **c**, energetically least favorable scenario, an out-of-plane magnetized thin platelet, resulting in large net magnetic poles at the surfaces (red, blue) and strong magnetic stray field (yellow). **d**, the same sample geometry uniformly magnetized in-plane yields smaller poles (red, blue) and reduced stray field (yellow). **e**, the energetically ideal case, an in-plane flux-closure domain pattern, eliminating all unmatched net magnetic poles and minimizing the stray field. The colors and arrows mark the direction of the magnetization within the domains. Panels **a**, **b** reproduced with permission from [86]. Panels **b**, **c**, **d**, created from additional artwork courtesy of collaborator E. Lysne.

The demagnetization interaction is often referred to as shape anisotropy, due to the major impact the shape of the magnet has. Remaining with the above example of a permanent magnetic material in vacuum and the magnetization being saturated everywhere, the only remaining degree of freedom is the orientation of the magnetization. Assuming a thin platelet magnetized perpendicular to the plane, see figure 2.1c, yields large stray fields and a strong demagnetization field. The latter can be explained in terms of a laterally expanded magnetic north and south pole, separated only by the relatively small thickness of the platelet. Note that the magnetic poles can be understood in the concept of a magnetic charge density, see equation 2.19, analogous to the surface charges in materials with electric polarization. In contrast, the same platelet magnetized in-plane (figure 2.1d) results in an energetically preferential state with smaller magnetic poles being spaced apart further and weaker magnetic stray field. Figure 2.1e shows the ideal orientation of the magnetization, causing the lowest energy contribution of the demagnetization term to the total energy. Here, due to the introduction of domains (confer section 2.1.5) the stray field can be eliminated almost completely and the formation of unmatched poles can be avoided alltogether. The formation of domains however results in an energy cost associated with the formation of domain walls in between domains of uniform magnetization. Here, the spins located in the boundary layer occupy an energetically unfavorable state due to the Heisenberg exchange interaction covered in the next section. At any given surface, the demagnetization interaction generally favors an in-plane configuration, which reduces the stray field and the formation of locally unmatched net magnetic poles.

Heisenberg exchange interaction

Many magnetic phenomena can be understood considering the mutual interactions transmitted via the magnetic field associated with the individual magnetic moments. Whilst in very close proximity, these interactions favor a parallel, so-called ferromagnetic, alignment of neighboring spins. Therefore, this interaction yields two problems. On one hand, this would rule out the existence of densely packed antiparallel aligned moments, i.e. the existence of an antiferromagnet. On the other hand, the energy gain associated with the ferromagnetically aligned dipole-dipole interaction is easily superseded by thermal fluctuations, long before the Curie temperature T_C, and a subsequent breakdown of the magnetic long-range order, is reached. Thus, the magnetic order must have a different and stronger source.

The Heisenberg exchange interaction resulting in the much stronger alignment is of quantum mechanical origin and a direct result of the coulomb interaction and the Pauli principle [87]. Following the outline of the Heitler-London method a system of two protons, A and B, fixed in space, orbited by two electrons, denoted 1 and 2, is considered. That is the equivalent of the H_2 molecule [83, 84]. This model system can be described by the Hamiltonian

$$\begin{aligned} \mathcal{H} &= \mathcal{H}_0 + \mathcal{H}' \\ &= \frac{1}{2m}\left(p_1^2 + p_2^2\right) - \frac{e^2}{4\pi\epsilon_0}\left(\frac{1}{r_\mathrm{A1}} + \frac{1}{r_\mathrm{B2}}\right) \\ &\quad + \frac{e^2}{4\pi\epsilon_0}\left(\frac{1}{r_\mathrm{AB}} + \frac{1}{r_{12}} - \frac{1}{r_\mathrm{B1}} - \frac{1}{r_\mathrm{A2}}\right), \end{aligned} \tag{2.33}$$

where p_i denotes the momentum and r_{xx} the distances in between the particles as shown in figure 2.2. Note the unperturbed first part $\mathcal{H}_0$ contains the

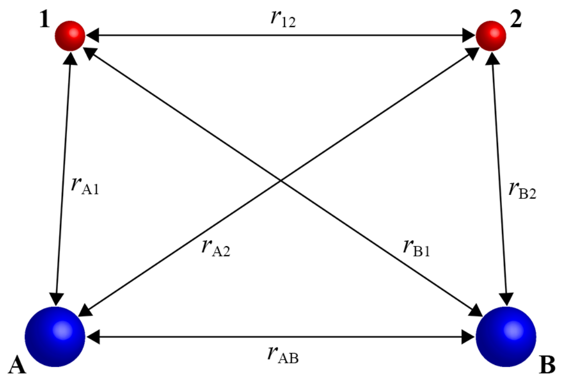

Figure 2.2: Schematic distances in the hydrogen molecule. Here, the blue spheres labeled A and B indicate the nuclei, which are considered fixed in space. The corresponding electrons (red) orbiting the nuclei A and B are labeled 1 and 2, respectively. The inter-particle distances are denoted accordingly. Recreated from [84].

kinetic and potential energy of the two free electrons, effectively representing the Hamiltonian of two infinitely spaced apart hydrogen atoms. The second part contains the perturbations attributed to the mutual coulomb repulsion of the two protons and two electrons, respectively, and the attractive forces of the protons on the electrons associated with the respective other proton. Solving the Schrödinger equation for the perturbed Hamiltonian yields two energy eigenstates [83, 84]:

$$E' = \frac{C \pm J}{1 \pm S^2} \propto C \pm J, \tag{2.34}$$

where C is the coulomb integral, J is the exchange integral and S is the overlap integral:

$$C = \int \mathrm{d}^3 r_1 \mathrm{d}^3 r_2 \; \mathcal{H}' \; |\psi_\mathrm{A}(\boldsymbol{r}_1)|^2 |\psi_\mathrm{B}(\boldsymbol{r}_2)|^2, \tag{2.35}$$

$$J = \int \mathrm{d}^3 r_1 \mathrm{d}^3 r_2 \; \psi_\mathrm{A}^*(\boldsymbol{r}_1)\, \psi_\mathrm{B}^*(\boldsymbol{r}_2) \;\; \mathcal{H}' \;\; \psi_\mathrm{A}(\boldsymbol{r}_2)\, \psi_\mathrm{B}(\boldsymbol{r}_1)\,, \tag{2.36}$$

$$S = \int \mathrm{d}^3 r \; \psi_\mathrm{A}^*(\boldsymbol{r})\, \psi_\mathrm{B}(\boldsymbol{r})\,. \tag{2.37}$$

Note, the energetically favored state depends on the sign of J. Initially $J > 0$ is assumed and subsequently the antisymmetric linear combination is the favorable state. This restriction acts on the spatial part $\psi(\boldsymbol{r}_i)$ of the total wave function

$$\psi(i) = \psi(\boldsymbol{r}_i)\chi_i \tag{2.38}$$

of the electron i with spin χ_i. Taking the Pauli exclusion principle into consideration, the total wave function has to be antisymmetric for fermions. Thus, the linear combination of the spin terms χ_1 and χ_2 has to be symmetric, resulting in the $\mathbf{s} = 1$ triplet state associated with ferromagnetic alignment. Analogous for $J < 0$, the symmetric linear combination of the spatial part of the wave function is favored, and therefore the spin part has to be antisymmetric, leading to antiferromagnetic alignment of the spins.

The Hamiltonian represents the simplest form of a two-atom system. It can be generalized to regard a N multi-electron-atom system [84]. The resulting Hamiltonian contains the ground state energy of all individual electrons $\mathcal{H}_0$ and a perturbation. The Heisenberg exchange [81, 84, 87]

$$\mathcal{H}_{\text{exch}} = -\sum_{i,j} J_{ij}\mathbf{S}_i \cdot \mathbf{S}_j, \tag{2.39}$$

expressed directly dependent on the individual spins $\mathbf{S}_i$ and $\mathbf{S}_j$, as well as their respective exchange constant J_{ij}. Analogous to the two-spin model the sign of J_{ij} determines whether parallel, i.e., ferromagnetic ($J_{ij} > 0$) or antiferromagnetic ($J_{ij} < 0$) alignment is favored. Both cases are illustrated in figure 2.3 for a 1D chain of spins. The sign of J_{ij} can in principle vary depending on the electrons considered. E.g. in case of a 3D layered crystal yielding ferromagnetic coupling within a layer but antiferromagnetic coupling in between layers. Cases like the latter and antiferromagnets in general are not well suited for study via micromagnetic considerations as they do not comply with the assumption of almost parallel spin alignment within the exchange length.

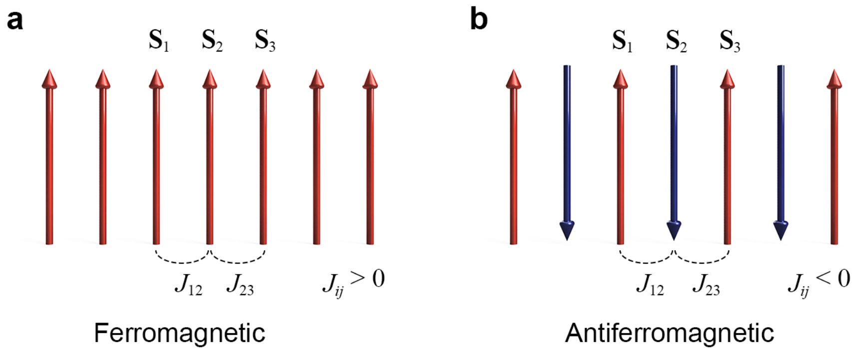

Figure 2.3: Heisenberg exchange. a ferromagnetic (parallel) alignment of neighboring spins, due to a positive exchange constant. **b** antiferromagnetic (antiparallel) alignment of neighboring spins due to a negative exchange constant. Recreated from [86].

In contrast, for ferromagnetic materials, it is sufficient to average the individual inter-atomic exchange constants in a general term. On the micromagnetic scale this yields the exchange stiffness:

$$A = N\frac{J_{\text{ex}}S^2}{a}, \tag{2.40}$$

where J_{ex} is the average exchange integral, a is the lattice constant, and N is a correction factor for the crystal structure. Subsequently, the exchange interaction can be rewritten in the form of the effective exchange induction [64]

$$\boldsymbol{B}_{\text{exch}} = 2\frac{A}{M_{\text{s}}}\nabla^2\boldsymbol{m}, \tag{2.41}$$

and the corresponding energy density is

$$\varepsilon_{\text{exch}} = A\left(\nabla\boldsymbol{m}\right)^2. \tag{2.42}$$

Interestingly, though acting on the spin configuration, the Heisenberg exchange is a purely quantum mechanical effect that outweighs the magnetic dipole-dipole interaction. Originating from Coulomb interactions and the Pauli Principle, it explains the origin of (anti-)ferromagnetism. Thus, any deviation in the form of a rotation between neighboring spins, e.g. in case of the aforementioned domain walls, is taxed in the energy term associated with the Heisenberg exchange, due to the scalar product $\mathbf{S}_i \cdot \mathbf{S}_j$.

Dzyaloshinskii-Moriya interaction

The interaction is formally known as antisymmetric exchange, termed by D. Treves and S. Alexander in 1962, when they reported the observation thereof in yttrium orthoferrite [88]. Today, it is most commonly referred to by the name Dzyaloshinskii-Moriya interaction (DMI), due to their seminal contributions to the explanation of the interaction. I. Dzyaloshinskii proposed a thermodynamic theory based on the work of L. Landau to explain weak ferromagnetism in antiferromagnets [89]. He derived an explanation for the anisotropic superexchange based solely on symmetry arguments. In the following years T. Moriya identified spin-orbit coupling as the mechanism behind the asymmetric exchange [90]. On the microscopic scale, the interaction is represented by an additional term to the total Hamiltonian

$$\mathcal{H}_{\mathrm{DM}} = -\sum_{i,j} \boldsymbol{D}_{ij} \cdot (\mathbf{S}_i \times \mathbf{S}_j)\,, \tag{2.43}$$

where $\boldsymbol{D}_{ij}$ is the Moriya vector, which can only be finite for bonds with no inversion center. The interaction favors orthogonal alignment of spins $\mathbf{S}_i$ and $\mathbf{S}_j$, as well as $\boldsymbol{D}_{ij}$.

In the continuum limit, such antisymmetric interactions are present only in non-centrosymmetric compounds, i.e. in materials missing the global inversion symmetry. In cubic chiral magnets the effective magnetic flux density related to such an antisymmetric term reads[91]

$$\boldsymbol{B}_{\mathrm{DM}} = \frac{2D}{M_{\mathrm{s}}} \left(\frac{\partial m_z}{\partial x}, \frac{\partial m_z}{\partial y}, -\frac{\partial m_x}{\partial x} - \frac{\partial m_y}{\partial y} \right). \tag{2.44}$$

Here D represents the strength of the interaction. The energy density of the DMI is given by

$$\varepsilon_{\mathrm{DM}} = D\boldsymbol{m} \cdot (\nabla \times \boldsymbol{m})\,. \tag{2.45}$$

Favoring an orthogonal orientation of spins, the DMI competes with the aforementioned Heisenberg and demagnetization interactions, which favor parallel or antiparallel spin alignments. The competition between these interactions typically results in canted spins for the energetic ground state of a system.

Magnetocrystalline anisotropy interaction

Possible reasons for the anisotropic behavior of the magnetic susceptibility are the shape anisotropy rooted in the dipole-dipole interaction and the magnetocrystalline anisotropy. The first explains anisotropic behavior, like the aforementioned favored in-plane magnetized state of a thin platelet, which is associated with the samples shape, and is neglected in the deliberations hereafter. Whereas the magnetocrystalline anisotropy accounts for the lattice, being the consequence of the relativistic spin-orbit interaction. Here, the partial quenched orbital angular momentum of electrons, contributing to the magnetic structure, is coupled to the crystalline electric field [84]. Thus, the electrons interact with the anisotropic lattice.

Generally, the concrete form of the anisotropy is deduced from the lattice symmetry and thus can be determined by the symmetry group. Uniaxial anisotropy occurs if the symmetry is highly restricted and only one high symmetry axis exists [64]. The direction of the anisotropy can be described by a single vector $\boldsymbol{u}$. Hence the scalar product $\boldsymbol{u} \cdot \boldsymbol{m}$ quantifies the alignment with the anisotropy. Due to symmetry reasons $+\boldsymbol{u}$ and $-\boldsymbol{u}$ are magnetically equivalent and thus the associated energy density can be expanded in even powers

$$\begin{aligned} \varepsilon_{\text{anis,u}} &= \sum_n -K_{\text{un}} \left(\boldsymbol{u} \cdot \boldsymbol{m}\right)^{2n} \\ &= -K_{\text{u1}} \left(\boldsymbol{u} \cdot \boldsymbol{m}\right)^2 - K_{\text{u2}} \left(\boldsymbol{u} \cdot \boldsymbol{m}\right)^4 + \mathcal{O}(\boldsymbol{m}^6), \end{aligned} \tag{2.46}$$

where K_{un} denotes the n^{th} uniaxial anisotropy constant. Usually considering the leading terms in the expansion K_{u1} and K_{u2} are sufficient to describe the anisotropy, while higher order terms can be omitted. The corresponding flux density in the micromagnetic framework is thus given by

$$\boldsymbol{B}_{\text{anis,u}} = \frac{2K_{\text{u1}}}{M_{\text{s}}} \left(\boldsymbol{u} \cdot \boldsymbol{m}\right) \boldsymbol{u} + \frac{4K_{\text{u2}}}{M_{\text{s}}} \left(\boldsymbol{u} \cdot \boldsymbol{m}\right)^3 \boldsymbol{u}. \tag{2.47}$$

In the discrete lattice model the corresponding Hamiltonian reads [84]

$$\mathcal{H}_{\text{anis,u}} = -\sum_{i,j} K_{ij} S_i^z S_j^z, \tag{2.48}$$

where K_{ij} is the anisotropy constant and S^z denotes the z-component of the spin. Evidently the energetically preferential state with respect to uniaxial anisotropy is given by all spins aligning along or opposite to the anisotropy axis.

Zeeman interaction

Lastly, the interaction of an external magnetic field with the magnetic material is considered. Unlike the aforementioned intrinsic interactions emerging naturally for a given system, the external magnetic field is easily tunable. Equation 2.23 already describes the energy gain attributed to lifting the degeneracy of the energy levels of an electron under the influence of an external magnetic flux density. As the levels split, the ones representing a magnetic moment aligned parallel with respect to the external flux density, are energetically lowered, whereas the antiparallel alignment yields a raise of the energy level. This is represented by the Zeeman Hamiltonian [84]

$$\mathcal{H}_{\text{Z}} = -2\frac{\mu_{\text{B}}}{\hbar} \mathbf{s} \cdot \boldsymbol{B}_{\text{ext}}, \tag{2.49}$$

considering a spin only system. The Zeeman interaction is directly represented in the micromagnetic framework by the external flux density $\boldsymbol{B}_{\mathrm{ext}}$, therefore the energy density yields

$$\varepsilon_{\mathrm{Z}} = -\frac{1}{2} M_{\mathrm{s}} \boldsymbol{m} \cdot \boldsymbol{B}_{\mathrm{ext}}. \tag{2.50}$$

Here the system gains energy, due to the occupation of parallel, thus favorable, energy levels. In the case of a paramagnet, the orientation of the magnetic moments is considered random in zero field. Hence, the easiest picture of lifting the (anti-)parallel degeneracy along the field direction is only partially explaining the Zeeman effect. Additionally, canting of the magnetic moment with respect to the field direction is associated with an energy cost. Overall the Zeeman interaction favors spin alignment parallel to the external field.

2.1.4 Emergent Magnetic Order

All materials exhibiting a net magnetic moment on the atomic length scale, in other words, all paramagnetic materials, are in principle capable of forming ordered magnetic states. These range from simple uniform magnetized states, over peculiar fragmented patterns, to spirals and skyrmions, laying the foundation for the topologically protected spin textures, covered in section 2.2. At room temperature though, only few pure elements like Fe, Ni, and Co exhibit long-range ferromagnetic order, and thus, are generally recognized as magnetic materials. A multitude of other materials on the other hand require low temperatures to spontaneously develop magnetic order.

The transition temperature below which materials exhibit ordered magnetic states is called Curie temperature T_{C} for ferromagnets, and Néel temperature T_{N} for antiferromagnets, respectively. Above the transition temperature the thermally induced random fluctuations outweigh the energy gain from occupying an energetically favorable ordered state. Therefore, the material is a paramagnet. Below T_{C} the saturation magnetization $M_{\mathrm{s}}(T)$ varies with temperature. Approaching the transition temperature from below, the saturation magnetization gradually decreases to zero at T_{C}, due to the thermal fluctuations. Only for low temperatures $T \ll T_{\mathrm{C}}$ the system reaches true saturation, where all moments are aligned.

For a fixed temperature $T < T_{\mathrm{C}}$ the saturation magnetization $M_{\mathrm{s}}(T)$ still satisfies the underlying assumptions of the micromagnetic framework as it can be considered constant. However, micromagnetic theory is not well suited to describe antiferromagnetic alignment. Hence, hereafter the considerations for emergent magnetic order are limited to systems where the spins form a ferromagnetic arrangement locally, though the magnetization direction show spatial variations on scales much larger than the lattice constant.

The ground state magnetization within a material at a given temperature is rarely uniform and the hierarchy of magnetic interactions determines the actual spin texture. The Heisenberg exchange interaction is usually the strongest interaction, with an effective induction of up to $\boldsymbol{B}_{\mathrm{exch}} = 1\,\mathrm{kT}$ [81] and thus the starting point. It favors parallel alignment of neighboring spins, and therefore, ferromagnetic long-range order. At this point the ferromagnetic order has no preferential orientation in space. This is altered due to the magnetocrystalline anisotropy which dictates favorable orientations relative to the lattice. The addition of the demagnetization interaction gives rise to more complex magnetic textures. As discussed above the demagnetization term generally favors magnetic textures avoiding large stray fields and the formation of magnetic poles. In certain cases, this can be realized by gradual rotation of the spins. However, in case of strong ferromagnetic coupling and magnetocrystalline anisotropy the resulting structure is commonly a complex pattern of small ferromagnetic regions, also called ferromagnetic domains. The magnetization of these domains can point along any of the energetically preferential directions. Depending on the type of anisotropy and the relative strength of the interactions a multitude of patterns can arise. A small selection of cases relevant for this work will be covered in the next section.

2.1.5 Magnetic Domains

Domains are spatially confined regions of uniform magnetization. Since a monodomain state is rarely energetically favorable for a material, multi-domain states form. Where these individual domains meet, a boundary layer called domain wall is formed. Within the wall, the magnetization gradually rotates bridging the mismatch of the orientation of the magnetization. Evidently, the slight canting between neighboring spins, required to gradually rotate the magnetization, is taxed in energy cost associated with the Heisenberg exchange. The respective energy density (equation 2.42), in the micromagnetic model, yields no contribution for the uniform magnetization within the ferromagnetic domains, where $\nabla \boldsymbol{m}(\boldsymbol{r}, t) = 0$. Thus, the only non-zero contributions to the exchange energy density originates from the domain walls. Therefore, in the context of materials solely exhibiting ferromagnetic domains, the contribution of the exchange interaction is often termed domain wall energy [64]:

$$E_{\text{wall}} = \int\limits_V \varepsilon_{\text{exch}} \mathrm{d}V = \sigma_{\text{wall}} \cdot A_{\text{wall}}. \tag{2.51}$$

Where V is the volume containing the domain walls, and A_{wall} is the actual area of boundary layer. Often the domain wall energy is alternatively expressed in the form of a domain wall energy density per unit area σ_{wall}. In the absence of antisymmetric interactions a 180° mismatch of two neighboring domains allows two types of walls as illustrated in figure 2.4. The spins can either rotate in the plane of the domain wall, forming a Bloch wall. Or a Néel wall is formed, where the spins rotate perpendicular to the wall.

In many systems, the magnetocrystalline anisotropy competing with the demagnetization interaction dictates the preferential orientations of the ferromagnetic domains. The special case of perpendicular uniaxial magnetic anisotropy (PMA), relevant for Fe_3Sn_2 is discussed in detail. In case of PMA, the uniaxial magnetic anisotropy is parallel to the surface normal of the sample. This results in a direct competition between the magnetocrystalline anisotropy, stabilizing an out-of-plane orientation of the magnetic moments, and the demagnetization interaction generally favoring an in-plane magnetization. The resulting magnetization distribution of lowest energy depends on the shape of the sample, external magnetic fields and other involved interactions. Thus, determining the ground state is a non-trivial task. Usually no analytic model can be employed

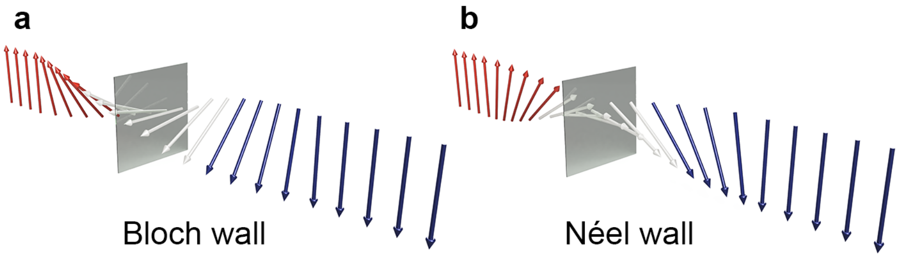

Figure 2.4: Fundamental types of magnetic domain walls. a, a Bloch wall, where the magnetization rotates in the plane of the wall. **b**, a Néel wall, where the magnetization rotates perpendicular to the plane of the wall. Recreated from [86].

to solve this problem exactly. The rare cases, that can be solved analytically, are limited to particular parameter sets, like very strong anisotropy competing with rather weak dipolar interactions. These results cannot be employed universally to explain the large variety of emerging domain patterns. But they represent easy-to-grasp examples, and therefore, a good starting point for instructive cases.

Focusing on the consideration of PMA in a ferromagnetic material in zero field, the resulting magnetization distribution is determined only by the balance of the magnetocrystalline anisotropy energy density, proportional to K_u and the shape anisotropy K_d, determined by the demagnetization energy density [64]. The quality factor [92]

$$Q = \frac{K_\mathrm{u}}{K_\mathrm{d}} = \frac{2K_\mathrm{u}}{\mu_0 M_\mathrm{s}^2}, \tag{2.52}$$

describes this balance, where for simplicity only the first order anisotropy constant, previously denoted K_u1 in equation (2.47), is considered, and all higher order terms are omitted. The shape anisotropy per unit volume,

$$K_\mathrm{d} = \frac{1}{2}\mu_0 M_\mathrm{s}^2, \tag{2.53}$$

is approximated by the magnetostatically least favorable state, a plate magnetized normal to the surface as illustrated in figure 2.1c. Further assuming $K_\mathrm{u} > 0$, and $Q \gg 1$, yields the analytically solvable case of very dominant anisotropy, where the magnetization is forced to align either up or down along the axis of the PMA. Charles Kittel showed that in such cases the demagnetization energy can be significantly lowered to a factor of $1/N$ by the introduction of N alternating domains [93]. A finite number of domains will form, as the introduction of new domains comes at the energy cost of forming domain walls. The width of these walls, i.e. the distance over which the magnetization gradually rotates is the second parameter of major influence for the formation of domains. The Bloch wall width [93],

$$\delta_\mathrm{Bloch} = \sqrt{\frac{A}{K_\mathrm{u}}}, \tag{2.54}$$

is determined by the exchange stiffness, see equation (2.40), and the strength of the anisotropy [93]. Most importantly the Bloch wall width defines a lower limit for the size of domains [64]. Additionally, the walls are the only area where the magnetization deviates from the strict up or down orientation. In order to minimize their subsequent negative contribution to the total free energy, the volume occupied has to be minimal. In this particular case, the walls have to be oriented perpendicular to the surface throughout the material. Thereby minimizing the wall area, hence for the fixed width δ_{Bloch}, the volume.

Stripe and bubble domains

Typical ground states of such thin magnetic film like samples with strong PMA are quasi-periodic maze patterns, band-, or stripe patterns. In order to understand these complex patterns, first their building blocks have to be understood. Hence, the energy gain due to the introduction of a single straight stripe domain of opposite magnetization in a ferromagnetic background shall be considered. The energy per unit length $\hat{L}$ of the stripe is given by [94]

$$\frac{\Delta E_{\mathrm{stripe}}}{\hat{L}} = -\left(1 - N_{\mathrm{stripe}} - \hat{H}_{\mathrm{ex}}\right)\hat{w} + \frac{\xi}{t}, \tag{2.55}$$

where t is the sample thickness, N_{stripe} is the demagnetization factor for a stripe domain, $\hat{H}_{\mathrm{ex}}$ is the reduced external magnetic field in quantities of $4\pi M_{\mathrm{s}}$, and $\hat{w} = w/t$ is the stripe width to thickness ratio. $\xi = \sigma_{\mathrm{wall}}/4\pi M_{\mathrm{s}}$ represents the domain wall energy and can be considered fixed per unit length for a given material. In zero field, this equation yields an optimal stripe width w_{stripe} for the given sample thickness t. The introduction of a single stripe of according width is associated with lowering the systems total energy. As the energy lowering is given per unit length, ideally this stripe grows to the maximum possible length.

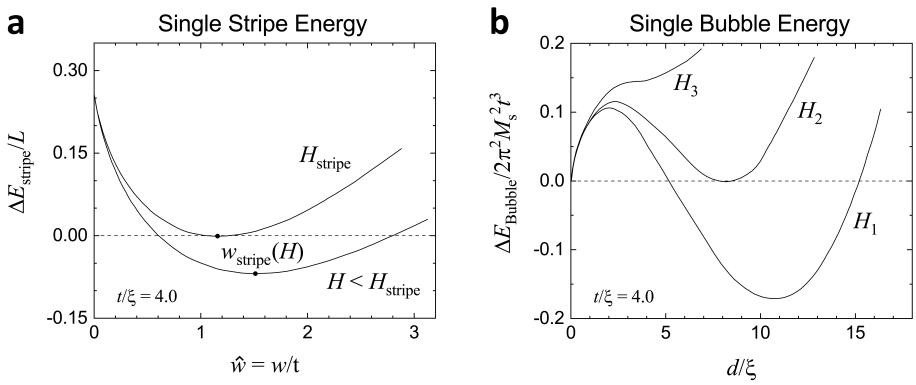

Figure 2.5: Plots of the energy of a single stripe and bubble. a, energy per unit length of a single stripe domain plotted versus the stripe width according to equation (2.55). **b**, energy of a single bubble dependent on its diameter according to equation (2.56), for different fields. Recreated from [94].

Lifting one of the previous assumed constraints, additionally the effect of the Zeeman interaction shall be taken into consideration. Applying small external fields parallel to the ferromagnetic background, the optimal stripe width is gradually decreasing until the critical field H_{stripe} is met. Fig. 2.5a illustrates this behavior, where the minimum of the curve shifts towards smaller width. At the critical field the energy lowering from the introduction of a stripe domain vanishes, i.e. the minimum of the respective curve is zero. Thus, for all fields $H > H_{\text{stripe}}$ applied, the stripes contract along their length as they are no longer energetically favorable. The contracted stripes give rise to another type of domain, the bubble domain. These are typically confined by a cylindrical domain wall. The latter implies circular shape, which is indeed the preferential shape, due to the minimized domain wall area for a given domain size with the above-mentioned constraints. The energy for such a single bubble domain embedded in a ferromagnetic background is given by [94]

$$\Delta E_{\text{bubble}} = -\left(1 - N_{\text{bubble}} - \hat{H}_{\text{ex}}\right)\hat{d}^2 + 2\left(\frac{\xi}{t}\right)\hat{d}, \tag{2.56}$$

where N_{bubble} is the demagnetization factor of the bubble and $\hat{d} = d/t$ is the bubble diameter to thickness ratio. Note, this equation describes a bubble far from the edge of the sample, as edge pinning and similar confinement induced influences are omitted. Analogous to the description of the stripe width, equation (2.56) yields an optimal diameter for the bubble. For a given sample thickness t, the application of external field $\hat{H}_{\text{ex}}$ results in one of three cases. The first one, represented by $\hat{H}_{\text{ex}} = H_1$ in fig. 2.5b, describes a bubble and its ideal diameter, which yields a lowering of the total energy when being introduced into the system. Thus, the bubble is stable and furthermore can form spontaneously. The upper field limit for this first case is shown by $\hat{H}_{\text{ex}} = H_2$, where the local minimum is zero. Hence, the formation of a new bubble is no longer preferential. However, shrinking and ultimately dissolving the bubble domain in fields larger than H_2 is hindered by the energy barrier (the local maximum in the curve), which is associated with intermediate diameters of the shrinking bubble during the transition. As a result, the preexisting bubble remains in a meta-stable bubble phase up to the critical field H_3, where the bubble is no longer stabilized, dissolves, and gives rise to the uniform ferromagnetic order.

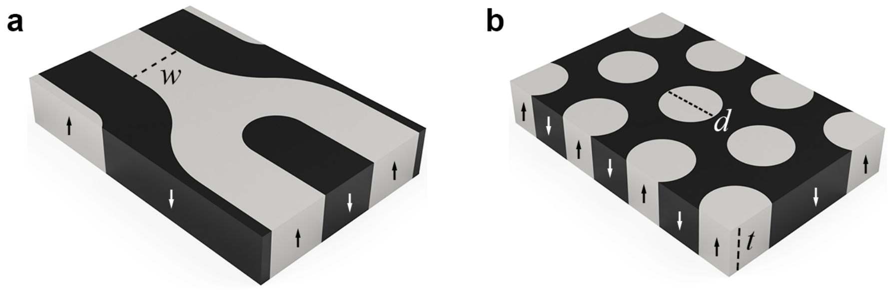

Figure 2.6: Schematic domain configurations for high Q materials. **a**, Typical periodic stripe domain pattern, and **b**, regular lattice of bubble domains for a material with $Q \gg 1$. The stripe width w, bubble diameter d and sample thickness t are marked accordingly. The black and white color denotes the out-of-plane orientation of the magnetic domains.

In summary, below a critical field the total energy of the system is lowered by the introduction of a stripe or bubble domain of opposing magnetization, i.e. they form spontaneously. In a small field range above this critical field, a preexisting bubble domain can persist in a meta-stable phase. Towards lower fields the bubble diameter increases slightly. Eventually, the bubble expands into a stripe, which generally tends to grow to maximum length. Note that the bubble can persist to fields $\hat{H}_{\mathrm{ex}} < H_{\mathrm{stripe}}$, in some cases even being the remanent state.

While the formation of a domain requires it to be energetically favorable, defects and random fluctuations usually are the nucleation points. Thus, a magnetic material rarely forms only a single domain, but several. Each formed domain contributes with the respective net reduction of the systems energy. However, as the domains become more densely packed, their interactions cannot be neglected either. The change in the total energy due to the introduction of multiple domains reads [94],

$$\begin{aligned}\Delta E_{\mathrm{total}} &= \sum_i \Delta E_{\mathrm{single,i}} + E_{\mathrm{int}} \\ &= N \cdot \Delta E_{\mathrm{single}} + E_{\mathrm{int}},\end{aligned} \tag{2.57}$$

where the sum is carried out over all domains i. $\Delta E_{\mathrm{single,i}}$ denotes the respective energy lowering associated with a single domain, which can be further simplified in case of N domains of equal type. E_{int} describes the inter-domain interactions collectively, which can be approximated by assuming the domains being large dipoles with an associated magnetic moment. Domains spread far apart have little to no effect on each other, whereas closely packed domains interact strongly. However, these interactions are strictly dependent on the exact type and shape of the individual domains involved. In-depth analyses are limited to the study of particular cases, and not covered here.

In zero field, the ground state is typically given by the equilibrium state of multiple stripes alternately magnetized up and down along the PMA. The gain from the demagnetization interaction is balanced with the energy cost of the domain walls. Each stripe nucleating from a quasi-random site grows to the maximum possible length, yielding endless variations of patterns of alternating up and down domains with a fixed stripe width [95]. The exact morphology of the stripe pattern (see figure 2.6a) either being oriented, or a random maze-like pattern, depends on numerous factors. Detailed predictions for such patterns are beyond the scope of this thesis.

Under the application of external field ($H_{\mathrm{stripe}} < H < H_3$) a pure bubble phase is realized. The preferential domain configuration for multiple bubbles is a densely packed lattice [96, 97]. Intuitively, a triangular lattice, as shown in figure 2.6b, yields the densest packing and should be favored. Detailed analysis of the inter-domain dipolar interactions, E_{int}, for a triangular and square lattice yields merely a difference of 1% [94]. Either lattice is thus readily formed when stabilized by sample geometry, interstitials, or dislocations.

Domain branching

In the simplest picture, for a high Q material ($Q \gg 1$) with PMA, the domain walls are perpendicular to the surface throughout the material. Thus, the domain width is the same near the surface, w_{s}, and in the bulk, w_{b}. In this context, bulk refers to the core region of a material, i.e. far from the surface for the respective geometry. Intriguingly, the ideal width or diameter of stripe and bubble domains, according to equations (2.55) and (2.56) above, is given in relation to the sample thickness. Hence, a thickness dependence of the domain width is expected. Indeed, the domain width scales with the specimen thickness [64]

$$w_\mathrm{s} = w_\mathrm{b} = \sqrt{\frac{\gamma_\mathrm{W}}{2C_\mathrm{s}} t} \propto t^{1/2}, \tag{2.58}$$

where γ_W is the specific domain wall energy, and C_s is a phenomenological parameter, describing the energy term associated with the closure energy. Flux-closure effects will be covered in more detail in the next section. This scaling law, with a $\sqrt{t}$ dependence, is commonly referred to as the Kittel scaling law [98, 99]. It does however not hold true universally, as it is only accurate in a limited thickness range. With increasing domain size, it is eventually superseded due to the onset of domain branching. Branching is a peculiar phenomenon, where the domain pattern at the surface deviates from the bulk, once a certain threshold thickness is overcome. This critical thickness for the onset of domain branching is given by [64]

$$t_\mathrm{branching} = \frac{\pi^4}{8} \gamma_\mathrm{W} \frac{F_\mathrm{i}^2}{C_\mathrm{s}^3}, \tag{2.59}$$

where the internal field energy is described by the phenomenological parameter F_i. In the specific case of a high Q material, the three relevant factors can be estimated as follows [64]

$$\gamma_\mathrm{W} = 4\sqrt{AK_\mathrm{u}} \tag{2.60}$$

$$C_\mathrm{s} = \frac{0.272\, K_\mathrm{d}}{1 + \sqrt{\mu^*}} \tag{2.61}$$

$$F_\mathrm{i} = \frac{0.5\, K_\mathrm{d}}{\mu^*}. \tag{2.62}$$

Here the rotational permeability tensor, μ^*, can be approximated to be [64]

$$\mu^* \approx 1 + \frac{1}{Q}. \tag{2.63}$$

The critical thickness is thus mainly determined by the strength of the magnetocrystalline anisotropy, the demagnetization energy and the exchange stiffness, which allows an estimate of the critical thickness [64]

$$t_\mathrm{branching} \approx 5000Q\sqrt{\frac{A}{K_\mathrm{u}}} = 5000Q\delta_\mathrm{Bloch}. \tag{2.64}$$

If the sample thickness exceeds $t_\mathrm{branching}$ domain branching sets in. Conceptually, it is the result of optimizing the demagnetization interaction, whilst minimizing the cost for the introduced domain walls. The latter is achieved by very wide domains in the bulk, effectively reducing the domain wall area per unit volume. At the surface, these imply large unfavorable domains in terms of the demagnetization interaction. This is mitigated by the introduction of small domains of opposite magnetization, penetrating only the surface area, within the larger ones. A schematic illustration of such domains is shown in figure 2.7. The introduced domains lower the stray fields significantly, whilst

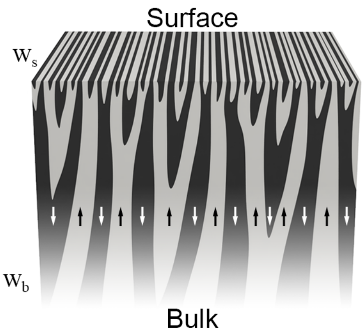

Figure 2.7: Domain branching in a high Q material. The effective surface area of the domains is reduced, due to the introduction of additional domains of opposite magnetization in the surface area. Recreated from [64].

imposing a rather small energy cost associated with their domain walls. Following previous arguments for segmentation of domains into smaller sizes, the existence of a lower limit for the size of the nested domains is apparent. Thus the domain width at the surface levels off at a constant value [64]

$$w_{\mathrm{s}} = 4\gamma_{\mathrm{W}} \frac{F_{\mathrm{i}}}{C_{\mathrm{s}}^2}. \tag{2.65}$$

In the bulk on the other hand, the morphology of the domains is now mainly influenced by the minimization of the domain wall area, as the demagnetization interaction is largely screened by the branched domain pattern at the surface. Hence, the rate at which the domains grow, relative to the thickness, increases further. The domain width in the bulk is given by [64]

$$w_{\mathrm{b}} = \sqrt[3]{\frac{4\gamma_{\mathrm{W}}}{\pi^2 F_{\mathrm{i}}} t^2} \propto t^{2/3}. \tag{2.66}$$

Evidently, only once the bulk area is significantly large compared to the near surface region, the gain from reducing the number of domain walls in the bulk balances the additional cost of the introducing small domains and partially bent walls at the surface.

Flux-closures and Néel caps

On the other end of the scale, the case of a very thin sample effectively represents the equivalent of a low Q material ($Q \ll 1$), where the demagnetization term is dominant over the magnetocrystalline anisotropy. To screen stray fields and minimize K_{d} these materials form so called flux-closure structures, where the magnetization is fully in-plane forming a closed loop. A simple case thereof is shown fig. 2.1e, where the flux-closure pattern is formed by domains. In accordance with the diminishing energy gain of domains compared to the cost of domain walls, numerical simulations predict the lower limit of the thickness for such closure-domain patterns is approximately [64]

$$t_{\mathrm{domain}} \approx 6\delta_{\mathrm{Bloch}}. \tag{2.67}$$

Below this thickness the formation of domains of uniform magnetization, arranged in a flux closure pattern, is superseded by a gradual rotation of the magnetization. Low Q states are of course not limited to very thin samples. In case of very weak magnetocrystalline anisotropy, which can occur independent of the sample shape, the magnetization behaves almost isotropic. Hence, allowing the magnetization to locally align with the overall magnetic flux. Whether domains are formed or the magnetization rotates gradually is determined by the relative strength of the exchange interaction and the dipolar interaction.

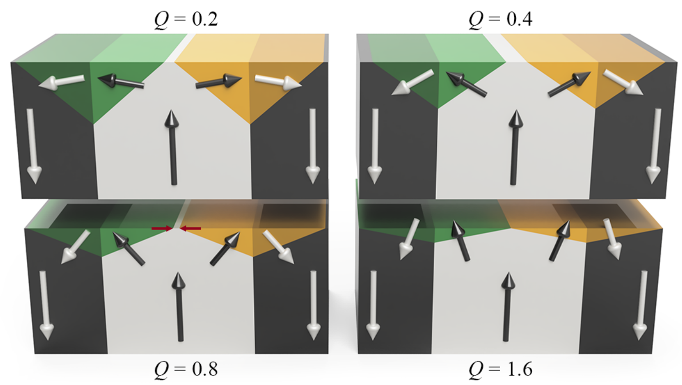

Figure 2.8: Possible flux-closure domains for intermediate Q materials. Four cases of flux-closure domains for different intermediate Q factors are shown. The arrows denote the orientation of the magnetization. The green and yellow domains represent domains of predominant in-plane magnetization, the flux-closure domains. Note the surface gap highlighted by the red arrows up to $Q = 0.8$. Recreated from [64, 86].

If the perpendicular magnetocrystalline anisotropy and the demagnetization interaction are evenly balanced, the emerging domain structure is hard to predict. Particularly analytical models, hinging on the assumption of either term being almost negligible compared to the other, fail to provide a good description. Therefore, in the intermediate Q range $(0.1 < Q < 1)$, where the interactions are balanced, numerical simulations are the means of choice to predict the magnetic texture. In contrast to the low Q materials where complete flux-closure is commonly observed, intermediate Q materials normally form partial flux-closure structures. These are termed partial, due to a remaining non-screened stray field, originating from a residual out-of-plane component of the magnetization at the surface [64]. A selection of flux closure domains patterns for different intermediate Q-factors is shown in fig. 2.8. Here, three trends with increasing Q-factor are evident. Firstly, the depth of the surface layer containing the flux-closure domains decreases. This is to be expected, as the volume fraction of non-aligned magnetization with the PMA is reduced. Secondly, the angle of canting decreases, which again is expected, due to the lower energy cost associated with the reduced misalignment. And lastly, a rather peculiar observation. The gap in-between opposing flux-closure domains shrinks towards higher Q-factors and eventually closes. But for low Q materials, it must and does vanish as well, as it contradicted complete flux-closure otherwise. Hence these unscreened surface areas are an entity of the intermediate Q materials.

Finally, a remark on the rotation of the magnetization through the domain walls. As mention above, for domain walls in-between 180°-domains the orientation of the rotation relative to the plain of the wall is not determined. Both Bloch and Néel walls are energetically equivalent with respect to their cost associated with the exchange. Whichever occurs is determined by additional interactions like the presence of DMI. Irrespective of the wall type in the bulk, the energetically favorable rotation to bridge the mismatch between flux-closure domains is perpendicular to the wall, i.e. of Néel-type. Furthermore, even the gradual rotation of flux-closure structures follows this direction of rotation. Hence the (partial) flux-closure patterns are also referred to as Néel caps. Though caps linguistically implies finishing a spatially constricted structure, like a bubble, the term Néel caps is also used in case of large, highly branched maze-like domain patterns exhibiting flux-closure.

Despite being the easy to grasp example, the case of PMA, as illustrated above, is by no means trivial to understand. Nevertheless, the field of micromagnetism is a lot broader and contains many more cases, like cubic magnets. Here even fewer restrictions are imposed and thus the complexity of the problem is significantly higher. Many of the basic concepts introduced can be adjusted to match these constraints. But particularly as analytical models fail to describe a vast majority of these cases, numerical simulations optimizing all interactions involved are a great tool to get an impression of the expected magnetic textures. An excellent summary, far beyond what is covered in this thesis, on the theory behind the micromagnetic textures and magnetic domains in general, can be found in the work of Hubert and Schäfer [64].

2.1.6 Magnetism on the Macroscopic Scale

In the macroscopic picture, magnetism is described in the context of collective behavior. In this picture, magnetic textures on the microscopic and mesoscopic scale can no longer be spatially and temporally resolved. In contrast to the definition given in equation (2.18), here the magnetization vector $\boldsymbol{M}$ is representing the average orientation of all moments within the volume occupied by the magnetic sample. The magnetic susceptibility χ, see equation (2.22), is the major observable, describing the response of the magnetization to the application of an external field. Dia- and paramagnetic behavior are discerned by a negative, respectively positive susceptibility.

Since the material investigated in this thesis is a ferromagnet, here, the consideration is limited to such cases. Upon cooling a ferromagnet below its Curie temperature, a random distribution of ferromagnetic domains of varying size emerges. This spontaneous emergence of magnetization manifests in hysteresis behavior, a non-linear response in the magnetization as a function of an applied field. Figure 2.9 depicts the typical hysteresis loop for a ferromagnet. The initial random distribution exhibiting no overall net magnetization is referred to as the virgin state. Upon applying a magnetic field, the domain structure adopts by reorientation, growth, and nucleation of domains [84]. Eventually, all intrinsic interactions are superseded by the Zeeman effect and a uniform mono-domain state is formed. This state represents magnetic saturation. The saturation value M_s extracted from the plateau in the curve, as denoted in the

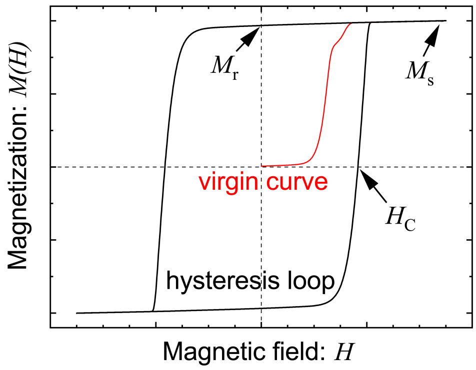

Figure 2.9: Schematic hysteresis loop. The graph shows the characteristic response of a ferromagnetic material to the application of external field H (black curve). Along the loop three distinct points are marked: the saturation magnetization M_s, the remanent magnetization M_r and the coercive field H_C. The virgin curve (red) differs from the loop until it reaches saturation.

figure, is still subject to thermal fluctuations. Only for temperatures $T \ll T_\mathrm{C}$ it resembles true saturation, which is reached asymptotically under the application of very large fields. Removing the field, yields the remanent magnetization M_r. In order to demagnetize the material, the coercive field H_C, opposing the existing magnetization, must be applied. H_C typically refers to the remanence coercivity, i.e. the field required to reduce the remanent magnetization, M_r, to zero. In the graph, H_C denotes the intrinsic coercivity, i.e. the field required to reduce the magnetization to zero, while it is applied. For the sake of completeness, the normal coercivity describing the field required to suppress the internal magnetic flux shall be mentioned as well. The latter is strongly influenced by the demagnetization field and the anisotropy fields. Upon applying strong enough field in the opposite orientation to the initial saturation, the magnetization decreases and eventually reaches saturation in the inverted orientation. Subsequently the loop can be completed back to $+M_\mathrm{s}$, by application of field in the original direction.

The area enclosed in the full loop is proportional to the energy required to fully switch the magnetization. Hence a hysteresis loop enclosing a large area, like the one displayed, characterizes a hard magnet. Hard refers to the robustness versus degaussing or switching. Soft magnets on the other hand excel at applications where constant switching is required, e.g. in a transformer, due to the low losses. The terms hard and soft magnets, thus describe the overall robustness, i.e. energy required to terminate or form a residual magnetization.

2.2 Topological Solitons

In the 1960s and 1970s classical field equations of the quantum field theory were studied in their fully nonlinear form. Some of the newly obtained solutions were interpreted as particles of the theory [100]. Unlike elementary particles originating from the quantization of the wave-like excitations of the field, the properties of these new solitons are mostly determined by the classical equations. These solitons are localized and have a finite energy. Furthermore, they are characterized by their topological structure which differs from vacuum. Hence, they are assigned a respective topological charge, which is a conserved quantity. Thus, these solitons cannot simply decay into a number of elementary particles.

In ferromagnetic systems, a soliton is a continuous magnetization field distribution, distinct from the ferromagnetic state. Due to the topological charge it is protected, i.e. it cannot be deformed continuously to the trivial uniform ferromagnetic order. A key requirement for the formation of solitons is the existence of a spontaneously symmetry-breaking phase transition yielding multiple degenerate ground states. In case of magnetism this transition is given by the paramagnetic to ferromagnetic phase transition, where time-reversal symmetry is broken. As a result, the magnetization field emerges which serves as the order parameter [70]. Upon lowering the temperature below T_C the full rotational symmetry of the paramagnetic phase is lost and the magnetization arranges in one of several energetically degenerate ground states [83].

The emerging topological solitons behave in many ways like particles, they are localized, possess a quantized topological charge, and move collectively under external stimuli [39, 101]. Therefore, they are often considered magnetic quasi-particles made up of collective spins. Additionally, peculiar emergent electromagnetic fields are generally associated with them, allowing efficient manipulation [40]. The first magnetic topological soliton discovered was the domain wall [102], but a much larger zoo of solitons has since been predicted, and several intriguing solitons were even observed experimentally. Particularly the two-dimensional solitons, the skymrions, attracted tremendous attention [25, 37, 40]. Skyrmions have a rich variety of novel properties associated with them. This makes them promising candidates as building blocks in spin-based electronic devices, often referred to as spintronics. Lower energy consumption, higher processing speeds, and increased data densities are predicted benefits of using skyrmion-based spintronics [21].

Beyond their emergence in magnetic materials [25, 37], skyrmions exist in Bose-Einstein condensates [103, 104], quantum Hall states [105, 106], and chiral nematic liquid crystals [107, 108]. Hence the topological theory behind their stabilization is a universal theory, and thus will be covered more generally before the topological solitons of highest interest for this work, the skyrmions, will be investigated in detail. Finally, a brief outlook towards application will be given and subsequently the peculiar phenomenon of Bloch points and lines will be considered.

2.2.1 The Role of Topology

Topology in its pure form is a classical field of study in mathematics. It is concerned with the study of geometrical objects and their properties under continuous deformations. A vivid example illustrating this study is the Möbius strip. Despite being a two-dimensional looped band, it requires a third dimension to exist, due to the embedded 180° twist. Furthermore, it is confined by a single edge and counterintuitively has only one surface. Through continuous deformations, such as bending, crumbling, and twisting, one can move the twist along the loop, but it is impossible to untwist the Möbius strip without breaking it. Here, breaking implies cutting open, untwisting, and regluing the loop. More generally, in the context of topology merging or forming new boundaries, particularly closing and opening of holes, and passing the object through itself are considered non-continuous transformations, which are forbidden. From a topological view point, the Möbius strip is thus inequivalent to the untwisted loop. Simply put, topology is concerned with the classification of geometrical objects, where all members of a class are considered equivalent as they can be continuously transformed into each other.

Now, this rough concept shall be formulated more precisely, in a framework fit to later describe physical phenomena in actual matter. The starting point for this is a so-called ordered medium, that is characterized everywhere by a continuously varying order parameter. Potential order parameters are the previously introduced magnetization or the electrostatic equivalent thereof, the polarization. Usually, the order parameter is parameterized as a vector describing its orientation and magnitude. The space solely containing all possible values the order parameter can take on, is termed the order-parameter space. In case of an ordered medium, every point $\boldsymbol{r}$ in real space can be mapped into order-parameter space by a function $f(\boldsymbol{r})$ [69, 109–111]. The crucial step, to evaluate the topological equivalence, is to map a contour in real space onto order parameter space, where the mapping yields a closed contour as well. Two mappings are homotopic, i.e. topologically equivalent, if their contours in order parameter space can be continuously transformed into each other.

To illustrate this process, a two-dimensional system, i.e. a medium in $\mathbb{R}^2$, where the order parameter is confined within the plane is considered. Additionally, the magnitude of the order parameter is assumed fixed to a constant value. Hence, the order parameter space is described by a circle of according radius. The circle is formally a sphere of dimensionality one, denoted S^1. Every potential direction the order parameter can take in real space is thus represented by the angle $\phi(\boldsymbol{r})$. The function mapping every point in real space, $\boldsymbol{r}$, to the order parameter space is therefore given by [110]

$$f(\boldsymbol{r}) = \boldsymbol{e}_1 \cos\phi(\boldsymbol{r}) + \boldsymbol{e}_2 \sin\phi(\boldsymbol{r}), \tag{2.68}$$

where $\boldsymbol{e}_1$ and $\boldsymbol{e}_2$ are orthogonal vectors in the plane. Now, a path in real space, e.g. a circle of diameter d, is chosen as the contour and thus the mapping function maps a sphere to a sphere,

$$f : S^1 \mapsto S^1. \tag{2.69}$$

Figure 2.10a, depicts this for the particular example of a uniform state in real space, where the order parameter is parallel to $\boldsymbol{e}_2$ everywhere. Mapping the contour in real space means mapping every point on the contour, while tracing counter clockwise along it. Here, for $f_1(\boldsymbol{r})$ every point on the contour in real space maps to one single point in order parameter space, independent of the diameter d and the location of the contour. Considering the distribution of

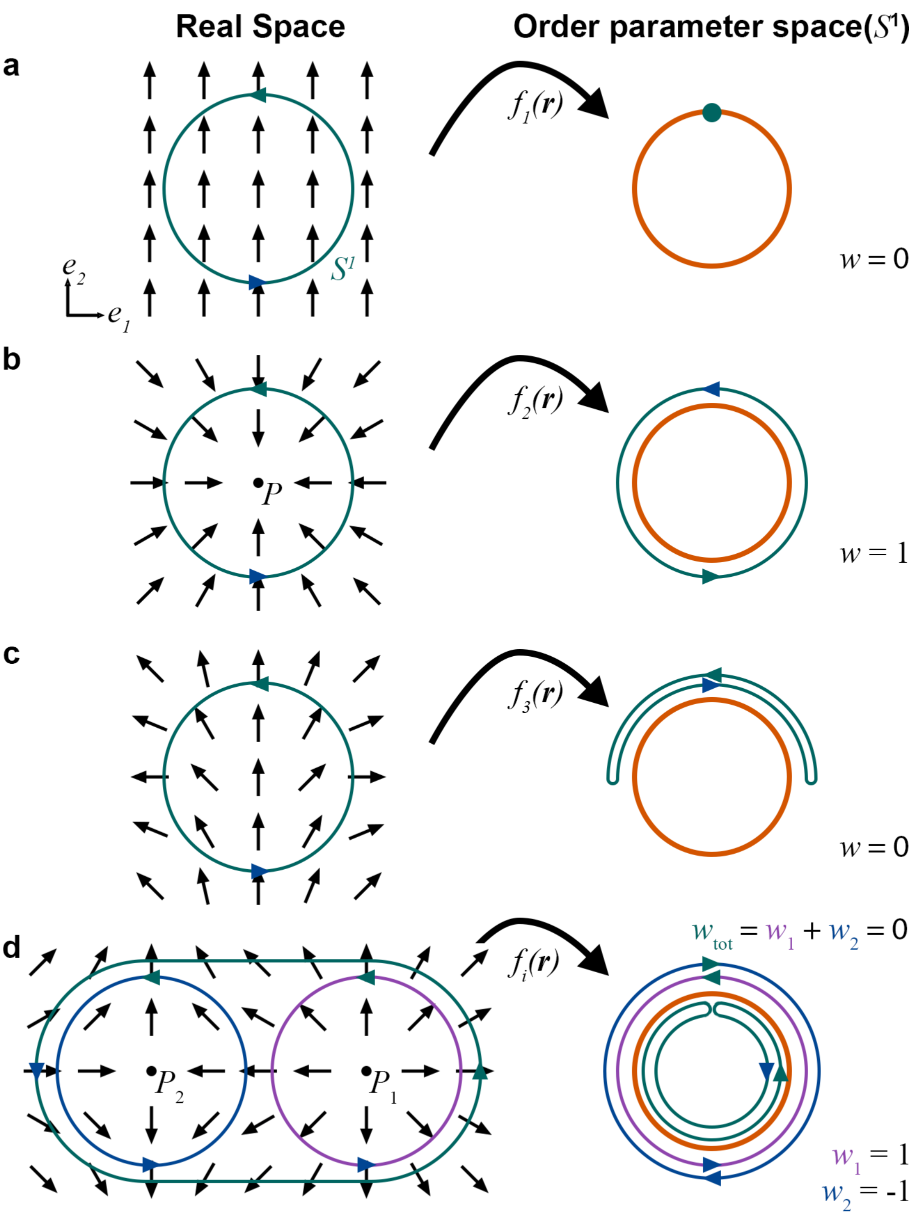

Figure 2.10: Schematic mappings of a planar order parameter. The order parameter with a fixed magnitude (black arrows) is spatially resolved in a two dimensional medium. The corresponding order parameter space is a circle (S^1, orange). Mapping, $f(\boldsymbol{r})$, a contour (green circle) into order parameter space yields a loop. The winding number corresponds to the number of times the loop wraps around the order parameter space. **a**, uniform state, $w = 0$. **b**, radial configuration around singularity P, $w = 1$. **c**, unstable defect, $w = 0$. **d**, the winding number of the total system (green loop) corresponds to the sum of the individual defects (purple and blue), $w_{\text{tot}} = w_1 + w_2 = 0$. Recreated from [112].

the order parameter around a singularity located in point P (see fig. 2.10b) shows a more complex behavior. Mapping a similar contour (S^1) enclosing the singularity, $f_2(\boldsymbol{r})$ results in a looped contour wrapping once around the whole order parameter space. Even if d is chosen almost infinitely large, as long as it encircles P, the resulting mapping will be similar. The number of times the contour wraps around the the order parameter space defines the winding number w. For this particular mapping it can be expressed as [111]

$$w = \frac{1}{2\pi} \int_0^{2\pi} \mathrm{d}r \frac{\partial}{\partial r} \phi(r), \tag{2.70}$$

where r is parameterized along the real space contour between $0 \leq r < 2\pi$. The winding number effectively counts the revolutions, in multiples of 2π, the order parameter turns, whilst tracing along the contour. For the uniform state, the winding number is $w = 0$, whereas for the radial singularity it is $w = 1$. Note, the sign of the winding number is determined by the match or mismatch of the direction of rotation of the real space contour and the mapped contour. For the singularity P, the contour is evaluated counterclockwise, i.e. mathematically positive, and the direction of rotation in the order parameter space is the same. Hence, the winding number is positive. A third example is illustrated in figure 2.10c. Mapping $f_3(\boldsymbol{r})$ yields a spaced-out loop that winds half way around the order parameter space and back. The respective winding number for this configuration is $w = 0$. The mapping $f_2(\boldsymbol{r})$ wraps the whole order parameter space once, thus it cannot be contracted to a point without violating continuity. $f_3(\boldsymbol{r})$, on the other hand, can be contracted continuously to a point, i.e. the equivalent of $f_1(\boldsymbol{r})$, representing the uniform state. The mappings $f_1(\boldsymbol{r})$ and $f_3(\boldsymbol{r})$ are homotopic.

$f_1(\boldsymbol{r})$ and $f_3(\boldsymbol{r})$ are just two specific of many examples of mappings, which are assigned the winding number $w = 0$. Analogous, numerous mappings are assigned the winding number $w = 1$, just like $f_2(\boldsymbol{r})$. All mappings assigned to a specific winding number form a homotopy class. Within one class all mappings are homotopic to each other, i.e. can be transformed continuously into one another. From the purely mathematical viewpoint, any transition from another class ($w \neq 0$) to the uniform state or in between two classes ($w_{\mathrm{from}} \neq w_{\mathrm{to}}$) has an infinite energy barrier associated with it. Hence, contours representing objects that map to classes $w \neq 0$ are termed topologically protected, as they cannot be transformed to the uniform state. In real systems, on the other hand, this energy barrier is finite due to the finite samples and finite confinements [110, 111]. Hence, topologically protected, in the context of real objects like magnetic spin textures, implies a finite energy barrier stabilizing peculiar textures. In the next section these topologically non-trivial spin textures are investigated in detail.

Furthermore, the mappings can be evaluated sequential. This behavior is illustrated in figure 2.10d. Evaluating the mappings of the contours enclosing either of the singularities P_1 and P_2 yields the winding numbers $w_1 = 1$ and $w_2 = -1$, respectively. Whereas the contour encircling both results in,

$$w_{\mathrm{tot}} = w_1 + w_2 = 0, \tag{2.71}$$

the sum of the individual singularities, which is commutative. Hence, evaluating the individual contours in arbitrary sequence or the large contour enclosing both defects, yields the same total winding number. Since the winding number is linked directly to the topological charge, which is a conserved quantity, this is important: While the formation of individual singularities in the uniform background is topologically forbidden, the pairwise formation of vortex and antivortex are possible.

The concepts of topology illustrated on the planar two-dimensional system can be expanded to the $\mathbb{R}^3$, that is equivalent to real space. An outline of this process as well as a mathematically more precise description are summarized in appendix A. Working in the framework of micromagnetic theory, the order parameter space is given by the two-dimensional surface (S^2) of a sphere with radius M_s. Analogous, a non-zero winding number is assigned, if the mapped contour fully wraps the order parameter space and topologically (non)trivial spin textures can be classified.

2.2.2 Skyrmions

Topological protected spin textures have been a hot topic in the past decades. In particular, one spin texture, the skyrmion, attracted tremendous attention after it was discovered in magnetic materials [25, 38]. Skyrmions can be classified by the assignment of a winding number. However, the winding number alone does not fully capture the topological state of the skyrmion. Therefore, the topological charge [113, 114],

$$N_\mathrm{Sk} = \int n_\mathrm{Sk}(\boldsymbol{r})\mathrm{d}^2 r, \tag{2.72}$$

where the integration is carried out over all of real space, is introduced. The integrand n_Sk is the topological charge density

$$n_\mathrm{Sk} = \frac{1}{4\pi}\boldsymbol{m}(\boldsymbol{r}) \cdot \left[\frac{\partial \boldsymbol{m}(\boldsymbol{r})}{\partial x} \times \frac{\partial \boldsymbol{m}(\boldsymbol{r})}{\partial y}\right], \tag{2.73}$$

which is calculated from the spatial distribution of the magnetization in real space. To obtain a skyrmion, a magnetization distribution yielding a non-zero topological charge under evaluation of the integral is required. A possible parameterization for such a magnetization distribution representing a skyrmion is given by [113]

$$\boldsymbol{m}(r,\phi) = \begin{pmatrix} \cos\boldsymbol{\Phi}(\phi)\sin\boldsymbol{\Theta}(r) \\ \sin\boldsymbol{\Phi}(\phi)\sin\boldsymbol{\Theta}(r) \\ \cos\boldsymbol{\Theta}(r) \end{pmatrix}, \tag{2.74}$$

where $\boldsymbol{\Theta}(r)$ and $\boldsymbol{\Phi}(\phi)$ are the polar and azimuthal angle of the magnetization, represented in spherical coordinates, respectively. Here polar coordinates, $\boldsymbol{r} = r(\cos\phi,\ \sin\phi)$, are used and the symmetry of the skyrmion has been exploited to express $\boldsymbol{m}(r,\phi)$. Calculating the topological charge yields

$$\begin{aligned} N_\mathrm{Sk} &= \frac{1}{4\pi}\int_0^\infty \mathrm{d}r \int_0^{2\pi} \mathrm{d}\phi \frac{\partial\boldsymbol{\Theta}(r)}{\partial r}\frac{\partial\boldsymbol{\Phi}(\phi)}{\partial\phi}\sin\boldsymbol{\Theta}(r) \\ &= -\frac{1}{2}\cos\boldsymbol{\Theta}(r)\Big|_{r=0}^{\infty} \cdot \frac{1}{2\pi}\boldsymbol{\Phi}(\phi)\Big|_{\phi=0}^{2\pi}, \end{aligned} \tag{2.75}$$

the product of two factors, one dependent only on the radial component r and the other one on the polar angle ϕ. The first factor, captures the inversion of the out-of-plane component of the magnetization, while tracing along the radial component, from the center of the skyrmion located at $r = 0$ to $r \to \infty$. It describes the polarity of the skyrmion,

$$p = -\frac{1}{2} \cos \mathbf{\Theta}(r)\Big|_{r=0}^{\infty} = \pm 1, \tag{2.76}$$

which can either be $p = +1$ for the magnetization in the center pointing up, or $p = -1$ for the center pointing down. Effectively the polarity is determined by the ferromagnetic background the skyrmion is emerging within. Due to continuity of the magnetization distribution, the azimuthal angle $\mathbf{\Phi}(\phi)$, must coincide with itself after a full revolution of ϕ. Thus, the second factor, the vorticity is defined,

$$m = \frac{1}{2\pi} \mathbf{\Phi}(\phi)\Big|_{\phi=0}^{2\pi} = 0, \pm 1, \pm 2, \ldots \tag{2.77}$$

which can only wrap around in integer multiples of 2π. The vorticity effectively describes the number of wrappings of the order parameter space, i.e. it represents the winding number. Together the polarity and the vorticity determine the topological charge,

$$N_{\text{Sk}} = m \cdot p = 0, \pm 1, \pm 2, \ldots \tag{2.78}$$

where $N_{\text{Sk}} = 0$ represents the topological trivial state. $N_{\text{Sk}} = +1$ yields the skyrmion illustrated in figure 2.11a, $N_{\text{Sk}} = -1$ the antiskyrmion (see fig. 2.11b) [115], and for $|N_{\text{Sk}}| \geq 2$ more complex higher-order skyrmion textures arise. While the topological charge captures the properties relevant to determine the topological stability it does not fully describe the skyrmions. Additionally, to the polarity and vorticity skyrmions possess another degree of freedom, the helicity. It describes the direction of rotation tracing radially along the spin helix, respectively the lack thereof in case of a cycloidal structure. In the framework above, the helicity is represented by a phase offset γ to the linear parameterization of the azimuthal angle [114],

$$\mathbf{\Phi}(\phi) = m\phi + \gamma. \tag{2.79}$$

For $\gamma \in \{0, \pi\}$ the magnetization rotates radially, yielding a Néel-type skyrmion, assuming $N_{\text{Sk}} = +1$. Whereas a Bloch-type skyrmion is the result if $\gamma = \pm\pi/2$. Unlike the polarity and the vorticity, the helicity is continuous, allowing mixed states between Néel and Bloch-type skyrmions [114]. An example of such a mixed state is shown in fig. 2.11c for $\gamma = \pi/4$.

Two rather peculiar examples of skyrmionic texture are illustrated in figure 2.11d and e, where both structures have a vorticity of $m = +2$. Whilst the higher order skyrmion behaves as intuitively expected by rotating the magnetization twice when circuiting the core once, the same winding number is obtained for the biskyrmion. Which is a clustered particle composed of two adjacent skyrmions, each with a vorticity of $+1$ and a helicity offset by a factor of π. Note, for clustered particles as well as densely packed lattices of skyrmions the helicity offset implies strict Bloch or Néel-type of all solitons. The antiskyrmion on the other hand exhibits alternating helical and cycloidal behavior

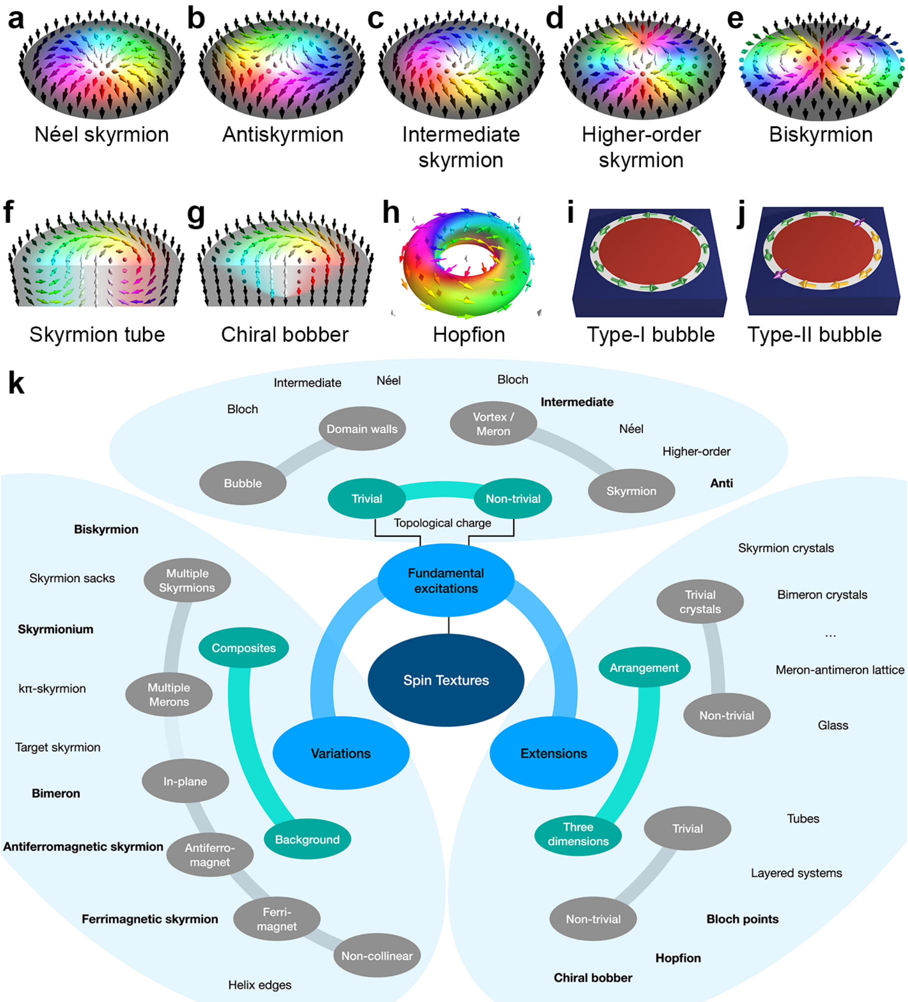

Figure 2.11: Overview of different magnetic skyrmions. **a**, Néel-type skyrmion ($p = +1$, $m = +1$, $\gamma = 0$). **b**, antiskyrmion ($m = -1$). **c**, skyrmion ($\gamma = \pi/4$), intermediate between Néel and Bloch-type. **d**, higher-order skyrmion ($m = +2$). **e**, biskyrmion ($m = +2$). **f**, Bloch-type skyrmion tube, unaltered extension of the skyrmion into the 3$^{\text{rd}}$ dimension. **g**, chiral bobber, a discontinued skyrmion in the 3$^{\text{rd}}$ dimension. **h** Hopfion, a non-trivial 3D soliton. **i**, type I bubble ($m = +1$). **j**, type II bubble ($m = 0$), topologically trivial, "onion state". **k**, classification of fundamental excitations in spin textures with corresponding variations and extensions. Recreated from [86], based on [114] (panels **a-h**, **k**) and [116] (panels **i** and **j**).

and is thus compatible with Bloch and Néel-type solitons, if aligned along the proper direction. Beyond the presented examples a variety of combinations yielding higher order (anti)skyrmions are theoretically possible.

Trivial extension of the skyrmion in the third dimension yields the skyrmion tube [117], exhibited in figure 2.11f. If on the other hand the skyrmion is terminated whilst penetrating the sample depth, see figure 2.11g, a chiral bobber emerges [118, 119]. In such a case, the three-dimensional real space has to be mapped to order parameter space, giving rise to a multitude of possible peculiar topological non-trivial spin textures. One example is the Hopfion [120], depicted in figure 2.11h, which has a toroidal shape. Taking a cross section of the tube it resembles a skyrmion, hence it can be understood as a looped skyrmion tube. To get an overview, figure 2.11k shows a classification scheme for these diverse topological protected structures and their variations. Though the zoo of theoretically existent topological protected structures appears near endless, only few and generally, the less complex ones are predicted to emerge in known materials. Even fewer have actually been observed experimentally.

Origin of topologically non-trivial spin textures

To understand why the number of observed and predicted skyrmion-like textures in magnetic systems is limited, it is necessary to understand the driving forces behind their formation. There are three possible reasons, plus combinations thereof, that can lead to the formation of skyrmions in a magnetic material. The first one is the DMI competing with exchange interaction resulting in a modulated state [43, 121, 122]. The second reason is frustration among several exchange paths. And finally, the competition between the dipolar interaction and the uniaxial magnetic anisotropy [123].

First the case of DMI shall be considered. This case is limited to non-centrosymmetric materials, where the broken inversion symmetry can either be an inherent property of the lattice or the effect of an interface. As described in detail in section 2.1.3, DMI favors orthogonal alignment of neighboring spins. Whereas the Heisenberg exchange prefers parallel alignment, thus leading to a competition. As a compromise a gradual rotating spin texture is formed. These textures can be cycloidal, e.g. for axial polar magnets, helical, like in the case of cubic or axial chiral magnets, or an intermediate spiral state. The energy of such a helical state is minimized for [124–126]

$$\boldsymbol{S}_i = \left[\boldsymbol{e}_1 \cos(\boldsymbol{q} \cdot \boldsymbol{r}_i) + \boldsymbol{e}_2 \cos(\boldsymbol{q} \cdot \boldsymbol{r}_i)\right], \tag{2.80}$$

where

$$\boldsymbol{q} = \frac{2\pi}{\lambda} \boldsymbol{e}_3, \tag{2.81}$$

and $\boldsymbol{e}_n$ with $(n = 1, 2, 3)$ are a set of orthogonal unit vectors. Figure 2.12 illustrates the helimagnetic order, where the spins rotate perpendicular to the propagation direction $\boldsymbol{q}$. Utilizing Landau theory the helical period and sub-

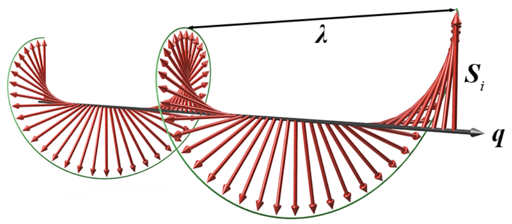

Figure 2.12: Helical spin texture. The spins $\boldsymbol{S}_i$ rotate in a plane perpendicular to the $\boldsymbol{q}$ vector with the periodicity λ. Recreated from [86]

sequently the $\boldsymbol{q}$ vector can be determined [127]. The periodicity

$$\lambda = 4\pi \frac{A}{D}, \tag{2.82}$$

is given by the relative balance of the exchange and the DMI. For stronger DMI with respect to the exchange the periodicity shrinks. Thus, it is not necessarily commensurate with the lattice constant. This single-q state is the ground state for respective materials.

The emergence of topologically non-trivial spin textures is limited to multi-q states, where several helices or cycloids are superimposed. The following illustrative description covers isotropic bulk DMI giving rise to the superposition of helical single-q states. This description is representative of the B20 compounds, which are the first materials where skyrmions (Bloch-type) were observed in [25, 36–38]. To form skyrmions a triple-q state is required, which can only be stabilized by the application of an external field. In such a helical triple-q state, the three propagation vectors $\boldsymbol{q}_j$ lie in one plane perpendicular to the field, where they span a 120° angle between each other. Hence, the spin configuration is given by the superposition of three spin spirals $\boldsymbol{q}_j$ $(j = 1, 2, 3)$ and the external field $\boldsymbol{H}$. The resulting spin configuration in real space, for the field applied along the z-axis, is given by [128]

$$\boldsymbol{S}_i = \boldsymbol{I}_{\text{temp}} \cdot \sum_{j=1}^{3} \begin{pmatrix} \sin(\boldsymbol{q}_j \cdot \boldsymbol{r}_i + \vartheta_j) \\ \sin(\boldsymbol{q}_j \cdot \boldsymbol{r}_i + \vartheta_j) \\ \cos(\boldsymbol{q}_j \cdot \boldsymbol{r}_i + \vartheta_j) \end{pmatrix} + \begin{pmatrix} 0 \\ 0 \\ m_z \end{pmatrix}, \tag{2.83}$$

where $\boldsymbol{I}_{\text{temp}}$ is a temperature dependent constant, m_z is the resulting magnetization from the spin canting towards the external field and the sum is evaluated for all three $\boldsymbol{q}$ vectors. The phase factors ϑ_j $(j = 1, 2, 3)$, required to satisfy $\cos(\vartheta_1 + \vartheta_2 + \vartheta_3) = -1$, describe the phase shift between the three helical structures. This triple-q state spin configuration describes the skyrmion lattice [24, 36–39, 129–133], which is a triangular lattice of skyrmions, generally incommensurate with the underlying crystal lattice. Altering the phase of the wave vectors results in a translation of the lattice. Hence, the three q vectors $\boldsymbol{q}_j$ fully characterize the lattice. Additionally, the sign of the DMI determines the chirality of the individual helices, i.e. whether the spins rotate counterclockwise or clockwise whilst tracing along the propagation direction. Thus the helicity of the resulting skyrmions is already determined by the DMI.

The second origin of skyrmions is frustration. A prominent and illustrative example of such a frustrated geometry in 2D is the triangular lattice with antiferromagnetic Heisenberg exchange. Evidently two antiferromagnetically arranged spins, sitting on two corners of an individual triangle, couple to the third one, where they favor opposing alignments. Hence the lattice is frustrated. The resulting ground state, considering nearest-neighbor interactions only, is a 120° canted in plane structure, which is commensurate to the lattice. Additionally, considering dominant further-neighbor interactions gives rise to incommensurate ground states. From a symmetry viewpoint, the latter have the advantage of possessing a three-fold degeneracy with respect to the choice of the three equivalent directions of the wave vectors on the lattice [128]. Consider a layered material, where within one layer all spins are coupled ferromagnetically to their nearest-neighbors, but the inter-layer coupling to nearest-neighbors J_1 and next-nearest-neighbors J_2 differs. The exchange energy of such a system is given by [83, 134]

$$E = -2NS^2 \left(J_1 \cos\theta + J_2 \cos 2\theta\right), \tag{2.84}$$

where N is the number of atoms per plain and θ the angle between spins in neighboring layers. Minimizing the energy of the system yields

$$\frac{\partial E}{\partial \theta} = 2NS^2 \left(J_1 + 4J_2 cos\theta\right) \sin\theta = 0. \tag{2.85}$$

Hence two trivial solutions, with $\sin\theta = 0$, for the ferromagnetic ($\theta = 0$) and antiferromagnetic coupling ($\theta = \pi$) exist. Furthermore, a non-trivial solution for $\cos\theta = -J_1/4J_2$, which is favored if $J_2 < 0$ and $|J_1| < 4|J_2|$, exists. It describes a modulated state with a gradual rotation of the spins in between layers which can also be incommensurate to the lattice. Through superposition such incommensurate modulated spin textures, appearing in two and three dimensional systems, can ultimately form skyrmions.

The last reason for the formation of skyrmions, the competition of dipolar interactions and anisotropy, has been elucidated in detail in section 2.1.5. Hence a detailed consideration how the textures are stabilized is forgone here, where the focus lies on the relevant topological properties. In summary, the competition between the long-range dipolar interaction, favoring in-plane orientation, and the uniaxial magnetocrystalline anisotropy, stabilizing out-of-plane configurations, yields bubble domains as the energetically favorable configuration, when modest external field is applied. Naturally this raises the question if these bubbles are similar to skyrmions, or weather distinct differences can be determined. First and foremost, the size of such bubbles is vastly different, generally, a lot larger [40], compared to skyrmions emerging due to the above mentioned mechanics, where the size ranges from the atomic scale [39] to 100 nm [41]. The core of a skyrmion is a single spin, whereas the bubbles are ferromagnetic domains, i.e. their core of ferromagnetically aligned spins has to exceed a threshold size. Despite the size difference, the topological properties remain unaffected. The topological properties are solely determined by the shape of the domain wall confining the bubble. The trivial configuration, a continuous domain wall enclosing a so-called type-I bubble, shown in figure 2.11i, yields a vorticity of $m = +1$. Analog to the skyrmion the polarity p is assigned based on the orientation of the spins in the domain. Additionally, the helicity is determined by the type of the domain wall, being either Bloch or Néel-type. The skyrmion can be seen as the limit of such a bubble domain contracting to a single point. Thus, the type-I bubbles are often also referred to as skyrmionic bubbles, as they are topologically equivalent [135, 136]. Particularly for very small bubbles it is often hard to mark down a clear limit between skyrmionic bubbles and skyrmions. This problem is further enhanced as they behave similar under external stimuli, e.g. current-induced motion [28]. Besides the size and mechanism of origin, skyrmions, also referred to as compact skyrmions [137], and skyrmionic bubbles usually differ in lifetime and temperature stability [123]. Despite exhibiting the intuitive domain wall configuration, the skyrmionic bubble is not the only type of bubble. In many systems type-II bubbles form. A schematic configuration of such a bubble is shown in figure 2.11j. It exhibits a characteristic shape, which does not fully wrap the order parameter space. Hence these bubbles are topologically trivial. Note, the domain wall also has two singularities, these will be covered in more detail in section 2.2.3.

To conclude, the origin of topologically non-trivial spin textures is either one, or a combination of the three reasons above. Generally, if only one of the driving forces behind the formation of skyrmions applies, the resulting objects are representatives of the less complex textures. This is readily understood from the case of isotropic DMI. Here the periodicity λ and subsequently the $\boldsymbol{q}$ vector, are defined by the ratio of the Heisenberg exchange and the DMI. Skyrmions ($m = 1$) are stabilized as the result of a triple-q state via the application of magnetic field. But these skyrmions are limited to the least complex non-trivial state, as more complex textures require the superposition of anisotropic or aperiodic $\boldsymbol{q}$ vectors, hence contradicting the isotropy of the the DMI. Whilst generally true, the formation of less complex textures is not exclusively the case. In certain systems anisotropic DMI, which is a key factor for the formation of anitskyrmions [138], is an inherent property of the lattice [139], which can ultimately lead to the formation of antiskyrmions [115]. Unlike DMI, the competition of long-range dipolar order and uniaxial magnetic anisotropy offers an additional degree of freedom for the orientation of the spins, the helicity γ. Whilst not contributing to the topological charge N_{Sk} it allows for greater freedom in the domain wall configuration without violating continuity, hence enabling the formation of more complex textures. Recently even higher order antiskyrmions ($m = -2$) coexisting with generic antiskyrmions, Bloch skyrmions of both helicities ($\gamma = \pm\pi/2$) and trivial type-II bubbles, all dipolar-stabilized, were observed in a multilayer compound [140]. Combining two or all three of the stabilizing mechanisms in a material, thus yields a variety of options to stabilize further spin textures. Tuning their relative strengths and optimizing materials to form stable and well distinguishable topological spin textures will be the key to realize spintronics based applications.

Spintronics - Applications of skyrmions

Beyond the interest from a pure academical perspective, topologically protected solitons, are promising candidates for future technological applications. The majority of topologically protected solitons are generally viable to be used as information carriers, however the focus of most works in this context lies on the skyrmions. In particular, skyrmions have been envisioned as potential information carriers in future memory devices. In order to realize such memory concepts, control of three major actions has to be achieved: creation, deletion and manipulation. As such, the state of the art for these three actions and subsequent detection is outlined in the subsequent paragraphs.

The simplest form of encoding data in a skyrmion based memory is the absence and presence of a skyrmion representing 0 and 1 in a binary format [137]. Here, the topological charge, coinciding with a finite energy barrier for creation or annihilation, stabilizes the information carrier itself. A prerequisite for this technology is the ability to create and delete skyrmions as well as detect them, or their absence, reliably to read the information. It has already been demonstrated that by the application of external stimuli skyrmions can be created or annihilated reliably, following several different mechanisms. These are optical methods such as the application of pulsed lasers [141, 142], spin-polarized electric currents [143–146], and the application of magnetic field [147]. Of these mechanisms, those based on electric currents are especially interesting as they are relatively easy to integrate into potential memory designs. However, as this thesis focuses on the application of static magnetic field here, the existence of various alternative approaches is only noted.

Potential memory designs bring up a major challenge, the unsolved challenge of detection. Fundamental research on skyrmions relies on established imaging techniques such as LTEM [37, 38, 52, 116, 122, 148–150], spin-polarized scanning tunneling microscopy (SP-STM) [143, 151], magneto-optical Kerr effect (MOKE) [40, 152], and MFM [153, 154]. These direct imaging techniques cover the atomic length scale up to the micrometer range, yielding extremely valuable insight for the study of the fundamental properties of skyrmions. However, none of the established techniques are viable read-out devices for memory applications. Because all of these techniques are incompatible with device architecture, where an integrated all electric read out like an integrated magnetic tunneling junction is required. In the related field of domain walls, such a integrated magnetic tunneling junctions have been shown to work reliably [155]. However, manufacturing them on such small scales is complicated and yielding sufficient signal from skyrmions has not been proven to work, let alone work reliably [155]. Alternative read-out operations have been presented at a proof-of-concept level, these are based on the topological Hall effect [156–159], or magnetoresistance [160, 161].

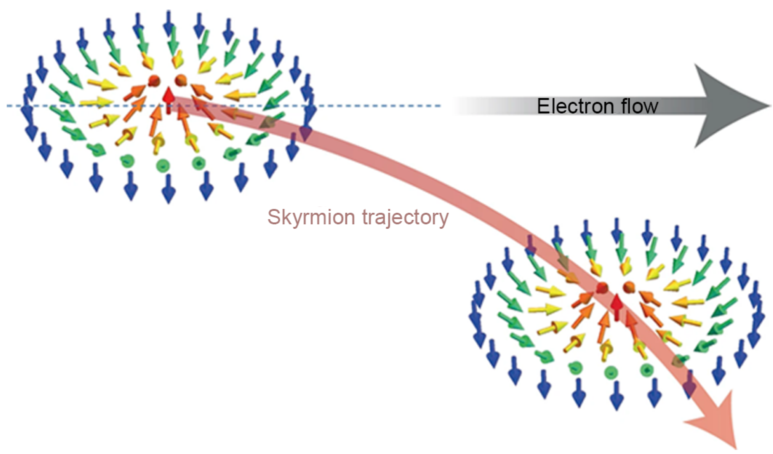

Figure 2.13: Skyrmion Hall effect. Illustration of the curved skyrmion trajectory deviating from the applied current (grey). Reproduced with permission from [162]

These challenges associated with the detector naturally lead to the idea of having single stationary detector, and moving the skyrmion array to the detector. This has the requirement that their dynamic behavior, and the manipulation thereof via external stimuli, must be understood to control them reliably. Two research focuses now come to the fore: how to accelerate the skyrmions, and how to control their direction. Considering the acceleration of the skyrmions first, spin-polarisated currents have proven to be viable candidates for this task as well. This can be a significant advantage on more classical domain wall based approaches as, taking MnSi as an example, the threshold current density yielding spin-transfer torque induced skyrmion motion, is up to six orders of magnitude smaller [26, 163, 164]. Spin-orbit torque-based approaches yielded even faster terminal velocities for domain walls [165]. Additionally, eliminating the magnetostatic fields by transitioning to synthetic antiferromagnetic structures improves these even further for domain walls [166, 167]. Analogously, further improvements of the terminal velocity of skyrmions are expected. However, all these potential solutions to the challenge of skyrmion acceleration have one problem: skyrmions do not follow a straight path along the current - showing our second challenge.

The trajectory of a skyrmion under the application of currents was originally described by A. Thiele [168], before being refined by [137, 169, 170] and always yields a velocity component perpendicular to the current, termed the skyrmion Hall effect [152, 162, 171]. As a result, the skyrmion moves on a curved trajectory as illustrated in figure 2.12. This leads to the second challenge, which is generally solved via geometric confinement. By limiting the quasi two-dimensional skyrmion host materials to e.g. a narrow strip the skyrmion is limited to propagate along what is essentially a track. While originally proposed with domains respectively domain walls as information carriers in mind, the racetrack memory [172, 173] exploits the quasi one dimensional confinement of the propagation of the magnetic textures. Altered version of the race track memory based on skyrmions have since been proposed [174]. But despite promising concepts and early stage prototypes showing results no commercial racetrack memory is currently available. Yet, the details of how geometric confinement effects skyrmion materials is an ongoing research area.

2.2.3 Bloch Points and Lines

Intriguingly the topologically trivial type-II bubbles, emerging naturally in materials with PMA, actually host non-trivial spin textures. From the schematic of a type-II bubble, depicted in figure 2.11j, it is evident the domain wall has two peculiar spots. There, so called Bloch lines (BL) emerge within the domain wall mitigating the discontinuity of the magnetization, where two Bloch wall segments of opposite helicity come together [175, 176]. Being part of the domain wall between an up and down domain along the z direction, the magnetization in between the two Bloch wall segments has to mitigate its mismatch by an in-plane rotation. A vertical line like defect along the wall, where it exhibits Néel-type character is the result. Figure 2.14a shows an in-plane cross section perpendicular to such a Bloch line extended along the z axis. Depending on the mismatch of the helicity, the Bloch line can be distinguished as head-to-head, or tail-to-tail, where the local magnetization points towards or away from the line, respectively [176]. From a topological viewpoint these are quite interesting. Overall the type-II bubbles, have a topological charge $N_{\text{Bubble}} = 0$, but evaluating the two Bloch wall segments yields $N_{\gamma^+} + N_{\gamma^-} \approx 1$. In the simplest case these segments are symmetrically spaced around the domain, thus each segment maps to the same half of the order parameter space. Hence the Bloch lines have to account for unwinding these half wrappings as well as constituting a continuous contour. Indeed, the helicity reversal in the plane coincides with

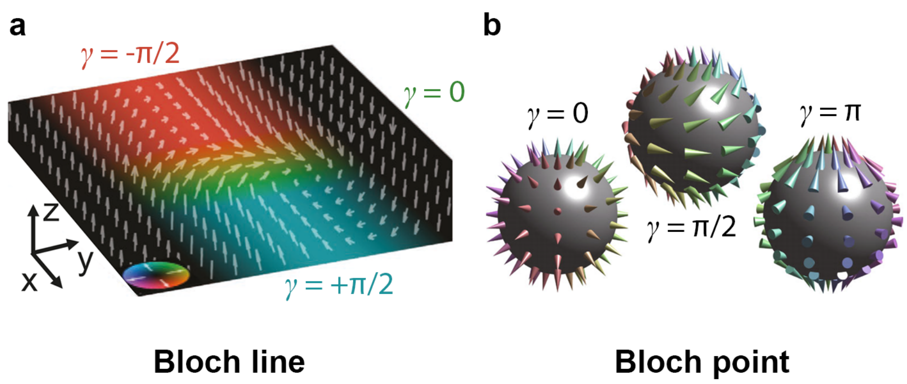

Figure 2.14: Bloch line and Bloch points. **a**, in-plane cross section of a domain wall between two domains pointing up and down along the z axis (black). The red and blue area show Bloch-type domain walls of opposite helicity. The green area shows the Bloch line, where the wall exhibits Néel-type character. **b**, schematic representation of Bloch points with a topological charge of +1. Analog to skyrmions the helicity can vary yielding a hedgehog, circulating or spiraling configuration. Panel **a** reproduced with permission from [175]. Panel **b** reproduced with permission from [177].

a topological charge $N_{\mathrm{BL}} = \pm 1/2$, which is localized at the Bloch line. Analog to the skyrmion's topological charge, the sign is determined by the direction of rotation relative to the direction the contour is evaluated along and opposes the Bloch walls segments. Due to the severe spin canting required to locally rotate the magnetization in such a way, Bloch lines are generally not stable as an individual object. They only form in certain cases when the balance of magnetostatic, magnetic domain-wall, and Zeeman energies, stabilizing bubble domains can be optimized by reducing the stray field of Bloch walls at the cost of introducing Bloch lines [64, 176]. Hence the underlying interaction governing the formation of Bloch lines is the dipolar interaction. Subsequently the Bloch line width [64]

$$\delta_{\mathrm{BL}} = \pi\sqrt{A/K_{\mathrm{d}}}, \tag{2.86}$$

depends on the dipolar energy density K_{d} and the exchange stiffness, rather than the anisotropy, K_{u}, which determines the Bloch wall width (see equation 2.54).

Additional complication is introduced for type-II bubbles in intermediate Q systems ($0.1 < Q < 1$), where Néel caps are present. The in-plane component of the corresponding Néel caps at the bottom and top surface of the material are antiparallel, due to their flux-closure nature. A vertical Bloch line, linking both caps, yields a problem. The orientation of the magnetization of the Bloch line, exhibiting Néel-type domain wall character, must coincide with the orientation of the Néel caps at the top and bottom, respectively. Hence, an intrinsic inversion of the magnetization along the one-dimensional Bloch line is required. Yet, the constraints of the Bloch line, being part of the domain wall and mitigating the helicity mismatch of π, remain in place. Thus, neither an out-of-plane nor an in-plane rotation of the magnetization is possible without violating either one. The result is a Bloch point (BP), which is a three-dimensional spin texture that cannot be mapped to the order parameter space represented by a sphere S^2, due to a singularity in the center, where the magnetization vanishes [178, 179]. In the simplest form the magnetization distribution parameterizing a Bloch point can be written as [179]

$$\boldsymbol{m}_{\mathrm{BP}}(\theta, \phi) = \begin{pmatrix} \cos(\phi+\gamma)\sin(\theta) \\ \sin(\phi+\gamma)\sin(\theta) \\ \cos(\theta) \end{pmatrix}, \tag{2.87}$$

in Cartesian coordinates, where θ and ϕ refer to the spherical coordinates of $\boldsymbol{r}$ and $\boldsymbol{m}$. Depending on the helicity either a hedgehog ($\gamma = 0$), circulating ($\gamma = \pm\pi/2$) or spiraling ($\gamma = \pi$) configuration is obtained, as depicted in figure 2.14b. Analog to the skyrmions, intermittent helicities yield mixed states. Bloch points also carry a topological charge, which is calculated analog to that of the skyrmion (see equations 2.72 and 2.73) [180, 181]. Adapted for the three-dimensional evaluation the equation reads [177]

$$N_{\mathrm{BP}} = \frac{1}{8\pi}\int \mathrm{d}A_i \epsilon_{ijk} \boldsymbol{m} \cdot \frac{\partial \boldsymbol{m}}{\partial \boldsymbol{e}_j} \times \frac{\partial \boldsymbol{m}}{\partial \boldsymbol{e}_k} = \pm 1, \tag{2.88}$$

where the integration is carried out over a surface A enclosing the Bloch point. Technically the topological charge is analog to the skyrmion, but the vorticity of the Bloch point is fixed at $m = +1$. Hence the topological charge effectively describes the polarity of the Bloch point. It is positive if the magnetization points from, respectively negative if it points towards the singularity. Note in case of a "combed" state ($\gamma \neq 0$) despite positive topological charge the helicity reversed spins can point towards the singularity, and vice versa. Similar to the Bloch lines, the antiparallel alignment of the magnetization surrounding the singularity is highly unfavorable due to the exchange interaction. Thus, Bloch points are mainly expected to emerge in dynamic processes, e.g. the transient state during magnetization reversal along a one-dimensional object [182, 183]. They are, however, not strictly expelled and can emerge statically, and were studied extensively both theoretically and experimentally [40, 43, 73, 172, 184]. Due to the inherent complexity of achieving both temporal and spatial resolution on the atomic length scale, generally the study of Bloch points is focused on static Bloch points and their quasi static motions [177, 183, 185, 186].

In summary both Bloch points and lines are mitigating local misalignment of the magnetization. Whilst they naturally emerge in materials with PMA, Bloch lines are not limited to the elucidated case of a type-II bubble. Generally, they can form even in walls of extended domains and their number is not limited to two. Bloch points on the other hand, emerging individually if local magnetization reversal is required in a one-dimensional object, can emerge under several other circumstances as well. E.g. in an interface of two materials hosting skyrmions of opposite helicity and polarity, Bloch points can arise at the point where the skyrmion cores line up [180]. One particular problem with the simulated magnetic textures containing Bloch points is, that the micromagnetic framework generally used to calculate the magnetic landscape, cannot cope with the ill-defined singular points.

3

Experimental Methods

Exploring their habitat and everything within it lies in the nature of humans. On one side of the length scale, this manifests in the desire to go and see as far as possible, whereas on the other side this means meticulous analysis of what is right there in the immediate surrounding. The latter implies looking closer and eventually the limit of what can be resolved by the bare eye is a limiting factor. Hence, magnification tools are a requirement. As early as the Greco-Roman empire, reports and findings of naturally occurring transparent crystals, hand-crafted to lens shapes, can be found [187]. Modern visible light microscopes, building on centuries of optical developments, are sophisticated tools, where the resolution is limited by diffraction rather than the optical quality. Ernst Abbe determined this limit to be

$$d_{\mathrm{min}} = \frac{\lambda}{2A_{\mathrm{N}}}, \tag{3.1}$$

where, λ is the wavelength of the light and A_{N} is the numerical aperture which depends on the refractive index of the microscope environment. Despite in parts successful attempts to achieve resolution below the diffraction limit of $d_{\mathrm{min}} \approx 200\,\mathrm{nm}$, visible light microscopy (VLM) is inherently unsuitable to reach nanometer let alone atomic resolution [188].

This chapter introduces two microscopy techniques, with atomic resolution. Scanning probe microscopy, which employs a fundamentally different principle of image acquisition via mapping of local probe-sample interactions, and electron microscopy, which utilizes the tuneability of the electron's wavelength. Furthermore, these microscopes have the advantage of enabling imaging modes sensitive to the local magnetization. A general introduction to both techniques is given and subsequently the routines for appropriate sample preparation.

3.1 Scanning Probe Microscopy

The field of scanning probe microscopy (SPM) was initiated in 1982 by the invention of the scanning tunneling microscope (STM) by G. Binning and H.

Rohrer at IBM Zurich [189]. Nobel Prize winners in physics only four years later for their invention. STMs measure the tunneling current between the sample and an extremely sharp conductive tip. The breakthrough idea lies in exploiting the tip sample distance dependent tunnel current as the input signal to a feedback loop, which readjusts the distance via piezoelectric actuators [190]. Thus, while scanning the sample surface, the extension of the piezo required to keep the current constant reveals the topography. This constant signal or feedback mode is the key to obtain resolutions down to the atomic scale.

To overcome the limitation to conductive samples of STM, G. Binning, C. F. Quate and Ch. Gerber developed the atomic force microscope (AFM) in 1986 [191]. It works similar to the STM, but tracks the forces acting on the probe suspended on a cantilever instead of the tunneling current. AFM measurements were quickly established as spectroscopic, imaging and manipulation tool throughout several fields of natural sciences, such as physics, chemistry, biology and nanotechnology [192–196]. Developments in the following decades expanded on the measurable interactions [197–201]. Furthermore, measurement conditions, ranging from ultra-high vacuum to immersion in liquids [202, 203], temperatures from milli-Kelvin up to several hundred degrees centigrade [204], as well as in-situ field application up to 38 T [205], are available.

3.1.1 Basic Principles of Atomic Force Microscopy

The fundamental idea behind the AFM lies in measuring the inter atomic forces between the sample surface and the probe. To obtain those, the probe is mounted on a cantilever of known spring constant acting as the force sensor. Hence, the deflection of the cantilever is proportional to the forces probed. The deflection is most commonly detected by a laser beam deflection method [206]. The laser points on the backside of the cantilever, where it is reflected to a four-segmented photodiode, see figure 3.1a. Deflections of the cantilever are detected by a shift of the laser spot on the photodiode. Up or down motion (bending and buckling), commonly referred to as deflection, as well as rotation (torsion) of the cantilever, generally referred to as lateral force, can be discerned using this method. The second common method is based on an optical laser interferometer. Figure 3.1b shows the partial beams of the coherent laser source reflecting on the backside of the cantilever and a reference plane, usually the end of the glass fiber, which are superimposed. The modulation of the path difference induced by the cantilever deflection is tracked and relative changes in the cantilever fiber distance are detected. The major drawback of this method is, it cannot detect the lateral force channel. The main advantages are the minimal spatial requirements, as the interferometer unlike the photodiode can be located in an adjacent electronics rack, and superior mechanical stability. These advantages are particularly relevant for low-temperature systems [207]. For both methods the sensitivity is ultimately limited by the thermal noise of the cantilever.

Piezo electric actuators moving the sample relative to the tip are used to acquire a spatially resolved image. Generally, three actuators, two for rasterized scanning in the xy plane and one for the z height are required. These are commercially available as stacks of individual piezos or piezo-tubes. Additionally the tip holder is equipped with a piezo actuator (dither), that is used

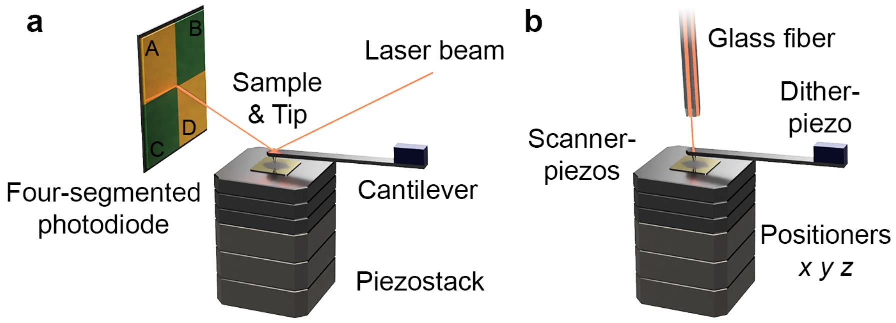

Figure 3.1: Schematic AFM setup. Both setups rely on a stack of piezo elements enabling rasterized scanning and an additional element to drive the cantilever oscillation. **a**, beam-reflection method, detection via a four-segmented diode. **b**, Laser interferometry based read-out. Recreated from [112].

to drive the cantilever oscillation, as can be seen in figure 3.1. Beyond these integral parts for the operation of the AFM and their respective electronics, numerous adaptations and add-ons, which enhance ergonomics, are available.

Tip-sample interactions and operation modes

The probed inter atomic forces can be differentiated in short-range (<1 nm) and long-range forces. Short-range forces are dominated by the effects of overlapping electron wave functions yielding either attractive (forming bonds) or repulsive (Pauli exclusion principle) contributions. Long-range forces contain Van der Waals, including dipole-dipole interactions, electrostatic and magnetic forces. Depending on the conditions the AFM is used in, additional forces, like capillary forces attributed to the formation of a water meniscus at the tip-sample interface, can occur. Assuming the AFM in vacuum, with no emergent electric or magnetic forces only repulsive short-range and attractive long-range interactions determine the tip-sample potential. Further reducing the consideration to two neutral atoms, representing the tip and sample surface respectively, the Lennard-Jones potential represents the interaction [197, 208]

$$V_{\mathrm{LJ}} = 4\epsilon \left[\left(\frac{\sigma}{z}\right)^{12} - \left(\frac{\sigma}{z}\right)^{6} \right], \tag{3.2}$$

where ϵ is the depth of the potential well, σ is the Van der Waals diameter, and z is the separation distance between tip and surface. Figure 3.2 shows the plot of the Lennard-Jones potential, as well as the first (repulsive) and second (attractive) term individually. From the potential the tip-sample forces can be derived as follows

$$F_{\mathrm{ts}} = -\frac{\partial V_{\mathrm{LJ}}}{\partial z} = -24\frac{\epsilon}{\sigma} \left[\left(\frac{\sigma}{z}\right)^{13} - \left(\frac{\sigma}{z}\right)^{7} \right]. \tag{3.3}$$

If the tip is far from the surface, the tip-sample forces are superseded by the internal elastic forces of the cantilever, which depend on the spring constant. Upon approaching closer the increasing attractive tip sample interactions result in the cantilever bending towards the sample, before it jumps into contact.

Further lowering the cantilever base, the tip gradually straightens out and eventually bends away from the surface. Throughout, the tip is in contact and thus constantly repelled by the short-range Pauli interactions. Upon reversing the approach, the tip bends back down, held in contact by the attractive Van der Waals forces until the internal strain of the cantilever is large enough to supersede.

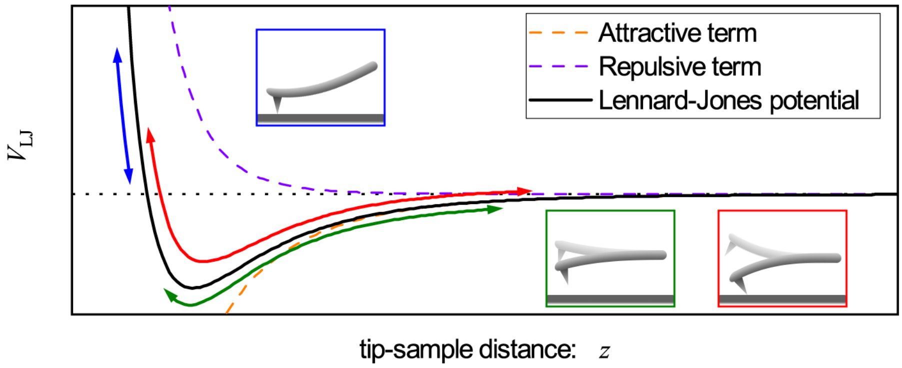

Figure 3.2: Tip-sample interaction. Schematic representation of the Lennard-Jones potential and the respective attractive and repulsive terms. Along the curve, regions for operation in contact (blue), semi-contact (red) and non-contact (green) mode are highlighted. The respective insets highlight the cantilever and tip position relative to the sample surface for the three modes.

With the tip pressed slightly onto the surface, the AFM is operated in contact mode. The resolution in this mode is, highly dependent on the tip's radius at the apex, and depending on the contact pressure the wear of the tip is rather large. Alternatively, the system can be operated in the non-contact or semi-contact mode. The signal to noise ratio is greatly increased by operating the AFM in dynamic mode [209], instead of directly reading out of the tip deflection. Using the dither piezo, a driven oscillation at the cantilevers eigenfrequency can be exited. Generally, a vertical oscillation (tapping) is excited. Rather weak excitation and subsequently a small resulting tapping amplitude (<10 nm), where the cantilever remains in the attractive potential close to the surface, is used, if the AFM is run in non-contact mode. Contamination layers and tip instabilities make this mode the most challenging [210], but only in this mode true atomic resolution is achieved [211, 212]. In semi-contact mode the tip is excited up to amplitudes exceeding 100 nm. Whilst tapping the tip periodically contacts the surface of the sample, hence analogous to contact mode the resolution is limited to the tip radius at the apex. In contrast to contact mode, the wear on the tip, due to grinding whilst laterally scanning the sample, is greatly reduced. Furthermore, the formation of menisci accompanied by capillary forces is hindered, thus the scan quality is improved.

Additionally, there are two feedback modes that can be used: constant height and constant force mode. In constant height mode, the height of the cantilever base and thus the tip relative to the sample is adjusted once, before starting the scan, and kept constant throughout taking the image. In more sophisticated setups it is possible to define the constant height as a tilted plane to correct for misalignment versus the sample surface. During scanning the deviations of the cantilever are mapped directly and recorded in either of the before-mentioned tip-sample interaction modes. Constant height scans have the major advantage of allowing very fast scan speeds, particularly in the non-contact mode. However, they run at the risk of breaking the tip or cantilever, if height deviations, e.g. contaminations like a dust particle, locally exceed the elastic range of either part. The second option is the constant force mode, which utilizes a feedback loop adjusting the sample height to mitigate any deviations sensed by the cantilever. Whilst the finite reaction time of the feedback loop describes the upper limit for the lateral scan speed, height differences can be mapped up to the extension limits of the z scanner piezo.

In the semi- or non-contact regime the AFM is generally used in AC, i.e. dynamic, mode, where the cantilever and tip oscillate. The excitation voltage of known frequency is applied to the dither piezo and serves as the reference to the lock-in amplifier. The laser read-out signal of the oscillating cantilever is then demodulated by the lock-in, yielding an amplitude and phase signal. The amplitude A is directly proportional to the physical amplitude of the tip. Every cantilever possesses an eigenfrequency f_{res} and thus sweeping the frequency in the vicinity yields the characteristic resonance peak of the unperturbed cantilever, as shown in the upper graph of figure 3.3. From this peak the quality factor is determined

$$Q = \frac{f_{\mathrm{res}}}{\Delta f_{\mathrm{FWHM}}}, \tag{3.4}$$

where Δf_{FWHM} is the resonance width, determined as full width at half maximum (FWHM). Additional repulsive or attractive forces acting on the cantilever modulate the resonance frequency, shifting it to higher or lower frequencies. The shift is proportional to the derivative of the force along the oscillation direction [209],

$$\Delta f = \frac{1}{2k}\frac{\partial F}{\partial z} f_0, \tag{3.5}$$

where k is the spring constant of the cantilever. During operation the dither piezo drives the oscillation at the unperturbed eigenfrequency f_0. If the resonance shifts due to additional forces, the resulting amplitude drop is detected and can be used as the input to the z feedback loop. To gain the information if an additional force is attractive or repulsive, the phase ϕ, is recorded. A phase shift to higher or lower values can be attributed to attractive, respectively repulsive, interactions, as depicted in the lower graph of figure 3.3. The phase describes the relation of the tip motion with respect to the base of the cantilever driven by the dither piezo. For small frequencies they are in phase, whereas for high frequencies they are out of phase, as depicted in the insets. As a technical note, the absolute value assigned to the phase can vary vastly as a linear offset is often applied, either to bring $\phi(f_0)$ to zero or $\pi/2$. Furthermore, in some systems even the whole phase curve is inverted.

For small Q factors, i.e. broad resonance peaks, the phase curve is behaving quasi linearly over a wide enough frequency range to directly image the phase shift, i.e. $\Delta\phi(x, y)$, during scanning. Additionally recording the frequency dependency of the phase shift, $\phi(f)$, allows reconstruction for quantitative evaluation of the data according to (3.5). Since the slope in the phase curve correlates with the sensitivity, such broad peaks yield limited sensitivity. In ambient atmosphere, most commercially available tips yield Q factors in this regime. Al-

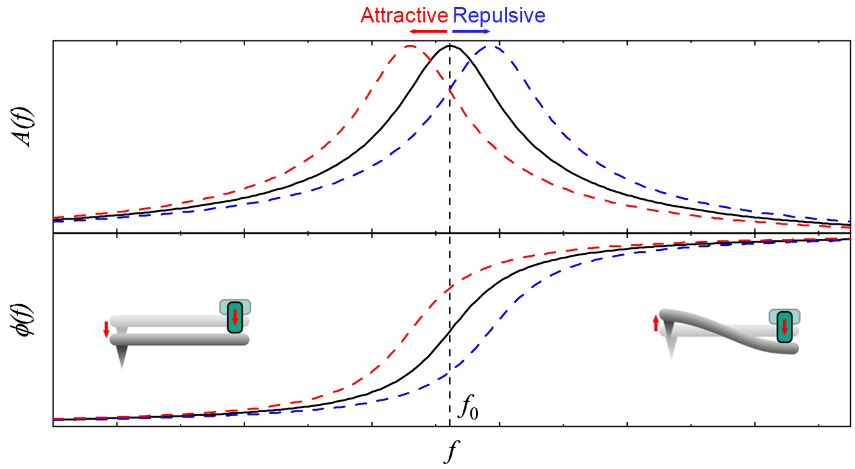

Figure 3.3: Frequency dependencies of amplitude and phase. The upper graph shows a characteristic resonance peak of a cantilever (black). The eigenfrequency and thus the resonance peak shifts to higher, respectively lower, frequencies for repulsive (blue), respectively attractive (red), forces acting on the tip. The lower graph depicts the corresponding phase signal, which in contrast to the amplitude is asymmetric. The insets to the lower graph emphasize the tip motion relative to the oscillation driving dither piezo.

ternatively, an additional phase sensitive frequency feedback loop (PLL), that readjusts the driving frequency accordingly is employed. Using such a feedback loop enables tracking of strong forces corresponding to frequency shifts Δf beyond the linearly sloped regime of the phase curve. Furthermore, working with high Q factor tips, i.e. extremely narrow resonance peaks and strong slopes in the phase curves, the sensitivity is improved. Hence, allowing measurements down to the atomic scale. For high Q factor measurements a tip with a naturally high eigenfrequency frequency f_{res} is advantageous. Low pressure and temperatures increase the Q factor further, which is accompanied by weaker internal damping. Thus, enforcing strongly reduced scan speeds. The minimum dwell time per pixel is limited by the time constant [201]

$$\tau = \frac{2Q}{f}, \tag{3.6}$$

where f is the actual frequency applied for the respective pixel. It gives an estimate of the time required for the tip to adopt to the varying forces in between neighboring pixels. Scanning with a high Q factor is a trade off between improved sensitivity and fast scan speeds. On a technical note, short scans are favored, because they reduce the risk of quasi random image artifacts occurring. Furthermore, ambient conditions like cryogenics are limiting the maximum scan time.

Topography scans

Topography scans are feasible with any combination of the above-mentioned modes. Due to the relative ease of use, constant force mode in contact is the standard technique to scan topography, if the resolution is sufficient. With small contact pressure applied, the tip rests on the surface and any height changes result in a deflection of the cantilever. The laser read-out signal of the deflection is fed into the feedback loop, which subsequently adjusts the z piezo accordingly. The required voltage $\Delta U_z(xy) \propto \Delta z$ can either be directly mapped or the signal of a extension height sensor of the z piezo is used. Additionally, tracking the deflection signal yields an error signal to the height map, which enables an assessment of the scan quality. If reduced tip wear or higher resolution are a concern, semi- or non-contact mode can be used. In that case the amplitude or phase signal of the driven oscillation serve as signal. In semi-contact the amplitude is used as the input signal to the z feedback loop, due to the phase being non-reliable when the tip makes contact with the sample. Upon approaching the surface, the free oscillation is damped gradually and eventually reaches a sharp cutoff where the tip makes physical contact with the sample. A setpoint amplitude A_{setpoint} amounting to damping from physical contact is used. Any height undulations during scanning translate into changes in the amplitude and the feedback loop corrects the z-piezo extension accordingly. In non-contact mode, both the amplitude or the phase can be used as input signals with respective setpoints. The feedback loop is run analog to semi-contact, respectively using the phase setpoint. Here, any deviations in the amplitude or phase signal serve as error signal and should be tracked as well. Depending on the exact mode used, the appropriate probe has to be chosen for the scan, as the tip radius at the apex, the Q factor and several other properties directly influence the scan quality.

Probe characteristics

AFM probes are commercially available in a vast variety of cantilever geometries, tip radii and spring constants. Additionally a multitude of coating for different purposes, which will be explored in more detail in section 3.1.2, can be applied. Probes are mainly made from single-crystalline silicon manufactured on wafers in batches by lithography [213]. Figure 3.4 a shows a classic geometry of an AFM probe. The exact geometry and predominantly the length l and thickness t of the cantilever determine the force constant, which can be tuned in a range of about 0.01-100 $\mathrm{N\,m^{-1}}$. In contact-mode based methods choosing a cantilever of appropriate force constant is the key to maintain good surface contact and steady contact force. Furthermore, the force constant affects the eigenfrequency, thus the Q factor and ultimately the sensitivity of the probe, which limits the z resolution. As mentioned, the tip radius r at the apex limits the maximum lateral resolution, whereas the tip height h plays a crucial role in mechanical stability. Additionally, the tip height represents the leaver lateral forces, acting on the tip, have on the cantilever. Figure 3.4 b elucidates the three potential excitations: bending due to a force normal to the surface plane, as well as buckling and torsion stemming from lateral forces along respectively perpendicular to the cantilever. Note, commonly the read-out channels are termed deflection and lateral, where the deflection channel also contains the signal attributed to buckling, i.e. a lateral force, as well. The contribution to the detected signal of the latter is expected to be superseded by the deflection signal in most cases. The lateral force channel, if available, only contains the lateral forces yielding torsional excitations. To obtain a good signal to noise

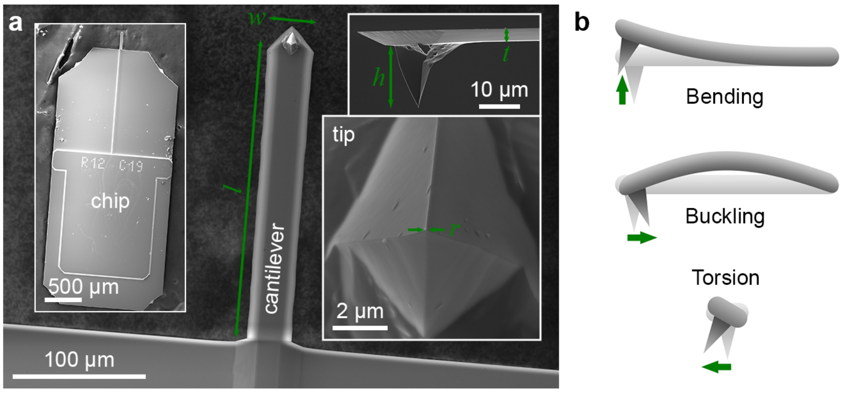

Figure 3.4: Detailed view of an AFM probe. **a**, SEM images of a standard AFM probe, the cantilver and tip. Relevant dimensions are marked. The demagnified inset on the left shows the full chip with the cantilever and tip attached on top. The insets on the right show a magnified view of the tip as well as a profile. **b**, the three potential stimuli exciting an oscillation.

ratio on the read-out, the backside of most cantilevers is coated, e.g. with aluminum, for enhanced reflectivity. Beyond the geometry the tip material must be adapted the experiment. Ranging from conductive coatings, like gold or platinum, to maximum wear resistant, potentially conductive doped, single crystal diamond tips, a multitude of options is commercially available [214–216]. More relevant for this work, magnetic coatings, e.g. made from Co-Cr alloys, are applied to create probes sensitive to magnetic interactions. The drawbacks of added coating are decreased spatial resolution due to the larger tip radius, and the potential delamination of the coating. For magnetic tips the guaranteed resolution of commercially available tips is usually in the range of 20-50 nm. Custom-build tips can reach radii, and thus resolution, below 10 nm [217, 218]. Depending on the tip geometry, as well as the thickness and type of the magnetic coating the remanent magnetization and coercivity of the probe can be adapted to the requirements of the intended experiment.

3.1.2 Advanced Scanning Probe Microscopy Techniques

Beyond topography scans, the AFM is established as a spectroscopic and manipulation tool in many labs. Several advanced scanning probe microscopy techniques, probing forces proportional to intrinsic material parameters of interest directly, or exploiting phenomena closely related to such, have been developed in the past decades [219].

Conductive atomic force microscopy (cAFM) allows the study of electrical transport properties on the nanoscale [220]. While scanning in contact mode, the tip-current is measured in a two-point configuration, where the voltage is applied between the sample back electrode and the tip [221, 222]. The obtained spatially resolved map of the conductivity, allows to determine if the conductivity is linked to certain conductive features, e.g. domain walls or defects. Piezoresponse force microscopy (PFM) is established as the standard technique for imaging and the study of ferroelectric domain structures on the nanoscale [223]. The strong emergent stray field, due to an AC voltage applied between the tip and the sample back electrode, excites the inverse piezoelectric effect. The resulting periodic contraction and expansion of the surface of the ferroelectric material, is detected in contact mode. Using a technique called vector PFM, i.e. combining the signal from the deflection as well as the lateral channels from two scans with the cantilever rotated 90° in between, it is even possible to fully reconstruct the three dimensional orientation of the polarization within domains [224]. Non-contact techniques, like Kelvin probe force microscopy (KPFM), allow to map relative changes of the work function of the surface [225]. To obtain this information the relative changes to the DC potential applied to the tip, in order to keep the electrostatic forces constant are mapped. KPFM is a more elaborate application of electrostatic force microscopy (EFM) [226, 227]. A technique that works analog to MFM except for the use of a non-magnetic conductive tip, sensitive to the electrostatic stray field. Evidently, cAFM, PFM and KPFM rely on the use of a conductive tip as well. In addition to scanning techniques the nanometer precision of the scanner piezos can also be used to investigate individual, or a spaced-out grid of points. Keeping the tip stationary not only eliminates errors attributed to lateral motion, but also allows point spectroscopy. Ranging from force curves over $I(V)$ curves to frequency dependent spectroscopy, modern AFMs can be configured to perform a multitude of experiments [228–231].

Magnetic Force Microscopy (MFM)

Probing the interactions related to magnetic domain textures is the main function of the AFM used in this work. The primary requirement for such experiments is a magnetic probe, as MFM quantifies the strength of the magnetic interaction of the magnetic stray field emerging from the sample and the magnetic moment of the probe [232, 233]. The major complication in the measurement lies in separating the magnetic forces from other contributions. The most common forces perturbing the magnetic measurement are related to the topography, i.e. strong short-range forces. These forces decay quickly with increasing tip-sample distance, whilst long-range forces remain detectable up to intermediate distances of several tens of nanometers. Hence, magnetic forces should be measured at a certain height above the surface, where short-range forces no longer interfere. Additionally, grounding the tip to the sample surface, mitigates signal from electrostatic forces.

MFM scans are typically performed in a dual pass technique, as shown in figure 3.5. In the first pass, the topography is obtained using either contact or tapping mode. For the second pass, the tip is lifted by d_{lift}, typically in the order 10 to 100 nm, and the previously recorded topography is retraced, with equidistant lift and disabled z feedback. Retracing is executed line by line to avoid thermal drift and other errors yielding misalignment of the two images recorded. During the second pass, the AFM is operated in non-contact mode, where it is most sensitive to small changes in the magnetic stray field. The amplitude ΔA, phase $\Delta\phi$ and potentially the frequency shift Δf are measured to image the magnetic interactions [209]. Figure 3.6 shows illustrative MFM images of permalloy obtained at room temperature. Panels a-c, depict the topography, amplitude and phase, these are image channels typically recorded with a low Q system using dual pass. Panels d-f, show the frequency shift, amplitude and phase derived during the second pass, when operating with the

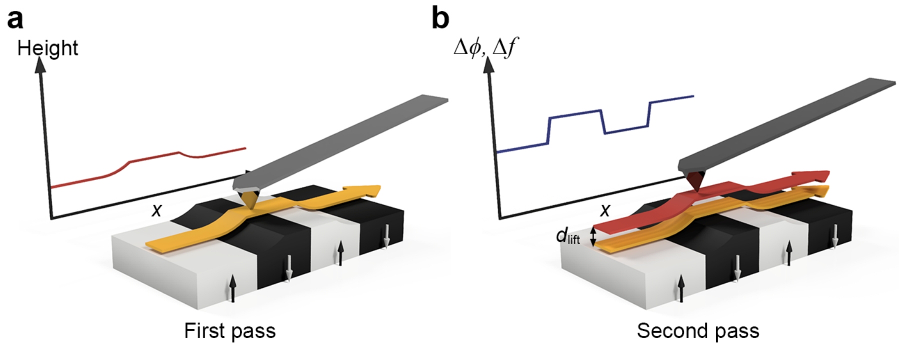

Figure 3.5: Magnetic force microscopy scheme. **a**, during the first pass a topography image is obtained. **b**, during the second pass, the tip retraces the topography with an additional height offset d_{lift}. Amplitude and phase, respectively the frequency shift, are recorded, containing information about the field distribution emerging form the underlying domain structure. Reproduced with permission from [86].

PLL. The phase signal, respectively the frequency shift, hold the quantifiable magnetic information. In case the PLL is used, the amplitude and phase serve as error channels. Permalloy forms ferromagnetic in-plane domains separated by sharp domain walls [234], coinciding with increased out of plane stray field. In the images the latter are clearly distinct from the domains. Particularly using the PLL it is evident, the feedback loop adopts well to gradual changes of the stray field within domains, but at the domain walls residual signal is visible in the phase channel.

Depending on the circumstances and the exact experimental setup several variations to the measurement procedure are possible. For very flat samples a single pass technique is sufficient, where a constant height non-contact scan sensitive to the magnetic signal, is executed at the lift height d_{lift} relative to the surface. In this mode the overall scan time is reduced by more than a factor of two, compared to a regular dual pass scan. Previously mentioned drawbacks of the constant height mode and potential artifacts in the magnetic signal due to tip-sample distance undulations are the major drawbacks of this approach. Increased lifetime and prolonged high-resolution imaging capabilities, due to the eliminated tip sample contact during the first pass, are the main advantages. Alternatively, bimodal dual AC mode, can be used to eliminate the need for a second pass [235, 236]. Here the resonance, and a higher resonance mode of the cantilever are both exited simultaneously. Whilst the resonance is used to track the topography in semi-contact, the higher mode is demodulated by an additional lock-in amplifier to obtain the magnetic signal. Remaining a semi-contact mode, with all positive and negative implications, the scan time is still reduced by over a factor of two, compared to the dual pass technique.

The classic and more sophisticated approaches to MFM explained above all, exploit the fundamental idea of different decay length and ultimately the existence of a practically unperturbed regime, where the magnetic forces supersede. However, electrostatic stray field decaying on a similar length scale, cannot always be evaded. A recent newly developed technique addresses this issue by an additional feedback loop compensating the electrostatic mismatch analog to KPFM, and is thus called Kelvin probe MFM (KPFM-MFM) [49, 237, 238]. An alternative approach is switching magnetization MFM (SM-MFM), where two scans with opposing tip magnetization are compared [239]. Summing the two images, the antisymmetric magnetic contributions should cancel, whereas contributions of non-magnetic origin, which remain unaltered with respect to the tip magnetization inversion, should add up. Subsequently, the non-magnetic contributions can be subtracted from the measured magnetic signal to obtain the unperturbed magnetic signal.

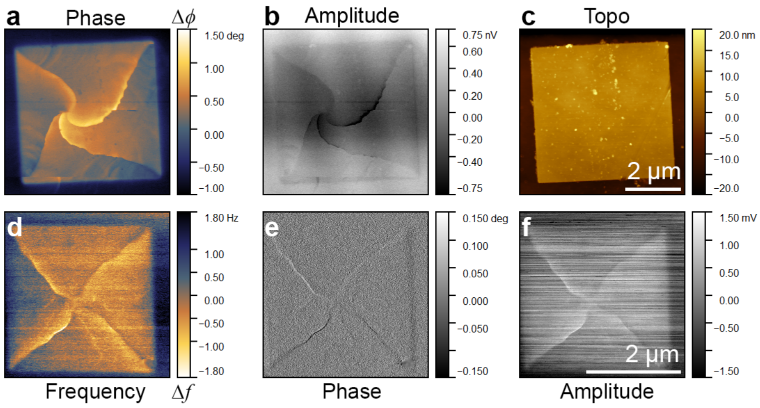

Figure 3.6: Magnetic force microscopy image of permalloy. **a**, **b**, phase and amplitude signal recorded during the second pass. **c**, corresponding topography image (first pass). **d**, frequency shift image obtained via a phase sensitive feedback loop during the second pass. **e**, **f**, corresponding phase and amplitude image serving as error channels.

Furthermore, the magnetic signal and the obtained image thereof are highly influenced by the mutual interaction of the tip magnetization and the sample. One of the reasons behind very weak magnetic interactions is the tip coating, which tends to break up into microscopic domains. The formation of such reduces the total magnetic moment of the tip and thereby lowers the sensitivity of the system. A problem that can be avoided by saturating the tip prior to scanning. However, very strong magnetic interactions, can lead to problems like imprinting of the magnetic signal in the topography, when scanning in tapping mode. To avoid such imprints, contact mode can be used for the first pass. While the topography signal is then generally unperturbed from the magnetic imprint, the magnetic interactions are actually strengthened due to the reduced mean tip-sample distance. Scanning in contact mode, but even a raised tip carrying a very large moment, yield a strong magnetic interaction, which can result in the tip actively altering the magnetic structure instead of imaging it. By comparison to less invasive magneto-optical Kerr effect microscopy the following three contrast regimes were classified [240]: The irreversible interaction regime is defined by strong interactions, sufficient to drag domain walls or locally switch the sample. The result is smeared out contrast, double images or significant mismatch of the back- and forward direction of the scan. In the reversible interaction regime, the tip induces local perturbations due to non-rigid magnetization in the tip or sample. Though, these relax back once the tip is removed, they lead to locally varying contrast. The negligible interaction regime, where the tip sample interaction is sufficiently small not to perturb either, yet still detectable, is the preferential one for imaging. To reach such conditions a hard-magnetic tip and large lift heights d_{lift} are the most promising. Hence, choosing an appropriate magnetic coating is required to keep the lift height within reasonable limits.

3.2 Electron Microscopy

Electron microscopy is another option to overcome the resolution limit of VLM [241]. First developed by E. Ruska in 1931, the importance of his invention was highlighted by the Nobel price in 1986. Peculiarly, a shared prize with G. Binning and H. Rohrer for inventing the STM. Unlike scanning probe microscopy, which takes a complementary approach to image acquisition, the fundamental principle of electron microscopes (EM) is similar to VLM. A beam of accelerated electrons is used as illumination source. The beam can be focused by specially shaped magnetic fields, so-called electron optical lenses. The diffraction limit (see equation 3.1), postulated by E. Abbe, applies to the electron beam analogous to visible light. However, the energy of the individual electron,

$$E = eU_{\text{accel}} = \frac{hc}{\lambda}, \tag{3.7}$$

and thus, its wave length, λ, can be tuned by the acceleration voltage, U_{accel}. The propagation speed of the wave is denoted c, that is the velocity of the electrons, which requires relativistic corrections for acceleration voltages exceeding 100 kV. Hence, by increasing the acceleration voltage, the wavelength, λ, and thus the diffraction limit decreases. For a 100 keV accelerated beam, the diffraction limit of 4 pm is sufficiently small to resolve subatomic features. As the excellent quality of the optical lenses manufactured for visual light microscopy is not matched by electron optics, resolution down to the diffraction limit is not achieved in electron microscopy. The resolution of electron microscopes is predominantly limited by the aberrations of the electron optical components. In 1936, O. Scherzer proved chromatic and spherical aberrations are inevitable flaws of the rotational symmetric electron lenses, whereas distortion and coma can be evaded [242]. Implementation and improvement of aberration corrections, are thus the only option to bring the resolution close to the diffraction limit. Additionally, the corrections are seminal to material studies, as higher acceleration voltages are inevitably linked to increased beam damage. Furthermore, increasing the acceleration voltage, beyond a few hundred kiloelectron volts, yields diminishing improvements in resolution. Initially developed to overcome the resolution limit of VLM, numerous benefits in using EM to study materials were discovered. Thus, making electron microscopes extremely valuable analysis and spectroscopy tools in modern labs across many fields, from natural over medical to forensic sciences [241, 243–245].

Following a brief introduction of fundamental operating principles and required components in section 3.2.1, an illustrative overview of the relevant capabilities of electron microscopes will be given. There are two types, transmission electron microscopy (TEM) and scanning electron microscopy (SEM), where various types of scattered electrons are detected for imaging. In section 3.2.2, the TEM is introduced, where particular focus lies on the three major imaging techniques, which visualize intrinsic magnetic structures. In section 3.2.3 the SEM will be introduced in the context of energy dispersive X-ray (EDX) analysis used for sample characterization. Furthermore, dual beam systems, with an additional focused ion beam (FIB-SEM), will be elucidated due to their key role in high precision sample manufacturing. Throughout, these sections are limited to a brief introduction to the respective topics.

3.2.1 Operating Principles

Before exploring the advantages and limitations of the two types of electron microscopes, their mutual operation principles are covered [241, 243, 246, 247]. Following the analogy of the VLM, electron microscopes can be divided in three major parts as well, the light source, the illumination system (condenser and objective lenses) and specimen stage, as well as the imaging system. Note that a distinction is made between a specimen, that is the individual piece of sample inserted in the microscope, and a sample, usually a single crystal, where multiple specimens can be obtained from. Generally, but not exclusively, EMs are built with a vertical column, where the electron gun sits on top. The latter contains both an electron source and the anode accelerating the emitted electrons to the desired speed, i.e. energy. Modern electron guns allow the use of variable acceleration voltages.

However, such changes require stringent adaptations of all electron optical components, like the magnetic electron optical lenses made of solenoids in the the column. In fact, while intrinsically working differently, the magnetic field of a solenoid acting on electrons resembles the effect of a convex glass lens to such a point, that magnetic lenses can be described by ray diagrams, as known from classic ray optics, too. Subsequently, properties like the magnification of a lens or lens system [241],

$$M = \frac{d_\mathrm{i}}{d_\mathrm{o}}, \tag{3.8}$$

the object and image distances d_o, d_i, as well as the focal length f are defined accordingly. Unlike the fixed curvature of a glass lens, the magnetic lens is based on a variable electromagnet. Hence, instead of switching or moving optical components, adaptations like changing focus or adopting to variable acceleration voltages can be done by adjusting the field, i.e. the current in the magnets. In the EM these lenses as well as the gun are all aligned along the optical axis.

Depending on the type of microscope, either a stage, where the specimen sits on top (SEM), or a specimen holder which is inserted into the column (TEM), both placing the specimen in the optical axis, is used [241, 243]. Stages and holders, usually feature multi-axis motion, including lateral and vertical translation, rotation about the optical and potentially other axes, and tilt. Furthermore, special upgrades and holders expand on possible sample orientation, allow cryogenic applications and even in-situ electrical biasing.

Finally, with the specimen placed in the desired orientation and conditions on the optical axis, it can be imaged. To obtain such images a series of highly specific detectors, ranging from simple counting over spatially resolved intensity mapping of electrons to energy selective radiation detection, is used. Each detector is tailored to measure a subset of specific signals generated when the incident electron beam hits the specimen.

Interactions of electrons with matter

The electron beam is a type of ionizing radiation. Ionizing is a term given to all types of radiation, if the energy transferred in a scattering event suffices to remove tightly bound, inner-shell electrons from a nucleus [241]. The advantage of using an incident beam of ionizing radiation is that it yields a vast variety of secondary signals. An illustrative overview of those relevant for this work, is given in figure 3.7. If the specimen thickness is sufficiently thin, i.e. electron permeable, the direct beam, which comprises the unscattered electrons of the incident beam, as well as (in-)elastically scattered transmitted beams, make up the majority of signal. For increasing thickness, the ratio of secondary signals increases, while the intensity of the transmitted beams diminishes. The

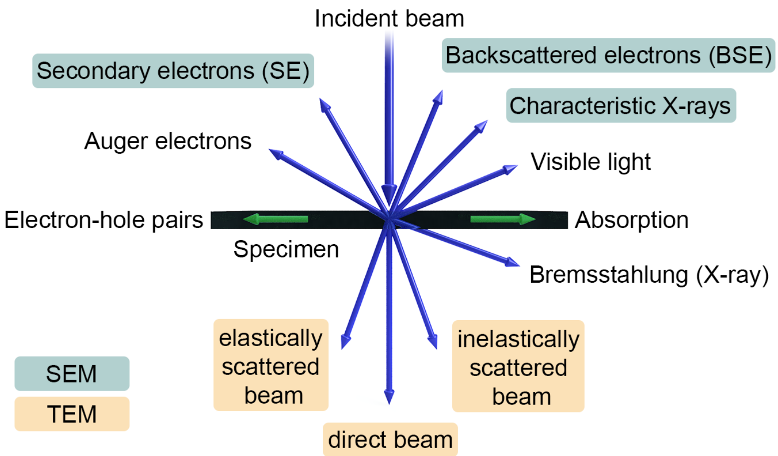

Figure 3.7: Scheme of EM signals. Recreated from [241].

secondary signals denote a large variety of electron types and radiations, which are the result of scattering and recombination events [241, 243]. When an electron hits the specimen the scattering cross-sections of the individual atoms in the specimen, each sitting on their respective lattice sites, determine the path it takes. The electron undergoes a cascade of scattering events, where the electron transfers energy to the material, until the low energy electron itself is absorbed. If the energy still suffices, the electron can also exit the material at some stage of the cascade. These electrons are known as backscattered electrons (BSE), if their direction is reversed, or make up the scattered beams, if the sample is thin enough. BSE are predominantly linked to elastic scattering with nuclei, hence obtained image contrast can be correlated to the atomic number of elements contained in the specimen. Electrons scattering with bound electrons transfer approximately half their kinetic energy, due to the equal mass, creating so-called secondary electrons (SE). Analogous, these start their own cascade of scattering events until they are reabsorbed, or exit the specimen, where they can be detected. The creation of a secondary electron yields a vacancy on the respective shell. Subsequently an electron from an outer shell jumps down to the vacancy, thereby emitting a photon of respective energy, i.e. a characteristic X-ray. The emission is isotropic, hence the likelihood of detecting such X-rays depends on the relative proximity to the surface of the emission, the composition and density of the material, as well as the detector position. Other byproducts of the scattering events potentially escaping the specimen are Auger electrons and visible light (cathodoluminescence). Furthermore, excited electron hole pairs, absorbed electrons, Bremsstrahlung and eventually phonons are the result of the incident beam. Note that a focused beam, as used in SEM and STEM, induces a severe and highly localized energy and charge input. For that reason, particularly the focused beam, but even a spread out, so-called parallel beam (TEM) can lead to non-reversible changes in the specimen, hence beam damage.

The scattering events elucidated above are well described by the electron in the classical picture of a particle, where (in-)elastic scattering describes loss free (afflicted) scattering events. Whilst this description is of major relevance to understand the concept of secondary signal generation, it omits the wave character entirely. The latter is relevant, when coherence, the in-phase relation of electron waves, is required. Imaging techniques, like holography, require coherent electron waves as these are based on interference of partial beams. Modern electron guns and aberration corrected optics fulfill these requirements.

3.2.2 Transmission Electron Microscopy

Electron transmission is inevitably linked to thin specimens [241]. The exact threshold specimen thickness to maintain permeability is strongly correlated to the energy of the incident beam. Modern TEMs typically work with up to 200 keV or 300 keV acceleration voltage, enabling clean imaging of specimen up to a few 100 nm. However, high resolution transmission electron microscopy (HRTEM), imaging down to the atomic length scale, routinely requires thicknesses of a few tens of nanometers, sometimes even down to solely a few atomic layers [248, 249].

Due to the design of the microscope, which includes optical components below the specimen holder, only transmitted beams scattered at low angles versus the direct beam can be collected and subsequently detected in the TEM. The actual detectors range from a fluorescent viewing screen to semiconductor, scintillator-photomultiplier, or charge-coupled device (CCD) based quadrant, sectioned, respectively pixelated, setups. Modern TEMs often have multiple types of detectors, and additional specific ones for analytical work.

A classical TEM image is obtained with one quasi parallel beam illuminating the sample, while the detector collects the resulting laterally resolved electron density distribution of the transmitted beams. These comprise information about crystal structure, defects and strain. Alternatively, the system can be used as scanning transmission electron microscope (STEM), where the beam is focused in a small spot, the probe, which is rastered across the specimen. At each raster point, the deflection of the transmitted beams is imaged. Either case is described by an amplitude image, as the observable is the spatially resolved intensity of the electrons on the detector plane. On a technical side note, here, amplitude contrast, comprises thickness contrast and contrast attributed to scattered electrons, which due to the induced path difference necessarily also includes phase information.

In contrast, imaging of the intrinsic magnetic structure of the specimen requires phase-contrast based imaging techniques. To obtain such contrast, two or more coherent beams are required. Superposition of a two beam system yields the intensity [250],

$$I = A^2 + B^2 + 2AB\cos(\varphi), \tag{3.9}$$

which is defined by the amplitudes, A and B, of the the two individual beams and a phase sensitive modulation. Here, φ describes the relative phase mismatch of the two beams. The image contains contrast analogous to a classical amplitude image, from the first two summands, and the phase-contrast as a superimposed perturbation.

Before elucidating the three common imaging techniques used, the effect of the intrinsic magnetization on the beam has to be considered. The Lorentz force [250, 251],

$$\boldsymbol{F}_\mathrm{L} = e(\boldsymbol{E} + \boldsymbol{v} \times \boldsymbol{B}), \tag{3.10}$$

which describes the effects of an electric field, $\boldsymbol{E}$, neglected in the consideration going forward, and the magnetic induction $\boldsymbol{B}$, stemming from the magnetization, on a single electron. Since, the velocity of the electron $\boldsymbol{v}$ is almost parallel to the optical axis, that is the z axis, the cross product yields no force, if the magnetization is parallel as well. Hence, for the standard specimen orientation, a laterally extended thin lamella in the xy plane, the electron beam is only perturbed by in-plane magnetized areas of the sample. In general, the TEM cannot image any magnetic structures magnetized along the optical axis, only those magnetized perpendicular. However, projecting the magnetization onto the xy plane in a series of images, with the sample gradually tilted up to 90°, allows full reconstruction of the intrinsic magnetization, via complex algorithms processing the tilt stack of images.

Additionally, a major concern when imaging the magnetic texture of a specimen is to actually image an unperturbed state. As mentioned electrons are focused using magnetic lenses and the objective lens, leaving a large enough gap for the specimen holder between the pole pieces, is a particularly strong one. The emergent field is typically up to 2 T, hence it cannot be used when imaging the virgin state of a sample. Fortunately, when needed, it allows in-situ application of magnetic field parallel to the optical axis in the TEM.

Lorentz transmission electron microscopy

LTEM, is an imaging technique, where the sample is uniformly illuminated by a single almost parallel incident beam. As a result, the laterally spaced out intensity is uniform above the specimen. The in-plane component of the magnetization (assuming according specimen orientation) results in locally deflected beams due to the Lorentz force, as illustrated in figure 3.8a [241, 251, 252]. With the assumption of the incident beam being coherent, superposition of an unperturbed and a deflected beam yields a detected intensity according to equation (3.9), i.e. phase-contrast. In order to make the phase contrast visible the TEM has to be used in Fresnel mode, that is in slight defocus. Overfocus (underfocus) technically describe an imaging condition, where the image plane lies above (below) the detector. Peculiarly, when switching from over to under focus, the contrast is reversed and it scales with the defocus. This scaling is exploited when using transport of intensity equation (TIE) based reconstruction of the magnetization [253]. A defocus stack of images, typically three, an in-, over and underfocused one of known defocus, are processed. Assuming linear scaling of the lateral intensity shift with the defocus, the local in-plane inductance required to yield the experimentally observed changes in the image contrast, can be calculated.

The resulting LTEM images are regular bright field images, that are intensity maps of the electron density, in varying defocii to maximize the magnetic contrast while maintaining reasonable levels of Fresnel fringing at thickness

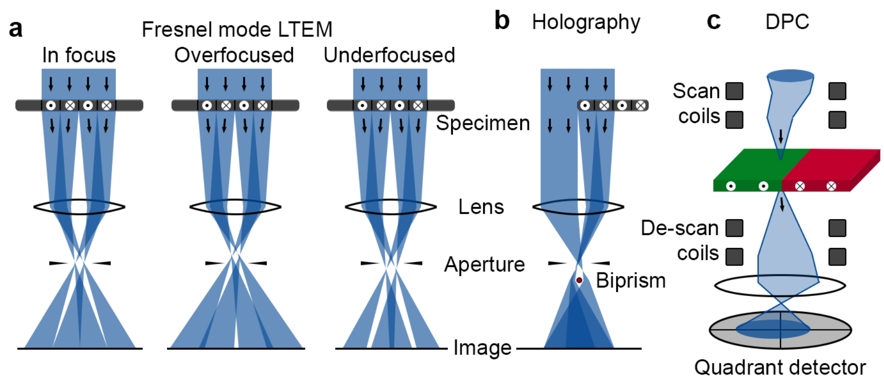

Figure 3.8: Overview of magnetic TEM modes. **a**, Fresnel mode LTEM. In focus, the image is uniformly exposed, whereas over- underfocused images yield intensity contrast. Note, the darker areas in the schematic correspond to increased electron density, i.e. bright regions in the actual image. **b**, off axis electron holography, using a biprism (red) to superimpose the reference beam (unperturbed, left) and the sampling partial beam (right). **c**, schematic setup of a differential phase contrast (DPC) scan in STEM mode. (De-)scan coils are used to (de-)raster the beam. The shift of the illuminated area on the detector is tracked for each spot. Panel **a** recreated from [252], panel **c** recreated from [251].

variations and grain boundaries. TIE reconstructed images are typically represented as phase images or false color plots, where the in-plane orientation of the induction is encoded in color and the magnitude of the in-plane component by the brightness. The major drawbacks of LTEM are, the complex deconvolution of phase contrast of magnetic origin and regular, e.g. topography induced, Fresnel contrast, as well as the non-quantitative nature when determining the size of objects. The latter is attributed to the assumptions made in TIE reconstruction and the out-of-focus imaging. The advantage is the quick image acquisition, usually not longer than a few seconds for clean images. For some specimen it is even in the several millisecond range, allowing live observation of domain morphology under stimuli like applied field. Live observation is limited to the (over-) underfocused bright field images, as TIE reconstruction is a complex task requiring precise and consistent image alignment. In this work LTEM refers only to the specific technique Fresnel mode LTEM.

Electron holography

Off axis electron holography is used to overcome the major drawbacks of Fresnel mode LTEM, which are inherently linked to the mandatory out-of-focus imaging. A hologram is obtained by superposition of an imaging and a reference beam [241, 251]. In the TEM this is realized by a biprism, which is essentially a very narrow diameter (<1 µm) positively charged wire, placed in the optical axis. The biprism is placed in the beam in a way that it superimposes the two partial beams, as depicted in figure 3.8b. One partial beam, which should account for about half the overall incident beam, serves as the unperturbed reference beam. The other one, illuminates the specimen. The resulting hologram contains the bright field image overlayed by a periodic structure, which contains the phase information. Simply outlined, using fast Fourier transformation (FFT) the image is transformed. The resulting center peak, containing the bright field image, and the characteristic side peak, containing the phase image, are cropped out and individually retransformed. The thereby filtered out phase image can subsequently be processed analogous to the TIE reconstructed phase image to obtain a false color in-plane inductance map.

Electron holography is imaged in focus, hence eliminating all undesired Fresnel contrast and allowing quantitative analysis of the size of magnetic nanostructures and domains. Properly calibrated imaging, even allows to eliminate electrostatic contributions from the hologram entirely and thus quantitative analysis of the observed induction. Besides an increased setup time of the experiment due to the alignment of the biprism, individual image acquisition is of comparable time scales to LTEM for clean imaging. Extracting information from the hologram is a more complex task, and thus the technique is not viable for live observations.

Differential phase contrast imaging

Differential phase contrast imaging (DPC) is one more technique, which is established for the study of magnetic samples [251]. In contrast to holography and LTEM, it is a STEM based technique. The idea lies in exploiting the local deflection of the probe, i.e. the focused beam, due to the Lorentz force as well. In the STEM setup, shown in figure 3.8c, the scan coils displace the probe laterally point by point onto the specimen. Below the specimen the previously induces displacement is reversed by the de-scan coils, yielding a stationary spot of controllable size on the detector. The presence of any magnetization in the specimen results in an additional deflection on the probe, which is not corrected for. Hence, from the shift of the spot on the detector the magnetization can be calculated.

From the lateral, that is two dimensional, shift of the spot, the two in-plane components of the magnetization can be reconstructed directly. Usually these are plotted individual or analogous to the other techniques in false color images. DPC is also sensitive to beam deflection of non-magnetic origin, e.g. topography or strain. Hence, interpretation of such images, should always include a reference image of non-magnetic contrast. DPC excels at high resolution imaging of magnetic textures down to sub nanometer spatial resolution [254]. However, the overall acquisition time of an image is drastically increased, as the detection per pixel is on the same time scale as acquiring a full LTEM image.

3.2.3 Scanning Electron Microscopy

In the SEM sample illumination works similar to the STEM, where the beam is focused on the surface of the specimen and scanner coils displace the beam along the rastered path as desired [243]. Regardless of sample thickness, any sample can in principle be studied in the SEM. However, as no electrons are transmitted, the energy of the beam, as well as the charge are locally discharged into the sample. Hence insulating materials, generally incapable of dissipating the energy and implanted charge, are a lot more challenging to image. Commercially available SEMs today typically allow for beam energies

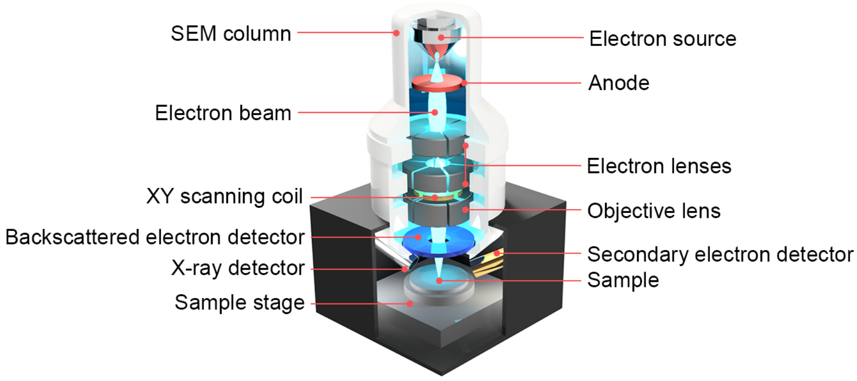

Figure 3.9: Scanning Electron Microscope SEM Reproduced with permission from [86].

up to 30 keV. On the lower end, the limit is in the range of a few hundred electron volts. In figure 3.9, the classic design principle of a SEM is depicted. The detectors are located above the stage on the sides of the chamber, as well as in the objective lens. Most commonly SEs are used to obtain an image in the SEM, where the contrast is revealing the topography of the specimen. Bright areas correspond to edges or tilted surfaces, where the relative number of secondary electrons escaping the material is larger. The actual detectors are scintillator-photomultiplier, or CCD based, and effectively count the number of electrons detected per pixel dwell time. The major advantage of a SEM compared to other techniques lies in the ease and variability of the magnification. Starting from approx. $M = 25$, commonly denoted 25x, which is roughly in the range generic optical microscopes allow, within seconds the magnification can be raised to several 1000x. The resolution limit of modern commercially available SEMs reaches the sub nanometer scale (≈ 0.5 nm).

Energy dispersive X-ray analysis

Besides electron detection, the SEM allows analytic spectroscopy on the microscopic scale [243]. One type, routinely used throughout this work to ensure sample quality and consistency, is EDX. Scattering events lead to the emission of characteristic X-rays, as described in detail above. Hence, if the energy of the incident beam, which is an ionizing beam, is sufficient to free up tightly bound inner-shell electrons, these characteristic X-rays are a regularly occurring by-product. Furthermore, they are characteristic, i.e. the energy of the emitted radiation describes one particular transition in one particular atom. Hence, by detecting the energy spectrum and quantity of the emitted radiation, one can assess the elements these originate from.

In practice EDX is a very fast technique, if coarse confirmation of stoichiometry (± 3 %) is sufficient. Exact analysis of the stoichiometry is rather complex and susceptible to errors. Such detailed analysis is beyond the scope of this work.

Focused Ion Beam

Another type of particle beam based system is the focused ion beam (FIB), which works similar to the SEM [246, 247]. It offers advanced functionality in milling, material deposition, and implantation, beyond analogous imaging capabilities to the SEM. In contrast to the SEM, the FIB beam consists of ions instead of electrons. For the optical components this has two major implications. The beam is created in a gun, which comprises a liquid-metal ion source, and it is focused with electrostatic field-based lenses. When hitting the specimen, the ions can trigger the emission of SE as well, hence the beam can be used to image analogous to the SEM. The major difference to the electron-based technique is that the ion beam is inherently destructive. Besides SE, the ion beam also triggers the emission of secondary ions, i.e. effectively sputters away the specimen, and implants incident ions up to a few nanometers below the surface. An illustrative overview of these processes is given in figure 3.10.

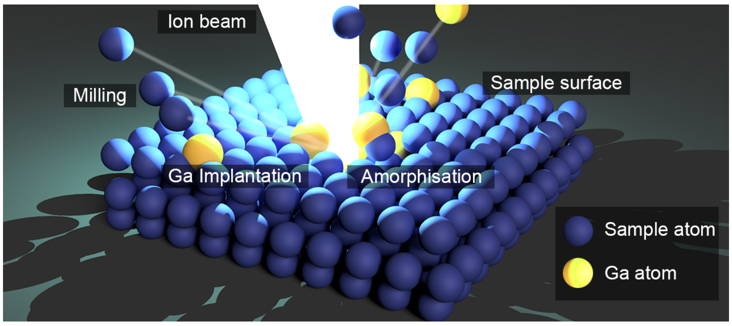

Figure 3.10: Focused Ion Beam (FIB) sample interaction Reproduced with permission from [86].

Today gallium ions (Ga^+) are established as the industry standard, but several nobel gas based systems are available as well. The advantages of gallium are, the easy manageability, due to the low melting point, and the intermediate weight. Since all scattering based interactions depend on the ratio of masses involved, very light ions are almost incapable of sputtering heavy atoms, whereas heavy accelerated ions cause severe sputtering damage on substrates containing light atoms. Gallium enables precise milling of most materials with tolerable damage. The ions are accelerated with up to 30 kV resulting in an amorphous damage layer at the surface, which is approximated to be about 1 nm/kV.

Individually the FIB is a sophisticated tool for milling, which is made even more powerful when combined with a SEM in a single instrument. The FIB-SEM, e.g. DualBeam or CrossBeam systems, combines a FIB and a SEM column attached to one chamber and stage for alternating or parallel in-situ use. Thus, the FIB can be optimized for ideal milling capabilities, enabling complex nano-structuring, while the SEM is used for damage free imaging. Furthermore, the capabilities can be extended by additional use of a gas injection system (GIS), which allows local deposition of a vast variety of materials, including conducting, e.g. platinum (Pt), aluminum (Al), tungsten (W), gold (Au), carbon (C) and insulating options, like silicon dioxide (SiO_2). Deposited materials are rather impure, due the organometallic compounds in the precursor, which are required to make them gaseous in the first place. Additionally, the FIB-SEM chamber is typically equipped with a micro manipulator, i.e. a piezo-driven microprobe, which can be used for in-situ physical manipulation. Combined, these components allow complex processes, such as lift-out of nanofabricated structures. Where, a thin lamella is milled out from the bulk specimen, welded to the manipulator and lifted out. Subsequently, the lamella is welded to a TEM grid for further thinning, or placed on a substrate for AFM study.

3.3 Experimental Equipment

Throughout this work several microscopes have been used for different magnetic characterizations and preparation techniques. In the following the instruments will be introduced very briefly. These are:

- **AFM**: attoAFM I by attocube (Wittenstein Group),
- **AFM**: Cypher ES Environmental AFM by Oxford Instruments (Asylum Research),
- **AFM**: NTEGRA AFM by NT-MDT (Spectrum Instruments),
- **FIB-SEM**: Gemini 2 Crossbeam 550 by Zeiss,
- **FIB-SEM**: Helios G4 UX DualBeam FIB by ThermoFisher Scientific (formerly FEI),
- **FIB-SEM**: FEI Helios NanoLab DualBeam FIB by ThermoFisher Scientific (formerly FEI),
- **TEM**: JEM-ARM200F / NeoARM by Jeol,
- **TEM**: JEM-2100F by Jeol,
- **TEM**: FEI Titan G2 60-300 by ThermoFisher Scientific (formerly FEI).

All AFMs are capable of MFM and further advanced scanning probe techniques. The Cypher, as well as the NT-MDT system, both located at NTNU, are used exclusively at room temperature. They are fully damped table top systems, additionally setup on an optical bench each, equipped with a four-quadrant diode for the signal read out. Hence, they yield extremely clean images at room temperature.

The attocube attoAFM I is designed as a very compact system, which fits inside a standardized 2-inch vacuum tube, that can be inserted in a cryostat, e.g. in our system equipped with a 2-2-5 T magnet. The AFM is operated in a temperature range from 1.3 K to 300 K and in-situ vector field is applied up to 2 T. The closed loop option allows nanometric precision for the tip position during operation.

All magnetic images are recorded with either of the three systems listed above, employing the dual or single pass techniques described in section 3.1.2. For the measurements one of the following tips by NANOSENSORS is used: PPP-MFMR (standard probe), SSS-MFMR (smaller tip radius), PPP-LM-MFMR (low moment) and SSS-QMFMR (high vacuum), based on necessity.

Both DualBeam FIB-SEMs, from NTNU Nanolab, are used to prepare lamellae for AFM studies. Besides AFM specimen preparation, the Crossbeam system is additionally used extensively for TEM preparation, as well as EDX analysis. Within the work for this projects the crossbeam was retrofitted with an additional rotation axis of the micro manipulator and the stage. Thereby in-situ specimen rotations including and exceeding 90° were enabled, facilitating advanced specimen preparations and nano-patterning.

Fresnel mode LTEM and DPC images of magnetic textures are measured on the Jeol TEMs. Electron holography measurements are conducted with the FEI Titan "Holo" system at the Ernst Ruska-Centre (ER-C), Jülich.

Concomitant micromagnetic simulations were performed at the Helmholtz Zentrum Dresden Rossendorf. Additional micromagnetic simulations were calculated at NTNU.

3.4 Sample Preparation

All characterized samples were provided by Dr. V. Tsurkan, Dr. L. Prodan and Dr. M. Kassem at the University of Augsburg. Single crystals have been grown by the chemical transport reactions method. As starting material for the growth, the preliminary synthesized polycrystalline powder has been used, which had been prepared by solid state reactions from the respective high-purity elements. Iodine has been utilized as the transport agent in the single crystal growth.

Individual crystals are selected for microscopic study, once the proper stoichiometry of sample badges has been confirmed and their macroscopic magnetic characterization is completed. Subsequently, the surfaces of the crystals are inspected via SEM. Furthermore, individual crystals are analyzed by EDX.

For TEM, single crystals are loaded in the FIB-SEM, where lamellae of desired orientation are cut and lifted out, following cross sectional or plane-view preparation procedure. Mounted to a TEM half-grid, they are thinned and polished by the ion beam to the desired final shape. Subsequently, the half grids are mounted in the TEM holder and directly inserted into the microscope. Alternatively, the polished lamellae, i.e. nanostructures, are placed flat on a substrate for AFM measurements. More details on lamellae preparation via FIB-SEM will be given in section 5.1.

Via AFM/MFM as grown facets of desired orientation, respectively, lapped and polished surfaces of specimen are investigated. The crystals are mounted on specimen carrier chips, which may include electrodes for optional in-situ electrical biasing. Subsequently, specimens, except FIB prepared nanostructures, are thoroughly cleaned following a protocol which involves high purity isopropanol, acetone and methanol applied consecutively by mull and dust free optical cleaning wipes, before mounting them in the AFM.

4

Target Material

Fe_3Sn_2

Since the 1940s Fe-Sn has been investigated focusing on the rich phase diagram of stable compounds of varying stoichiometry and their magnetic properties [56, 57]. Recently, one phase - out of the plethora of interesting magnetic compositions - Fe_3Sn_2 has been in the scientific focus due to the observation of stable skyrmions at room temperature [52]. This specific composition crystallizes in the rhombohedral space group $R\overline{3}m$, with a tripled hexagonal unit cell. The lattice parameters are $a, b = 5.3145\,\text{Å}$ and $c = 19.7025\,\text{Å}$. The centrosymmetric crystal structure consists of offset kagome bilayers. Kagome lattices are two-dimensional networks of corner-sharing triangles, as depicted in the bottom left of figure 4.1a. Fe occupies the sites of the kagome lattice, whereas Sn fills the hexagonal vacancies. Each kagome bilayer, see the upper frame, is separated by a Sn spacing layer. The relative orientation of the latter is shown on the bottom right. The unit cell contains 6 Fe_3Sn kagome layers with a total of 18 Fe ions [59, 255].

Beyond the scope of what is primarily relevant for this work, the kagome-based system has been investigated for a vast variety of exotic properties. The itinerant system exhibits spin frustration [59] and can host numerous magnetic phenomena due to the competition of multiple magnetic interactions, including a low-temperature spin glass phase (below 80 K) and the anomalous Hall effect (AHE), that is the emergence of a large hall resistivity, which cannot be explained by classical transport theory. The emergence of the AHE is related to the Berry Phase, skew-scattering and side-jump scattering [59] and was extensively studied [59, 60, 257, 258]. Angle-resolved photoemission spectroscopy (ARPES) revealed massive Dirac fermions, which were linked to the AHE [61].

Early characterization of Fe_3Sn_2, analogous to many other Fe-Sn compounds, focused on the magnetic properties. These properties lay the foundation for the peculiar domain structures investigated throughout this work. Mösbauer spectroscopy and magnetometry studies were performed across a broad temperature range [58, 259–262]. These studies concluded a mean magnetic moment of approximately $2\mu_B$/Fe at low temperatures and a Curie tem-

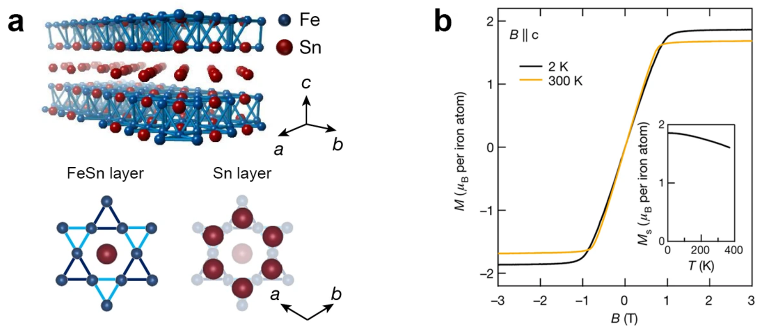

Figure 4.1: Fe_3Sn_2 crystal structure and magnetic hysteresis. **a**, crystal structure of Fe_3Sn_2, including the orientation of the crystallographic axes. Lower illustrations show the FeSn kagome lattice (left) and the relative orientation of the Sn honeycomb lattice in the spacer layers (right). **b**, magnetic hysteresis curves for $\boldsymbol{B} \parallel c$ at room temperature (yellow) and 2 K (black). The inset depicts the temperature dependence of the saturation magnetization. Reproduced with permission from [86] based on [61, 256].

perature of $T_C = 640\,\mathrm{K}$. Furthermore, the majority of spins were found to align along the easy-axis, which is the c axis, above 250 K, whereas below, the system undergoes a transition to an easy-plane (ab plane) configuration. Figure 4.1a illustrates the relative orientations of the axes. The low temperature spin reorientation was studied in depth, revealing that the gradual rotation is not associated with a rotation of the easy-axis, but more accurately represented by the coexistence of the easy-axis and easy-plane orientation during a first order phase transition [62]. This transition was found to occur at around 120 K using a superconducting quantum interference device (SQUID), and was subsequently directly observed via MFM [263]. Furthermore, the magnetic properties of Fe_3Sn_2 are linked to the itinerant $3d$ electrons of the Fe atoms [60]. Hysteresis measurements, as depicted in figure 4.1b, show linear behavior up to the saturation for room temperature, as well as 2 K. Due to the lack of coercivity, Fe_3Sn_2 is a soft ferromagnet. Additionally, the weak temperature dependence of the saturation value is corroborated by the inset.

A numerical study of spin frustration in kagome crystal systems, like Fe_3Sn_2, predicted stable skyrmions at room temperature [264], which were first observed in 2017 by Hou *et al.* [52]. In their work, experimental observations by LTEM are supplemented by micromagnetic simulations. They report on the occurrence of stripe domain patterns, as well as both type I (skyrmionic) and type II (topologically trivial) bubbles in the material. Furthermore, they attribute the stability of individual domains to the magnetocrystalline anisotropy and implicitly identified the material as an intermediate Q system, see equation (2.52). Based on bulk magnetoresistance and susceptibility data, the phase diagram, shown in figure 4.2a, is proposed. Figure 4.2b, illustrates the characteristic stripe patterns in zero field, observed via LTEM. Applying external magnetif field of 300 mT, $\boldsymbol{B} \parallel c$, the system exhibits bubble domains, as shown in figure 4.2c. Figure 4.2d-g, illustrate the field evolution of a single bubble domain transitioning from type II to type I. The corresponding TIE reconstructed induction maps are shown in figure 4.2h-k. Figure 4.2d and h depict the topologically trivial type II bubble, which exhibits two wall segments of opposite helicities. Whereas the non-trivial bubble domain shown in figure 4.2g and k, constitutes of one continuous domain wall analogous to a skyrmion.

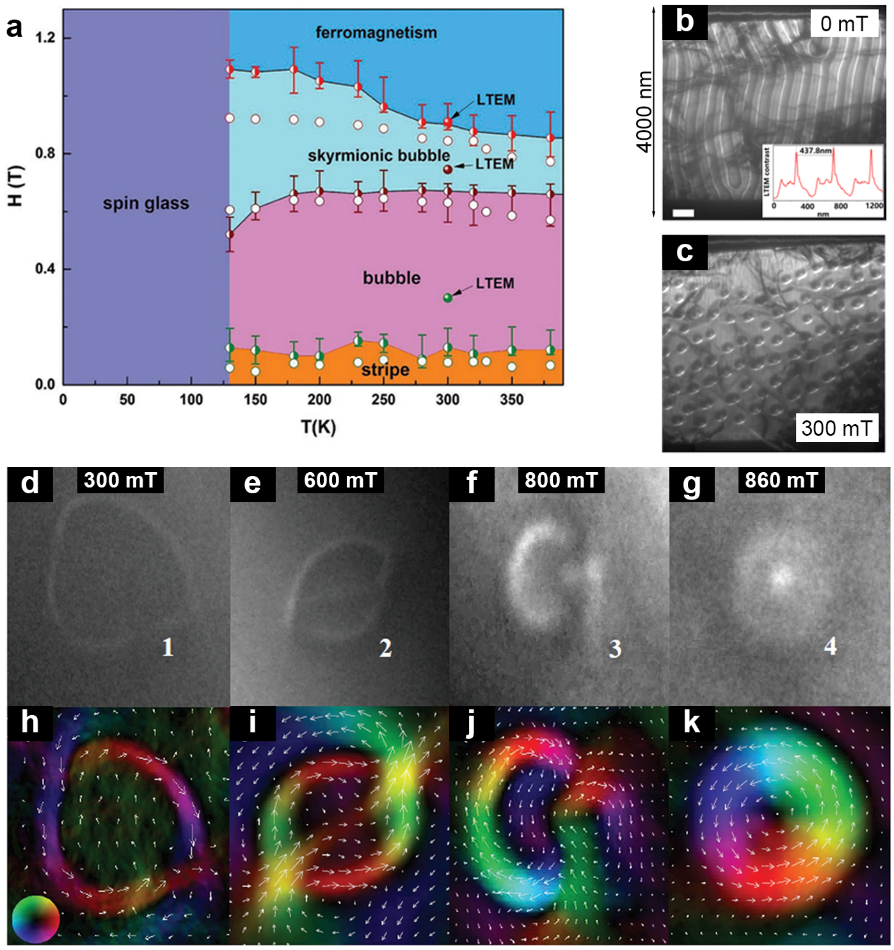

Figure 4.2: Phase diagram and observation of bubbles in Fe_3Sn_2. a, temperature, T, and magnetic field, $\boldsymbol{H} \parallel c$, dependent phase diagram. **b**, bright field LTEM image of a Fe_3Sn_2 lamella at room temperature and in zero field exhibiting stripe domains. The inset shows the intensity along a line section. **c**, analogous image in field (300 mT), revealing magnetic bubbles. **d-g**, bright field LTEM images of four different magnetic bubbles of type II (**d**, **e**) and type I (**f**, **g**). **h-k**, corresponding TIE images, where the in-plane magnetization is encoded according to the color wheel in panel **h** and emphasized by the white arrows. Reproduced with permission from [86] based on [52, 53].

Further studies by Hou *et al.* revealed intriguing properties of Fe_3Sn_2 [53, 265, 266]. Geometrical confinement can stabilize type I over type II bubbles and drastically decrease the required external magnetic fields by an order of magnitude. Thus, bringing temperature and field values closer to values required for potential applications [265]. Interestingly, early results of current-induced dynamics experiments reveal helicity reversal by spin transfer torque [266].

5

Results and Discussion

5.1 Towards Technological Relevant Functional Objects

Modern digital infrastructure demands miniaturization of all components to the nano-scale [267]. Magnetic storage media, i.e. data encoded in magnetic domains, have been the key technology of high capacity memory for decades. However, the miniaturization of individual domains beyond a limit makes these domains prone to random undesired switching. This problem could be solved by using topologically protected spin textures as the bits of information. Hence, model systems like Fe_3Sn_2, which exhibit topologically protected domains even above room temperature, are ideal candidates to address this problem. Such insights gained on model systems are relevant for the design and material choices of potential future applications.

Fe_3Sn_2 single-crystalline samples grow in the shape of hexagonal laterally extended sheets in the *ab* plane of up to several millimeters. The thickness along the crystallographic *c* axis ranges from 20-40 µm [54]. Due to their large dimensions, the as-grown single-crystalline samples do not serve as good model systems for micron- to nano-scale devices, where limited sample size is required to enforce constraints on the magnetic texture. Hence, to obtain control over the magnetic texture, geometrical constraints were introduced. Therefore, for the present work, a series of lamellae were prepared via FIB-SEM, allowing subsequent studies of magnetic textures via MFM and LTEM. Experimental details of the methods can be found in sections 3.1.2, 3.2.2, and 3.2.3.

5.1.1 Plane-view FIB-SEM Preparation

Here, *ab* plane lamellae are studied, therefore the PMA is expected to stabilize an out-of-plane domain configuration. Due to the layered structure of Fe_3Sn_2, the as-grown single crystals regularly exhibit severe delamination at the edges. Thus, the preparation of *ab* plane lamellae from an edge, following established procedures for cross-sectional preparation is an unsuitable approach. Instead, plane-view lamellae are prepared. First, the single crystal is mounted on a SEM stub, either using conductive carbon tape or silver paste and loaded into the

FIB-SEM. Once a suitable region is determined, a large trench is coarsely milled with the FIB. An ion beam acceleration voltage of 30 kV and beam currents ranging from 30-100 nA, depending on the required size, are used. This initial trench is angled versus the *ab* surface of the Fe_3Sn_2 single crystal. Subsequently, the stage is rotated by 180° and a similar trench is cut so that both trenches meet under the lamella bridge. The results of these initial steps are shown in figure 5.1a. The best compromise between FIB cutting efficiency and obtaining the largest possible triangular prism-shaped volume is obtained for trenches cut at approximately 45° with respect to the *ab* surface. Finally, a trapezoidal shaped cross-sectional cut, angled 90° to the *ab* surface and the orientation of the trenches is used to expose one end of the prism-shaped volume. Following coarse milling, the exposed volume is cleaned up by cross-sectional cuts at 3 nA beam current of matching angles yielding the exposed volume depicted in figure 5.1a. Note, matching angles to obtain plane parallel cuts to prior cuts always

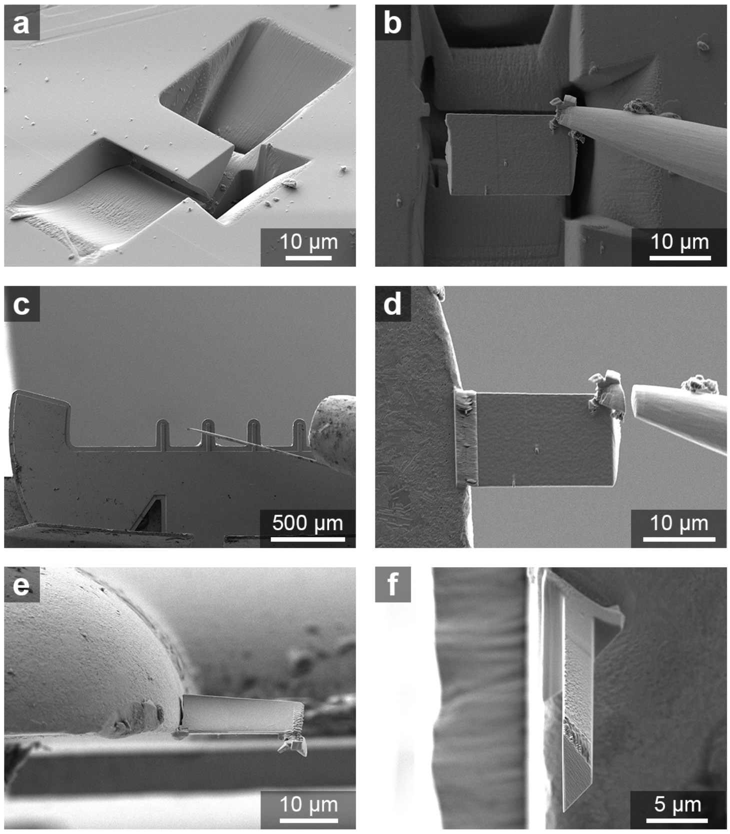

Figure 5.1: FIB-SEM based plane-view lamella preparation. **a**, isolation of triangular prism-shaped volume. **b**, lift-out. **c**, transfer to TEM half grid oriented horizontal. **d**, welding to TEM half grid. **e**, triangular prism-shaped volume on TEM grid oriented vertical. **f**, early stage of thinning of lamellae.

implies consideration of beam current specific additional tilt to compensate for the beam profile. Once, the lamella is cut free from the volume on three sides, a perpendicular cut is made on the fourth side so that the lamella is only held in place by a thin bridge.

Now that the lamella is cut free, with minimal redeposited material present, it can be lifted onto the TEM half grid. To do this, the crystal is orientated in a way that the *ab* plane is horizontal and the exposed volume is accessible both by the FIB to cut and deposit material, as well as the micro-manipulator. The latter is welded on the topside to the prism-shaped volume with ion beam deposited platinum. Once a solid weld is confirmed, the remaining bridge is cut by the FIB freeing up the triangular prism-shaped volume for lift-out, as shown in figure 5.1b. The volume is then lifted out using the micro-manipulator and transferred to a TEM half grid, see figure 5.1c. During lift-out, the micro-manipulator is ideally solely retracted and extended along the radial axis. Any lateral displacement, as well as any change in height, generally coincide with adjusting the orientation of the manipulator in spherical coordinates, i.e. introduce angular mismatch of the lamella. The TEM grid is mounted horizontal in the FIB-SEM, matching the orientation of the prism-shaped volume, which is welded to the latter, see figure 5.1d. Using the Kleindiek RoTip Shuttle, which is an additional 360° free rotation axis on top of the sample stage the TEM grid is mounted to, the TEM grid can be tilted upwards by 90° in-situ. Furthermore, use of the tilt axis of the RoTip shuttles in combination with the stage rotation allows to compensate for angular mismatch introduced during lift-out and transfer. Figure 5.1e shows the desired orientation of the prism-shaped volume, with the *ab* plane oriented in line with the SEM respectively FIB beam. Using the FIB at gradually decreasing beam currents, 3 nA down to a few tens of pA, the volume is finally thinned to a lamella of desired thickness. An illustration of part of this process is given in figure 5.1f, where the thickness is being reduced from both sides with a large beam current of 3 nA.

Following this plane-view lamellae preparation procedure, triangular prism shaped volumes, see figure 5.2a, are isolated as the starting point for all lamellae investigated within the scope of this thesis. From this common starting point, subsequent steps differ, depending on how the magnetic textures will be imaged. These alternative steps are described individually below.

Lamellae for TEM studies

This section continues from the common procedure, outlined above, to describe the steps needed for TEM lamellae preparation. Lamellae remaining on the TEM grid are thinned by applying cross-sectional plane parallel cuts of successively decreasing beam current down to a few tens of pA. That means the lamella is thinned layer by layer. In the case of the semi-metal Fe_3Sn_2, this process generally does not require special compensation methods for beam drift. However, the material is relatively soft and tends to curl, when its thickness goes down below 100 nm. Furthermore, it is highly susceptible to curtaining. Curtaining describes an obtained undulating cutting pattern, despite cutting in a straight line. This is a particular problem as lamellae are thinned from a previously cut surfaces, which may already exhibit curtains (see top surface of the prism in figure 5.2a). To obtain precise lamellae, it is vital the prism-shaped volume is carefully prepared with clean surfaces. Supporting structures in line with the desired lateral size of the lamella have to be preserved. Alternatively,

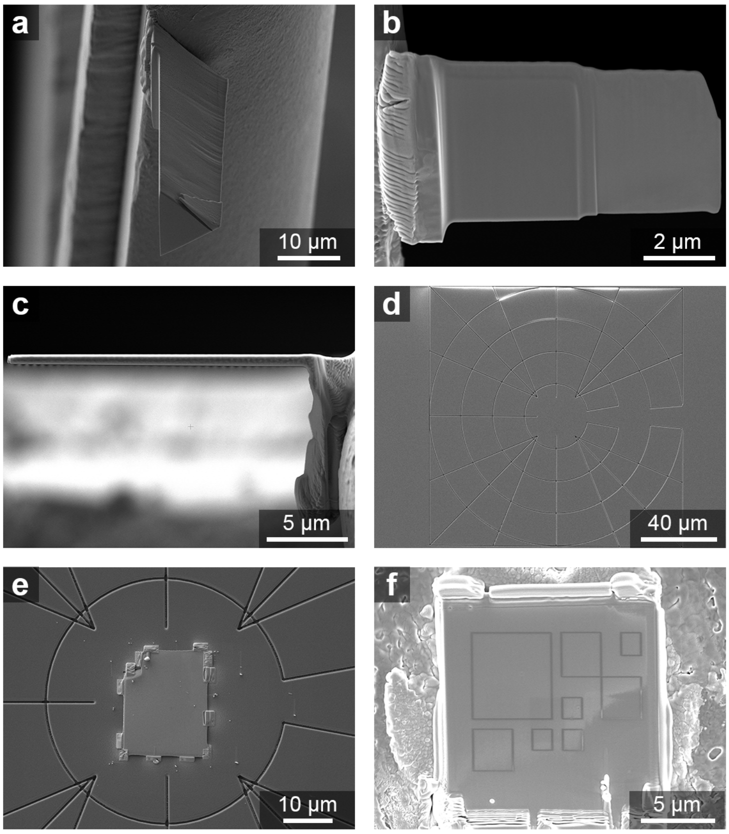

Figure 5.2: Preparation of lamellae for TEM and SPM. **a**, universal starting point: triangular prism-shaped volume. **b**, fully prepared lamella for TEM on half grid. **c**, thinned lamella for SPM. **d**, FIB cut landing zone on substrate for SPM. **e**, lamella transferred to substrate. **f**, in-situ FIB patterned lamella for SPM on substrate.

the thin region of the lamella can only be a window between thicker supporting structures.

Deviating from classic plane parallel preparation, wedge-like lamellae are obtained by milling at a small inclination. An example is shown in figure 5.2b, where the left side is plane parallel with a thickness of approx. 200 nm followed by a step-like reduction of the thickness to about 150 nm. On the right side, it is wedged from full thickness at the top to below 50 nm at the bottom. Once the target measures of the lamellae are reached, they are polished at 5 kV ion beam acceleration voltage and 200 pA, respectively, 10 pA to reduce the damage layer suffering from Ga implantation.

Lamellae for SPM studies

In principle, preparing lamellae for SPM follows the same thinning procedure, but there are two additional caveats. First, such lamellae are required to be even stronger, as they have to withstand another lift-out process including welding. Secondly, lamellae should be placed flat on the substrate without the introduction of strain (unless intended). Hence, their backsides are required to match the surfaces of the substrates. Due to these constraints, lamellae prepared for SPM study are usually not thinned below 100 nm. Figure 5.2c shows such a large lamella intended for SPM study with a target thickness of about 600 nm.

A major difference between TEM and SPM lamella is the substrate they are placed on: while for TEM specific grids are commercially available for the SPM these are prepared in house. There are two challenges that arise not experienced in the TEM: Firstly, electrostatic charging of the mm sized substrate and subsequent improper grounding of the specimen. Secondly, finding the ten-micron square lamella on a mm sized substrate. To prevent spurious electrostatic forces, it is important to have the SPM tip and the sample back electrode well-grounded to the same earth. To achieve this, a thin layer of gold is deposited on the silicon wafer. Since the SPMs have limited maximum scan ranges of a few tens of micro-meters and the lamellae are often effectively undetectable on the substrate with the build-in optical microscopes, a FIB cut pattern marking the landing zone for the lamellae is prepared on the coated substrate. Figure 5.2d depicts one exemplary pattern, where the uncut path from the right hand side ensures grounding to the back electrode. The pattern is approximately 200 µm large and thus identifiable. Once the substrates have been prepared and mounted in the FIB, the previously thinned lamellae are oriented horizontally in the FIB-SEM by tilting the TEM grids back by 90°. Subsequently, the micro-manipulator is welded to the lamellae on the edge far from the TEM grid posts and the lamellae are cut free on the other side. Then the lamellae are lifted and placed in the center of the landing zone where they are provisionally welded in placed. Next the micro-manipulator is cut off and retracted, re-enabling free stage rotation, so the lamella can be firmly welded into position, as depicted in figure 5.2e.

Welding the edges, as well as cutting off the micro-manipulator, inevitably introduces undesired redeposition of material on the lamellae. To mitigate this the surface facing up is subsequently polished with a low angle beam of 10 pA and 5 kV. Note, an unpolished backside of such lamellae was found to have no impact on the scan quality and is thus left unpolished. To maintain an exact region of interest over several scans, e.g. when studying a temperature evolution, it is often helpful to have an unique identifier on the surface of the lamella. Figure 5.2f shows a possible layout of such, where a distinct pattern is milled into the surface, yielding traceable topography signal.

In addition to the wedge-shaped lamellae used for TEM studies, which have a maximum thickness dictated by electron transparency, wedge-shaped lamellae for SPM studies were prepared in collaboration with E. Roede. Following the plane-view preparation process, triangular prism-shaped volumes are extracted. The original *ab* plane surfaces are polished and placed facing downwards on the substrates. Note, the lamellae have to be placed close to the edge of the substrates. Subsequently, the prisms are cut at an angle versus the base plane from the apex yielding wedge-shaped lamellae. Finally, wedge-shaped lamellae are polished as well.

5.1.2 Advanced Lamella Geometries

In order to fully understand the magnetic textures exhibited by Fe_3Sn_2 the introduction of geometrical confinement is one key parameter. In line with the requirement to miniaturize the functional building blocks, the FIB-SEM offers a unique flexibility for the fabrication of lamellae, which allow such studies. These lamellae can be cut to precise measures as cuboids or tapered, yielding wedge-like gradual sloped specimen. Furthermore, the FIB-SEM in combination with an additional free rotation axis allows to precisely shape any pre-prepared lamella in the *ab* plane, hence effectively enabling 2D and 1D confinement. These challenging sample preparation steps form an integral and crucial part of my PhD research.

Beyond the reduction of the thickness of lamellae and tapering thereof, the FIB-SEM is used to introduce lateral confinement, e.g. by reducing the width of a lamella, effectively yielding a stripe, or an in-plane wedge. Such geometries are prototypical for spintronics applications, e.g. race track memories [86]. Their potential as future building blocks in spintronics applications is explored in section 5.3. Three exemplary TEM lamellae are prepared, taking into account different types of lateral and horizontal constraints, as well as the thickness dependency.

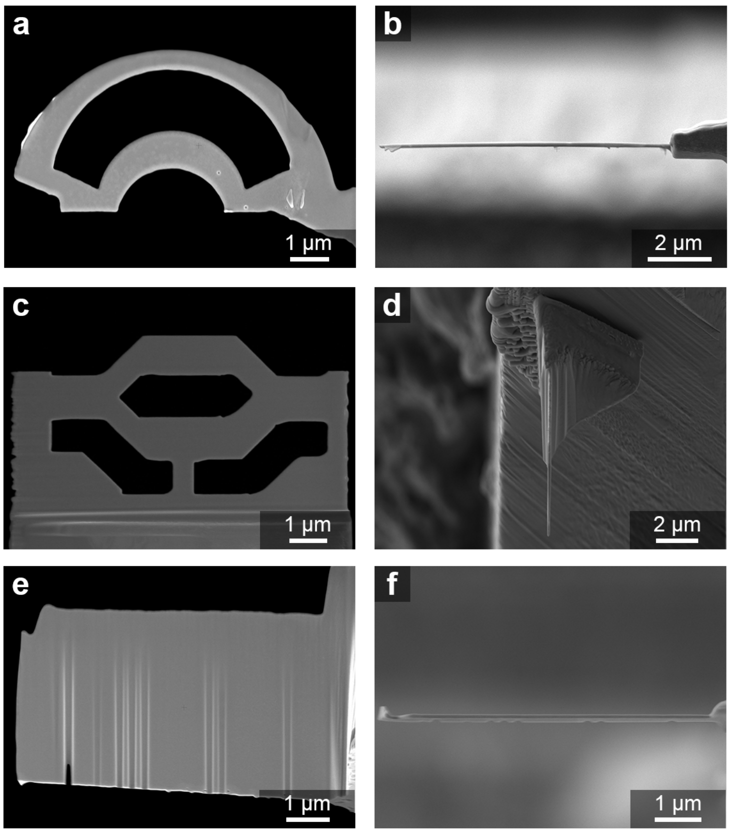

Figure 5.3: Various FIB cut lamellae geometries. **a**, **b**, nested half ring. **c**, **d**, Y-selector-collector.**e**, **f**, thickness grating.

Nested half-ring lamella

Figure 5.3a and b illustrate the side and top view of a nested half-ring lamella, respectively. The width of the larger outer half ring is almost 1 µm at the ends and tapers down to just above 500 nm at the narrowest point in the middle. The width of smaller inner ring is tapered inverse, where the middle is the widest at almost 1 µm and it narrows down to 700 nm at the edges, where the rings are connected. A detailed overview of the dimensions is given in figure B.1 in the appendix. To cut such complex patterns first a regular lamella of desired thickness, here about 150 nm, is prepared. Using the RoTip shuttle the lamella is then oriented horizontal, analog to the process for SPM lift out. Subsequently, it is patterned via the FIB. Here, it is critical to limit the exposure to the minimum necessary, as the perpendicular focused ion beam, is particularly prone to induce beam damage [268]. Furthermore, not all geometries manufactured allow subsequent polishing along the *ab* plane.

Y-selector-collector lamella

Here the initial lamella is no longer a plane parallel one of constant thickness, but a wedge. This has major implications during cutting with the perpendicular focused ion beam, as the required dose to obtain a clean cut varies with the lateral position of the exposed area. In the specific case shown in figure 5.3c and d, the thickness is gradually reduced from 150 nm (left side) to about 100 nm (right side). The geometry cut represents a Y-shaped selector, respectively collector, where the wide arms on the left and right side break up into narrower ones angled at 45°. The narrow-split arms are connected on the top and bottom, respectively. Thus, allowing study of the magnetic texture along the whole thickness gradient in combination with the defined angular mismatch. Detailed dimensions are given in figure B.2 in the appendix.

Grated lamella

A lamella exhibiting a grating like texture, as shown in figure 5.3e and f, is prepared. Unlike the previous two examples, this lamella is not cut by the FIB in a perpendicular orientation. Instead, analogous to the preparation of wedged specimen for TEM, a slight inclination of less than 3° is used. Following the preparation of a plane parallel lamella, a series of approximately 140 nm wide trenches are cut in the lamella at the low tilt angle. As a result, these yield thickness undulations, which gradually form defined steps of up to several tens of nano-meters along one direction. Perpendicular to this direction the result is an almost unperturbed thickness trailing along one edge, whereas the opposing edge is broken up into several sections by the trenches. Distinct dimensions are given in figure B.3 in the appendix.

5.2 Imaging and Analysis of the Magnetic Texture of Fe_3Sn_2

In the intermediate Q system Fe_3Sn_2 with $Q \approx 0.15$, confer equation (2.52), the uniaxial magnetic anisotropy at room temperature is along the crystallographic c axis ($K_u \parallel c$). As a result, in *ab* plane lamellae, alternating ferromagnetic domains pointing up and down along the c axis are expected. MFM probes the gradient of the out-of-plane component of the stray field, making it an ideal tool to image the expected spin textures of Fe_3Sn_2.

However, certain phenomena cannot be understood by the consideration of the out-of-plane component alone. Such phenomena include discerning topologically trivial and non-trivial bubble domains. For this matter, LTEM and off-axis electron holography are employed. These TEM based techniques probe the in-plane components of the magnetization making them particularly complementary to the MFM approach. One limitation of these TEM based techniques, however, is that they integrate the contrast along the optical axis, i.e. through the specimen thickness.

To overcome the challenges of the individual techniques, and bring all the data together in a holistic understanding, micromagnetic simulations are used. These render the spatially resolved orientation of the magnetization of the three-dimensional structure of magnetic objects. Subsequently, the obtained contrast in techniques like LTEM can be simulated based on the obtained modeled magnetic textures. Qualitative comparison of experimental and simulated data, thus, allows to link the theoretical model of the magnetic textures to the obtained data.

5.2.1 Bulk Specimen

Magnetic force microscopy, like all SPM based techniques, is a surface sensitive technique, and does not provide information into the depth. A result of this is that MFM is highly sensitive to changes in topography and it can be hard to deconvolute magnetic contrast and topographic contrast, thus to obtain clean images of the magnetic texture a flat surface is required. Conveniently, Fe_3Sn_2 grows in the shape of laterally extended *ab* plane platelets, which are the surfaces of interest to image the domain structure. Figure 5.4a depicts one crystal in the as-grown state. Due to the hexagonal outline, the crystals can be oriented easily. However, from the image of the optical microscope, figure 5.4a, defects on the surface are already observed.

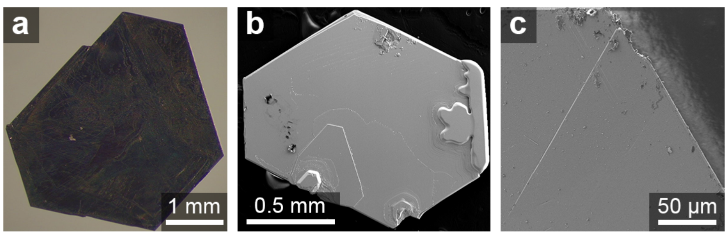

Figure 5.4: Bulk Fe_3Sn_2 specimen. **a**, imaged by an optical microscope. **b**, **c**, imaged via SEM.

SEM and EDX analysis

Using the enhanced resolution of the SEM, the surface defects observed with the optical microscope can be resolved into defects and growth terraces, as depicted in figures 5.4b and c. Defects can either be attributed to mechanical interference, e.g. traces of handling the crystal with tweezers, or are an inherent artifact of the as-grown state. Examples for the latter are deposits of non-stoichiometric material or pure elements. To ensure the quality of the crystals investigated, a number of crystals of each growth batch are analyzed by EDX. In table 5.1 the quantitative results obtained from the EDX analysis for three crystals of the same growth batch denoted A1, A2 and A3 as well as two additional ones from different batches denoted B1 and C1, respectively, are listed. These results confirm proper stoichiometry of all the single crystals

Atom%	A1	A2	A3	B1	C1
Fe	59.15%	59.09%	58.84%	58.99%	60.48%
Sn	40.85%	40.91%	41.16%	41.01%	39.52%

Table 5.1: EDX results for various Fe_3Sn_2 single crystals.

probed. Importantly, as the results deviate in the range of 1% from the target distribution, i.e. well within the error margin of ±3 % for EDX analysis (confer 3.2.3). Furthermore, samples within a single batch exhibit very consistent results. Mapping the EDX counts of the probed area allows to clarify whether residue and deposits on the surface are stoichiometric, i.e. twinned crystals or defects.

Magnetic force microscopy analysis

High quality MFM images were obtained on polished surfaces of single crystals. Despite the as-grown surfaces yielding sufficiently flat areas to study Fe_3Sn_2 via MFM, it is often impractical to scan such. The crystal depicted in 5.4b for example, has terraces on the right side, where the thickness increases in the micro-meter range. Such large height steps can not only be a source of error due to erratic stray fields, when scanning in the vicinity but can ultimately block access to the region of interest when scanning. Additionally, during coarse repositioning of the sample, such steps can severely damage the tip or break the cantilever. As such, to minimize the risk of tip damage and to avoid spurious stray fields, the samples are lapped and polished.

Figure 5.5a shows a dual pass MFM image (procedure described in section 3.1.2) of a $30{\times}30\,\mu m^2$ region recorded on a polished ab plane surface of a bulk Fe_3Sn_2 single crystal. It shows a peculiar dendrite pattern of alternating domains pointing up and down along the c axis. Here, the color encodes the locally resolved phase shift. The underlying superstructure of alternating stripe-like domains along the vertical axis is superimposed by the formation of dendrites. These dendrites are highly branched. The corresponding topography depicted in figure 5.5b shows distinct mechanical defects in the form of horizontal scratches. Additionally, individual particles can be seen. In the MFM image these can be correlated to point defects, presumably due to tip sample contact in the second pass. These are an artifact of the finite adjustment speed of the height during the first pass, which can be mitigated and theoretically vanish with an infinity slow scan speed - which is experimentally impractical. Figure 5.5c shows the MFM phase signal plotted for a 4 µm line section across a domain, as marked in panel a. Despite representing a line segment, across two domain walls in between anti-parallel domains, the phase signal depicts a smooth continuous behavior. These findings match the behavior expected

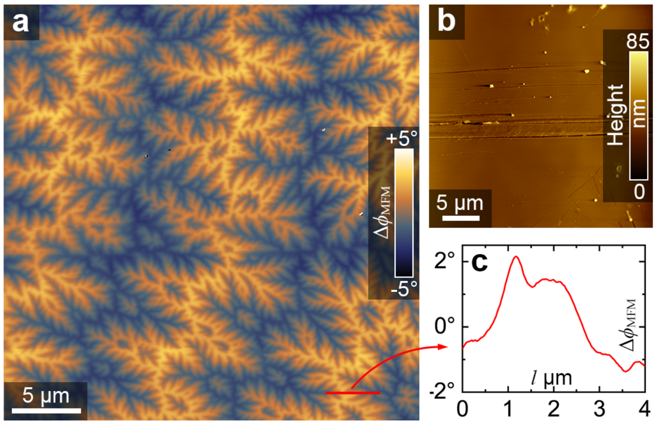

Figure 5.5: MFM on polished *ab* plane surface of bulk Fe_3Sn_2. a, MFM image. **b**, corresponding topography. **c**, MFM phase profile across a domain as marked in **a**.

for an intermediate Q material like Fe_3Sn_2 [64, 263, 269]: The superstructure, that is the predominantly vertically oriented alternating pattern, is rooted in the wide stripe domains within the volume of the bulk. Whereas at the surface branching occurs to minimize the stray field. The latter yields the imaged dendrite structure, which exists only in the surface region and exhibits local perturbations where the crystal structure is impaired at the surface. Finally, the gradual transition of the MFM signal in between neighboring anti-parallel domains, due to the continuous gradual variation of the stray fields is consistent with the emergence of Néel caps [64].

Although the MFM contrast of the image shown in figure 5.5a fits the expectation for a bulk Fe_3Sn_2 single crystal, the proper origin of the presumable magnetic contrast must always be ensured. In the case of MFM, this is easily done by reversing the tip magnetization. Electrostatic contributions to the image contrast yield unperturbed image contrast when the tip magnetization is reversed, whereas the image contrast attributed to magnetic forces is inverted. Following the convention illustrated in figure 5.6c, the tip is magnetized in "north", or "south" orientation, i.e. in both cases sensitive to the out-of-plane component of the magnetic stray field. MFM images of the same area, see 5.6a and b, imaged with opposing tip magnetization exhibit inverted contrast. Hence, Figure 5.6 shows that the dendrite textures are of magnetic origin. The deviating bright spot on the right side, is a topography feature used to align the frames.

The magnetic contrast exhibited here for a $30{\times}30\,\mu m^2$ area, coincides with previous observations. While figure 5.5 shows the generally expected structure, different crystals from the same batch show slightly different trends. For instance, figure 5.6 shows a more developed maze-like texture and the superimposed dendrites exhibit a reduced order of branching. Generally these observations are still in line with the expectations of an intermediate Q material [64]. However, as the superstructure appears narrower, this implies narrower domains in the bulk. This assumption is furthermore corroborated by the reduced order of branching. A reduced domain width in the bulk is known to coincide with a reduced thickness of the sample according to equation (2.66). Since these images and the data presented in figure 5.5a have been obtained on two different crystals, according mismatch in thickness is likely. Irrespective of the exact thicknesses of the individual bulk crystals, these results confirm a strong codependency of the micromagnetic texture and the thickness. However,

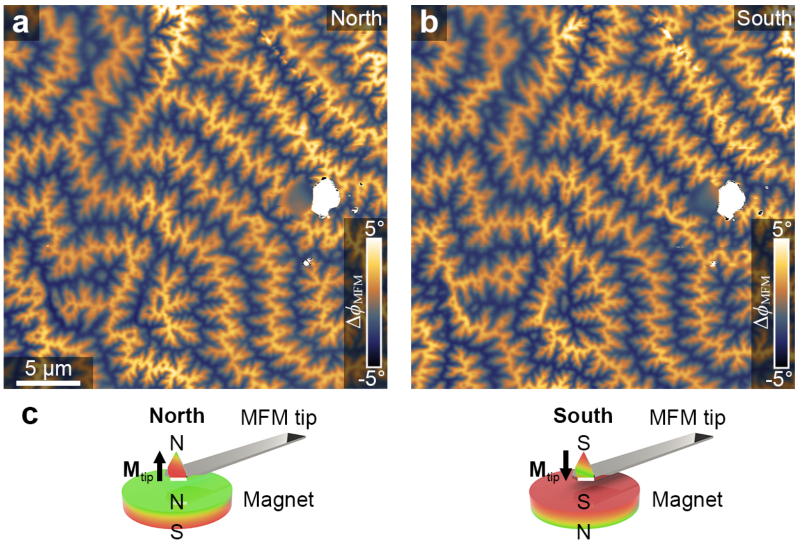

Figure 5.6: Proof of magnetic origin of the image contrast. **a**, MFM image with tip magnetized "north". **b**, MFM image with tip magnetized "south". **c**, schematic tip magnetization via a permanent magnet prior to scanning. Schematic in **c** reproduced form [86].

whilst the superstructure, excluding the fine branching, hints the size of the underlying stripe domains in the bulk, it is not sufficiently distinct to actually quantify any correlations of the bulk stripe width w_{b} and the sample thickness. Additionally, MFM is a surface sensitive technique and complex reconstruction of domain width via branching into the depth cannot be excluded by merely quantifying the order or branching. Hence, detailed quantitative analysis of the bulk stripe width is forgone at this point.

5.2.2 From Bulk Specimen to Lamellae

As observed above, the magnetic texture is affected by the thickness, even in bulk samples. However, quantitative analysis of the thickness dependence via MFM is limited to a thickness range, where the magnetic texture shows unobscured stripe domains at the surface. This is known to be the case for thicknesses in the range of tens to a few hundred nanometers, where stripe domains were observed via LTEM before [52, 53]. Whereas domain branching, as shown in figure 5.7a, emerges for bulk specimen, where the thickness exceeds a few tens of micro meters. Evidently, the upper thickness limit for unbranched stripe domains lies in between. In this section, the transition from branched to unobscured stripe domains is investigated. Subsequently, the thickness dependence of the stripe domain width is qualitatively analyzed.

MFM on plane-view lamellae

As discussed in section 3.2.3, the FIB is an ideal tool to prepare specimen with well-defined thickness along the c axis. Besides the already discussed preparation of lamellae to investigate functional objects (confer section 5.1.2), a 200 nm thick lamella was prepared in collaboration with E. Roede and placed flat on a gold covered substrate. This prime example, depicted in figure 5.7b, is used to introduce some common features of magnetic textures in these thin structures. MFM imaging on the $4{\times}4\,\mu m^2$ area marked with a red square reveals unobscured stripe domains arranged in a maze-like pattern, see figure 5.7d. These stripe domains qualitatively reproduce the domain patterns observed via LTEM in literature [52, 53].

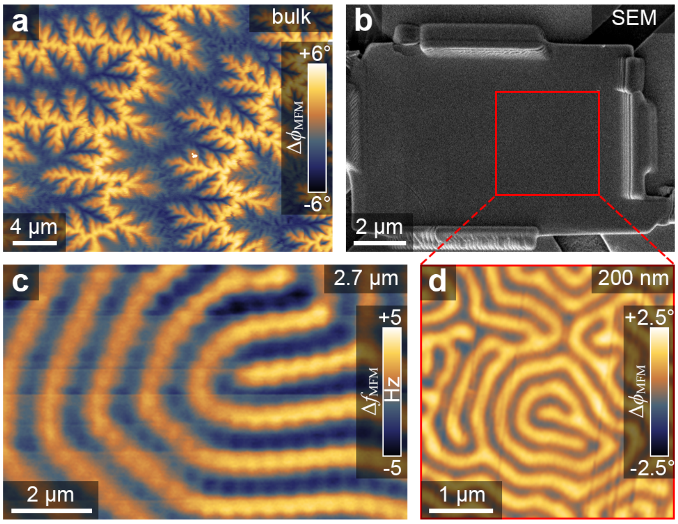

Figure 5.7: MFM and SEM images of specimen of varying thickness. **a**, MFM image of a bulk specimen. **b**, SEM image of a lamella placed on a substrate for SPM analysis. **c**, MFM image of a specimen of thickness 2.7 µm. **d**, MFM image of a specimen of thickness 200 nm.

For another lamella, precisely cut to a thickness of 2.7 µm, the obtained MFM image is shown in figure 5.7c. Here, the color scale encodes the frequency shift Δf_{MFM} of the resonance. For the presented case of ambient imaging conditions, this color scale can be interpreted analogous to the phase-shift $\Delta\phi_{\mathrm{MFM}}$. In the image, individual stripes can still be clearly distinguished, but the domain walls separating these stripes show the characteristic undulating structure for the onset of domain branching [64]. Hence, the upper thickness limit for the study of unperturbed stripe domains is just below 2.7 µm.

MFM on a wedge-shaped lamella

To quantify the relation between the thickness along the c direction and the magnetic texture, a wedge-shaped lamella prepared in collaboration with E. Roede is studied. Figure 5.8a shows a 3D rendering of the obtained topography of the wedge-shaped lamella during the first pass of an MFM scan. In the image, both the z axis and the color scale encode the height. Over the length of 14.7 µm the thickness increases from 400 to 900 nm. Due to the profile of the FIB beam the cut does not yield a linear but slightly curved height profile. The corresponding MFM image is shown in figure 5.8b in an analogous

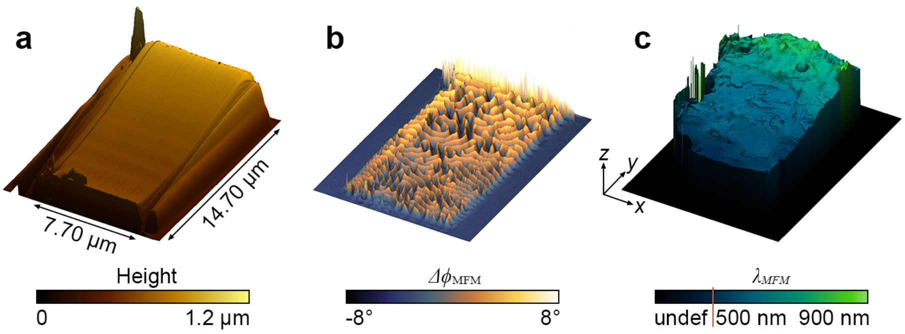

Figure 5.8: Spatially resolved loacal periodicity of stripe domains. a, topography of wedge-like lamella. **b**, corresponding MFM signal. **c**, computed local periodicity λ_{MFM}. For the lower part of the color bar the periodicity is undefined.

3D representation. Here, the z axis and the color scale encode the phase shift. The image shows a maze-like pattern of stripe domains. These are qualitatively equivalent to the unobscured stripes. MFM images recorded with inverted tip magnetization confirming the magnetic origin of these stripe domains are presented in the appendix, see figure B.4. The MFM images recorded on the wedge-like lamella indicate gradual widening of the observed stripe domains from the thin end of the lamella to the thick end.

Kittel scaling of stripe domains

A MATLAB script was developed for the quantitative evaluation of the stripe width in relation to the thickness. The script evaluates the local periodicity $\lambda_{\mathrm{MFM}}(x, y)$ for each pixel, within a cropped region of interest, based on the magnetic texture in its vicinity. In section D of the appendix, the script is explained in detail.

The obtained periodicity λ_{MFM} is equivalent to two times the stripe width. Figure 5.8c shows the 3D representation of the spatially resolved local periodicity λ_{MFM} for the magnetic texture shown in panel b. The height and color scale encode the periodicity in nano-meters, where the lowest values are undefined, and set to zero artificially. Along the y axis a gradual increase of the periodicity is visible, whereas the perturbations along the x axis are negligible. Thus, the data confirms the assumption of gradual widening of the stripes with increasing thickness.

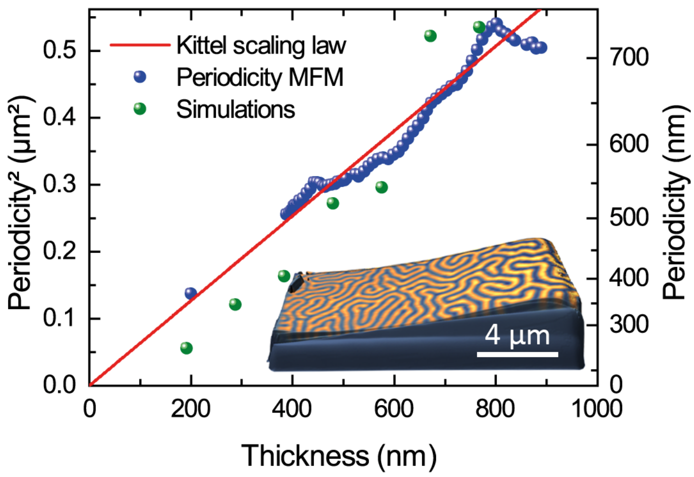

Figure 5.9: Quantitative analysis of domain width and thickness. Plot of computed periodicity versus sample thickness for experimental data and micromagnetic simulations. The inset highlights the correlation via the 3D rendering of the lamella colored with the MFM signal. It is placed to coarsely align with the abscissa.

In order to properly correlate the computed periodicity data to the sample thickness and evaluate the results, the thickness of the lamella for every pixel is determined. The original topography image contains a large area of the flat silicon substrate, which is not displayed in figure 5.8a. This area is used to determine the plane background the wedge-like lamella rests on, which is subtracted from the topography image. The resulting height map represents the spatially resolved thickness $t(x, y)$ for every pixel. The local periodicity $\lambda_{\mathrm{MFM}}(x, y)$ is subsequently averaged for all pixels of equal thickness. Figure 5.9a shows the averaged computed local periodicity λ_{MFM} plotted versus the thickness of the lamella (blue datapoints). Additionally, the data point representing the periodicity calculated for the whole MFM image of the 200 nm thick lamella, presented in figure 5.7d, is plotted. In the plot, the periodicity is squared to linearize the Kittel scaling law, see equation (2.58), represented by the red line. The experimental data agrees well with the fit confirming Kittel scaling of the domain width in the thickness range below the onset of branching. Furthermore, the results of micromagnetic simulations provided by collaborator E. Lysne, depicted in figure C.1 in the appendix, are also plotted as green data points in figure 5.8. The periodicity derived from these simulations is scaled by a factor of 1.12 to match the scaling law of the experimental data the best. Thus, Kittel scaling is not only experimentally observed, but also corroborated by micromagnetic simulations.

5.2.3 Domain Morphology under Static Magnetic Field

Sample thickness, confirmed by the Kittel scaling behavior, already denotes one tuning parameter for the magnetic texture. Here, the impact of static magnetic field as a further tuning approach is studied. Figure 5.10 shows the field dependence of the magnetization for a macroscopic single-crystalline sample at 300 K with the magnetic field applied out-of-plane, i.e. parallel to the c axis. In zero magnetic field, the sample has no remanent magnetization, which agrees with the stripe domain pattern observed by MFM. Following a linear increase, the magnetization saturates at 750 mT to the value of 2 μ_B per Fe atom.

Evolution of magnetic texture in plane-view lamellae

The detailed evolution of the domain pattern is documented by a series of MFM images recorded on a 450 nm thick Fe_3Sn_2 lamella at 300 K, depicted as insets in figure 5.10. From a remanent maze-like domain pattern a parallel stripe pattern is obtained by a field-treatment process described in detail below. Application of a modest field of 200 mT fosters domains with magnetization along the field to grow, which manifests in the respective stripe domains widening. Domains with opposite magnetization shrink. This behavior is enhanced for increasing magnetic field to 400 mT, where additionally the first bubble domain is observed. Further increasing the field to 600 mT yields a pure bubble phase, before the system reaches saturation and all antiparallel domains are expelled entirely at higher fields. As indicated by the MFM images, this process is reversible. In decreasing magnetic fields, first, the bubble domains reappear below 600 mT and subsequently stripe domains are formed. At 200 mT a maze-like pattern predominantly formed of stripe domains is formed, which corresponds closely to the remanent state.

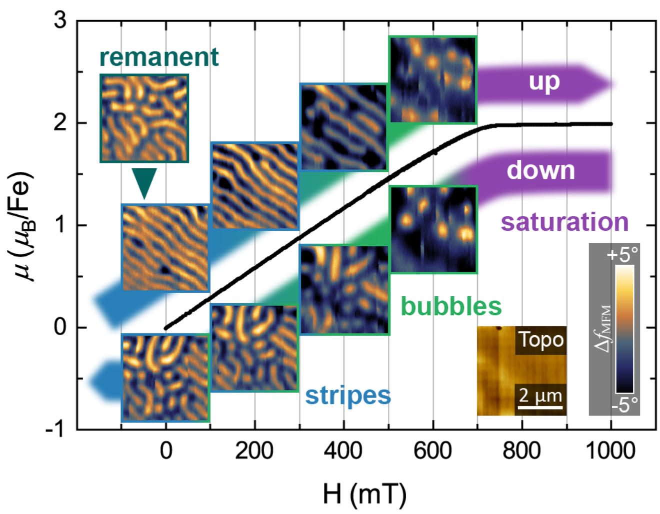

Figure 5.10: Response to static magnetic field. The graph shows the $M(H)$ virgin curve for Fe_3Sn_2 at 300 K. The insets show MFM images recorded over the same area at the respective fields at 300 K, as well as the corresponding topography image.

This evolution of the magnetic texture is further confirmed by the same measurement at 200 K, which is presented in Figure B.5 of the appendix. In field steps of 50 mT (100 mT) the same evolution of domain morphology is observed, corroborating the room temperature results. In 600 mT, i.e. just below saturation, a pure bubble phase is realized for both data sets. Since MFM is not sensitive to the in-plane component of the local magnetization, it is not possible to determine, whether these are type I or II bubbles. From figures 5.7 and 5.8 the quasi random maze-like patterns are identified as the ground state or remanent state. While the domain patterns observed in zero field before and after the field treatment look very similar, the exact positions of the individual domain walls differ vastly for the remanent state before and after field is applied. This shows no substantial pinning occurs in the Fe_3Sn_2 lamellae. Furthermore, this proves fabrication of lamellae via FIB-SEM, inevitably linked to Ga implantation and other defects, does not perturb the magnetic texture severely.

Evolution of the magnetic texture in the wedge-shaped lamella

The combined effect of magnetic field and variable sample thickness is studied in figure 5.11a-e, which show MFM images of a wedge-shaped lamella in static magnetic field. In all images the lamella is oriented in a way, that the thin end is left and the thicker one points to the right. Up to modest fields of 250 mT, stripe domains exhibiting Kittel scaling are observed similar to zero field. Additionally for fields exceeding 200 mT, bubble domains begin to form predominantly at the edges of the lamella. Further increasing the field to 380 mT boosts this behavior with an increased number of bubble domains emerging. Finally at 450 mT the majority of domains are bubbles with several residual stripe domains agglomerated predominantly in the center of the lamella. The bubble

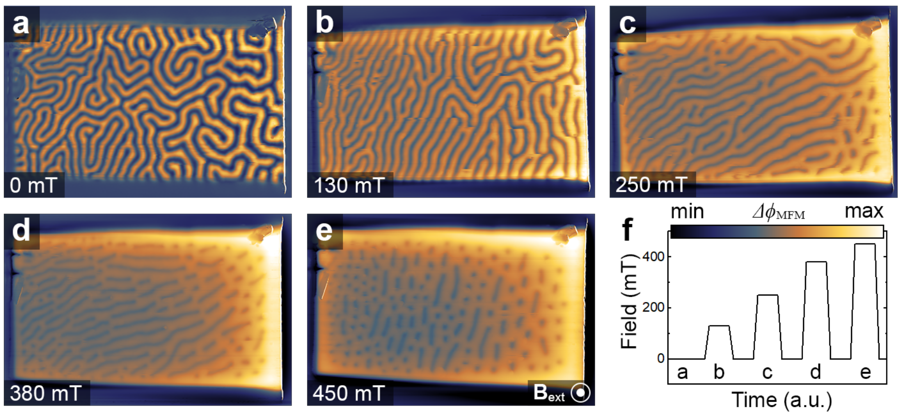

Figure 5.11: MFM of the wedge-shaped lamella in field. a-e, MFM images in various fields. **f**, schematic of the applied magnetic field over time.

domains also follow Kittel scaling analogous to the stripes. The aforementioned scripted evaluations fail for bubble domains, thus the diameter of individual bubbles was evaluated manually by applying three cross-sections to each and averaging the obtained values. Figure B.6 in the appendix shows the selection of five representative bubbles for three thicknesses and the corresponding plot of diameter versus thickness confirming the scaling behavior.

For the study of the wedge-shaped lamella, a room-temperature MFM with exchangeable static permanent magnets was used. The applied field is schematically illustrated in figure 5.11f. Thus, the study on the wedge-shaped must not be confused with the study of the morphology in continuously driven magnetic fields. Peculiarly, the stripe domains in modest fields exhibit a predominant orientation. Hence, the question arises, if the sloped geometry can be ruled out as a reason for the orientation due to this approach. In 130 mT the stripes are oriented perpendicular to the slope, whereas for 250 mT and 380 mT the orientation follows the slope. As the residual stripe domains in 450 mT have the same perpendicular orientation, an inherent link to the slope seems unlikely. This infers that the orientation could be an artifact from placing the permanent magnet under the sample, which - unless moving from infinity - necessarily coincides with the application of oblique fields ($\boldsymbol{B} \nparallel c$). This serendipitous observation suggest oblique magnetic fields could be used to control the stripe directions, a hypothesis that is investigated in the next section.

Magnetic texture in oblique magnetic fields

So far, only out-of-plane fields have been deliberately applied. In the following, the impact of oblique magnetic fields on the magnetic texture is investigated in order to prove these can be used to align the stripe domains. To test this hypothesis a series of MFM images of remanent states is collected. Remanent states are imaged because these resemble the previous observations of the oblique field being applied prior to scanning. Furthermore, applying oblique

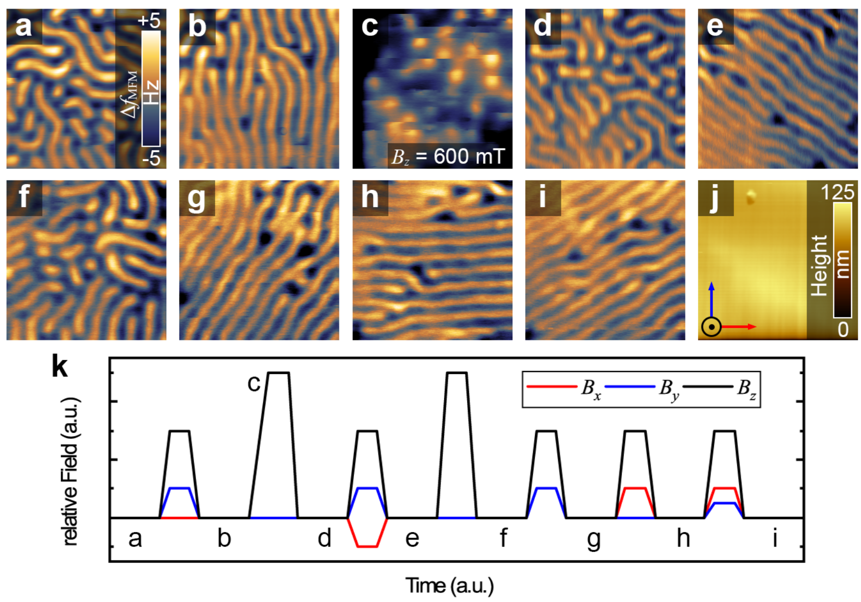

Figure 5.12: MFM images in oblique magnetic fields. **a**, **b**, **d-i**, in zero field after field treatment in different orientations, as indicated in **k**. **c**, MFM image of domain configuration in 600 mT. **j**, corresponding topography. **k**, schematic of the applied magnetic field over time, for panels **a** to **i**. MFM images recorded at 200 K.

fields during scanning yields an oblique tip magnetization that can lead to non-trivial MFM contrast. To overcome the latter problem, the in-plane component of the field is kept weak relative to the out-of-plane component and it is turned off prior to scanning to ensure the proper orientation of the tip magnetization. Figure 5.12a-i show the MFM image series recorded at 200 K. The corresponding topography for all images is shown in figure 5.12j, where the relative orientations for the applied field are denoted as well. From the maze-like remanent state, presented in figure 5.12a, an ordered state aligned vertical (y axis) is obtained by applying external field with an in-plane component along the y direction. Application of 600 mT out-of-plane field, see figure 5.12c, reveals a pure bubble state and subsequently, a remanent maze-like state, confer figure 5.12d, is observed. Applying the in-plane component of the field along $(\boldsymbol{B}_x, \boldsymbol{B}_y) = (-1, 1) \cdot B_{\text{ip}}$ yields stripe domains following this diagonal orientation, see figure 5.12e, which can be reset to a maze-like pattern afterwards, see figure 5.12f, analogous to the previous step. Varying the in-plane component in the following steps to $(1, 1) \cdot B_{\text{ip}}$, figure 5.12g, $(1, 0) \cdot B_{\text{ip}}$, figure 5.12h, and $(2, 1) \cdot B_{\text{ip}}$, figure 5.12i, remanent stripe patterns oriented along the image diagonal, horizontal and angled are obtained. It is evident that the orientation of the stripe pattern follows the orientation of the previously applied in-plane field. However, since MFM is limited to the study of the out-of-plane component of the domains, it is not the optimal technique to discern this behavior.

Bright-field LTEM studies of the application of oblique magnetic fields

LTEM is a technique sensitive to the in-plane magnetization. Magnetic fields along the optical axis yield no Lorentz force on the electrons and thus no perturbation to the uniformly distributed intensity, i.e. they are not imaged. In a simple picture, magnetization oriented perpendicular to the optical axis of the microscope perturbs the electrons locally resulting in a shift of the corresponding intensity. In the resulting bright field (BF) image, this precipitates a dark spot for reduced and a bright spot for enhanced intensity. The maximum gradient of the intensity lies perpendicular to the magnetization, additionally the direction flips with inversion of the defocus. A more detailed explanation of the working principles of LTEM can be found in section 3.2.2. Note that all TEM experiments are conducted at room temperature unless explicitly stated otherwise.

Unlike the SPM, where a vector magnet allows in-situ application of oblique fields, in the TEM the objective lens is used to apply the magnetic field, which are required to be axial. To work around this challenge, a double-tilt sample holder was used so oblique fields could be applied. This kind of holder allows the specimen to be tilted about two independent tilt axes perpendicular to the optical axis, i.e. orient it so the field is applied in oblique orientation with respect to the crystallographic c axis. For the data presented in figure 5.13, a rotation α coincides roughly with a rotation about the long edge of the lamella, whereas a rotation approximately about the short edge is quantified by β. LTEM images are recorded in an almost horizontal, that is perpendicular to the optical axis, orientation to obtain contrast corresponding to the in-plane (ab plane) magnetization. Before imaging, the specimen is tilted to $(\alpha, \beta) = (18°, 4°)$, for figure 5.13a, $(-2°, 24°)$, for figure 5.13b, and $(0°, 0°)$, for figure 5.13e. Subsequently, static magnetic field is applied up to several hundred milli-tesla. Once the field is removed, the specimen is oriented horizontal for imaging.

Remaining with the study of controlling the stripe domain direction by the application of oblique fields, figure 5.13a shows the underfocused LTEM image for a plane-view lamella in the remanent state. The oblique field was applied in a way that the in-plane component of the field aligns with the short edge of the lamella as indicated by the red arrow. The bright horizontal lines are artifacts of the step cuts, which are the effects of the steps that are discussed later. The curved dark lines following no predominant orientation are attributed to strain in the lamella. The alternating bright and dark contrast corresponds to the magnetic domain walls, which are predominantly oriented horizontal in the image. Within the domain walls the magnetization is oriented in-plane, hence the walls yield contrast. Except for the bottom segment all stripes and thus all domain walls align along the direction the in-plane component of the external magnetic field has been applied along. Analogous, in figure 5.13b the

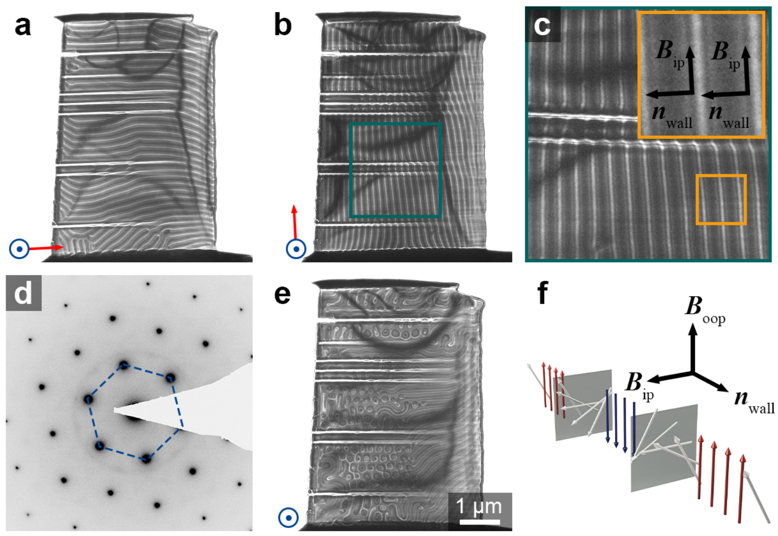

Figure 5.13: Field controlled stripe orientation imaged via LTEM. **a**, bright field (BF) LTEM image of remanent state. **b**, BF LTEM image of remanent state. **c**, detailed view of contrast magnified from panel **b**. The inset (orange region) shows an even further magnified area overlayed with the schematic orientation of the domain wall and in-plane field. **d**, diffraction pattern (DP) of the lamella. **e**, BF LTEM image of remanent state. **f**, schematic of the domain wall and corresponding oblique fields applied.

underfocused LTEM image shows similar artifacts and the domain structure orients along the long axis of the lamella. Here, the in-plane component of the field has been applied along the long axis previously, as indicated. The area marked by a green square is magnified in figure 5.13c. An alternating pattern of bright and dark contrast is evident. This is highlighted by the further enlarged view displayed in the inset for the corresponding region marked orange. The direction of the magnetization within an individual Bloch-type domain wall[1], i.e. a pair of a dark and bright stripe, is constricted parallel to the orientation of the stripes. However, from a single LTEM image the direction along the

[1]Bloch-type domain walls have been confirmed via LTEM in Fe_3Sn_2 [52, 53]

stripes remains degenerate, particularly as the contrast flips upon reversal of the defocus. But, the relative orientation of the in-plane components of neighboring walls, can be determined. Here, the strictly alternating pattern dictates, the in-plane components of neighboring walls all point in the same direction, that is either towards the top or bottom of the image. This is emphasized by the schematic orientations in the inset that correspond to the schematic view of the magnetization rotation through such domain walls, depicted in figure 5.13f. Figure 5.13d shows the diffraction pattern obtained in the TEM for the lamella. The hexagonal array of the spots, indicated by the dashed blue hexagon, confirms proper orientation of the zone axis of the lamella. Note, the incident beam is shaded to prevent damage to the camera. The static magnetic field has been applied along the c axis and subsequently, the remanent state is imaged, as shown in Figure 5.13e. Peculiarly, in an extended region where the selected area spot diffraction pattern was used to align the zone axis, bubble domains represent the remanent state. Along the right and the top edges, stripe domains oriented perpendicular to the edges emerge.

The conclusion from this section of work is that, analogous to the MFM measurements, oblique fields in the TEM allow to control the orientation of stripes. Furthermore, the in-plane component of the domain wall magnetization points in the same direction for all domain walls, which is parallel to the previously applied in-plane component of the magnetic field. Applying out-of-plane magnetic field ($\boldsymbol{B} \parallel c$), the remanent state shows no predominant orientation of stripe domains. From this behavior the following is concluded: The application of oblique magnetic fields yields domain walls with $\boldsymbol{n}_{\text{wall}}$ perpendicular to both the out-of-plane and in-plane component of the applied magnetic field, as depicted in figure 5.13f. Since the helicity of the Bloch-type wall is not fixed in Fe_3Sn_2, the magnetization rotates in a way that the in-plane component is parallel to the in-plane component of the applied field. Thereby minimizing the energy cost associated with the Zeeman term for all spins within the domain walls.

Flux-closure domains in a wedge-shaped lamella

Kittel scaling has been confirmed for the domains emerging in Fe_3Sn_2 specimen up to a thickness of 2.7 µm, see 5.2.2. Even thicker specimen exhibit domain branching, as depicted in figure 5.5. On the other end of the scale, very thin specimen are effectively described as low Q materials, see section 2.1.4. For such thin specimen, the shape anisotropy, represented by K_{d}, is dominant and fosters the formation of a flux-closure structure. For Fe_3Sn_2, the Bloch wall width is $\delta_{\text{Bloch}} = 21.6$ nm [86], and thus, from equation (2.67) the lower limit for the formation of flux-closure domains is estimated to be 120 nm. That means, for specimens with corresponding thickness flux-closure patterns are the expected ground state.

In the following, the emergence of a flux-closure pattern is investigated. From the MFM studies above, stripe domains are the confirmed ground state of specimen with thicknesses exceeding 200 nm. Therefore, a wedge-shaped lamella with gradually reducing thickness, from 150 nm at the thick end, is imaged. Bright field (BF) LTEM images obtained in over-, in-, and underfocus for this lamella are shown in figure 5.14a, d, and g, respectively. While the in-focus image displays contrast solely attributed to the topography of the lamella, and strain, the additional magnetic contrast observed in the over- and underfocused images reveals opposing brightness, i.e. the LTEM contrast flips. This is most

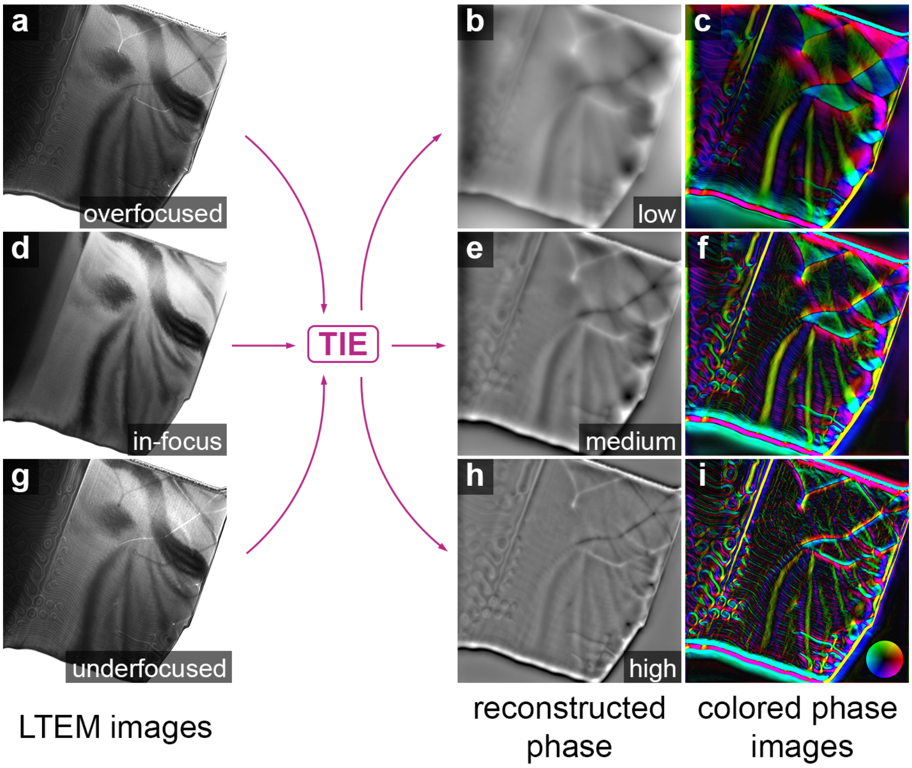

Figure 5.14: BF LTEM and TIE of wedge-like Fe_3Sn_2 lamella. a, **d**, **g**, over-, in-, and underfocused BF images. **b**, **e**, **h**, TIE reconstructed phase images for different filter settings. **c**, **f**, **i**, TIE reconstructed phase images, colored according to the orientation of the in-plane magnetization in **i**.

notable, for the distinct sharp lines at the top end, which is also the thinnest region of the lamella. In line with previous SPM and LTEM observations, a series of ordered stripe domains and a few scattered bubble domains are observed along the bottom edge, where the thickness is approximately 150 nm. Unlike the stripe and bubble domains, where the domain walls manifest as adjacent bright and dark lines in the BF images, the sharp lines at the top are either bright or dark. Since in-plane magnetization perturbs the uniform brightness into a region of enhanced and a region of reduced brightness by shifting the locally resolved intensity, neither one can occur individually. Hence, the area enclosed by separated lines of sharp BF contrast must coincide with laterally extended regions of uniform in-plane magnetization. In such regions the contrast attributed to coaligned neighboring spins cancels, except for those at the edge of the area. That means, sharp lines of unpaired bright and dark contrast denote the edges of laterally extended in-plane magnetized regions, i.e. represent the domain walls of a flux-closure pattern. From the BF images alone, it is very difficult to interpret the obtained contrast.

In order to visualize the flux closure domain pattern, processing via transport of intensity equation (TIE) of the images has been performed. The TIE software calculates a phase image that is proportional to the in-plane induction required to yield the observed intensity shift of the aligned image stack of BF images. Subsequently, a filter is applied to suppress undesired contrast, e.g. from strain, in the phase images. Figure 5.14b, e, and h display the obtained reconstructed phase images for a low, medium, and high filter setting. Analogously, these maps can be displayed colored, as shown in figure 5.14c, f, and i, where the hue encodes the direction of the in-plane magnetization according to the color wheel in figure 5.14i. The brightness corresponds to the strength of the in-plane component, i.e. black regions are magnetized out-of-plane. Low-filter settings reproduce laterally extended in-plane magnetized regions accurately, as depicted in figure 5.14c. In-between the lines of sharp contrast, that are the domain walls, the extended areas are uniformly colored, i.e. domains of uniform in-plane magnetization. These domains are flux-closure domains, where the magnetization of neighboring domains rotates by approximately 90°. However, the contrast attributed to strain is hardly suppressed either. A high-filter setting suppresses such undesired contrast, but equally it does negate areas of in-plane magnetization on the thin end of the lamella, see figure 5.14i. Such a setting is preferable in cases where the only contrast is from the Bloch-type domain walls between out-of-plane domains, as it enhances the clarity of the image. As this work focuses on discerning domain wall structures, high filter settings for TIE are generally used henceforth. The medium-filter setting is a compromise, where spurious contrast is vastly suppressed, yet sufficient contrast of the in-plan domains remains to determine their orientation. Such a setting should be avoided unless imaging the coexistence of both domain types within one image, as presented here for a wedge-like lamella in figure 5.14f.

In summary, applying a high-filter setting, the obtained contrast can be constricted to the domain walls. When the low-filter setting is used, the TIE reconstructed induction maps illustrate laterally extended regions of in-plane magnetization well. The latter confirms the formation of a flux-closure domain pattern on the thin end of the wedge-shaped lamella. Thus, there is a lower thickness limit below which the system effectively turns into a low Q material. This limit also denotes the lower limit for Kittel scaling of the domains, i.e. by thinning the specimen the domain size cannot be decreased below the corresponding minimal size.

Morphology of magnetic domains in magnetic field

Building on the previous MFM observations of the application of out-of-plane static magnetic fields, the effects are imaged with LTEM. The transition from stripe to bubble domains investigated by MFM, see figures 5.10 and 5.11, already revealed that either domain type can be selected by the applied external field. In addition, LTEM studies resolve the in-plane component of the magnetic texture with a high spatial resolution, allowing imaging of the domain wall of each magnetic object. Critically, for bubble domains, that means topologically trivial (type II) and non-trivial (type I) bubbles can be discerned.

The application of magnetic field in the TEM does come with the caveat: While homogeneity of the field is ensured for the lateral extensions of the lamellae, the absolute field strength given for the individual images is an estimate[2].

[2]For both TEMs in Augsburg, the absolute values of the field corresponding to the HEX

Thus, all field values given for the TEM images are an approximation and not confirmed absolute values.

In order to qualitatively reproduce the domain morphology, the field evolution of a lamella of uniform thickness (approximately 200 nm) is imaged. Figure 5.15a shows the domain pattern of the remanent state. The imaged state in zero field is generally a remanent state, as the lamellae have usually been exposed to magnetic field prior. The lamella exhibits an uniform stripe domain pattern, except for the bottom region, where the proximity to a topography step leads to the formation of a few bubbles. In line with the conclusion for

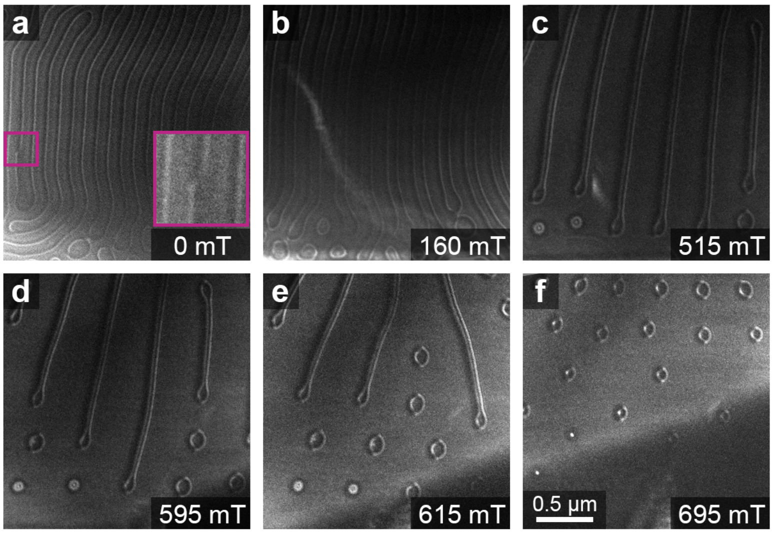

Figure 5.15: Field evolution of a lamella of uniform thickness. a-f, BF images of the same area of a 200 nm thick *ab* plane lamella under the application of static out-of-plane field. The inset in **a** shows a magnified view of the area marked by the purple square.

oriented stripe patterns, the majority of domains are oriented vertical in the image. The imaged contrast reveals the previously described same orientation of the in-plane magnetization for neighboring domain walls. Hence, at the top and bottom ends of the individual stripe domains, where the domain walls of opposite helicities meet, Bloch lines are formed. In the BF images, Bloch lines (confer section 2.2.3) are distinguished by flipped contrast along one individual domain wall, as shown in the inset in figure 5.15a. The stripe domain on the left reveals the Bloch line more clearly, where the Bloch line is highlighted by the purple square. Quantitative analysis of object size is forgone here, due to the inherent flaws attributed to imaging in defocus. The relative domain widths of neighboring domains of opposite out-of-plane orientation are almost the same. Applying modest field of 160 mT, figure 5.15b, changes the domain

values encoding the current manually applied to the objective lens are not mapped. For a limited number of magnetic transitions of known field, the corresponding HEX values are determined. The magnetic field values corresponding to the HEX values are linearly extrapolated based on this limited number of data points. In general, the linear approximation is expected to break down around 500 mT.

pattern only slightly. Merely the domains opposing the external field narrow. At the end of the domains, where the Bloch lines are located, the initial width is preserved. Images representing the detailed field evolution in incremental steps both up to the maximum field and back down to the remament state can be found in the appendix, see figure B.7. From these, a gradual transition to an oriented stripe pattern in 515 mT, depicted in figure 5.15c, is observed. Additionally, a slight tilt of the field away from the c axis is concluded, which yields a small in-plane field along the vertical direction of the image the stripe domains align along. Furthermore, as a function of increasing magnetic field, the stripe domains opposing the out-of-plane component of the field are spaced further apart and severely narrowed. Their ends, however, preserve a similar size to the bubble domains, which decrease in size compared to the zero-field state marginally. Unlike the almost maze-like pattern of densely packed bubbles in between stripes at low fields, the bubble domains order in a lattice with the stripes in higher field. Upon further increasing the field to 595 mT and 615 mT, respectively, the stripes begin to break up into bubbles, which remain in an ordered lattice of the mixed domains. Typically, the preferred lattice for bubble domains is the triangular lattice. However, in the present case, the coexistence of stripes still stabilizes a square lattice. As these lattices barely differ in energy, stabilization of either one due to pinning or defects is not uncommon [94, 96, 97]. Increasing the field to 695 mT finally breaks up all stripe domains and a pure bubble domain phase is formed. These appear to maintain the previous degeneracy between a triangular and square lattice.

Curiously, not all the bubble domains exhibit the same LTEM contrast. For instance, the two bubbles appearing on the bottom left side of 5.15c persist up to the highest fields in roughly the same location. Whereas other bubbles forming during the field evolution appear more volatile, that is to say, they seem to emerge and disappear across a much smaller field window. An example of the latter, the single bubble on the bottom right of panel c either moves or disappears before a field of 695 mT is applied. This is readily understood if the persistent bubbles (the ones on the left) are topologically protected type I bubbles, while the volatile ones are topologically trivial type II bubbles. A more complete classification of the different bubbles, and how they can be distinguished, is given in section 5.2.4.

Bubble domain formation in magnetic field

Before an in-depth investigation of the different types of bubble domains is conducted, a brief reminder of the key criteria, introduced in section 2.1.5, needed before a material transforms from stripe to bubble domain patterns is provided. It has already been observed, via MFM and TEM in figures 5.11 as well as 5.15, and discussed that bubble domains form when an out-of-plane magnetic field is applied to a stripe domain pattern in Fe_3Sn_2. Bubble domains predominantly start populating the regions close to the edges of the lamella, whereas residual stripes are contained in the center. While such magnetic field driven bubble to stripe transitions are classically expected [94], the details have not been shown in Fe_3Sn_2.

Previously, it was shown that magnetic field drove the formation of bubble domains in both MFM and TEM studies, despite having lamellae of different thicknesses. Now this transformation is studied in more detail and the bubbles that form are characterized. Figure 5.16a depicts the domain pattern of the 200 nm thick Fe_3Sn_2 lamella in 475 mT, where coaligned stripe domains alter with intermittent bubble domains. Interestingly, the square lattice of the bubble domains follows the positions of the stripes. Note, the dislocation in the lattice above the marked short stripe domain. Upon increasing the field by 5 mT, the marked stripe domain contracts to a single type II bubble domain. This newly formed bubble domain arranges neatly with the preexisting ones in the lattice. The dislocation in the stripe lattice follows this reconfiguration. Dislocations pushing the bubble domains towards the edges of the stripe domain lattice could, therefore, explain the predominant population of bubble domains at the edges of lamellae.

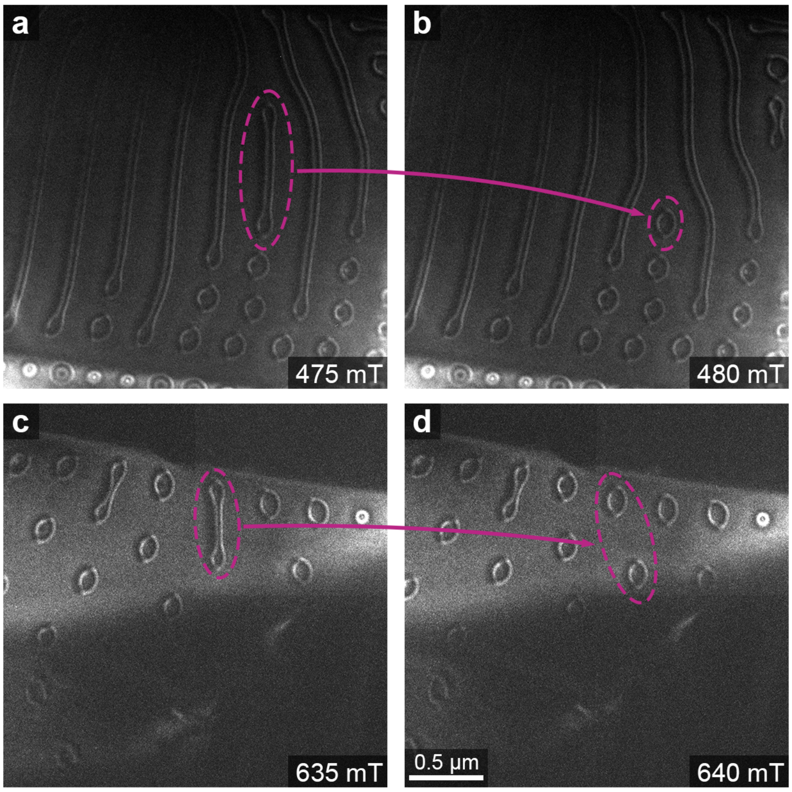

Figure 5.16: Morphology of bubble domains. a, **b** Stripe domain contracting to a bubble domain. **c**, **d** Stripe domain breaking up into two bubble domains.

Stripe domains breaking up into several bubble domains is the second mechanism behind the formation of bubbles. Direct evidence for this breaking-up mechanism is provided by LTEM studies as well. Figure 5.16c shows the domain configuration at 635 mT in the same lamella. The magnetic texture has been transformed to a predominantly bubble domain structure, with a few residual stripe domains, an example of which is highlighted. Under the application of slightly increased field of additional 5 mT this particular stripe domain breaks up into two separate bubble domains, as shown in figure 5.16d. Both newly formed bubble domains arrange on the highly distorted preexisting bubble lattice. On a technical side note, even the smallest incremental increases of field, much smaller than 5 mT, were not able to image any transition states, neither for the contracting, nor the splitting behavior. This is not surprising as even the shortest exposure time in the milli-second range required for imaging in the TEM, exceed the time scale expected for the spin reorientation by several orders of magnitude [270]. Based on the observation, that the ends of stripes do not narrow and thus preserve a similar shape to a bubble domain, it is likely one such end is pinched off to form a new bubble domain, while the stripe end is reconfigured. This process requires the formation of two Bloch lines, one for the newly formed type II bubble, as well as one for the reconfigured end of the stripe domain. Due to the lack of imaged transition states, this process requires further investigations beyond the scope of this work.

Figure B.8 in the appendix, presents additional images of the field evolution corroborating the regular occurrence of the mechanisms presented in figure 5.16. These are the contraction of stripe domains to a single bubble and stripe domains pinching off individual bubbles at their ends, respectively breaking up into multiple ones. To conclude, both mechanics are confirmed origins of bubble domains in Fe_3Sn_2. In the observed examples the mechanism fostered the formation of type II bubbles.

5.2.4 Emergence of Topologically Non-Trivial Spin Textures

Intriguingly, the bubble domains emerging in Fe_3Sn_2 are not exclusively of type II, i.e. topologically trivial. As shown in figure 5.15, bubble domains of comparable size with a completely different domain wall configuration are observed as well.

Topographical pinning of non-trivial spin textures

This section looks at where the different types of bubbles form, as a function of applied magnetic field and lamellae thickness, before moving on to build a more detailed understanding of the BF LTEM contrast. Therefore, an extended area of the wedge-shaped region and the step linking it to the uniformly thick lamella of approximately 200 nm are imaged, see figure 5.17. Naturally, the variations in thickness required for this experiment means that at the thickest parts of the sample (top region of the image) the electron beam is strongly attenuated and contrast is reduced due to depth effects. Furthermore, at higher fields a shadowing effect occurs from the bottom right of the images, this is attributed to an additional aperture inserted with the intention of blocking undesired reflections. In the remanent state, depicted in figure 5.17a, the wedge-like lamella exhibits a peculiar domain pattern. On the left side, where the lamella is very thin, barely any contrast is observed, this most likely coincides with an in-plane closure domain pattern, which remains hidden as no distinct domain walls are imaged. In the central region the image shows densely packed stripes of gradually increasing width, predominantly oriented vertically. On the right side, a densely packed lattice of bubble domains is observed, which reveals that the lamella has been well aligned during the last exposure to out-of-plane field. The observed type II bubbles are aligned in almost vertical chains, where

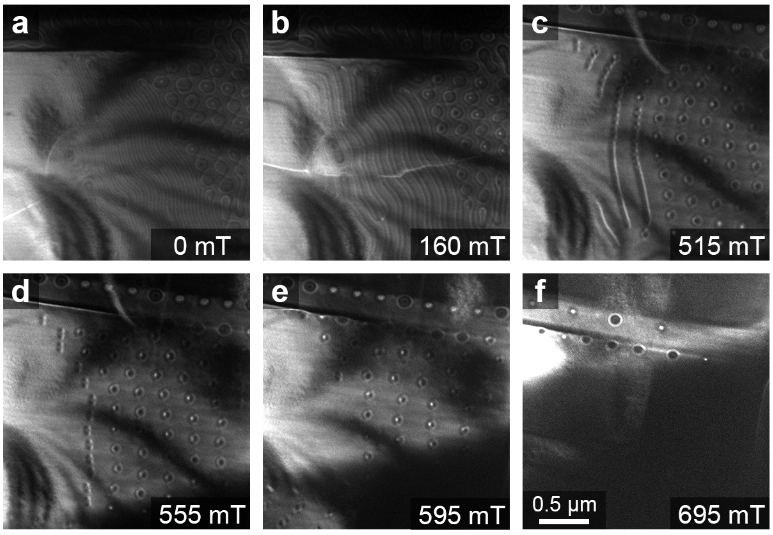

Figure 5.17: Field evolution on the stepped and wedged area of the lamella. a-f, BF images of the same region under gradually increased static out-of-plane magnetic field.

neighboring chains are offset by approximately half a bubble diameter yielding a triangular lattice.

Upon application of modest out-of-plane magnetic field of 160 mT, figure 5.17b, all domains exhibit classical behavior: Namely, all the domains opposing the external field are reduced in size [64]. Further increasing the field to 515 mT yields peculiar results. Note, incremental field steps omitted here can be found in figure B.9 of the appendix. At 515 mT, all stripe domains have broken up into a chain of bubble domains. In figure 5.17c these are hardly discernible as their contrast still overlaps. The previously densely packed bubble domains at the right edge of the image now occupy almost half the imaged region, forming a square lattice in the center, while maintaining the triangular lattice towards the top of the image.

Furthermore, on the step in thickness, an aligned chain of domains is observed. Their slightly larger size is explained by the locally increased thickness of the lamella. However, their corresponding LTEM contrast also differs, hinting these are type I bubbles. Applying even higher fields of 555 mT and 595 mT, see figure 5.17d and e, gradually expels almost all traces of the bubble domains originating from the narrow stripes. Additionally, several of the residual type II bubbles of the remanent state are expelled. The resulting bubble lattice has an increased distanced between the bubbles but still occupies the same total area. Only the bubbles pinned to the step remain virtually unperturbed. Finally, further increasing the field to 695 mT, all type II bubbles on the wedged region are expelled as depicted in figure 5.17f. Whereas bubbles pinned to the step, regardless whether they are on the step or at the bottom, persist, although, no bubbles are remaining in the thick region. Hence, the pinning and stability of the bubbles is not due only to thickness but rather correlates with a change in thickness. As mentioned above, while these bubbles are expected to be topologically non-trivial type I bubbles, which makes them more stable, additional pinning processes are still required to prevent them from moving in the external field. These results and previous observations for figure 5.15 imaging the area above the step imply the emergence of topologically non-trivial bubbles is linked to the step-like thickness transition. Whereas, in the area of equal thickness and on the gradual thickness slope, stripe domains break up into type II bubbles.

BF LTEM contrast of different types of bubble domains

To discern the different types of bubble domains imaged, and whether they are topologically protected or not, the structure of their domain walls has to be studied in detail. As described for figure 5.13, the in-plane component of the magnetization responsible for the contrast is oriented perpendicular to the brightness gradient in the image contrast. That means, an extended straight Bloch-type domain wall results in a bright and dark stripe adjacent to each other, while introducing curvature to the wall yields additional variation. Curvature induced superposition of bright or dark regions corresponding to different domain wall segments can yield even stronger contrast or compensation. Hence, interpretation of the obtained contrast requires a firm understanding of the expected domain textures in the investigated material.

To help explain the observed contrast in Fe_3Sn_2, a series of schematics are used to link the different observed textures with the real local magnetic texture. Figure 5.18 provides an overview of BF LTEM images and corresponding sketches of the magnetic spin textures for all bubble types observed so far. In the schematic representation the black and white arrows encode the helicity of the corresponding domain wall segment. The arrow emphasizes the direction of the in-plane component of the magnetization during the gradual rotation in the domain wall. Figure 5.18a, and f depict the end of a stripe domain. In the

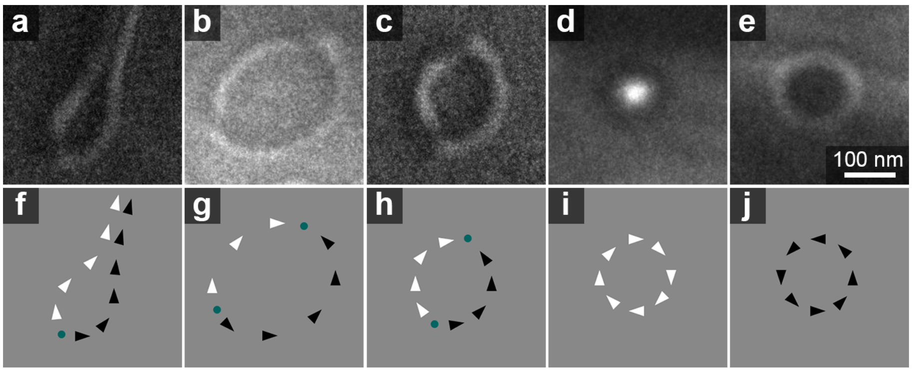

Figure 5.18: Detailed study of BF contrast. **a-e**, BF images of domain strucutres. **f-j**, corresponding schematic orientation of the in-plane magnetization of the domain walls. **a**, stripe end in field. **b**, type II bubble in zero field. **c**, type II bubble in 595 mT. **d**,**e**, type I bubbles of opposing helicity.

widened area it is clearly visible that the left and right domain wall segment depict the same brightness gradient. Hence the in-plane component of both domain wall segments points in the same direction. Evidently, this requires the helicity of the wall segments to be inverted. Thus, a Bloch line, indicated by the green dot, must emerge at some point along the domain wall. The Bloch line mitigates the helicity mismatch, as described in detail in section 2.2.3. Towards the top of the image, the stripe domain narrows severely, leading to the superposition of the bright and dark region of the two wall segments. Here, the contrast is hardly discernible.

Figure 5.18b, g, and c, h depict a type II bubble in zero field and 595 mT, respectively. Analog to the stripe domain, the type II bubbles constitute of two wall segments of opposite helicity. Hence, where the in-plane components of the magnetization meet head-to-head or tail-to-tail Bloch lines are formed. In zero field, see figure 5.18b and g, the bubble domain is slightly deformed, which is most probably attributed to interactions with neighboring domains, as these are populated densely. In static out-of-plane magnetic fields, see figure 5.18c and h, the type II bubble exhibits the typically observed onion-like shape [116, 271], which is characterized by an oblong shape with the Bloch lines on opposite ends.

Type I bubbles are given in figures 5.18d, i, and e, j, these bubbles are characterized by a continuous domain wall, which maintains the same helicity throughout, and are, therefore, topologically non-trivial. Some preceding work by Hue et al. [52] experimentally observed these first. Taking the domain wall curvature and their size into account, the obtained BF image contrast is a bright (dark) spot surrounded by a ring of dark (bright) contrast. Depending on the helicity, the Bloch-type skyrmionic bubble acts like a lens focusing either bright or dark contrast in the middle. An inherent challenge of LTEM images is that the type I bubble domain, exhibiting bright contrast in the center, see figure 5.18d, appears a lot smaller than its counterpart of opposite helicity. This perceived size mismatch is rooted in the measurement technique and does not resemble the actual spatial distribution of the underlying spin texture.

TIE reconstruction of magnetic objects

One possibility to overcome this perceived mismatch in size of different bubble domains is TIE. Colored maps of the reconstructed in-plane induction, calculated from the aligned stack of BF images, make it possible to distinguish different magnetic textures much more easily [92, 272]. Figures 5.19 and 5.20 show the same lamella as in 5.17 to illustrate this improvement on both the wedge-like region and the thick area that previously yielded no meaningful information. For every bright field image, the corresponding TIE reconstructed induction map is displayed, where the domain walls are easily distinguished as the bright colored structures. The hue and saturation encode the orientation and strength of the in-plane induction as encoded by the color wheels in figures 5.19b and 5.20e. Figure 5.19a and b show a remanent state. Beyond the in-plane flux-closure texture (top right of the image), all areas representing domain walls light up in their corresponding color. From the TIE image many of the complex domain patterns are readily understood: The uniform red to purple color of the stripe domains confirms collinearity of the in-plane magnetization of all neighboring domain walls. That means, neighboring domain walls, which confine a single stripe domain, exhibit opposite helicities. Furthermore, the chain-like arrangement of bubble domains extending the stripe domains is apparent, and the bubbles are distinguished to be topologically trivial, as they

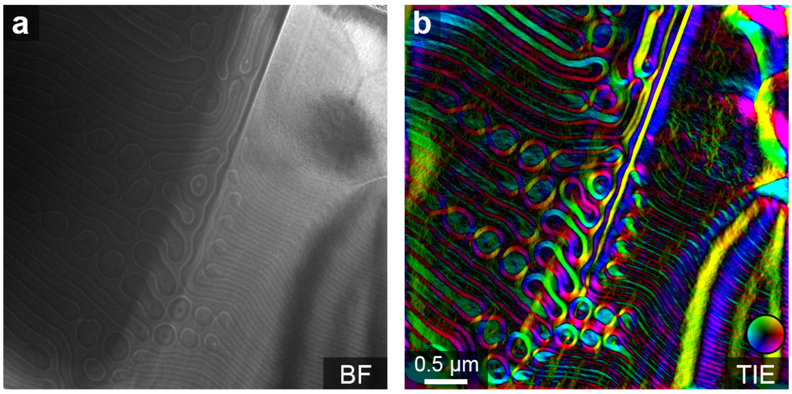

Figure 5.19: Side by side comparison of BF and TIE image. a, BF image and, **b**, corresponding TIE reconstructed induction map for the step like region in zero field.

consist of two wall segments of opposite helicities. In contrast, in the center of the image skyrmionic bubbles emerge. These are characterized by mapping the full color wheel within the domain wall. Furthermore, a peculiar type of stripe-like domain is observed, bridging the thickness mismatch from the intermediate step to the uniform 200 nm region. These exhibit a continuous domain wall of conserved helicity enclosing the core, i.e. the expanded equivalent of a type I bubble. The coexistence of these domains in zero field is corroborated by literature [52].

Analogous study of the domain morphology, upon applying out-of-plane field, is shown in figure B.10 in the appendix, which highlights the field evolution and the corresponding magnetic textures in more detail. TIE based analysis in magnetic field allows to trace the evolution of domain walls and bubble domains in the vicinity of topographic features. The combination of BF LTEM and MFM studies yields three characteristic phases: the stripe, the mixed and the pure bubble phase, selected by the application of magnetic field (confer figures 5.11 and 5.17, as well as [54]). In 300 mT, see figure 5.20a and d, a laterally extended predominant stripe domain pattern, where a few type I and II bubbles are already formed in the vicinity of the topographic step, is observed. Both the BF image and the TIE reconstructed induction map confirm that horizontal domain walls exhibit the same contrast, while the vertical domain walls in the vicinity of the edge exhibit a different orientation of the in-plane magnetization. Hence, the domain walls exhibit the helicities observed in zero field. Applying higher filed of 535 mT, see figure 5.20b and e, bubbles are formed at the step, analogous to the discussion of figure 5.17. Note those pinned directly at the step are of type I, whereas those forming in the vicinity are topologically trivial. From the TIE reconstruction, neighboring domain walls, confining a domain magnetized antiparallel to the applied field, are hardly discernible. As the out-of-plane magnetized stripe domain must still be present, this implies laterally extended domain walls or the domain walls are strongly reconstructed along the thickness of the specimen. Finally, in even higher fields of 645 mT, the mixed square and triangular lattice of type II bubble domains is reproduced in the area of uniform thickness. The type I bubbles

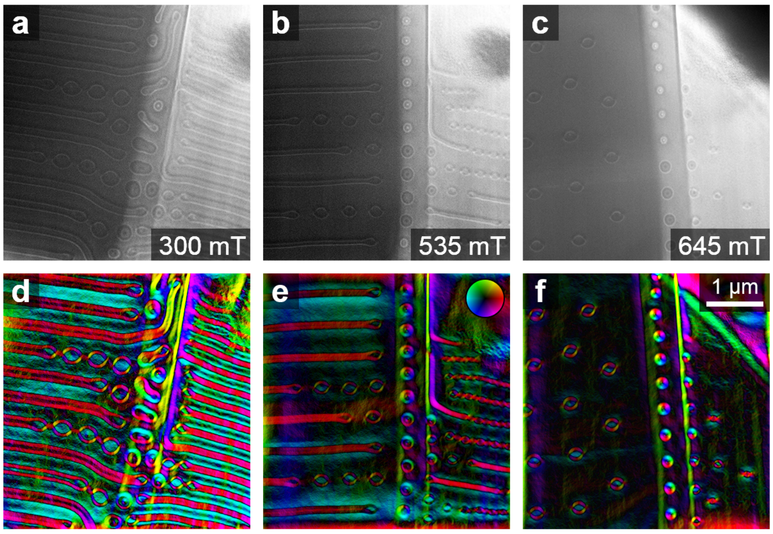

Figure 5.20: Field evolution revisited by BF and TIE images. a-c, BF images of the stepped region in different fields. **d-f**, corresponding TIE reconstructed induction maps.

remain pinned to the step, as shown in figure 5.20c and f. In the wedge-like region only a few type II bubbles persist. Applying even higher field expunges all type II bubbles, before eventually also the pinned, topologically protected, skyrmionic bubbles are erased.

Peculiar magnetic contrast in the grated lamella

From the above work on wedge like lamella, it became apparent that step like features generated more advanced topological objects than the continuous wedge. This naturally opens questions about why and how. As such, a systematic study of a lamella with a number of gradually deepening trenches and distinct distance thereof is conducted, figure 5.3e and f. One of the questions this study addresses is, whether these steps can be used for target-oriented design of bubble domains. Figure 5.21a and b shows the BF and TIE image of a remanent state, after strict out-of-plane field has been applied. On the right half of the lamella, where the trenches yield only slight or no thickness undulations, the domains remain unperturbed. They extend across the trenches and their relative alignment does not vary. In contrast, on the left half of the lamella, the domains are discontinuous at the trenches, immediately suggesting a minimum critical thickness mismatch is required. Furthermore, individual bubble domains are constrained in some of the trenches. These bubble domains form a triangular lattice. The center of the lamella, where the zone axis has been aligned, reveals densely packed slightly distorted bubbles domains, with several of the bubble domains exhibit oblong shape. Additionally, a few short stripe domains are observed surrounding the area. At the bottom and right edges a stripe pattern is maintained.

Beyond the mere location of individual bubbles, the lamella reveals more peculiar details linked to them. Unlike the previously classified bubbles, confer

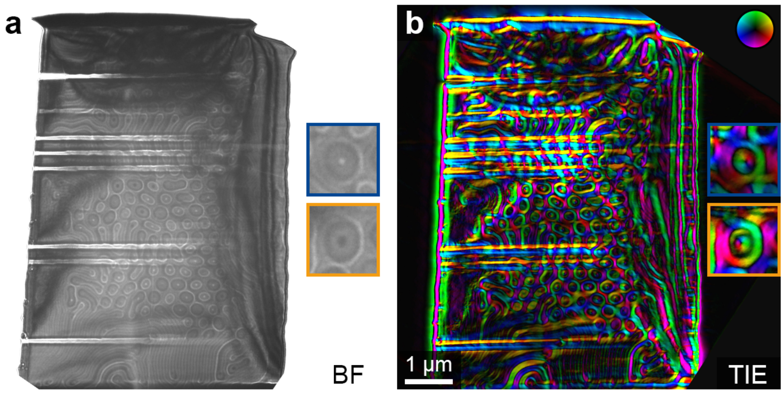

Figure 5.21: Remanent domain configuration of the grated laella. a, BF image. **b**, corresponding TIE reconstructed induction map. Note, the color wheel is rotated in accordance with the image rotation. The insets depict two representative bubble domains magnified.

figure 5.18, many of the observed bubbles exhibit additional highly localized contrast, which is emphasized by the two exemplary bubble domains depicted in the insets to figure 5.21a and b. In the BF images these are manifested in a distinct bright or dark spot, whereas in the TIE reconstructed induction maps, these spots yield analogous contrast to a skyrmion [147, 155, 273]. While, similar contrast could also be observed for point-like structural defects of lamellae, these can be ruled out as the origin, as the contrast is inevitably linked to bubble domains. Furthermore, these spots are nested within the domains. For bright field LTEM images and the TIE maps reconstructed thereof, such accumulated contrast could be the result of Fresnel fringing so that with increasing (decreasing) defocus, there is an increased (decrease) superposition of higher order fringes at the center leading to brighter (dark) spots. This is consistent with the observations in bubble domains, however, some bubbles do not exhibit such center-spots. Furthermore, for laterally expanded stripe-like domains these spots are often observed, only in one of the ends, i.e. inconsistent with the hypothesized origin due to Fresnel fringing. Thus, the correlation of the origin of the spot-like contrast and the magnetic texture of the individual domains, has to be investigated further.

Off-axis electron holography confirmation of peculiar contrast

In order to test if any Fresnel mode related artifacts are the origin of the spot like contrast nested in the domains, off axis electron holography is performed on a representative specimen. Holography measurements are performed in focus, thus any defocus artifacts, e.g. attributed to Fresnel fringes do not occur. Figure 5.22a shows an overfocused BF image of the investigated area for reference. In the image, multiple bubble domains exhibiting the nested spot-like contrast are visible. For the off-axis electron holography study, the biprism is inserted in the optical axis below the sample. The obtained image contains an in-focus BF image of the area superimposed by the periodic structure from the interference of the partial electron beams. FFT based processing enables

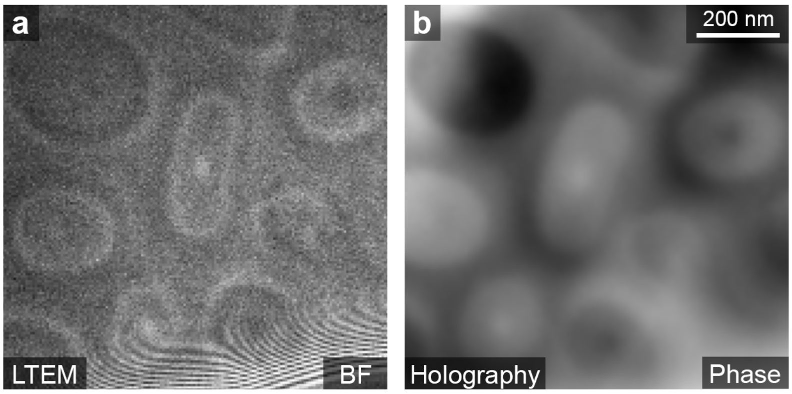

Figure 5.22: Off axis holography of bubble domains. **a**, reference BF image of the edge of the step-like sample in zero field. **b**, corresponding separated phase image obtained by processing the holography image. Holography data obtained in collaboration with A. Kovács.

the deconvolution of the amplitude image, i.e. the equivalent of the BF image, and the phase image presented in figure 5.22b. The phase image contains the relevant magnetic information analogously to the phase images obtained from TIE reconstruction. For several representative bubble domains, it confirms the spot like contrast in the center. This provides evidence that the magnetic origin of the spots is not linked to Fresnel fringes but the magnetic texture itself.

Field evolution of the grated lamella

Now that the existence of non-trivial topological objects exhibiting the peculiar spot-like contrast has been established in a grated lamella, their evolution as a function of field is investigated in figure 5.23[3]. Figure 5.23a and b, show the BF and TIE images for an applied field of 410 mT. Despite extended regions exhibiting a stripe pattern, due to the accidental application of slightly oblique field, the vast majority of skyrmionic bubbles remains intact. Upon close inspection, even the nested spots are preserved, as shown in the insets. The rigidity of the spots versus the application of modest field is particularly interesting: it implies that these are part of the naturally occurring domain wall. Increasing the field further to 520 mT causes the ejection of some bubbles. For those preserved, it is no longer possible to discern potentially persistent spots form the shrinking domains. Additional intermediate field steps can be found in the appendix, see figure B.11.

Electron holography implies the origin on the spot like contrast is linked to the peculiar three-dimensional reconfiguration of the domain walls, which is corroborated by their rigidity versus external fields applied. Thus, they appear to be an inherent consequence of all the magnetic iterations involved,

[3]Note, for improved visibility the lamella is aligned in every panel to correct for the inherent rotation of the field application via the objective lens. However, during TIE reconstruction this is not possible, and thus the color wheel is rotated accordingly, i.e. the absolute in-plane orientation encoded is inconsistent in between images.

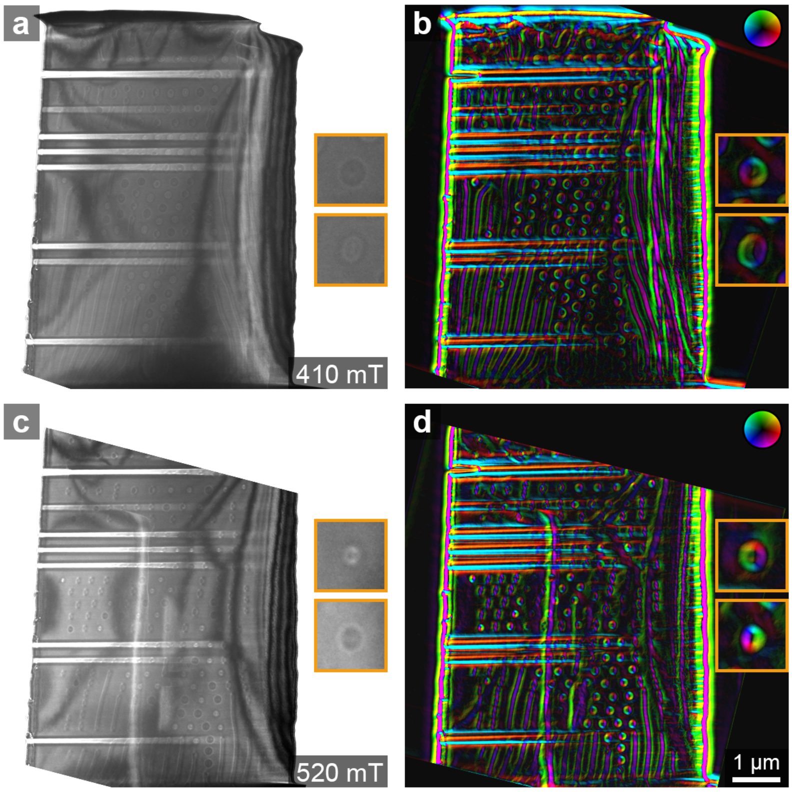

Figure 5.23: Field evolution of grated lamella. **a**, **c**, BF LTEM images. **b**, **d**, corresponding TIE reconstructed induction maps. Note, the color wheel is rotated in accordance with the image rotation. The insets depict two exemplary bubble domains magnified.

rather than an arbitrary in-plane spin orientation occurring only under peculiar circumstances in the absence of notable Zeeman interaction.

In contrast to previous studies in figure 5.17, in the grated lamella, the stability of type II bubbles appears to exceed the type I bubbles. The origin of this peculiar behavior is rooted in the magnetic interactions: The circular continuous domain wall of a skyrmionic bubble is topologically protected and, furthermore, yields the most favorable spin configuration with respect to the Heisenberg exchange. Type II bubbles, require the emergence of energetically unfavorable Bloch lines. In case of oblique fields, the energy cost of the Bloch lines can be superseded by the energy lowering due to the wall segments of opposite helicity aligning with the in-plane magnetic field. Analogously, the Zeeman interaction, renders the type I bubble less favorable, as the in-plane components of the partial wall always oppose the applied in-plane field. Thus, by tuning the angle of mismatch to the c axis and strength of the applied field, the formation of a desired bubble phase is regulated. For increasing mismatch, type I bubbles can be expelled, whereas for strict out-of-plane field type I bubbles persist while type II bubbles are already erased. This understanding allows us to control the formation of different bubbles types, both in this material, and provides a road map that can be used in other materials.

Coexistence of composite bubble domains

From the previous analysis of BF images depicting bubble domains, two types of bubbles were determined, confer figure 5.18. These are type II bubbles, exhibiting Bloch lines, where the LTEM contrast inverts, separating the two Bloch wall segments of opposite helicity. As well as type I bubbles, characterized by a continuous Bloch-type domain wall. The latter can be observed for either helicity, i.e. yielding a dark or bright center surrounded by a ring of opposing brightness. Additionally, either type of bubble can exhibit the spot-like contrast in the center. In the following, the variety of these occurring bubble domains is discussed in detail.

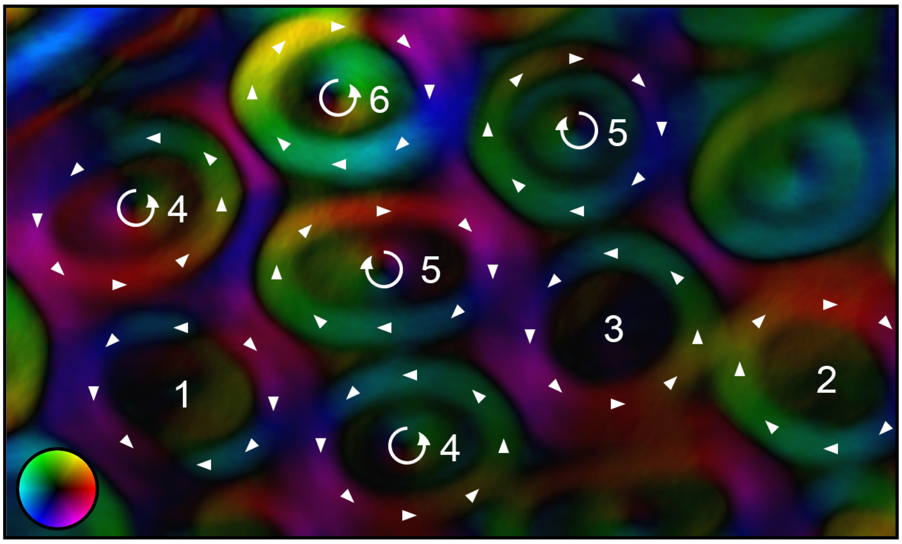

Figure 5.24: Coexistence of various domain wall configurations. Magnified view of the central area of the TIE reconstructed induction map depicted in figure 5.21b.

Henceforth, a helicity $\gamma = +\pi/2$ corresponds to a counter-clockwise swirl of the magnetization. Thus, an object of helicity $\gamma = +\pi/2$ yields a counter-clockwise swirl in the TIE images. Note, inverted helicity does not change the sequence of colors tracing along the wall, it interchanges colors at opposite points of the perimeter. That means, if for a type I bubble of helicity $\gamma = -\pi/2$ the color at the 12 o'clock position is red, the same position is colored light blue for $\gamma = +\pi/2$. Tracing along the domain wall counter clockwise in either case the color sequence remains: green - blue - red - yellow, just like the color wheel. Figure 5.24 depicts a distinct magnified area of figure 5.21b, where several types of bubble domains have been imaged. These are:

1: A type II bubble, where the two wall segments of opposite helicities cover the same half of the color wheel. Both domain wall segments cover approximately the bottom half of the color wheel, i.e. map to the same half sphere in order parameter space. At the top and bottom, where the in-plane components meet tail-to-tail, respectively head-to-head, the Bloch lines mitigate the mismatch.

2: A type I bubble, characterized by a continuous clockwise swirl of the magnetization in the domain wall. Hence, the helicity $\gamma = -\pi/2$ is assigned. Upon mapping, the whole order parameter space is wrapped once, thus, the bubble is topologically non-trivial.

3: Type I bubble of opposite helicity $\gamma = +\pi/2$.

4: Type I bubbles, of helicity $\gamma = +\pi/2$, which exhibit the spot-like contrast in the center. Due to the matching contrast of the spot to the wall, it can be assigned the same helicity.

5: Type I bubbles, of helicity $\gamma = -\pi/2$, with a corresponding spot-like contrast of helicity $\gamma = -\pi/2$.

6: A type I bubble, of helicity $\gamma = -\pi/2$, where the spot-like contrast exhibits reversed helicity $\gamma = +\pi/2$.

Note, despite previous results suggesting the spots are part of the complex domain wall, the terms 'wall' and 'spot' are used to differentiate here. Furthermore, meticulous investigation of the whole lamella reveals type II bubbles exhibiting spot like contrast. In the following, beyond simply listing up the different observed magnetic objects observed, the composite bubble domains are classified.

Classification of composite bubble domains

While, the coexistence of bubble domains of opposite helicity in Fe_3Sn_2 is evident from results shown in figure 5.24, and the literature [52, 266], the observed variety exceeds expectations. Thus, all bubble types observed are classified in the scheme depicted in figure 5.25. Here, for every type the observed TIE reconstructed induction map, the corresponding BF image and a schematic of the in-plane magnetization is given. The helicity is encoded in the schematic drawing by the arrows. Black represents $\gamma = +\pi/2$ and white $\gamma = -\pi/2$. The green dots denote the location of Bloch lines.

Type A describes type I bubbles where the helicities of the outer ring and the spot match. Type B represents all skyrmionic bubbles which lack the spot-like contrast in the center. Domains exhibiting inverse helicities of the spot and the ring are assigned to type C. Note, that for all types of topologically non-trivial bubbles, the exemplary case depicts cases of $\gamma = -\pi/2$ for the ring. This solely serves clarity and any corresponding structure of reversed helicity is classified accordingly. Type D represents all classical type II bubbles, which do not exhibit a spot. Finally, type E describes topologically trivial bubbles exhibiting a spot of either helicity.

Quantitative analysis of the occurrence of different bubble types

While, the coexistence of these different types of bubbles in close proximity is confirmed by figure 5.24, a single magnified area is not representative of the whole lamella, let alone lamellae cut from the material in general. Additionally, as the discussion of figure 5.23 revealed, several of these peculiar bubble

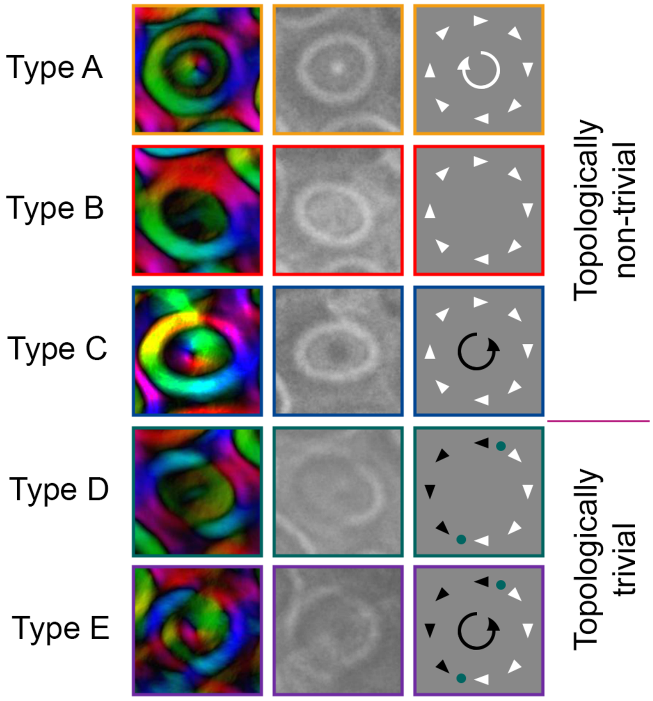

Figure 5.25: Classification of bubble domains observed via LTEM. TIE, BF and schematic representation of the in-plane magnetization for all types of bubbles observed.

domains are stable up to modest fields, while others are not. Thus, quantitative analysis of the occurrence of bubbles of either type, evaluated over the full area of the lamella, is performed. Furthermore, the analysis is expanded to analogous quantitative assessment of the field evolution. For that purpose images corresponding to modest fields up to 520 mT are analyzed. The results are summarized in table 5.2. L23A denotes the lamella and the respective field is given for each row. All cells contain two values. These are the absolute number of respective domains identified and the relative share. The reference for 100% is the total number of identified bubbles per image. Considering the total number varies when new domains form and others are expunged, small variations in the relative occurrence of certain types of domains occur. For each lamella and field value the BF LTEM image and the corresponding TIE map, with all identified bubbles marked accordingly, are presented in the appendix and the corresponding figures are indicated in the last row.

This analysis allows to draw two conclusions: First, in zero field the number of topologically non-trivial bubbles comprises 80% of all bubbles. This is for the remanent state after out-of-plane field has been applied. Secondly, while the share of type II bubbles increases due to the application of modest oblique field, the share of skyrmionic bubbles shifts in favor of type A. Applying a field of 520 mT, the bubbles shrink to the point, where any contrast correlated to the spot is no longer discernible, i.e. all bubbles are assigned either type A or D, respectively.

	type A	type B	type C	type D	type E	Figures
L23A, 0 mT	29 35%	20 25%	17 20%	11 14%	5 6%	B.12 B.13
L23A, 320 mT	26 29%	10 11%	25 27%	20 22%	10 11%	B.14 B.15
L23A, 410 mT	36 42%	21 24%	8 9%	14 16%	8 9%	B.16 B.17
L23A, 520 mT	57 51%	- -	- -	55 49%	- -	B.18 B.19
L13A, 565 mT	8 24%	1 3%	2 6%	18 55%	4 12%	B.20 B.21

Table 5.2: Absolute and relative occurrence of different types of bubbles. The figures listed in the last column show a bright field and TIE reconstructed image with all bubbles marked accordingly.

Additionally, one image of the step linking the uniformly thick section and the wedge-like section is evaluated with an out-of-plane field of 565 mT applied, see the last row of table 5.2. The data confirms the coexistence of all types of bubbles even in higher fields. As a general statement, the type A and D bubble domains are the most common under these circumstances.

For the MFM studies, as well as the BF LTEM images discussed initially the observed contrast matches well with the theoretically predicted domain configuration, confer section 2.1.5. For the intermediate Q system Fe_3Sn_2 these predictions are stripe domains in zero field, which transition to bubble domains in field. The domains are separated by Bloch-type domain walls and exhibit Néel caps. The latter are corroborated by the gradual transition of the MFM signal in between opposing oriented domains. Néel caps do not imply total flux-closure, i.e. for each domain an uncapped partial region may exist, confer figure 2.8. In case of bubble domains, respectively similar shaped ends of stripe domains, such laterally highly constricted regions should appear centered over the domain. That is, where the skyrmion-like TIE contrast, attributed to the spots, naturally occurs. Thus, this spatial correlation is investigated for a causal link.

The LTEM contrast obtained from the spots resembles a regular Bloch-type skyrmion, i.e. vorticity $m = 1$ and helicity $\gamma = \pm\pi/2$. From an experimental perspective, this is reasonable as only Bloch-type skyrmions can be observed in an aligned specimen via LTEM [274]. Néel-type skyrmions, $\gamma = 0$ or π, essentially shift the intensity in a circle, thus, compensate their own LTEM contrast. From theory, intuitively the partial flux-closure is expected to be of Néel-type. Hence, if a circular residual uncapped region exists, it should resemble the contrast of a Néel-type skyrmion not a Bloch-type one. Furthermore, the TEM essentially integrates all perturbations along the paths of the imaged electrons. In other words, it probes the full thickness of the lamella at once. That means, it also probes two surfaces, the top and bottom one of the specimen at the same time. Thus, perturbations originating on either or both surfaces contribute to the LTEM contrast. In order to actually determine a causal link of the spot-like contrast to partial flux-closure textures, it is not sufficient to validate the results based on conceptual accordance. Instead a proper model of the three dimensionally resolved magnetization of Fe_3Sn_2 specimen of comparable shapes is required.

5.2.5 Micromagnetic Simulations

Micromagnetic simulations are carried out in collaboration with A. Kákay, based on the work of E. Lysne [86]. The simulations are performed using MUMAX3 [275], where the energy terms included in the model are the Heisenberg exchange, first-order uniaxial anisotropy, the Zeeman, and demagnetization energy terms [54]

$$\epsilon = \int\limits_{V_\mathrm{s}} \left[A_\mathrm{ex} \left(\nabla \boldsymbol{m}\right)^2 - K_\mathrm{u} m_\mathrm{z}^2 + M_\mathrm{s} \boldsymbol{B}_\mathrm{ext} \cdot \boldsymbol{m} - \frac{1}{2} M_\mathrm{s} \boldsymbol{B}_\mathrm{demag} \cdot \boldsymbol{m} \right] \mathrm{d}\boldsymbol{r}. \tag{5.1}$$

Here V_s denotes the sample volume and the Zeeman term is adopted for external field along the out-of-plane component. The values used for the constants are listed in table 5.3. In order to avoid edge-induced effects, periodic boundary conditions are applied along the in-plane directions (x and y). Open boundary conditions are used along the out-of-plane direction ($z \parallel c$), reflecting the constraints of ab plane cuts of defined thickness. The mesh is constructed of $8 \times 8 \times 8\ \mathrm{nm}^3$ cells, i.e. within the limit of the exchange length l_ex. The base geometry is set to a square cuboid of width and length of 4096 nm. The thickness is set to 256 nm. With these setting the magnetic texture depicted in figure

M_s ($\mathrm{kA\,m^{-1}}$)	A_ex ($\mathrm{pJ\,m^{-1}}$)	K_u ($\mathrm{kJ\,m^{-3}}$)	l_ex (nm)
566	10.0	30.0	8.34

Table 5.3: Constants for micromagnetic simulations. Based on literature values [86, 265].

5.26 is obtained, after relaxing a random initial magnetization distribution. In this figure, the out-of-plane component of the magnetization, the z component, is encoded by the color scheme. Red means magnetization oriented along $+z$, whereas regions colored blue are magnetized in the opposite direction. White areas represent domain walls of predominant in-plane magnetization. All surfaces of the cuboid are colored accordingly. Additionally, the top half in the front of the cuboid is hidden. Here, iso-surfaces of $\pm 90\%$ magnetization along the z direction are depicted in the according color. Hence, areas enclosed by a red or blue iso-surface of constant magnetization represent the core of a domain, which is almost fully aligned with the uniaxial magnetocrystalline anisotropy. Whereas, regions in between opposing iso-surfaces are part of the domain wall.

Modeled ground state of lamellae

In agreement with the predictions from theory, a stripe domain patter is deduced from both the iso-surfaces, and the colored surfaces of the cuboid. Furthermore, from the edges of the displayed data, which are equivalent to crosssections, a significant reconstruction of the domain wall width along the thickness of the lamella is evident. The widening of the domain walls towards the top and bottom surfaces and the weak out-of-plane contrast at the surfaces

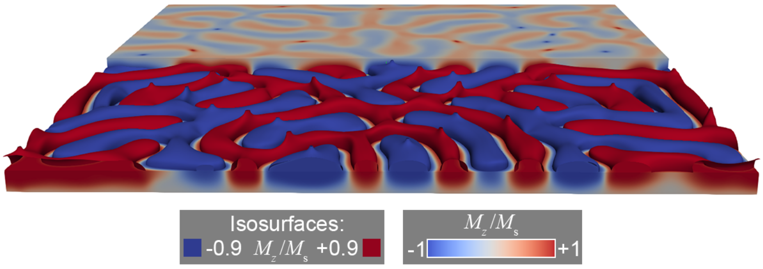

Figure 5.26: 3D rendering of the micromagnetic texture. Out-of-plane domain texture for a $4096 \times 4096 \times 256$ nm^3 volume.

imply the occurrence of Néel caps (confer figure 2.8). For the definitive confirmation thereof, the orientation of the in-plane component following Néel-type behavior must be confirmed. Additionally, small regions of strong saturation, nested within the individual domains, are observed on the top surface. The iso-surfaces depict corresponding neck-like structures extending towards the top surface. These are the residual areas of strong out-of-plane magnetization, which are not covered by the partial flux-closure at the surface, and these are described in detail below.

First, the overall domain pattern is studied. The simulated volume resembles an infinitely extended *ab* plane lamella of thickness 256 nm, due to the periodic boundary conditions. In contrast, experimentally observed lamellae are of finite lateral dimensions but these regularly exceed the dimensions of the cuboid. Thus, there is a competition between reasonable calculation time, forcing smaller simulation volumes, and avoiding edge induced artifacts arising from small simulation volumes: Periodic boundary conditions are the reasonable compromise. As the simulations in figures 5.26 and 5.27 are obtained using periodic boundary conditions, they can be considered representative of a 4×4 µm^2 area cropped from a larger lamella.

Figure 5.27a shows the top-down view (along $-z$) of the iso-surfaces for the micromagnetic simulation previously presented in figure 5.26. The maze-like stripe domain pattern is severely branched, additionally, several residual small stripe domains are visible. Peculiarly, the red domain is one large connected domain, whereas the blue domains are multiple scattered ones. This behavior is attributed to the nucleation sites embedded in the seed for the micromagnetic simulations. In figure 5.27b to j the magnetization for the top, middle, and bottom layers is depicted in the three rows. The color encodes the x, y, and z components of the magnetization individually in the three columns. For the x and y components the contrast is very strong in the top and bottom layer, whereas in the middle layer it is clearly confined to the sharp domain walls. The z component behaves inversely. The middle layer emphasizes the maze-like stripe domain pattern. The top and bottom layers depict a weak imprint thereof and the spots. These are nested centrally within the domains, which agrees with previous experimental observations of the spot-like contrast. The positions, where spots appear in the top layer are corroborated by the neck-like structures in the iso-surfaces. Furthermore, several of the spots in the top and bottom layer align. Since these are the most promising origin of the peculiar contrast in LTEM studies, they are investigated in more detail.

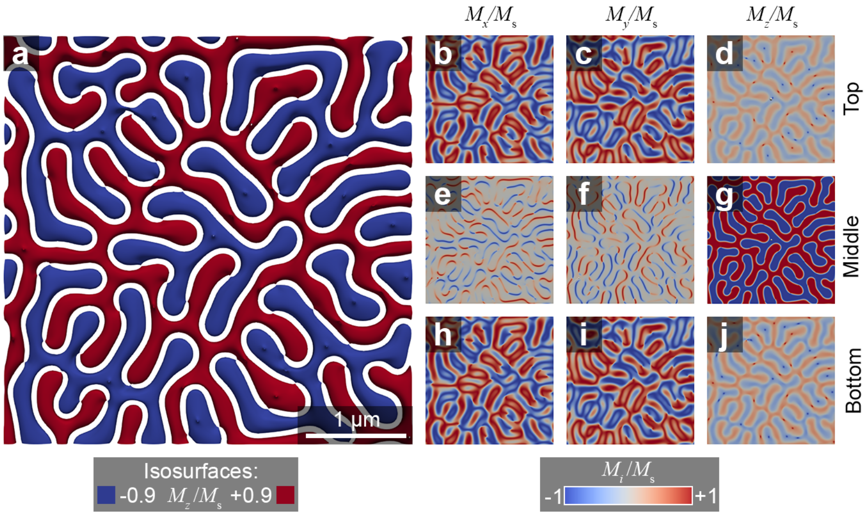

Figure 5.27: Detailed consideration of micromagnetic simulation. a, top-down view of the iso-surfaces of $\pm 0.9\, m_z$. **b-j**, individual layers of the simulated data colored by m_i, where $i \in \{x, y, z\}$. **b-d**, top layer. **e-g**, middle layer. **h-j**, bottom layer. **b**, **e**, **h**, m_x. **c**, **f**, **i**, m_y. **d**, **g**, **j**, m_z.

Observation of vortices at the surfaces

For a more detailed look at the oddities within the simulations, a region exhibiting Néel caps, and four spots, associated with the neck-like structures, is cropped out and magnified.

Note, that these spots formed on the bottom surface, and so, in figure 5.28a the bottom surface is displayed facing up (view along $-z$). The out-of-plane magnetization of the iso-surfaces, and the arrows are encoded by color analogously to figure 5.27, thus, white exhibits maximum in-plane magnetization. For clarity, the local orientation of magnetization in the surface layer is represented by arrows. The arrows over the white regions, that are the domain walls, are oriented parallel to the normal of the wall n_{wall}. Thus, Néel-type walls at the surface, i.e. experimentally hypothesized Néel caps, have been computationally confirmed.

Focusing on the four spots, these are quickly distinguished to be made up of 3 different types of structure, schematically illustrated in figure 5.28e to g. First, the spot marked purple is considered in more detail. A further enlarged view, as well as a schematic representation are depicted in figure 5.28b and e, respectively. For the schematic the arrows are colored by hue and saturation. Hue encodes the in-plane orientation, similar to TIE data, whereas reduced saturation towards black (along $+z$) and white (along $-z$) describe the out-of-plane orientation. In the vicinity of the spot, the magnetization is oriented almost radial. Thus, the helicity, $\gamma \to 0°$, which is termed Néel-type, consistent with the earlier observations of Néel caps. Counterintuitively, the Néel caps do not extend to the spot. In close proximity to the unperturbed out-of-plane magnetization exhibited at the spot, the in-plane component of the magnetization is oriented almost tangential. Hence, the spot is surrounded by a small

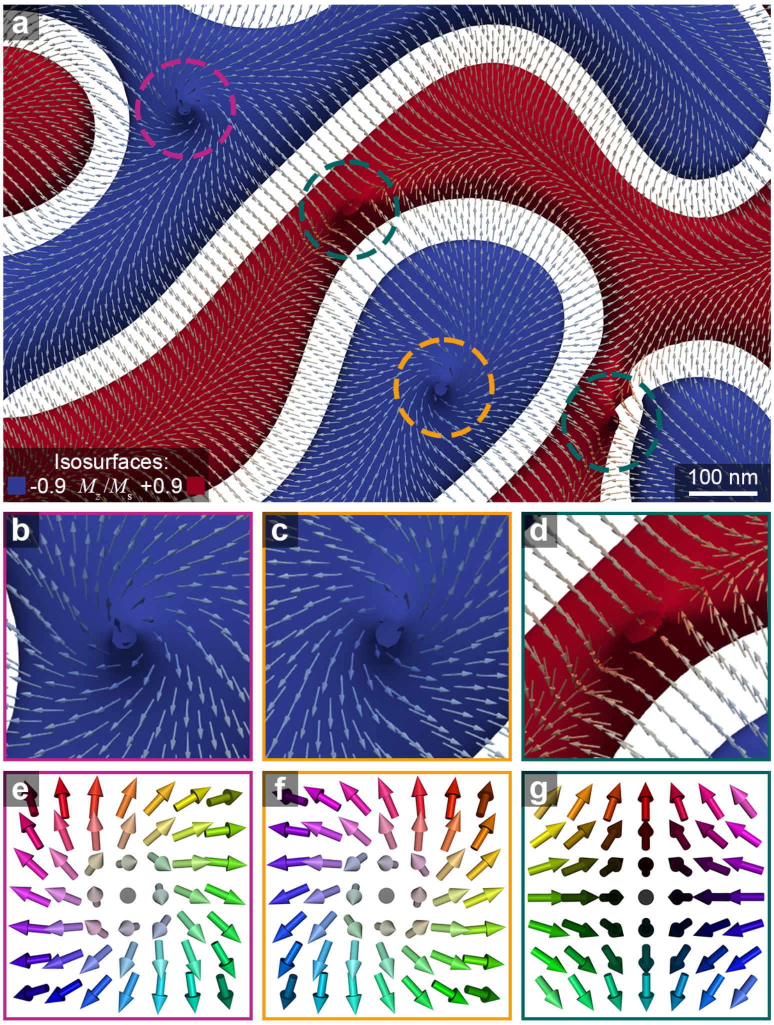

Figure 5.28: Spin texture around the partial flux closure. a Magnified view of the iso-surfaces exhibiting neck-like structures to the surface. The orientation of the magnetization in the top layer is represented by the arrows. **b-d**, detailed view. **e-g**, corresponding schematic view of the observed spin textures.

area exhibiting predominant Bloch-type domain wall character, which gradually transitions to the Néel-type in the vicinity. Analogous behavior is observed for the second spot, marked orange, which depicts an inverted direction of the swirl in close proximity, figure 5.28e and f. Therefore, spots can exhibit Bloch-type behavior of either helicity, $\gamma \approx \pm 90°$. Hence, in Fe_3Sn_2 there are vortices of the same vorticity ($m = +1$) but opposite helicity. Topologically, they map to the norther (southern) hemisphere of the order parameter space. Thus, they mimic the inner half of Bloch-type skyrmions of either helicity.

In addition to the two vortices of opposite helicities described above, a third distinct type has been identified, highlighted in green in figure 5.28a, with a magnified view and a schematic provided in 5.28d and g, respectively. Unlike the previous spots, this one is not rotationally invariant, but rather has a two-fold rotational symmetry (C_2). Along the domain, the magnetization points from the spot, whereas trailing perpendicularly out over the domain wall, the magnetization points towards the spot. In between, the magnetization rotates to bridge this mismatch, leading to an object with a vorticity of $m = -1$: i.e., the spot is an antivortex. The fourth spot in this region is also an antivortex, with an analogous magnetization configuration differing only in its lateral position, which is slightly offset towards one side of the domain. Peculiarly, a similar neck-like structure is visible on the opposing surface, which is likely identified as an (anti-)vortex. These could be traces of the creation of a vortex-antivortex pair from a Bloch point, previously nested in the domain wall between the two stripes. However, as the observation of antivortices in Fe_3Sn_2 is currently limited to the micromagnetic simulations, and in-depth study is not part of this work.

Correlation of micromagnetic simulations to experimental observations

Having ascertained what types of vortices are present within micromagnetic simulations, here this computational data is directly compared to the experimental data. More specifically, the obtained contrast from LTEM studies is qualitatively matched to the results from micromagnetic simulations.

Therefore, the micromagnetic simulation results are processed to yield comparable representations. This is done by using the PyLorentz code, version 1.0 [276]. The Python based code computes LTEM contrast for the micromagnetic simulation results. Within the code, a microscope is defined with matching specifications of the experimental setup, including parameters like defocus and specimen tilt. From the modeled three-dimensional micromagnetic texture BF images, and TIE contrast, are simulated for the defined experimental settings. Compared to simpler approaches, e.g. averaging the in-plane components along the thickness, this method has the major advantage that it actually reproduces analogous artifacts to experimental TEM study. Most notably, working with too large defoci yields rippled contrast associated with severe Fresnel fringing, whereas too small defoci yield weak contrast. Hence, by adjusting, or deliberately misaligning the focus, even realistically imperfect experimental results can be reproduced.

Figure 5.29a shows the BF image of a representative region. It contains, both stripe and a few bubble domains. Furthermore, some of the stripes, as well as some of the bubbles, exhibit continuous domain walls, while others are characterized by the emergence of Bloch lines. This domain pattern is matched by the modeled micromagnetic texture, depicted in figure 5.29b. Note, for improved visibility the images are scaled to match the size of the emerging domains, as quantitative size comparisons are inopportune, because of some remaining challenges of the technique, such as sample thickness mismatch. Both the BF image defocus stack and the modeled magnetic texture are processed to obtain TIE induction maps. The induction maps, depicted in figure 5.29c and d, finally allow qualitative comparison of results based on analogous data representation. Looking beyond the quantitative mismatch of when domain structures transform into each other, all the salient features

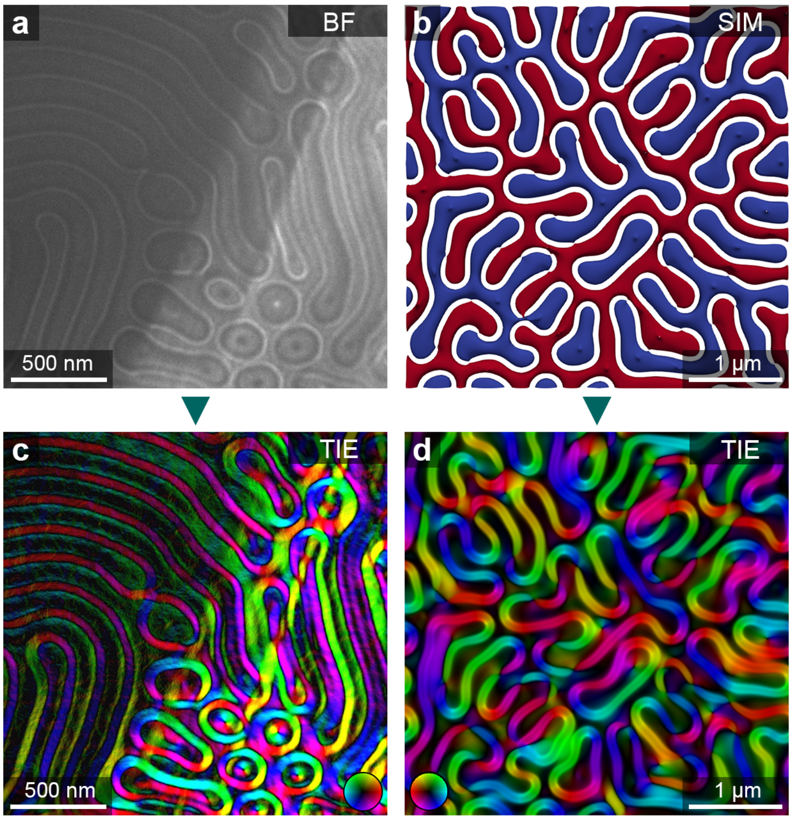

Figure 5.29: Comparison of experimental and simulated results. **a**, BF image. **b**, simulated micromagnetic texture. **c**, TIE reconstructed induction map, obtained from the image stack corresponding to **a**. **d**, simulated TIE induction map based on the modeled micromagnetic texture in **b**.

are observed: Large stripe domains, exhibit Bloch lines in either image. Only short stripes, which could also be termed elongated skyrmionic bubbles in many cases, maintain a continuous domain wall.

Considering the modeled data, at the bottom of figure 5.29d an elongated type I bubble domain without nested spot-like contrast is observed. Whereas, spot like contrast is observed in the simulated TIE for other domains: On the right-hand side, in a bubble, where the outer and inner contrast match. In the center of the image, where the spot-like contrast sits centered in one of the ends of the short stripe, as well as in the center of the large branched domain. And finally, at the top edge, where the spot is nested in a type II bubble. While, the locations of these spots match the locations of vortices identified in figure 5.29b, the latter appear far more numerous. Hence, not all vortices yield spot-like contrast in the TIE indcution map. On the flip side, this matches the experimental results, where not all bubble, respectively stripe domains exhibit the spot-like contrast either. The lack of spot-like contrast in the experimental results could coincide with the lack of partial flux-closure for such domains. But from simulations partial flux closure is predicted for all domains. Hence, the more likely reason for the lack of vortex related contrast is rooted in the second surface. As denoted, the vortices tend to appear laterally centered over the domain. Thus, averaging through the whole depth via TIE reconstruction includes not only the effect of the vortices at the top surface, visible in figure 5.29b, but also their counterparts on the bottom surface.

Introduction of the layer based model

Given the spot-like TIE contrast nested in domains presumably originates from vortices appearing at both surfaces of the specimen, individual analysis of the respective depth regions is conducted to understand the reasons for the emergence, or lack, of spot-like TIE contrast nested in domains. Therefore, a major strength of magnetic simulations is exploited: While in the experimental setup, probing the full thickness is a requirement of TEM studies, this is not the case for the simulated TIE. In fact, the simulated contrast can be obtained from a micromagnetic simulation representing as little as sub-nanometer thickness. Thus, in case of the $8 \times 8 \times 8\,\mathrm{nm}^3$ cells used for the simulations in this work, every single layer of the modeled magnetic texture could be evaluated individually. Hence, the individual features in the TIE contrast can be attributed to the layers in the bulk or at either of the surfaces they originate from. This approach is corroborated by an analogous study of an individual bubble domain in literature [277].

The micromagnetic texture, depicted in figure 5.30a, is obtained by re-relaxing the domain pattern, simulated for 575 mT out-of-plane field, in zero field. The result is a mixed domain configuration of oblong bubbles and short stripes, which match the experimentally observed remanent domain patterns closely, including the presence of vortices. Analysis of cross sections reveal the neck-like structures in the iso-surfaces are constrained in the top and bottom three layers of the simulated magnetic textures. The central ten layers are representative of the domain size in the bulk. Thus, these groups of layers are extracted for separate analysis. As depicted by the iso-surfaces in figure 5.30b to d, the central layer reproduces the domain pattern in the bulk, whereas the top and bottom layers merely depict a few scattered spots corresponding to the vortices. The locations of the majority of the vortices matches on the top and bottom surface. For each of the separated subsets of layers, as well as the modeled domain configuration representing the full thickness, the TIE contrast is simulated. For all four simulations the presumed microscope and experimental settings, like the defocus, are kept fixed. The resulting TIE contrast is depicted in figure 5.30e to g for the separated subsets and in figure 5.30h for the full thickness. The latter depicts contrast qualitatively matching previous experimental results (confer figure 5.21b). From figure 5.30h, the domains and the spot like contrast attributed to the vortices are clearly visible. The TIE contrast calculated for the separated subsets at the top and bottom corroborates previous results discussed for figure 5.27. Note, the diffuse contrast is not related to the Néel caps as these do not yield discernible BF contrast and subsequently no TIE contrast. It actually correlates to the onset of the domain wall reconfiguration towards the Bloch-type walls in the bulk. The vortices yield the presumed skyrmion-like TIE contrast. Evaluation of the center region, figure 5.30f, reveals contrast solely linked to the Bloch-type domain walls in the bulk. Hence, the origin of different features in the TIE contrast being

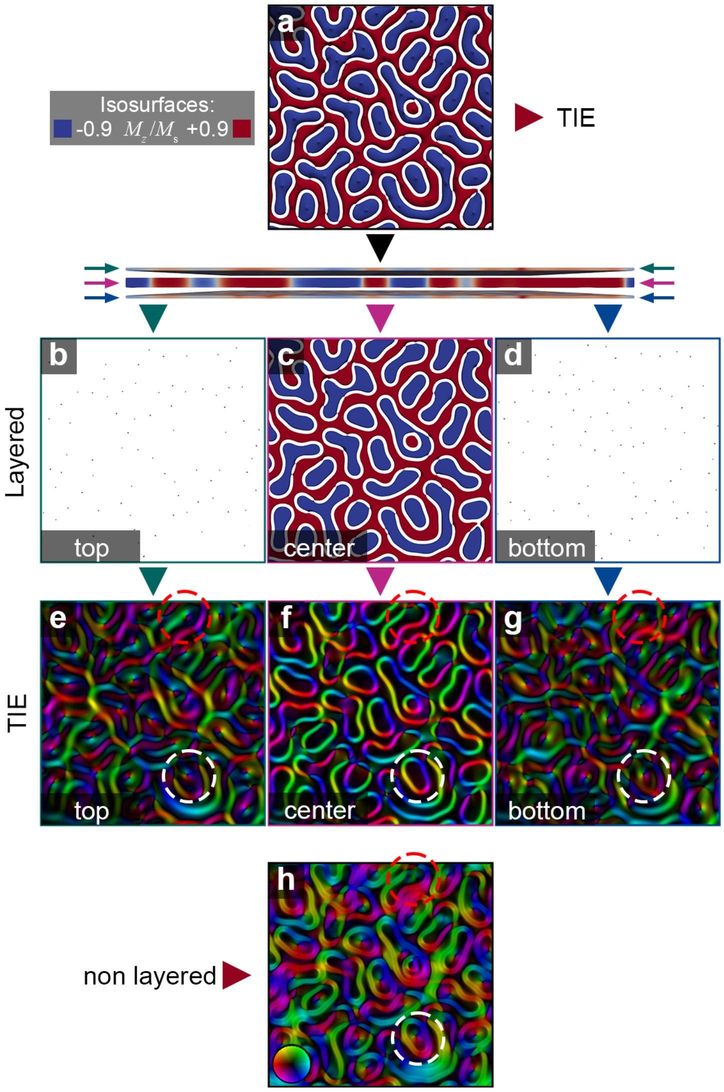

Figure 5.30: Layer based model in simulations. **a**, remantent modeled domain configuration and separation into the top and bottom three as well as the central ten layers. **b-d**, modeled domain configuration in the top, central and bottom region, respectively. **e-g**, corresponding simulated TIE contrast. **h**, simulated TIE contrast for the full thickness.

attributed to either surface, respectively the bulk, is confirmed.

In the TIE images of figure 5.30, one domain is highlighted in white. For the full thickness, this particular domain depicts the ring-like texture, as well as the center spot attributed to a vortex. Comparing the area in the models of the separated layers, the ring-like structure is reproduced in the center, whereas both the top and bottom surface depict matching spot like contrast. The behavior of the bubble domain marked in red differs. Here, the type II domain exhibits no nested spot-like contrast for the full thickness. The observed domain wall is reproduced from the bulk region. Although slightly perturbed, the top and bottom slabs depict spot-like contrast, nevertheless. Careful analysis reveals the two vortices exhibit opposite helicities, i.e. their LTEM contrasts cancel one another. Thus, proving the lack of nested spot-like contrast in experimental data originates from intrinsic cancellation due to opposite contrast attributed to laterally aligned vortices at the top and bottom surfaces.

Detailed consideration of three representative bubble domains

Furthermore, the layer based model explains the origin of several different types of bubble domains classified in figure 5.25. In order to elucidate this, three representative bubble domains obtained from micromagnetic simulations are considered in detail, reveling the origin of the contrast for type A, B and E bubble domains, respectively.

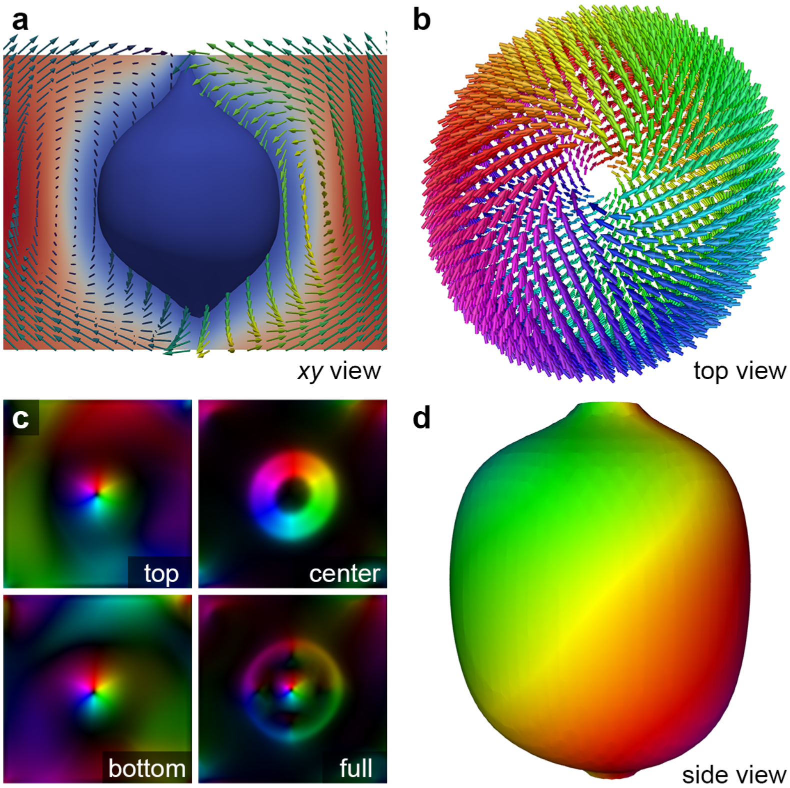

Figure 5.31: Topologically non-trivial bubble of type A. a, cross section overlayed with arrows. **b**, arrows representing the domain wall configuration. **c**, simulated TIE contrast for the layered and full model, respectively. **d**, iso-surface of maximum in-plane magnetization.

The first one is depicted in figure 5.31a, b, and d, where a cross section, as well as the domain wall represented by colored arrows, and the iso-surface of maximum in-plane orientation, are shown. These representations not only emphasize the strong variance of the domain wall along the thickness of the specimen, they also give insight to the local orientation of the magnetization. In the cross section to the left of the iso-surface of $-0.9m_z$ the arrows are colored purple, indicating an orientation into the page, whereas to the right, the arrows are colored yellow to green, indicating the opposite direction. This is true from the very top of the specimen to the bottom, which compels the same helicity at the top, in the center and at the bottom. This is, furthermore, corroborated by the matching swirl indicated by the arrows in figure 5.31b at the top and bottom. In figure 5.31c, the detailed analysis via layered TIE evaluation is presented. Matching helicities for both the vortices at the top and bottom, as well as the center region is confirmed. Thus, the evaluation of the full region yields ring-like contrast with a nested spot that is equivalent to the type A bubble observed in experiments.

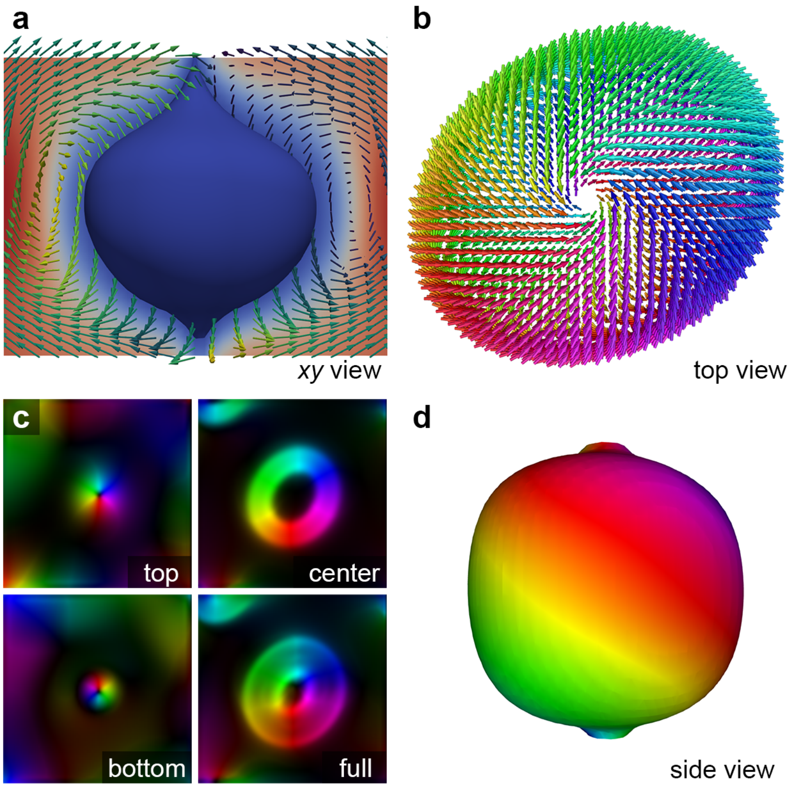

Figure 5.32: Topologically non-trivial bubble of type B. a, cross section overlayed with arrows. **b**, arrows representing the domain wall configuration. **c**, simulated TIE contrast for the layered and full model, respectively. **d**, iso-surface of maximum in-plane magnetization.

The second bubble analyzed in detail is shown in figure 5.32a, b, and d, using the same color schemes and format to allow ease of comparison. The general shape of the bubble matches the previous one, but the local orientation of the magnetization differs. Here, the magnetization to the right of the iso-surface, depicted in figure 5.32a, is pointing into the page at the top and center, but reverses the orientation at the bottom. To the left of the iso-surface, this behavior is mirrored but the orientation is locally inverted. From the top view, this inversion can be confirmed by an inverse direction of the swirl at the top and bottom. Simply put, the domain wall shows helicity reversal along the thickness. These results are corroborated by the TIE simulations, which depict inverse color contrast for the bottom layers compared to the central and top ones. The evaluation of the full thickness, thus yields a ring structure, which lacks contrast associated with the vortices, recreating the observed structure of the type B bubbles experimentally observed (section 5.2.4).

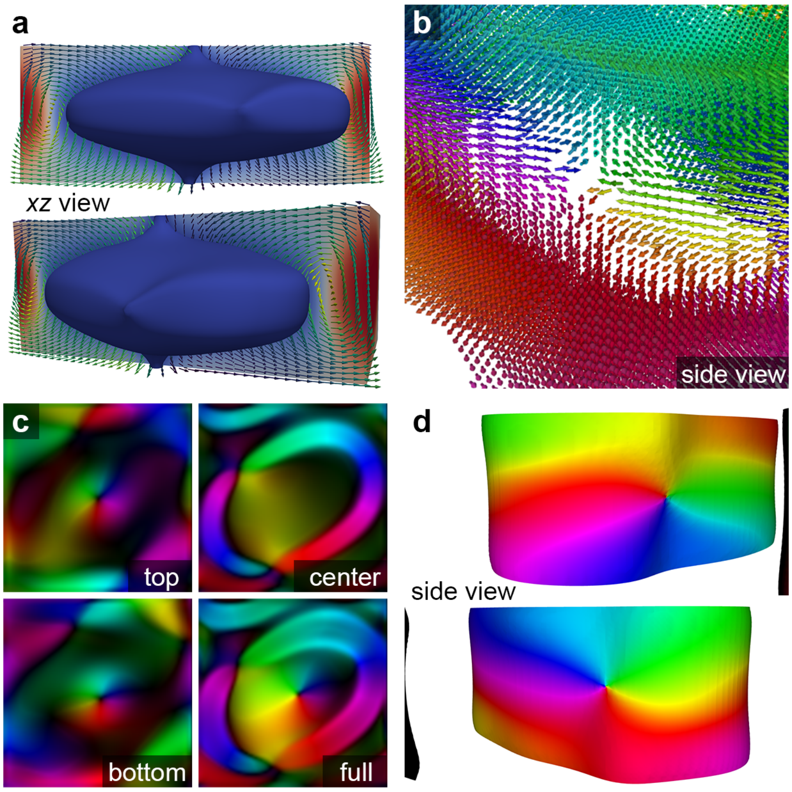

Figure 5.33: Topologically trivial bubble of type E. a, cross sections overlayed with arrows. **b**, arrows representing the domain wall configuration. **c**, simulated TIE contrast for the layered and full model, respectively. **d**, iso-surfaces of maximum in-plane magnetization.

Finally, a type II bubble, that is a topologically trivial bubble, is investigated. Using the same layout and color scheme as before, figure 5.33a, and d, show an altered shape. Trivially, it has a much larger equatorial region but excitingly, it has an additional texture on the iso-surface. The domain shows bulges on the $-0.9m_z$ iso-surface, which also appear on the colored iso-surface of maximum in-plane magnetization, i.e. the domain wall, as spots. These peculiar spots are Bloch points, which naturally occur in the domain walls of type II bubble domains in Fe_3Sn_2, due to the constraints for the orientation of the magnetization imposed by the helitity reversal in the Bloch lines and the Néel caps. A detailed explanation is given in section 2.2.3. In figure 5.33b, the region of the Bloch point is enlarged, where the singularity is marked for clearer visualization by the diverging orientation of the arrows. From the left and right, the magnetization meets head-to-head constricted by the helicity of the wall segments. From above and below, the magnetization is constrained tail-to-tail by the Néel caps. Additionally, being part of the domain wall, this yields a naturally occurring singularity in the magnetization, where the mismatch in orientation cannot be mitigated by any rotation. Note, a second Bloch point emerges in the second Bloch line, where the helicity constraints of the domain wall segments enforce the magnetization in a tail-to-tail configuration. Beyond the emergence of Bloch points, the type II bubble exhibits vortices analogous to the type I bubbles. TIE simulation-based analysis reveals, in this particular case these are of equal helicity, and thus, for the full thickness model nested spot-like contrast is observed. Therefore, the bubble is assigned type E according to the scheme in figure 5.25.

Summary for the layered evaluation of the helicity

Using the above three exemplary bubbles as representative cases, it is apparent that an understanding of any magnetic object requires a consideration of its 3D nature. Here, the understanding of the 3D nature allows the origin of the experimentally observed curious contrast signals to be deduced and understood. In order to properly formulate their behavior and assign them to their type, the bubbles cannot be described by one overall helicity assigned to them, instead, the helicity for each of the layers contributing to the observed contrast has to be denoted. In figure 5.34, the schematic for the naming convention is displayed. To fully describe a bubble domain, it is necessary to list the helicity

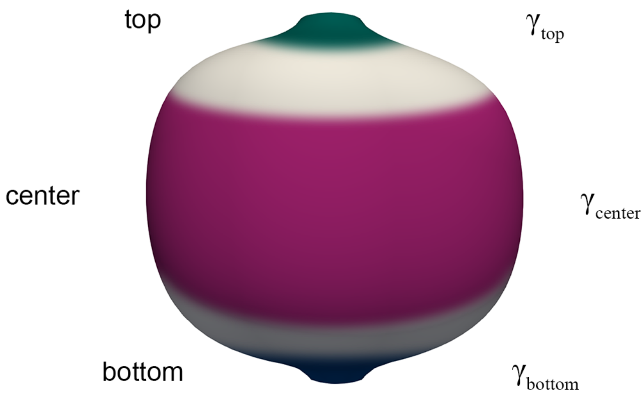

Figure 5.34: Schematic helicity of the top, center, and bottom region.

corresponding to the bulk region, γ_{center}, as well as the helicities for the top, γ_{top}, and bottom, γ_{bottom}, surfaces. Here, γ_{center} describes the domain wall in the bulk, which corresponds to the ring-like contrast. Whereas, γ_{top} and γ_{bottom} describe the helicities of the vortices at the corresponding surfaces. Evidently, whether they match or mismatch determines the occurrence of spot-like contrast nested within the ring.

Finally, this leaves one type of experimentally observed bubble domains unaccounted for, that is type C. This type is characterized by a ring of opposing helicity to the spot-like contrast in the center. That means both vortices, must exhibit the same helicity for the top and bottom surfaces, $\gamma_{\text{top}} = \gamma_{\text{bottom}}$, which are inverted relative to the bulk, i.e. γ_{center}. From the select few bubbles observed in the micromagnetic simulations this behavior was not reproduced. But this does not prove such a state cannot occur. Since the helicity reversal within the domain wall is confined to the near surface region of the vortex and occurs in several bubbles either at the top or bottom surface, it may as well appear on both surfaces for the same bubble. An additional challenge comes from the micromagnetic simulations themselves (as used here): they yield a single state as the final solution. As such this minimum energy state does not necessarily correspond to the global minimum in energy for a given parameter set. Furthermore, the observed final state is generally closely linked to the seed used. Thus, any other seed or the inclusion of additional perturbations from the experimental setup could foster the emergence of such bubbles.

For all Bloch-type domain walls the absolute value of the helicity is $|\gamma| = \pi/2$. Following the convention introduced in figure 5.34, topologically trivial and non-trivial bubbles can be discerned by γ_{center}. For type I bubbles the values $\gamma_{\text{center}} = \pm\pi/2$ occur. Type II bubbles exhibit two wall segments of opposing helicity and thus, no single values can be assigned to γ_{center}. The (mis)match of the helicity of the vortices at the top and bottom surface determines, whether these depict spot-like contrast. In table 5.4 all possible distributions of $(\gamma_{\text{center}}, \gamma_{\text{top}}, \gamma_{\text{bottom}})$ are assigned to the types of bubbles observed experiementally. Most bubble domains can be unequivocally identified

helicity	center γ_{center}	top γ_{top}	bottom γ_{bottom}
type A	$+\pi/2$	$+\pi/2$	$+\pi/2$
	$-\pi/2$	$-\pi/2$	$-\pi/2$
type B	$+\pi/2$	$+\pi/2$	$-\pi/2$
	$+\pi/2$	$-\pi/2$	$+\pi/2$
	$-\pi/2$	$+\pi/2$	$-\pi/2$
	$-\pi/2$	$-\pi/2$	$+\pi/2$
type C	$+\pi/2$	$-\pi/2$	$-\pi/2$
	$-\pi/2$	$+\pi/2$	$+\pi/2$
type D	-	$+\pi/2$	$-\pi/2$
	-	$-\pi/2$	$+\pi/2$
type E	-	$+\pi/2$	$+\pi/2$
	-	$-\pi/2$	$-\pi/2$

Table 5.4: Distributions of helicites assigned to the bubble types.

from experimental results: These are type A, type C and type E. Even their exact helicity configuration is discernible from the depicted swirl of the magnetization in TIE reconstructed induction maps. But some bubble domain types, namely type B and type D, remain degenerate with respect to their exact identification in experimental results as the contrast attributed to the top and bottom vortex cancels, their absolute helicity cannot be determined. That is to say, whether the top or bottom vortex exhibits helicity reversal relative to the core and respective other vortex cannot be determined for a type B bubble domain. Type B bubble domains are, thus, the only type which is obtained from four instead of two configurations. Peculiarly, this does not translate into more numerous occurrence of this type, as denoted for table 5.2. Hence, the emergence of any type is strongly influenced by the overall domain configuration, rather than a particular type being favorable in general. Simulated results corroborate this, as the reduced complexity in the model fosters the emergence of domains exhibiting simpler domain wall configurations.

5.2.6 Low Temperature Studies

Heritage et al. [263] demonstrated that in bulk Fe_3Sn_2 single crystals the uniaxial magnetocrystalline anisotropy undergoes a transition to easy-plane anisotropy below 250 K. The focus of this thesis is on lamellae of the same material at room temperature. This section addresses the question, how those observed properties change across this magnetic transition. Surprisingly, from MFM studies at room temperature and at 200 K, figures 5.10 and B.5, there is no evidence of substantial deviation in the domain morphology. However, MFM is limited to the observation of out-of-plane magnetization, thus, gradual changes, i.e. minor perturbations in domain size or shape, could be overlooked.

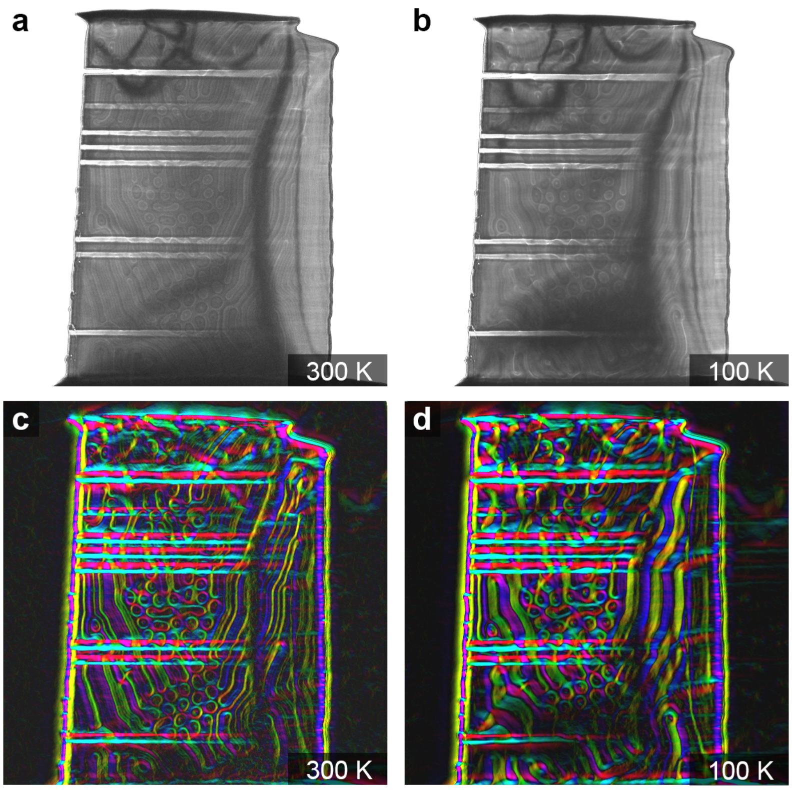

Figure 5.35: Temperature dependence in zero field. a, **b**, BF images, **c**, **d**, corresponding TIE reconstructed induction maps.

Exploiting the enhanced resolution of the TEM, temperature-dependent studies are conducted. Figures 5.35a and c depict the BF image and the corresponding TIE reconstructed induction map obtained at 300 K. Consistent with previous results a mixed state of bubble domains agglomerated in the center, surrounded by stripe domains along the edges of the lamella is observed. Figures 5.35b and d depict the corresponding BF, and TIE images at 100 K. Additionally, the intermediate steps of 250 K, 200 K, 150 K, and 120 K are shown in the appendix in figure B.22. The magnetic texture of the specimen remains almost unchanged upon cooling down to 100 K. This result is corroborated by literature [52], where negligible deviations in LTEM images were observed upon cooling from room temperature to 170 K. Furthermore, figure B.26 provides evidence in laterally confined specimen, discussed in section 5.3, the magnetic texture remains unperturbed upon cooling to low temperatures as well.

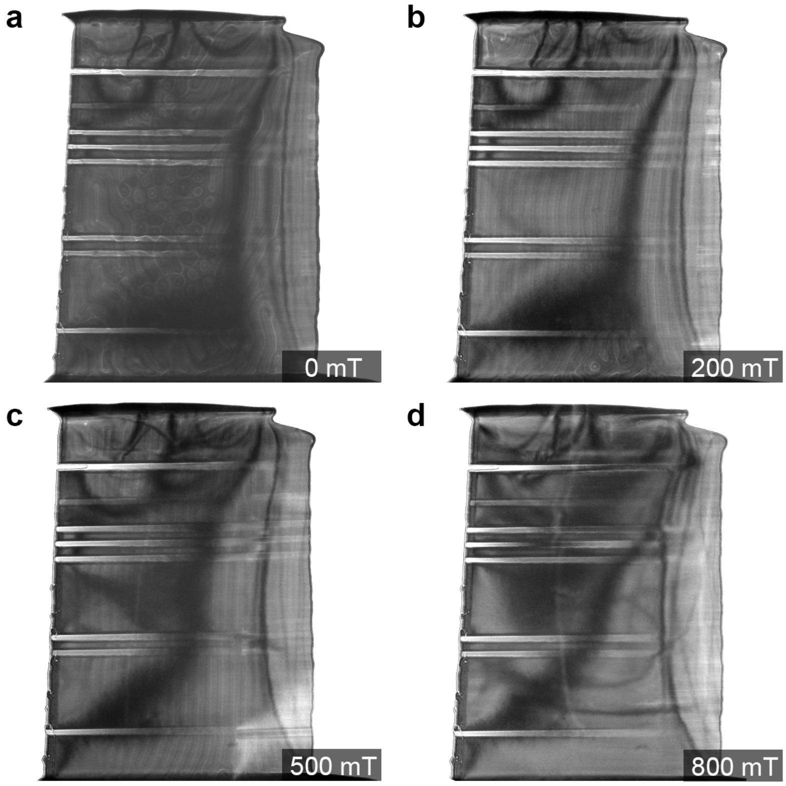

Figure 5.36: Field evolution at low temperature. a-d BF images obtained at $T = 94\,\mathrm{K}$.

Additionally, the field evolution is also revisited in the TEM at 94 K. Subsequent to thermal stabilization at 94 K, magnetic field up to 800 mT is applied. Due to limitations imposed by the use of the liquid nitrogen cooled single-tilt specimen holder, this assembly fosters in-plane domain configurations, coinciding with the projected in-plane field. Figure 5.36 presents BF images in zero field, 200 mT, 500 mT, and 800 mT. Intermediate 100 mT steps are shown in figure B.23 of the appendix. Most notably, the application of 200 mT is sufficient to stabilize an almost completely aligned stripe domain pattern. While the emergence of an aligned stripe domain pattern, matches the domain morphology for applied oblique field, the fact that all bubble domains vanish is peculiar. Compared to room temperature results, see figure 5.23, where an oblique field of 410 mT merely stabilized a mixed domain pattern, the field seems to be reduced by several hundred milli-tesla. Subsequently, the stripe pattern remains practically unperturbed up to a field of 500 mT. Applying fields exceeding 500 mT, the stripe domains vanish, giving rise to the mono domain state, which is reached between 700 mT and 800 mT.

In summary, lowering the temperature from 300 K to 100 K does not lead to a reconfiguration of the remanent ground state. The application of oblique field in contrast, does foster the formation of an aligned stripe pattern. Most curiously no bubbles are stabilized by the magnetic field. This behavior implies increased easy-plane anisotropy stabilizing stripe domains at 94 K, that are aligned with the projected in-plane component of the applied field. The caveat, that the application of severely oblique fields fostering the stripe domains cannot be ruled out. Hence, while the transition from an easy-axis to an easy-plane magnetocrystalline anisotropy is not sufficiently distinct to reconfigure the ground state in a lamella, enhanced easy-plane anisotropy is still likely at low temperatures.

5.3 Towards Functional Building Blocks for Applications

For the realization of functional building blocks for future applications in information technology, based on Fe_3Sn_2 or similar intermediate Q materials, it is important to meticulously understand the magnetic texture in detail enabling domain engineering. As such the preceding sections have focused on understanding and cataloging what magnetic objects emerge in Fe_3Sn_2, and looking at in-plane and out-of-plane magnetic components both experimentally and computationally. The major problems identified from this work for potential applications are: The ground state is represented by a maze-like stripe domain pattern, which is quasi random. Furthermore, a pure bubble phase, which is the most promising to encode data, e.g., for storage media, is realized only in static fields above several hundred milli-tesla. These problems were identified in laterally unconfined lamellae, and so this section considered whether lateral confinement can help to overcome these challenges.

5.3.1 Controlling Domain Configurations by Lateral Confinement

Introducing lateral geometrical confinement has been proven to influence the emerging domain pattern while simultaneously lowering the field required to stabilize the bubble domain phase [265]. Following this idea, a series of lamellae were shaped to laterally confine the magnetic texture in order to gain control over the exhibited domain patterns.

Stripe width as tuning parameter

The first one is an in-plane wedge shaped geometry depicted in figure 5.37a, where the lateral dimensions are measured via an AFM topography scan. Note, the ends to the left and right of the marked area are covered by platinum from the FIB deposition, making unperturbed MFM imaging of this region impossible. The lamella is of uniform thickness of 200 nm. Figure 5.37b depicts the

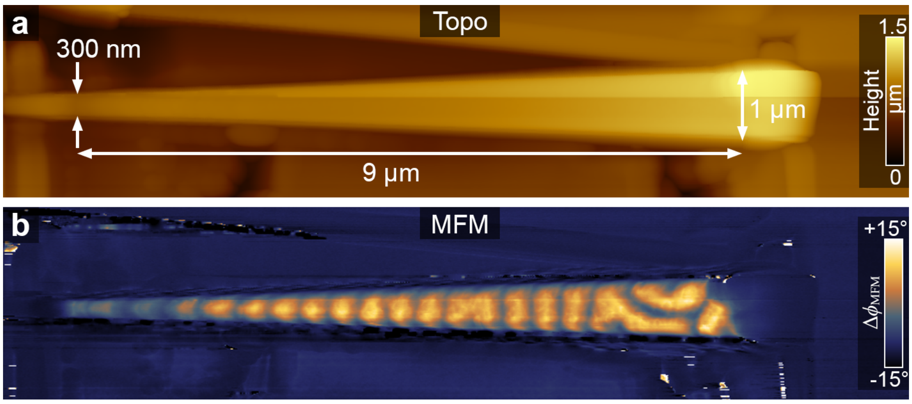

Figure 5.37: In-plane wedge-shaped lamella. a, topography scan revealing the dimensions. **b**, MFM image.

MFM image, where the phase shift corresponding to the out-of-plane magnetization is encoded by the color bar. On the narrow end, i.e. for width below

400 nm the observed contrast is rather weak, which is probably caused by the platinum contamination of the surface. In the intermediate range the lamella depicts an aligned arrangement of domains oriented perpendicular to the edges. For lamella widths exceeding approximately 900 nm, this pattern gives rise to the previously observed maze-like stripe domain patterns, e.g. in figure 5.7d. Hence, the intermediate range is of most interest to tune the shape of the domains. While towards the wider end these are clearly identifiable as stripes, towards the narrow end it is not so clear. At the narrow end it is not possible to discern whether the contrast of the stripe domains is perturbed at the edges, giving rise to bubble domain like contrast, or actual bubble domains form centered in the wedge-like lamella.

Stray-field coupled lamellae

Analogous, to the out-of-plane wedge, the gradual change of width gradually tunes the shape anisotropy. Thus, the formation of the domain pattern in the intermediate width range is verified by a second geometry. That is a stripe of similar dimensions and fixed width of 500 nm. Furthermore, a second stripe of the same dimensions is placed 500 nm apart. The corresponding topography image is shown in figure 5.38a. Consistent with the predictions, both stripe-like

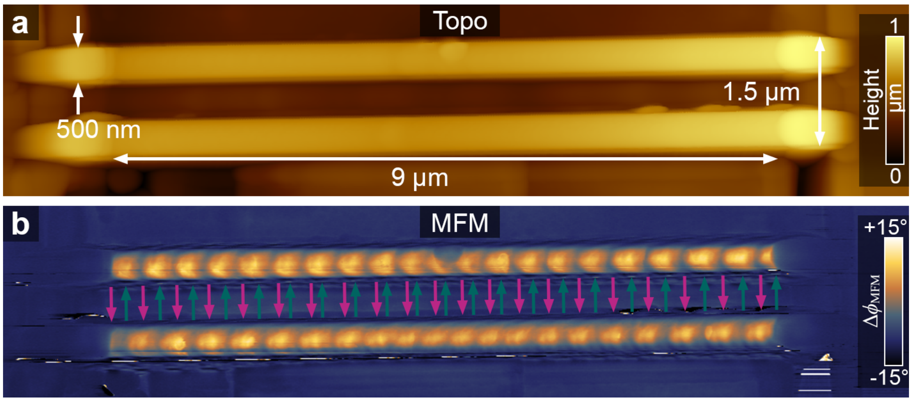

Figure 5.38: Stripe pair. a, topography scan revealing the dimensions. **b**, MFM image.

lamellae exhibit alternating domains pointing up and down along the c axis in the MFM image, see figure 5.38b. Analogous to the in-plane wedge-like specimen on the narrow end, it is not possible to discern whether these are bubble or stripe domains. However, upon close inspection the upper stripe depicts 20 domains of bright contrast and a partially covered one on the right, that are highlighted by the green arrows. The lower stripe exhibits the same number of bright domains, marked by the purple arrows, yet starts with an almost fully covered one. This is remarkable, as it indicates, that there is a correlation of the magnetic textures between both stripes leading to the formation of the alternating domain structure. This structure is the mutual energetically favorable state of the neighboring stripes. Based on this preliminary result, a stray-field coupler of domains seems feasible. Such a device enables electric field free domain motion in one array, driven by a coupled array, following established methods for induced domain motion (confer section 2.2.2, Spintronics).

Dynamics of domains

Focusing on the study of collectively moving the domain patterns, an additional aspect has to be considered: Bubble (stripe) domains are spaced based on their diameter (width) and the collective interactions with each other. Introducing the lateral geometrical confinement to a quasi 1D geometry, represented by the stripe, they form an alternating chain of up and down domains. However, any repellent interaction from the edges acting on bubble domains (pinning of stripe domains to the edges) on the ends of the stripe imposes an energy barrier to collectively move all domains towards or away from that edge. In order to overcome this artificial barrier, a ring geometry, see figure 5.39a, which is prototypical for a racetrack memory based on Fe_3Sn_2 [86] is prepared. Beyond

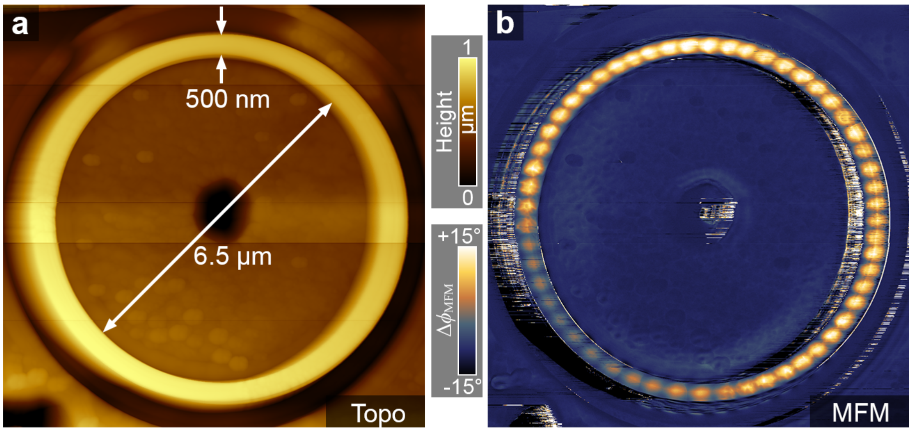

Figure 5.39: Ring structure. a, topography scan revealing the dimensions. **b**, MFM image.

eliminating the challenges associated with the ends of a stripe, the ring adds the curvature as an additional parameter. In the presented case, the ring has an inner diameter of 6.5 µm and retains a width of 500 nm all around. For the itinerant ferromagnet Fe_3Sn_2, the magnetic order is not expected to be coupled to the lattice. Hence, throughout the isotropic shape of a ring, domains should be able to form irrespective of the local mismatch of the constraining edges versus the crystallographic axes. Indeed, the alternating domain pattern is observed throughout the ring, as shown in figure 5.39b. Note, deviations in the MFM contrast of certain regions are attributed to the topography and scanning along one direction. This provides evidence that the introduction of curvature in quasi 1D geometries does not perturb the alternating domain pattern, making Fe_3Sn_2 a viable candidate to study complex racetrack geometries for memory applications. Furthermore, the reduced current densities required to collectively move the domain pattern, due to the eliminated ends of the race track, paired with the rigidity of the individual domains, allow to reduce the accelerator to a part of the track [86]. Based on the joint work with E. Lysne and colleagues a patent application is filed for such a partially accelerated racetrack memory [278]. In a successive step, stray field coupled acceleration, eliminating the need for biasing currents in the data carrying geometry entirely, could broaden the range of skyrmion host materials applicable in racetrack memories, while simultaneously spatially separating the energy dissipative acceleration from the information storage in the memory application.

While MFM has already been established as an excellent tool to image the out-of-plane magnetic textures in general (confer figures 5.7 and 5.11), it has major challenges when imaging non-planar specimen. Scanning artifacts arise along the edges of laterally confined lamellae, since, the height feedback loop cannot adjust to the steps in the topography quick enough under ideal imaging conditions for regions on the lamellae. Thus, employing MFM as a tool to study the dynamics of bubble domains in detail remains a challenging task. However, it seems feasible to image domains and possibly trace their movement performing non-contact single-pass scans with low-moment tips, as the stray field coupler demonstrates even in 500 nm distance the emergent stray fields are sufficiently strong.

LTEM studies of laterally confined lamellae

To tackle the challenges of MFM studies on complex geometries, LTEM seems to be an ideal technique, which is particularly useful for dynamic studies due to image acquisition times down to few tens of milliseconds. Furthermore, despite Fresnel fringing, magnetic contrast can often be well maintained close to the edges of the specimen, giving the possibility to distinguish between stripe and bubble domains. LTEM provides a high-resolution option to discern the exact shape of the domains in the quasi 1D confined geometries. For this purpose the lamella introduced in figure 5.3a, which exhibits a nested half ring structure, is investigated. The stripe width of the individual half rings is tapered. Thus, yielding a combination of the in-plane wedge-like and the ring structure.

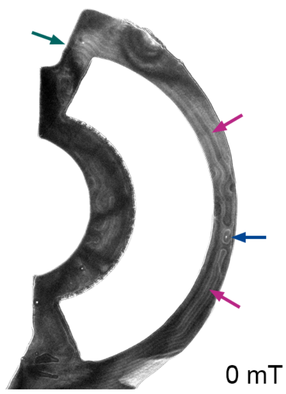

Figure 5.40: BF LTEM image of the nested ring structure. The arrows highlight domains.

Figure 5.40 depicts the BF image obtained in zero field. In line with previous observations for remanent states, relaxed from pure out-of-plane field, a mixed stripe and bubble domain phase is imaged, highlighted with the green, purple, and blue arrows, respectively. For the larger ring, a stripe domain centered on the specimen is observed (purple arrows). For intermediate width, it follows the curvature of the ring-like structure. In the center the stripe is intermittent by a single type I bubble domain (blue arrow). At the top, where the structure widens, additional stripe domains align parallel to the long stripe domain (green arrow). Peculiarly, here, the stripe ends are pinned to the edges. Despite, the Fresnel fringes partially obscuring the magnetic contrast, no severe pinning or other edge effects are observed. Magnetic contrast in the smaller ring is predominantly superseded by contrast attributed to strain. Additionally, field sweeps, shown in figure B.24 in the appendix, confirm the analogous field evolution of the domains to laterally unconfined lamellae.

Here, the focus lies on possible functional structures, stabilized by lateral geometrical confinement, and thus, determining the resilience of domain orientations stabilized by geometrical confinement versus external stimuli. That means, understanding whether the curved stripes following the curved geometries are reshaped by the projected in-plane fields applied or remain unperturbed. Elaborating on the inconsistent orientations of some stripes relative to the edges, remanent domain patterns obtained after applying oblique fields are investigated.

Resilience of confined domain structures versus magnetic field

In figure 5.41a three regions of interest are highlighted: The first one, marked purple, is the top end of the outer ring where the 940 nm wide end of the ring connects at an angle of 90° to a 600 nm wide stripe. The second region, is the center of the small half ring, which is marked blue. At the widest point this strongly curved stripe-like geometry is 980 nm wide. The third region of interest is the center of the large half ring, where the width is reduced down to 530 nm. Detailed measures for the full lamella are shown in figure B.1 in the appendix. Figures 5.41b, c, and d show the remanent domain pattern

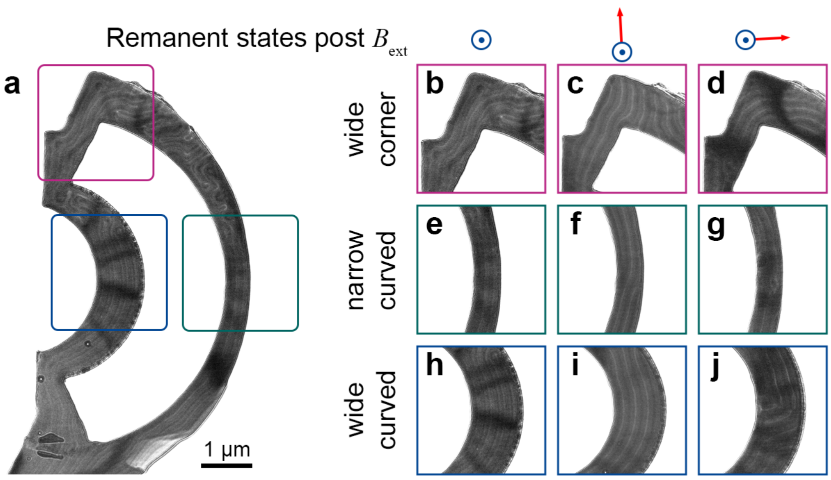

Figure 5.41: Remanent states post application of oblique field. a, BF image and reference for regions of interest colored purple, blue, and green. **b-j**, BF images for the regions of interest. The field has been applied as indicated above the columns.

for the first region of interest. For pure out-of-plane fields, a stripe pattern following the geometrical constraints is observed. Following the 90° corner, the stripes bend accordingly. For previous application of a field with an in-plane component along the vertical axis of the image, the stripe pattern in the wider arm aligns with the projected field. In the narrow arm the geometrical constraints preserve a slight mismatch. Applying the in-plane component of the field along the horizontal direction before imaging, this behavior is replicated. In the narrow arm the orientation of the stripes is preserved. Subsequently, they bend almost 90° before following the horizontal stripe pattern in the wider arm. This behavior is corroborated by the other two regions of interest. For the narrow curved region, see figures 5.41e, f, and g, the application of oblique field yields negligible perturbations of the domain pattern. All three remanent states depict domain patterns following the slightly curved geometry rather than the previously applied in-plane field. The center of the small half-ring is depicted in figures 5.41h, i, and j. It exhibits a curved domain texture following the geometrical constraints, in case out-of-plane field has been applied. If the in-plane component has been oriented along the vertical axis, the domain pattern appears unperturbed, as in the widest area the geometrical confinement favors the same orientation. Finally, if the in-plane component of the field has been oriented perpendicular prior to imaging, the central region depicts stripe domains following this direction.

The oblique fields, have been applied at angles $\alpha \approx \beta \approx 20°$, i.e. the projected in-plane component of the field amounts to approximately 35% of the few hundred milli-tesla applied in total. As a result, the lateral geometrical constraints imposed by a stripe width of 500 nm supersede the effect of the application of in-plane fields of at least up to 100 mT. Hence, narrow stripe-like geometries are ideal candidates to foster single chains of bubble domains in modest field. In other words, quasi 1D geometries of Fe_3Sn_2 facilitate the formation of rigid bubble domains, which could be used to encode data, in prototypical racetrack memories based on intermediate Q materials.

In summary, lateral geometrical confinement is a viable tool to tune the domain configuration. Quasi 1D confinement, i.e. narrow stripes of width below 500 nm, fosters the formation of a single domain centered in the geometry. These geometries are not limited to straight lines. Curvatures as well as sharp corners can be introduced, allowing the realization of prototypical geometries for racetrack memories and other applications. These stripe domains are stabilized versus in-plane field of at least 100 mT. Additional application of modest out-of-plane fields stabilizes a chain of bubble domains instead of the single stripe. Furthermore, by constraining wider areas with rectangular, or accordingly distorted edges, emergent bubble domains can be tuned to populate triangular or square lattices.

5.3.2 Towards Skyrmion Device Based Logic Applications

In addition to the stray-field coupler and ring structures for racetrack memories, applications like logic gates require another feature for data processing, that is a selector, or collector for functional magnetic objects[29]. Therefore, a Y-shaped lamella is FIB prepared to study the envisaged side selection of bubble domains. All corresponding measures for this geometry are given in figure B.2 in the appendix. In agreement with prior results, the lamella exhibits a mixed bubble and stripe domain pattern in zero field, which follows the established domain morphology in out-of-plane magnetic field at room temperature (figure B.25), and exhibits no deviations in the remanent state down to 100 K (figure B.26). Figure 5.42 shows the stabilized bubble domain pattern in 630 mT at room temperature. On the right, a triangular lattice of various bubble domains

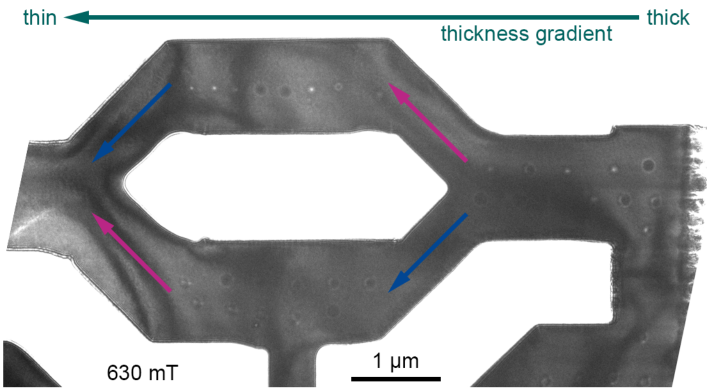

Figure 5.42: BF LTEM image of the Y-selector-collector. Imaged in 630 mT out-of-plane field.

is formed, whereas the lower arm depicts a square lattice. The upper arm, which is slightly narrower, exhibits a single chain of bubble domains. Note, in the angled sections, which are even narrower, lower fields are sufficient to stabilize the bubble domain chain, which is already expelled in 630 mT. This variation should be avoided for future proof of concept device applications, instead stripes of uniform width, and if required severely narrowed structural support structures, should be used.

In the prototypical Y-selector-collector geometry lateral motion of the bubble domains is driven by the thickness gradient and increasing external out-of-plane field. The reduced thickness towards the left in figure 5.42 drives the bubble domains in the same direction. This behavior is rooted in the reduced energy cost attributed to the Zeeman interaction of a smaller antiparallel oriented volume of the domain. The volume of the domains shrinks, due to the gradually narrowing height of the individual bubbles, that is proportional to the thickness, and the corresponding down-scaling of the diameter. Exploiting this driven motion yields only very limited lateral displacement before bubbles eventually dissolve. Furthermore, no incentives, besides a potentially favorable stripe due to geometrical mismatch, are given to actively select either path at the Y-junction. In contrast, upon exploiting STT by applying a biasing current $\boldsymbol{j}_{\mathrm{drive}}$ across the junction, the skyrmion hall effect could serve as the selecting rule. It is known that skyrmions and antiskyrmions exhibit an opposite Hall angles Φ [279], i.e. their velocities $\boldsymbol{v}$ deviate in opposing directions from the driving current $\boldsymbol{j}_{\mathrm{drive}}$. Furthermore, the Hall angle $\Phi(\gamma)$ of skyrmions depends on the helicity [280, 281]. For Bloch skyrmions, the Hall angle is $\Phi(\pm\pi/2) = 0$, which means they follow the direction of the current. For Néel and intermediate skyrmions $\Phi \neq 0$. These exhibit a deviating trajectory as depicted in figure 2.13, which can be used to select them in a side track. The coexistence of dipolar-stabilized skyrmions and antiskyrmions [140], as well as the tuneability of the helicity of individual skyrmions [282] have recently been demonstrated, highlighting a pathway to utilize a STT driven Y-junction as a functional building block for logic architectures.

6

Conclusions

Numerous challenging demands arise for novel information technology, ranging from upscaleability of manufacturing to improved functionality. For memory applications, this means higher information density and superior access times, while reducing the power consumption. To achieve such advances in technology, profound understanding of the elementary building blocks in these devices is required. One particular paradigm of novel memory devices is based on spintronics [21–23]. Topologically protected spin textures, like skyrmions, are of special interest for spintronics based memory applications, as spin-transfer torque can be exploited for writing individual bits and data transfer [283–287]. First concepts for such memories have been proposed over a decade ago [172, 173, 288], yet no spintronics-based memory device is available commercially up to now. This is predominantly owed to the challenges of miniaturization with the added complexity of working with extremely sensitive skyrmion host materials.

This work focuses on fundamental research aspects of mesoscopic spin textures motivated by the development of functional building blocks for spintronics applications. For this purpose, Fe_3Sn_2 is chosen as a promising candidate material and its complex magnetic patterns are investigated by magnetic force microscopy and Lorentz transmission electron microscopy. Corroborating micromagnetic simulations are used to model the three-dimensional magnetic textures observed by these imaging techniques. The results obtained in this thesis elucidate the following fundamental questions posed in the introduction:

i) What magnetic objects emerge in Fe_3Sn_2?

Microscopy studies reveal a maze-like pattern of alternating out-of-plane magnetized stripe domains as the zero-field virgin state of focused ion beam (FIB) prepared Fe_3Sn_2 lamellae. In the bulk of the lamellae, i.e. away from the exposed large surfaces, these are separated by Bloch-type domain walls of helicity $\gamma_{\mathrm{center}} = \pm\pi/2$, whereas at the top and bottom surfaces the material exhibits Néel caps and partial flux-closure. Coinciding with the uncapped regions of the partial flux-closure structures, vortices are observed.

In finite magnetic fields, and in the remanent state after field cycling, bubble domains emerge. These can be distinguished as topologically trivial (type

II) or non-trivial (type I, skyrmionic) by the shape of their domain wall in the center region. Towards the surfaces all bubble domains exhibit Néel caps and the vortices attributed to partial flux-closure. From the bright field (BF) images, and transport of intensity equations (TIE) reconstructed induction maps, five types of bubble domains are discerned. Simulated three-dimensional spin textures reveal that these are the result of composite magnetic objects, which comprise the central region, that is the Bloch-type domain wall, and the two caps. The central region may be assigned a helicity $\gamma_{\mathrm{center}} = \pm\pi/2$, and the caps representing the two characteristic vortices at the top and bottom surfaces are assigned $\gamma_{\mathrm{top}} = \pm\pi/2$ and $\gamma_{\mathrm{bottom}} = \pm\pi/2$. In Fe_3Sn_2 these three parts can exhibit helicities independently, leading two eight different composite domains of non-trivial topology. Based on their exact composition $(\gamma_{\mathrm{center}}, \gamma_{\mathrm{top}}, \gamma_{\mathrm{bottom}})$ these skyrmionic bubble domains are classified in three types: Those assigned the same helicity throughout (type A), those where the top and bottom cap exhibit opposite helicities, leading to cancellation of contrast in BF images (type B), and those where the helicities of both caps are reversed relative to the center region (type C). Additionally, topologically trivial bubbles lacking a defined helicity γ_{center} are classified by the opposite (type D) or matching (type E) helicities of the caps.

Furthermore, the domain walls of type II bubbles and most stripe domains in Fe_3Sn_2 naturally give rise to Bloch points. Where the Bloch wall segments of opposing helicities in the bulk of the specimen meet head-to-head or tail-to-tail, Bloch lines emerge mitigating the helicity mismatch. The Néel caps on the opposing surfaces dictate antiparallel alignment of the magnetization at either end of the Bloch line, thus a Bloch point must emerge along the one-dimensionally constrained spin texture.

ii) How is the stability of these magnetic objects influenced by geometrical confinement?

The observation of unperturbed stripe and bubble domains is limited by the geometry of the investigated specimen. Most notably, the thickness of the specimen influences the magnetic texture stringently, while lateral confinement above a threshold size has no notable effect. Focusing on the study of specimen unperturbed by lateral confinement, bulk specimen of thicknesses exceeding tens of microns reveal domain branching. In contrast, the introduction of geometrical confinement via FIB cut lamellae of defined thickness validates Kittel scaling for both stripe and bubble domains below the critical thickness of 2.7 µm, above which domain branching sets in. Below a minimum thickness of approximately 100 nm, the formation of alternating out-of-plane magnetized domains is superseded by in-plane flux-closure domains.

Lateral confinement, when introduced on the same order of magnitude as the spin textures, can be exploited to shape the domain pattern. By introducing quasi one-dimensional constraints, chains of bubble domains or stripe domains can be constrained in both straight and curved geometries. Such geometries effectively resemble prototypical race-track memory layouts.

Within the above mentioned limits, severe step-like perturbation in the specimen thickness are demonstrated to act as pinning sites for bubble domains. Furthermore, topologically non-trivial bubbles are prone to emerge in the vicinity of these steps, whereas gradually sloped thickness variations, as well as uniform regions, foster the emergence of type II bubbles.

iii) How are the magnetic objects affected by external magnetic fields?

In addition to geometric confinement, static magnetic field is the determining parameter to influence the domain type. Applying finite out-of-plane fields to planar FIB cut lamellae exhibiting antiparallel stripe domains, these domains gradually narrow and eventually transform to bubble domains. In modest fields, a mixed phase of domains is observed, whereas towards higher fields (>600 mT), a pure bubble domain phase is realized. The latter is further discerned, by the coexistence of topologically trivial and non-trivial bubble domains, and a small field range, where type I bubbles persist exclusively.

Applying static magnetic fields in oblique orientations, the projected in-plane field fosters parallel alignment of the in-plane magnetization within the domain walls. Thus, stripe domain patterns can be oriented parallel to the applied in-plane component of the field. Additionally, the application of oblique fields stabilizes type II bubbles. Hence, by tuning the exact strength and mismatch pure type II bubble domain phases can be realized. On a technical side note relevant towards application, domain configurations imposed by lateral confinement are rigid versus the application of in-plane fields up to 100 mT.

iv) Which device geometries can be useful for future applications?

Lateral confinement introduced via FIB cut patterning of thinned lamellae has proven to be a valuable tool to study prototypical geometries for functional building blocks. Beyond limiting the magnetic textures to confined quasi one-dimensional geometries, the FIB enables the ability to prepare coupled structures or precisely patterned junctions.

Building on the concept of prototypical race-track memory via lateral confinement, ring structures overcome pinning at the ends of stripe-like geometries, lowering the energy barrier to collectively move the domain patterns. Furthermore, for a pair of straight stripes, a stray-field coupled domain pattern emerges, implying the possibility to separate the acceleration of a racetrack memory and the information storage into two separate tracks. A prototypical Y-selector-collector geometry foreshadows potential use in logic gate applications.

Combining results form literature and the detailed study of micromagnetic texture in Fe_3Sn_2 presented in this thesis, the material and its properties are well elucidated. It serves as a model system for host materials of topologically non-trivial spin textures stabilized by the competition of the dipole-dipole interaction and the uniaxial magnetocrystalline anisotropy, but also for a wider range of intermediate Q materials. Prototypical behavior investigated in detail is thus expected to be applicable in a larger range of similar systems.

From a microscopy perspective, Fe_3Sn_2 reveals an abundance of interesting properties on imageable length scales, corroborating its role as a model system for the investigation of phenomena relevant for future applications. Among those, are the dynamics of the skyrmionic and trivial bubbles on prototypical race-track memories and side selectors, which can ultimately help design skyrmion based logic architectures and thus expand the applications beyond binary encoding of data for memory. However, commercial skyrmionic applications based on Fe_3Sn_2 are difficult in practice due to the limited potential to miniaturize the individual domains. The Bloch points and lines occurring spontaneously in this material, indeed show the potential to control and study interesting dynamics at the appropriate scale, paving the way for further studies in a new and exiting field.

Appendices

A

Topology

Beyond the illustrative description of topology given in section 2.2.1 on the example of a two dimensional planar system, here a mathematically more precise description is given. As a brief recapitulation, in an ordered medium every point $\boldsymbol{r}$ in real space can be mapped into order-parameter space by a function $f(\boldsymbol{r})$. Mapping closed contours in real space yields closed contours in order parameter space, as illustrated in figure 2.10. Two mappings are homotopic, i.e. topologically equivalent, if their contours in order parameter space can be continuously transformed into each other (confer $f_1(\boldsymbol{r})$ and $f_3(\boldsymbol{r})$ in figure 2.10a and c).

More precisely, a one parameter continuous family of maps $h_t(\boldsymbol{r})$ exists, where $t \in [0,1]$ is the index parameter and the limits are $h_0 = f_1(\boldsymbol{r})$ and $h_1 = f_3(\boldsymbol{r})$. Such a family of maps is called a homotopy. Evidently, many other mappings, not contained within one particular homotopy, are homotopic to each other as well. All these homotopic mappings form a homotopy class C, and all possible classes subsequently form a homotopy group G. Each group G has to fulfill the group axioms and has an operation denoted by "$\bullet$". It also has to be abelian with respect to this operation, meaning:

$$a \bullet b = b \bullet a. \tag{A.1}$$

For the group of homotopy classes of mappings $f(\boldsymbol{r})$, the group operation is defined by sequential evaluation of individual contours. Simply put, evaluating one contour and subsequently a second one, yields the same result as evaluating a large contour encircling both or reversing the order of evaluation.

Coming back to the illustrative example of the planar order parameter, the group G is denoted by $\pi_1(S^1)$, the first homotopy group for all mappings $f : S^1 \mapsto S^1$. This group is isomorphic to the group of integer numbers $\mathbb{Z}$, i.e. exactly one element of the first group (a homotopy class C) can be assigned to exactly one element of the second (an integer value), and no integer in the second class remains unassigned. The isomorphism between $\pi_1(S^1)$ and $\mathbb{Z}$ is given by the assignment of the winding number w (equation 2.70). Such an isomorphism is not universally given for all mappings, hence the assignment of a winding number is limited so special cases. As a consequence, each mapping $f_i(\boldsymbol{r})$ resulting in the same winding number belongs to the same homotopy class and is therefore termed topologically equivalent.

Generally, all mappings belonging to a homotopy class assigned $w \neq 0$ are termed topologically protected. They cannot be transformed to the trivial state as the local surgery required for such a transformation requires infinite energy. The same applies for transitions in between any two homotopy classes. Note, in the examples given in figure 2.10 the real space contours enclose singularities located at the point P. Effectively describing the topological protection of what is known as a defect in physics.

The planar two-dimensional case serves as an excellent example to illustrate the basic concepts, however these concepts are not limited to such highly constraint geometries. In principle any n^{th} order sphere S^n can be mapped into the order parameter space F,

$$f : S^n \mapsto F, \tag{A.2}$$

yielding an according group of mappings $\pi_n(F)$. All these groups have topologically non-trivial or protected elements, if at least one class of homotopies does not contain the uniform state. Distinguishing between the classes via the assignment of a winding number is limited to certain cases. Fortunately, if the order parameter space is given by a sphere of dimension n, the n^{th} homotopy group is isomorphic to the group of integers [111]

$$\pi_n(S^n) \cong \mathbb{Z}. \tag{A.3}$$

Hence mapping $f : S^n \mapsto S^n$, a winding number can be assigned to all classes of the group $\pi_n(S^n)$. A particularly relevant trait, if the order parameter has a constant magnitude, as it generally maps to a respective n-sphere.

This fact, strongly impacts the consideration of magnetic phenomena discussed in this thesis. In the micromagnetic framework, the order parameter is assumed to be of constant magnitude and free orientation in three dimensional space, thus resulting in the order parameter space being the surface of an ordinary sphere (S^2) with radius M_s. However, the assignment of a winding number, requires the real space contour mapped, to be a sphere of second order as well. This is not trivial, as generally real space, characterized by three orthogonal vectors, i.e. $\mathbb{R}^3$, is studied and has to be mapped fully. For simplicity, the consideration is limited to a two-dimensional case here. This is equivalent to the assumption of the spin orientation being unperturbed along one axis. An assumption not too far-fetched in case of a thin platelet with strong PMA for example, where the domain walls are perpendicular to the surface as well. In such cases it is sufficient to evaluate the topological stability only for the surface plane or a similar plane in the depth. Yet simply reducing the problem to $\mathbb{R}^2$ is not sufficient. Additionally, a stereographical projection of $\mathbb{R}^2$ to a sphere-like object, a punctured sphere, is required. This projection works only if the order parameter asymptotically reaches a constant value η as $|\boldsymbol{r}| \to \infty$, and the real space plane is projected onto a sphere with a missing point ($\mathbb{R}^2 \mapsto S^2$). Mapping the punctured sphere, representing all of real space, to order parameter space finally yields $f : S^2 \mapsto S^2$, and thus the group $\pi_2(S^2)$, where a winding number can be assigned to all homotopy classes. Note, here all of real space is mapped at once. Hence the real space curvature is no longer limited to enclose singularities. In other words, topological protected objects ($w \neq 0$) are no longer limited to defects.

Summed up, every point of an ordered medium in real space can be mapped to order parameter space. Mapping a closed contour, enclosing a defect or representing all of $\mathbb{R}^2$ via a stereographical projection, yields a closed contour in order parameter space as well. These mappings are homotopic, i.e. topologically equivalent, if they can be continuously transformed into each other by local surgery. For certain special cases the mapped contours can be classified by the amount of times they wrap the order parameter space, hence assigning the respective winding numbers. Within one class, all mappings are homotopic and have the same winding number. The class assigned $w = 0$ contains the trivial uniform state. Transitions in between homotopy classes are forbidden, i.e. associated with an infinite energy barrier, from a purely mathematical view point. Hence, objects with an assigned winding number $w \neq 0$ are termed topologically protected.

B

Experimental Data

B.1 Focused Ion Beam Scanning Electron Microscopy

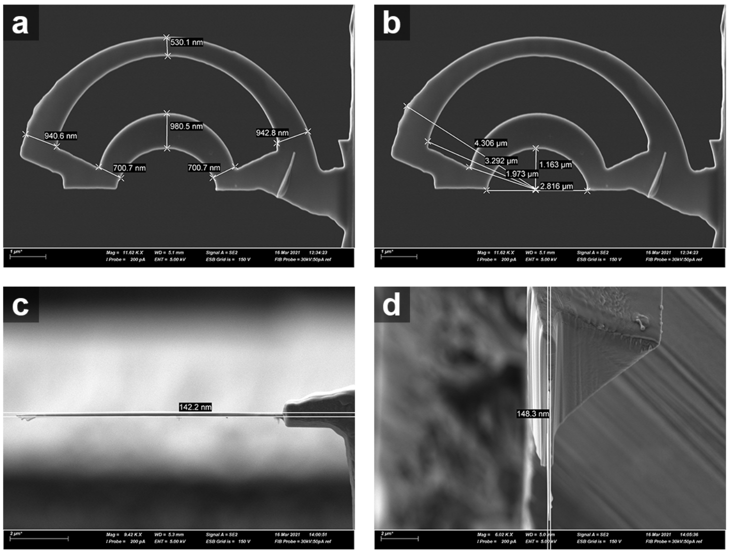

Figure B.1: Dimensions for the nested half ring.

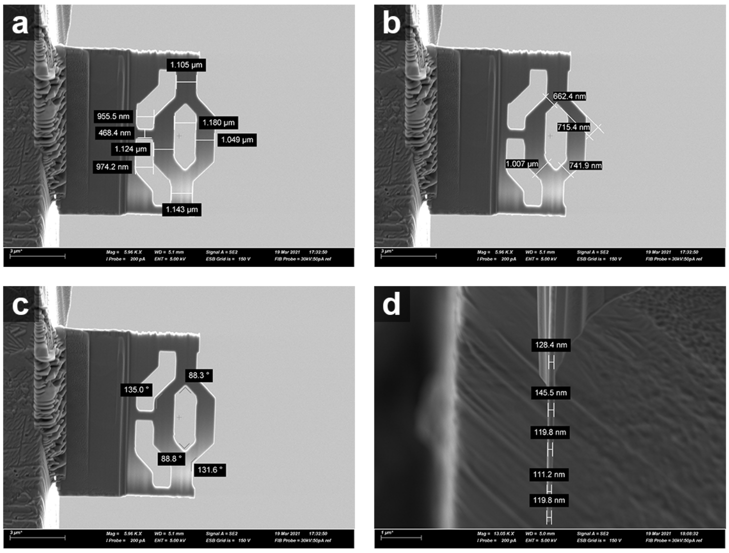

Figure B.2: Dimensions for the Y-selector-collector.

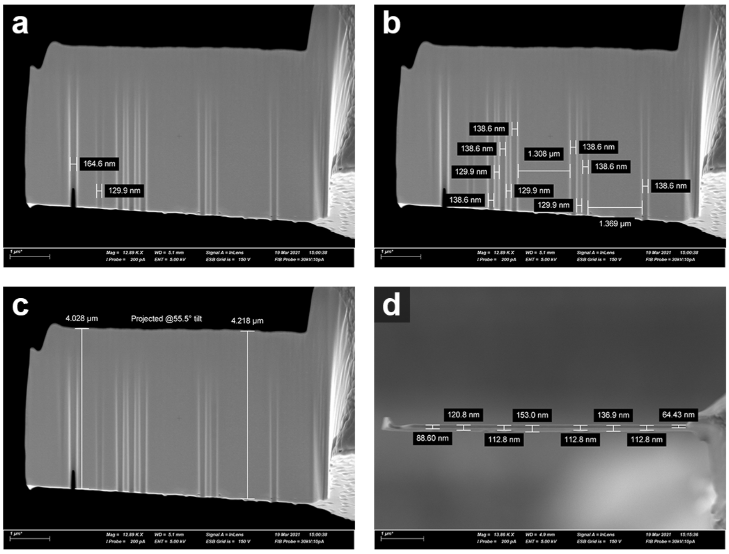

Figure B.3: Dimensions for the thickness grating.

B.2 Magnetic Force Microscopy Data

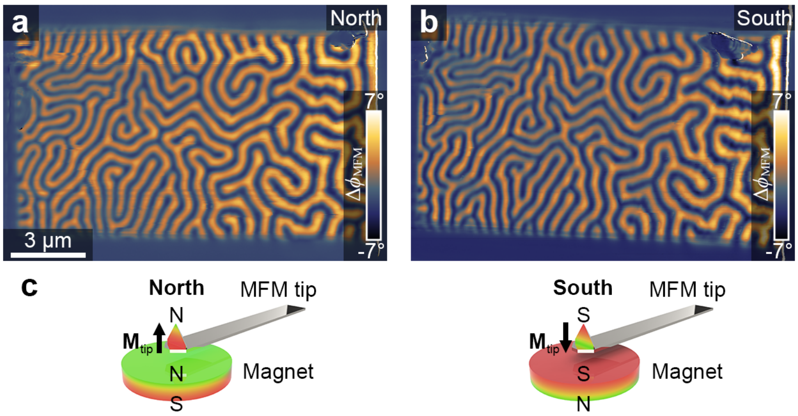

Figure B.4: Inversion of MFM signal via tip magnetization reversal. **a**, MFM image with tip magnetized "north". **c**, MFM image with tip magnetized "south". **c**, schematic tip magnetization. Schematic in **c** reproduced form [86].

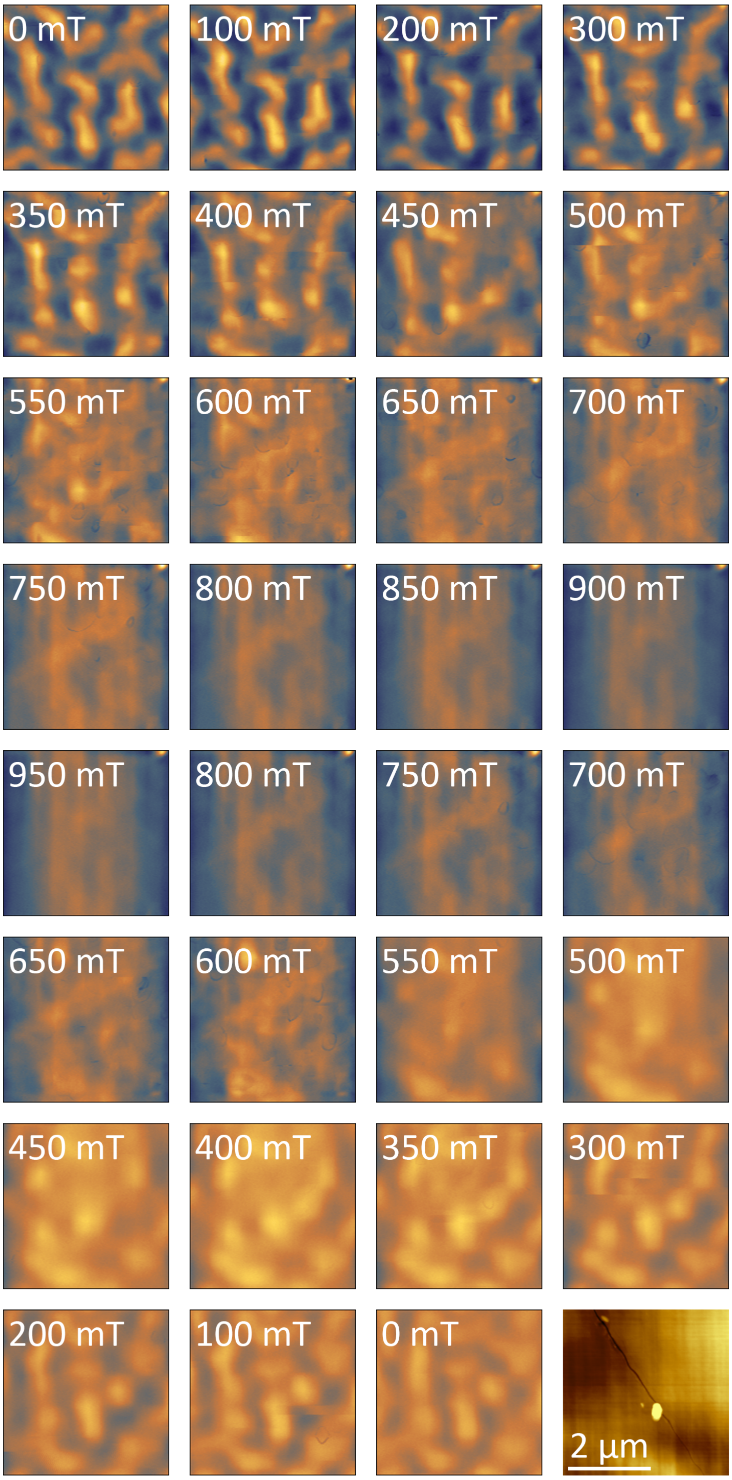

Figure B.5: Field evolution at low temperature. MFM images obtained in 50 mT, respectively 100 mT steps at 200 K on a 450 nm thick area. Reproduced with permission from [54].

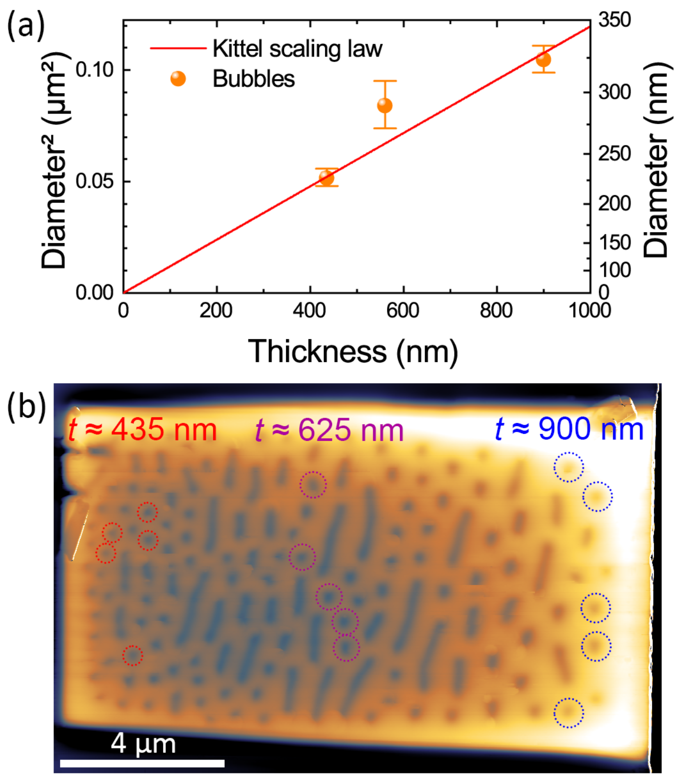

Figure B.6: Scaling of bubble domains. **a**, Kittel scaling of representative bubble domains emerging due to the application of a static magnetic field of 450 mT along the out-of-plane direction. **b**, overview of the selected bubbles and corresponding approximate thickness. Reproduced with permission from [54].

B.3 Transmission Electron Microscopy Data

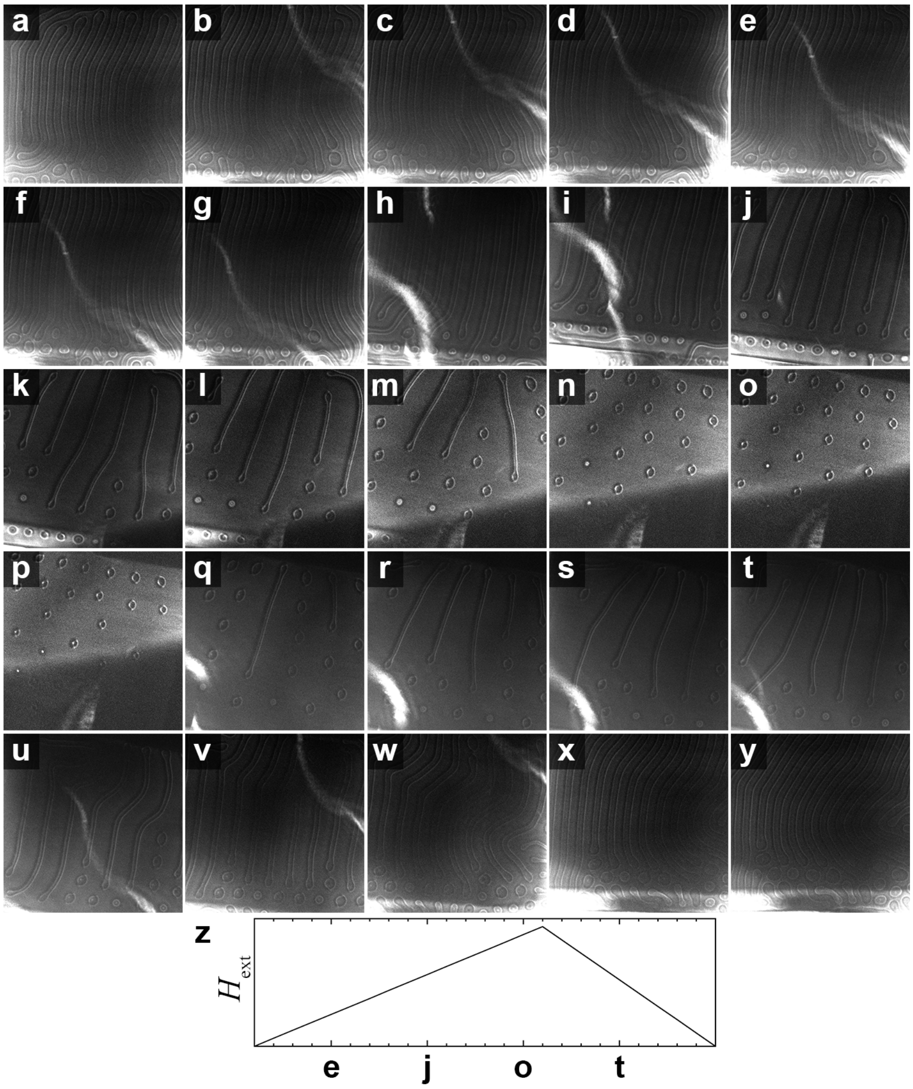

Figure B.7: Full field evolution representing the domain morphology. **a-y**, BF images of the same area with respective out-of-plane field applied. **z**, schematically plotted corresponding field strength for panels **a-y**.

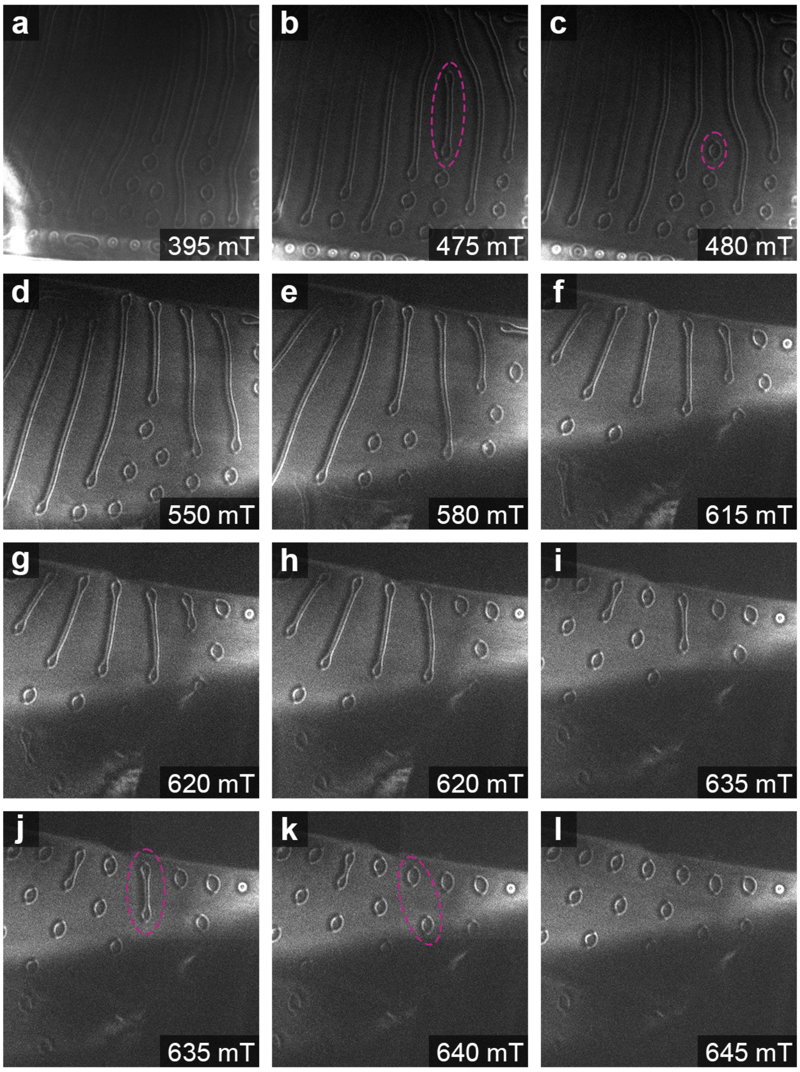

Figure B.8: Full field evolution for the morphology of bubble domains. a-i, BF images of the same area with respective out-of-plane field applied. The marked domains correspond to the highlighted ones in figure 5.15.

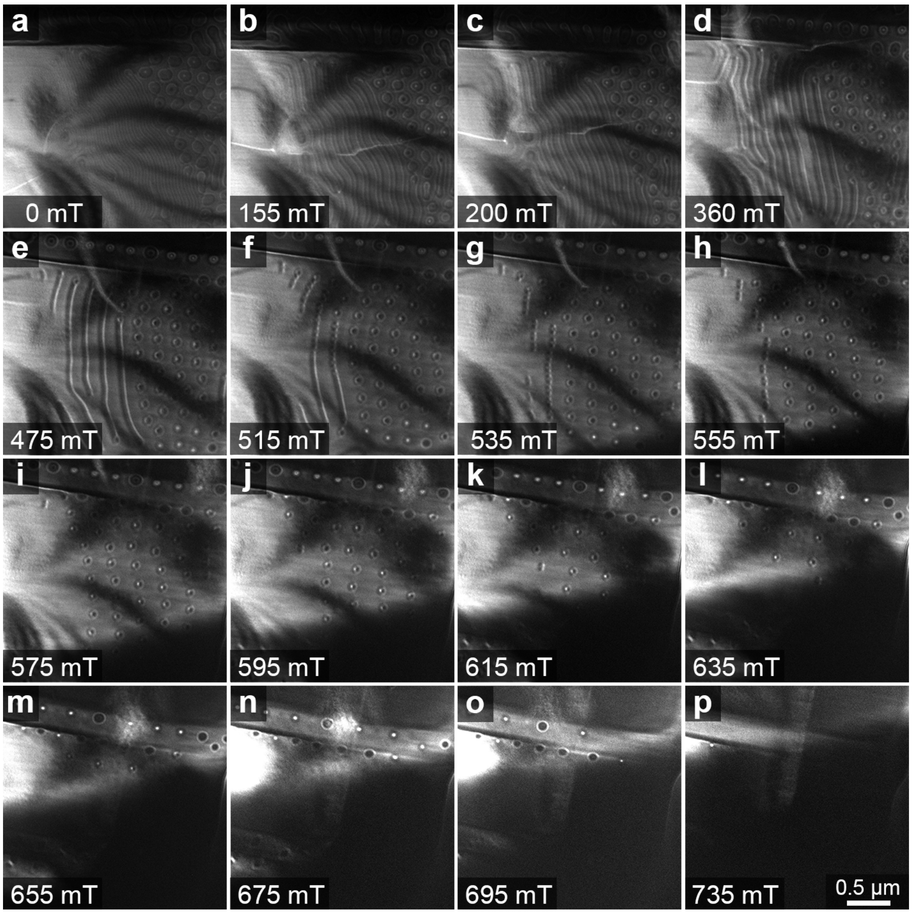

Figure B.9: Detailed field evolution of the stepped and wedged lamella. a-p, BF images of the same area with respective out-of-plane field applied.

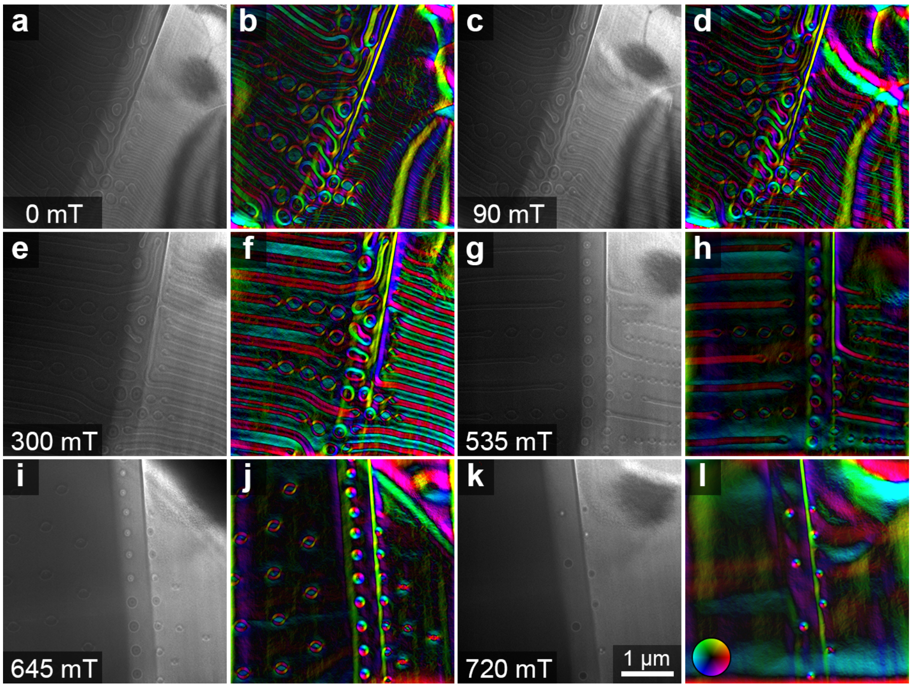

Figure B.10: Side by side comparison of BF and TIE images. **a**, **c**, **e**, **g**, **i**, **k**, BF images. **b**, **d**, **f**, **h**, **j**, **l**, corresponding TIE reconstructed induction maps.

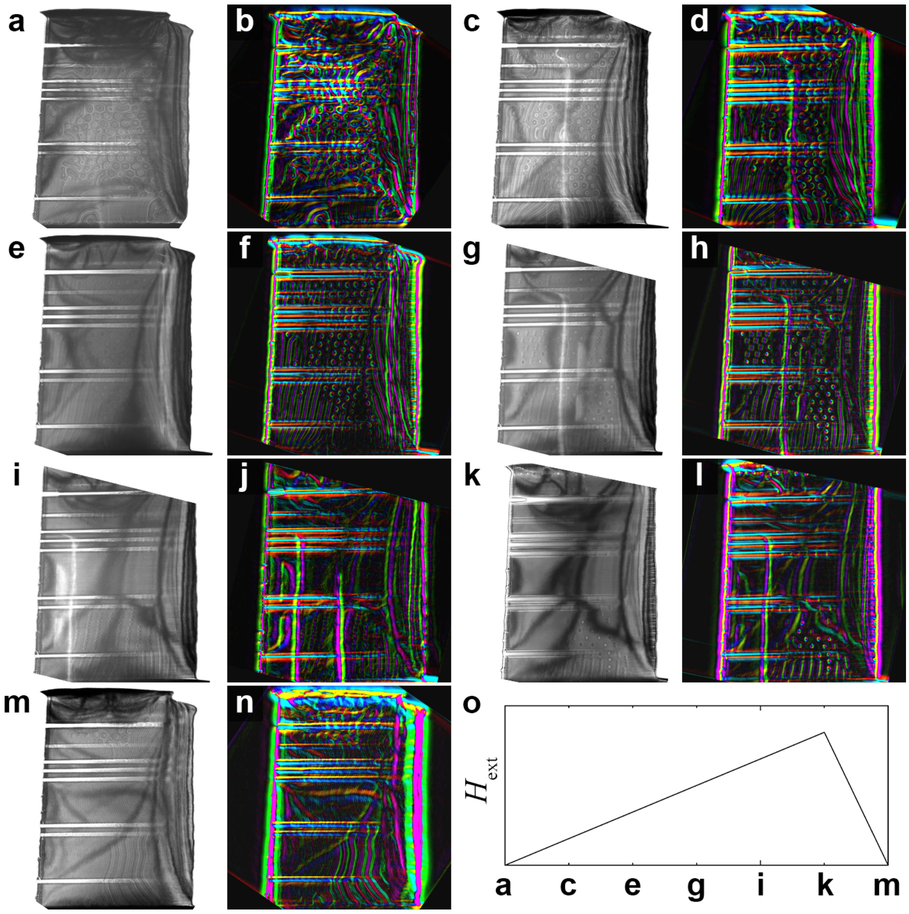

Figure B.11: Detailed field evolution of the grated lamella. a, **c**, **e**, **g**, **i**, **k**, **m**, BF images. **b**, **d**, **f**, **h**, **j**, **l**, **n**, corresponding TIE reconstructed induction maps. **o**, schematic field evolution.

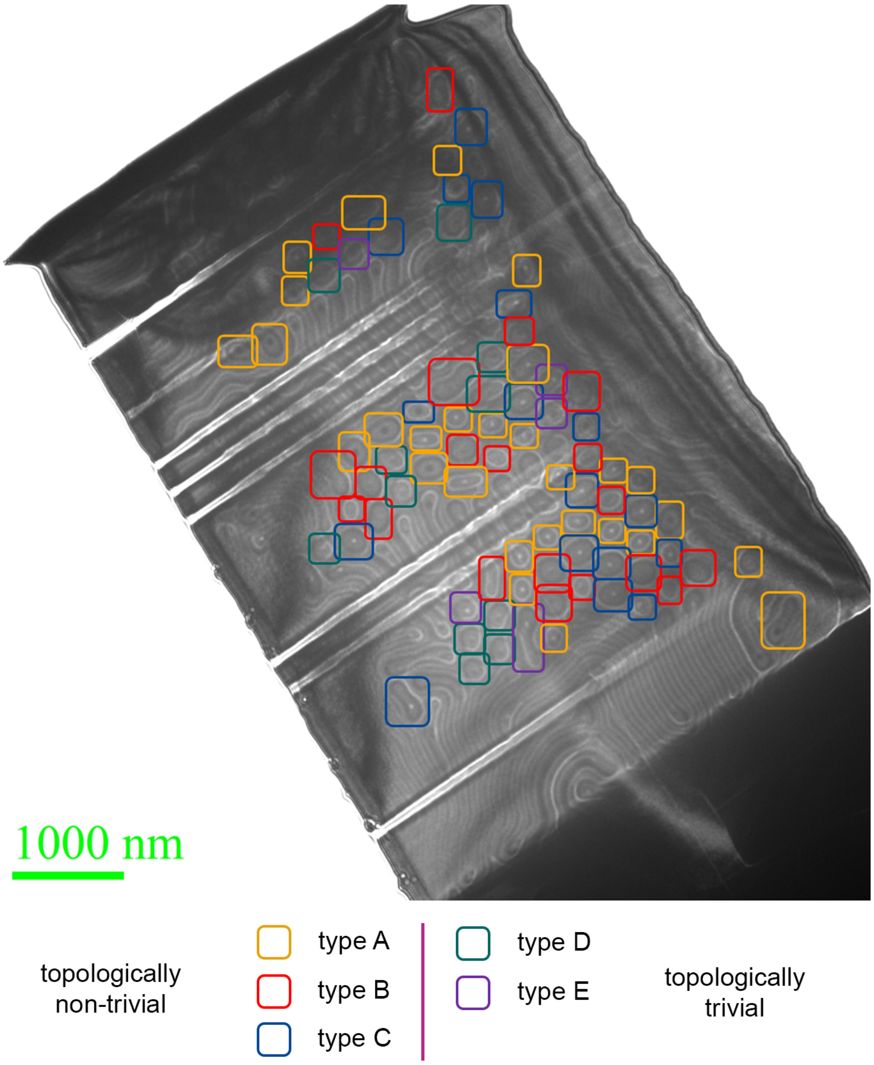

Figure B.12: Marked bubbles L23A. BF image in zero field.

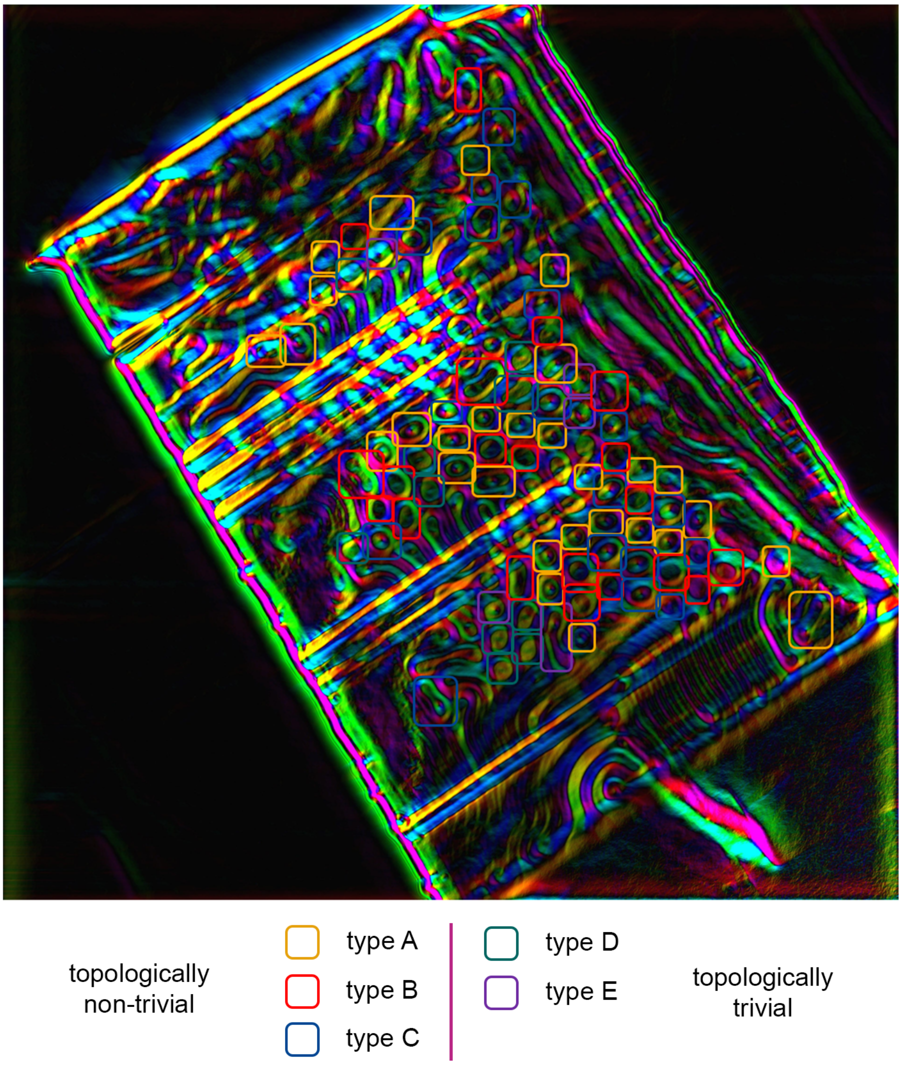

Figure B.13: Marked bubbles L23A. TIE reconstructed induction map in zero field.

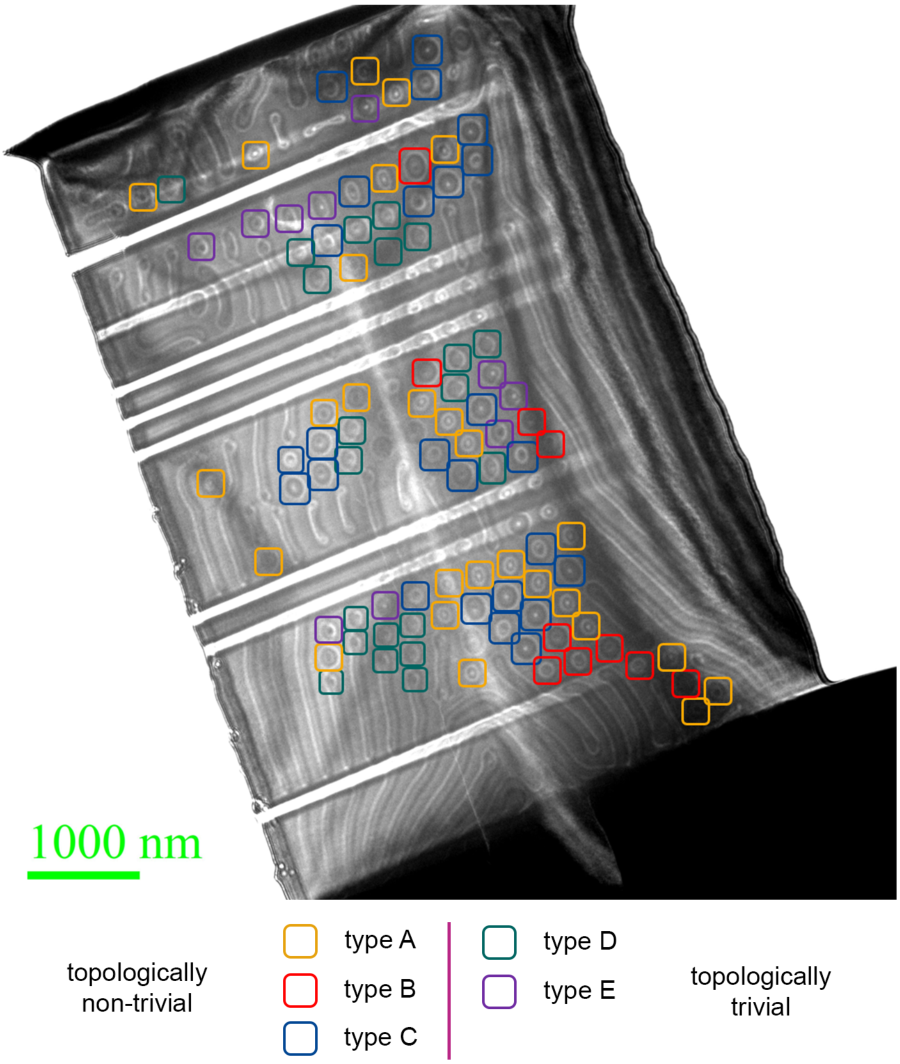

Figure B.14: Marked bubbles L23A. BF image in 320 mT.

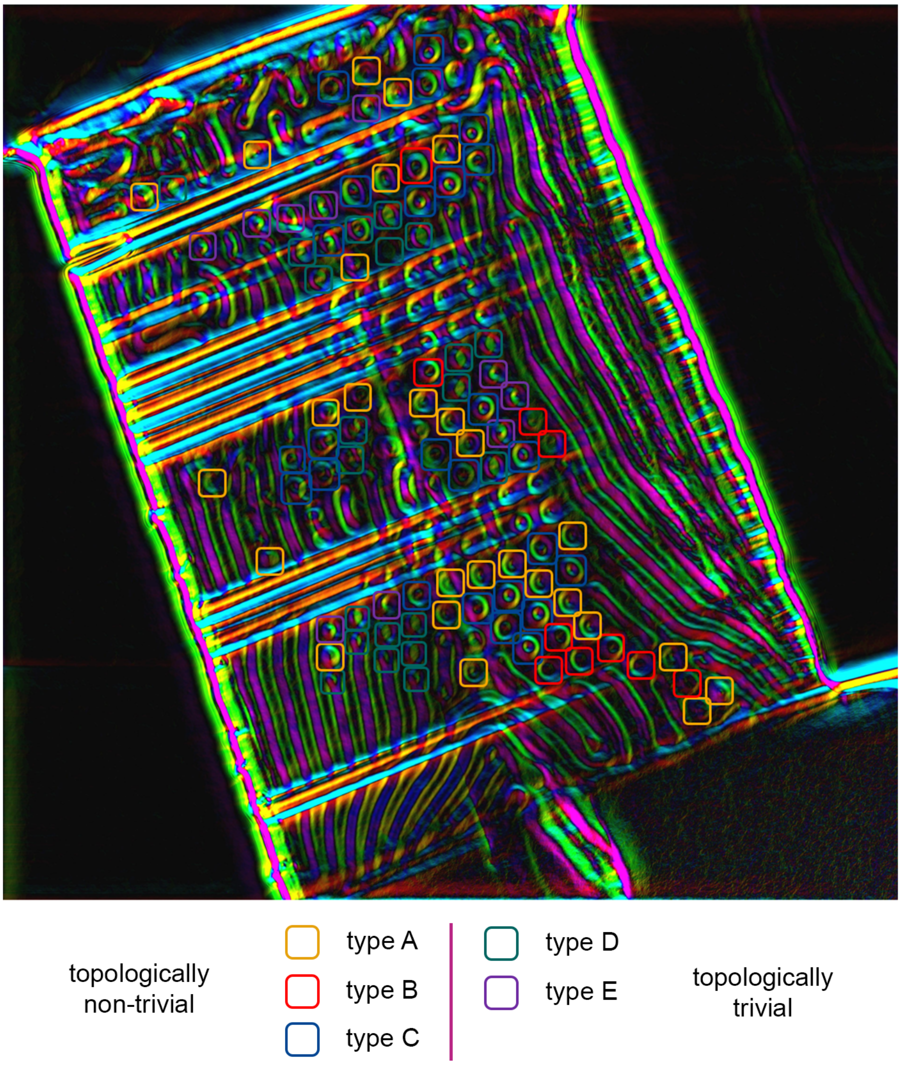

Figure B.15: Marked bubbles L23A. TIE reconstructed induction map for 320 mT.

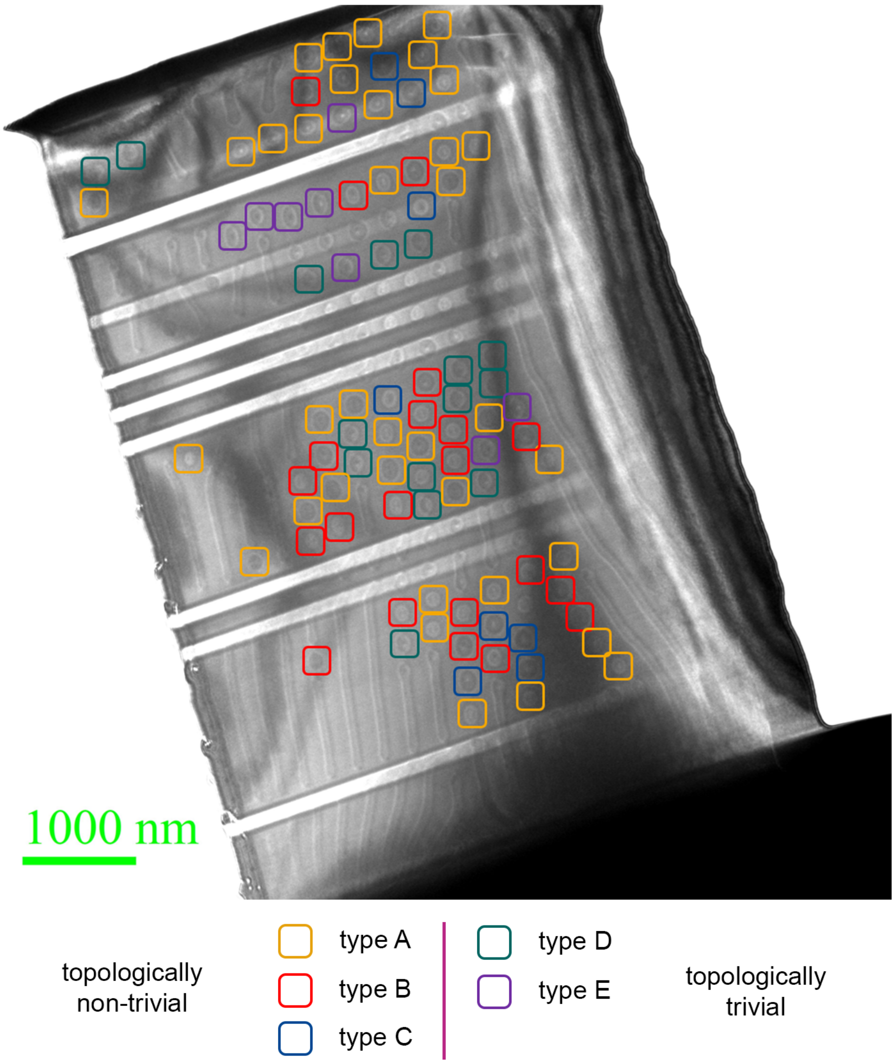

Figure B.16: Marked bubbles L23A. BF image in 410 mT.

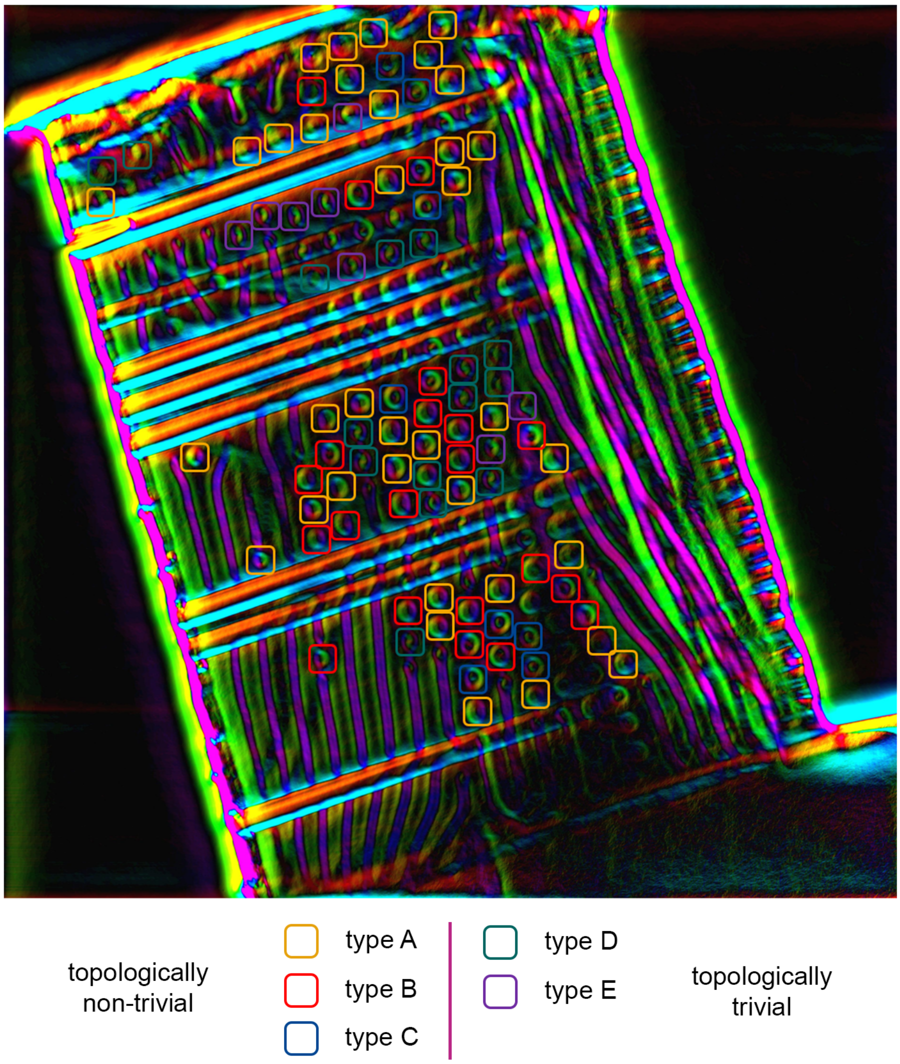

Figure B.17: Marked bubbles L23A. TIE reconstructed induction map for 410 mT.

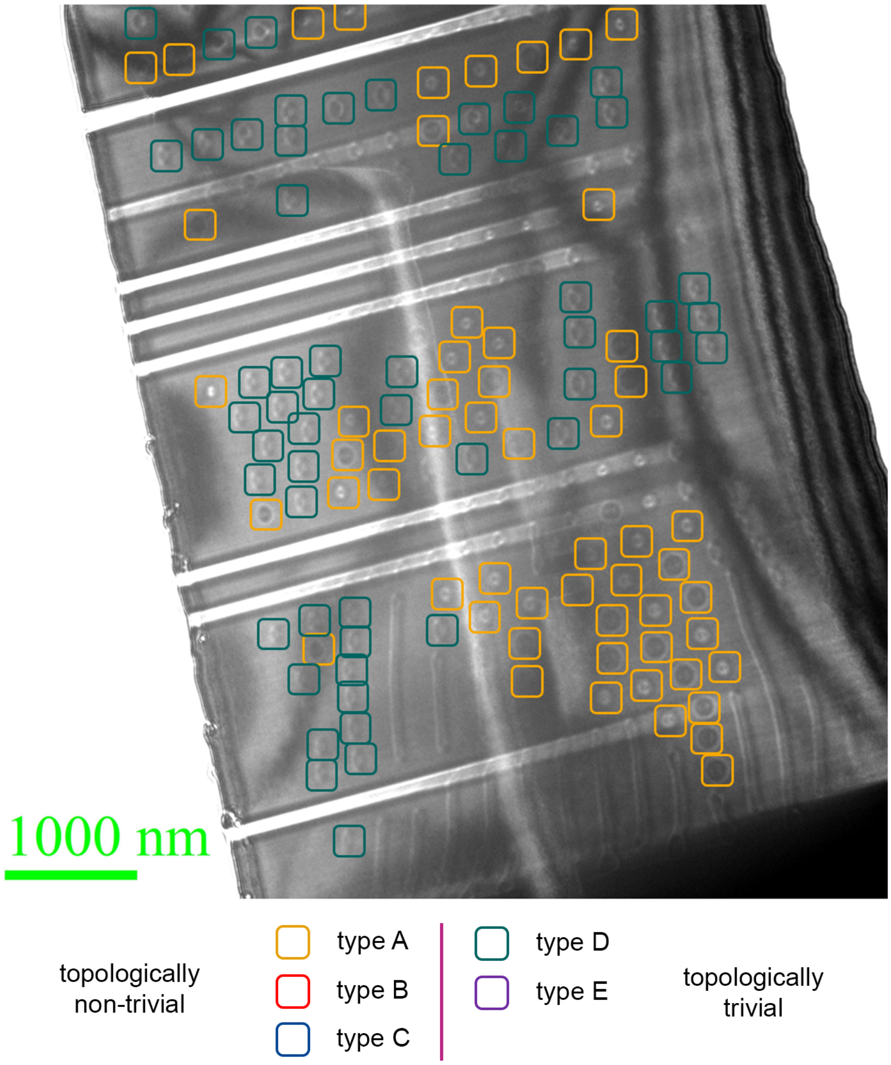

Figure B.18: Marked bubbles L23A. BF image in 520 mT.

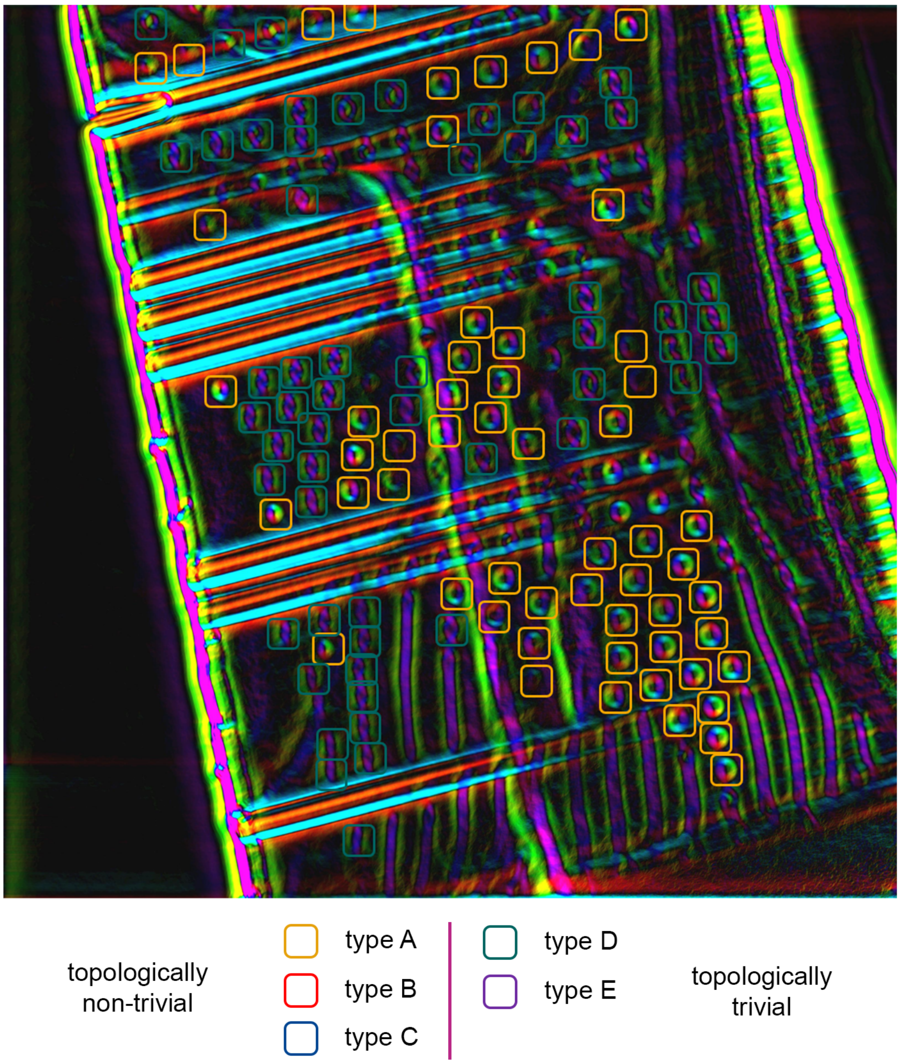

Figure B.19: Marked bubbles L23A. TIE reconstructed induction map for 520 mT.

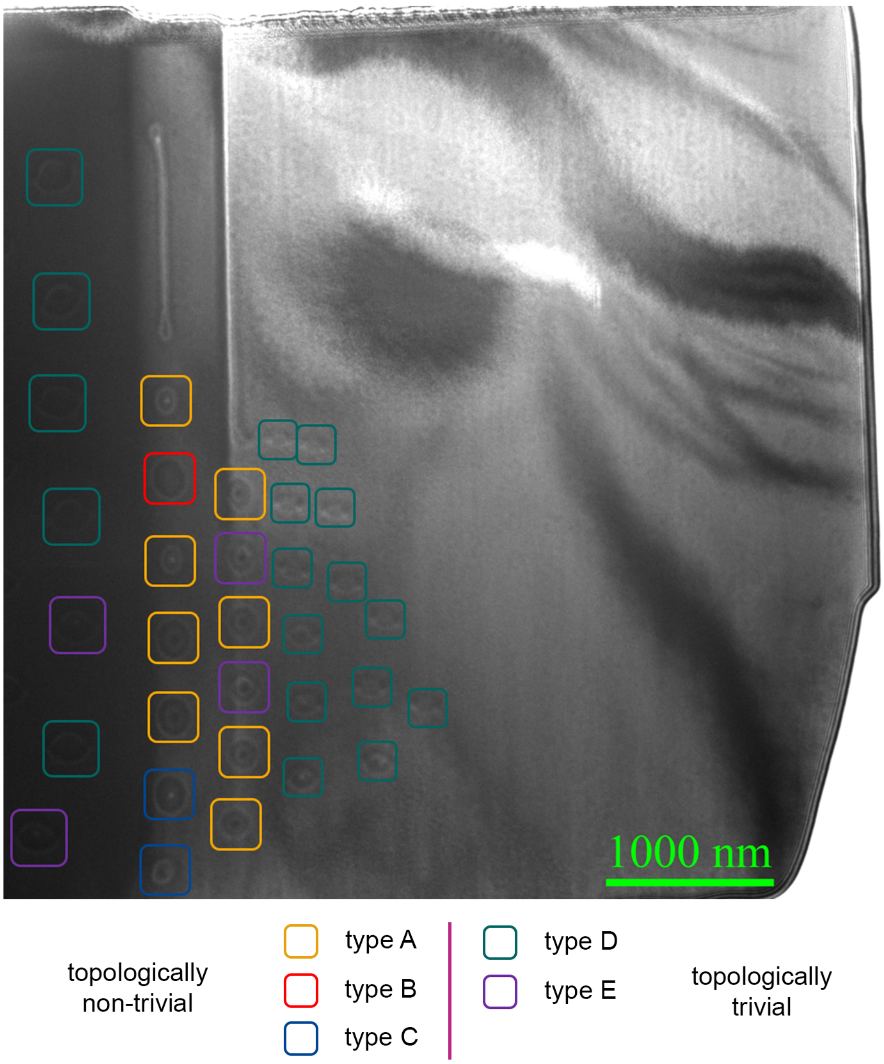

Figure B.20: Marked bubbles L13A. BF image in 565 mT.

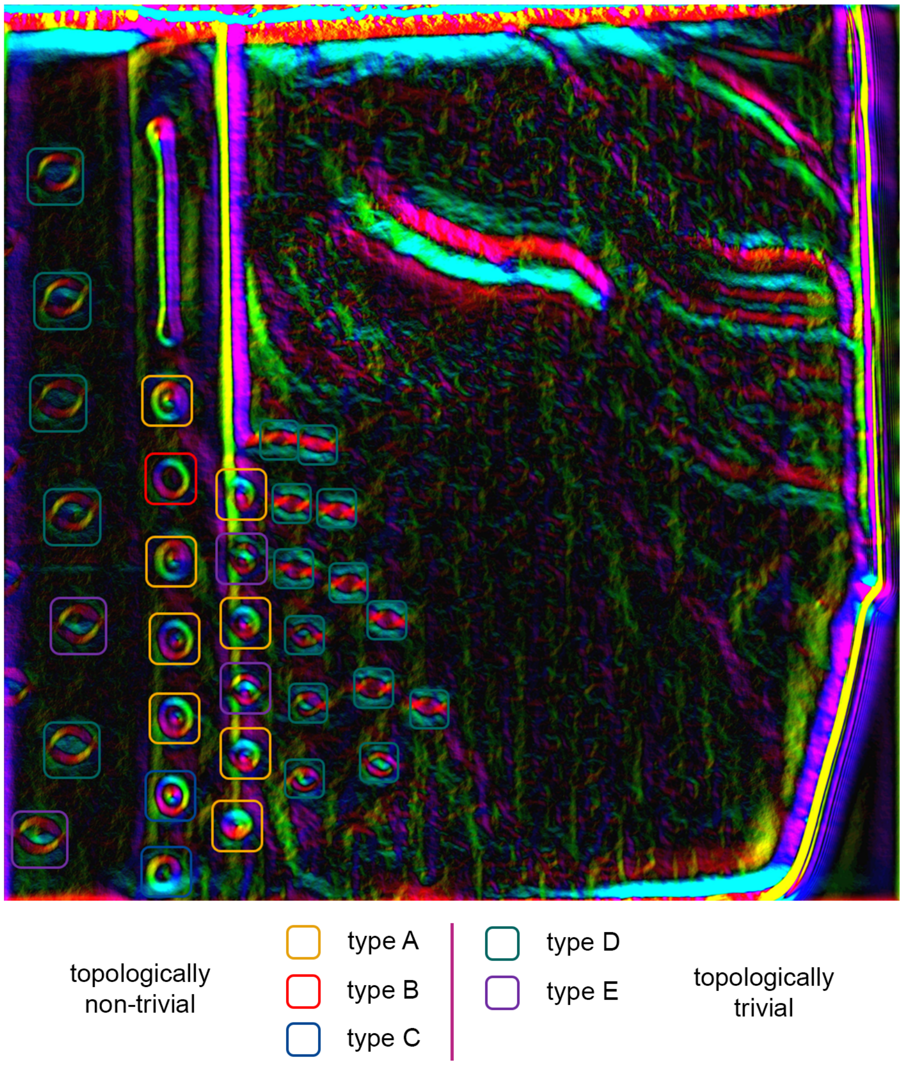

Figure B.21: Marked bubbles L13A. TIE reconstructed induction map for 565 mT.

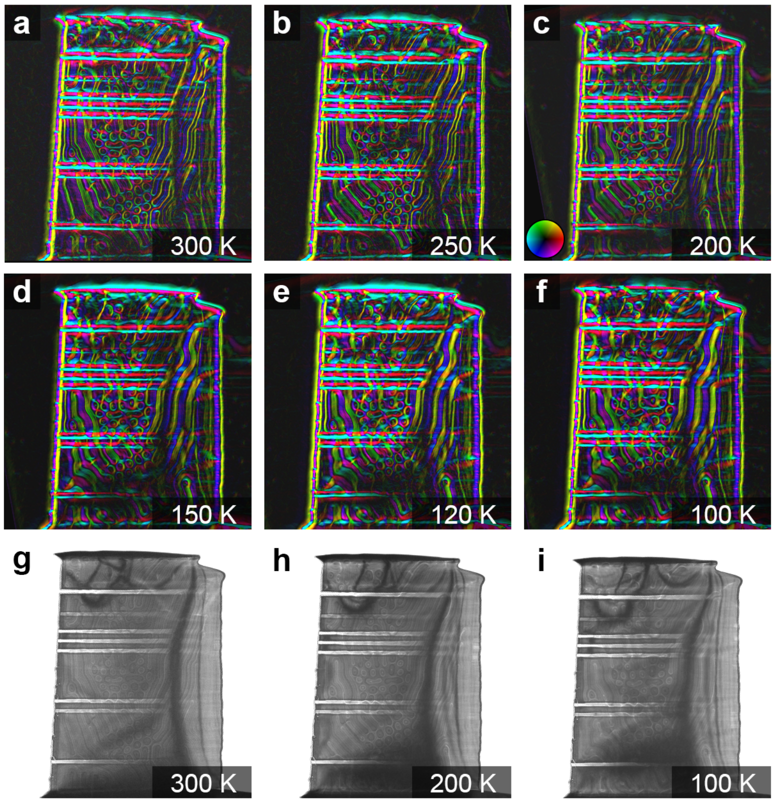

Figure B.22: Detailed temperature dependence in zero field. a-f, TIE reconstructed induction maps for different temperatures. **g-h**, BF images.

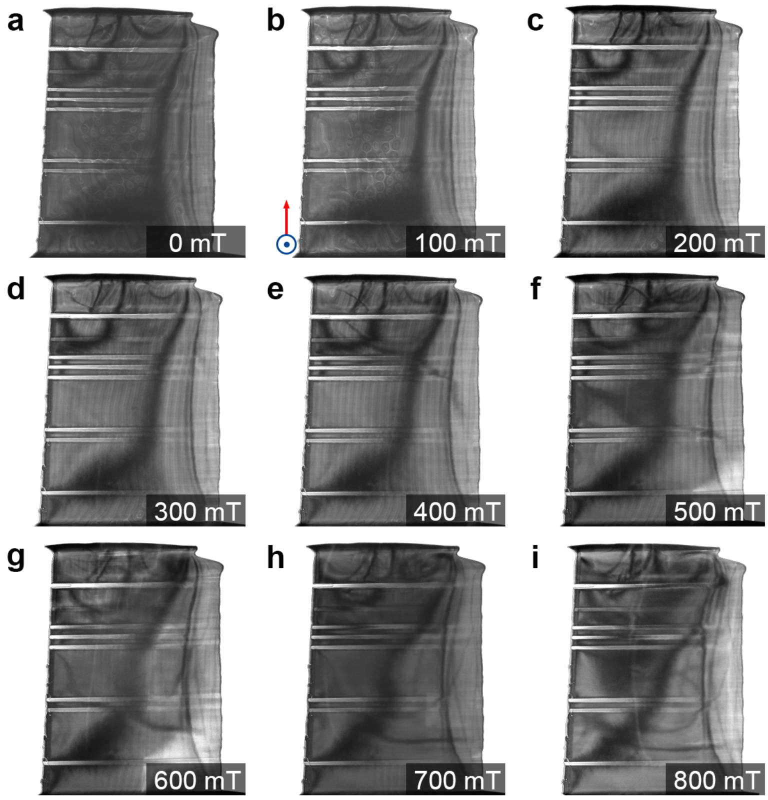

Figure B.23: Detailed field evolution at low temperatures. a-i, BF images at T =94 K for varying field.

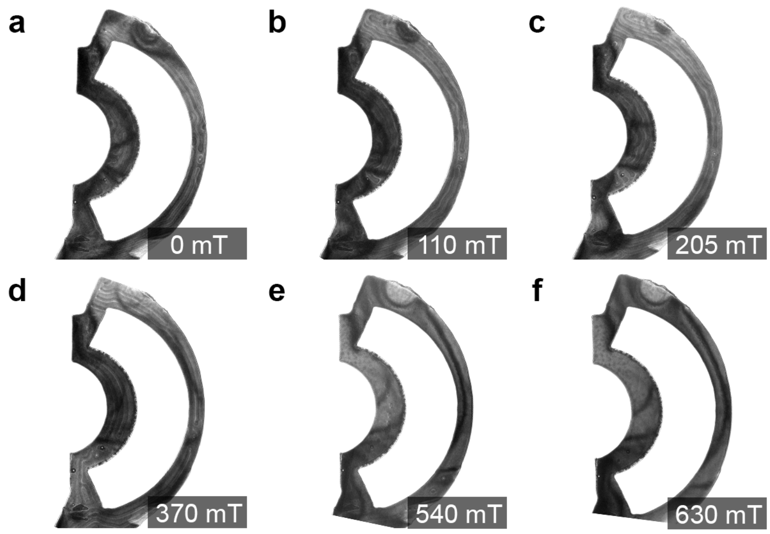

Figure B.24: Detailed field evolution for the nested ring structure. a-f BF images in out-of-plane magnetic field.

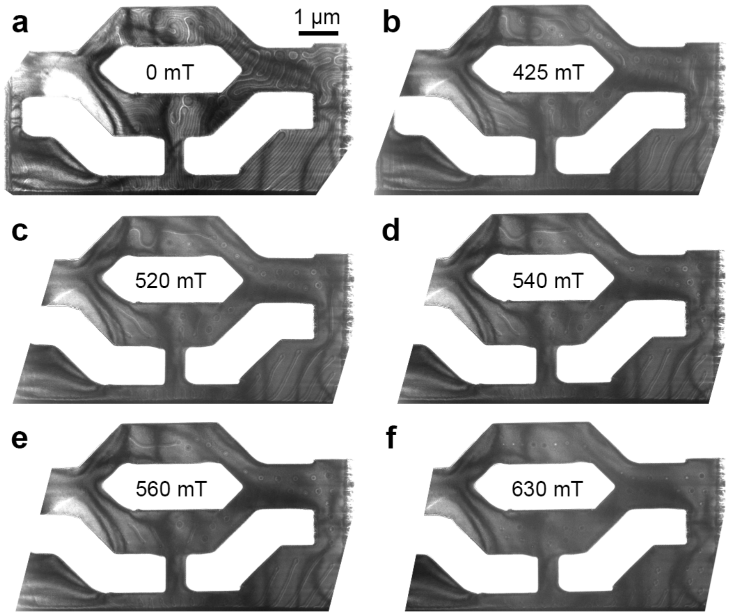

Figure B.25: Field evolution of the Y-selector-collector. a-f BF images.

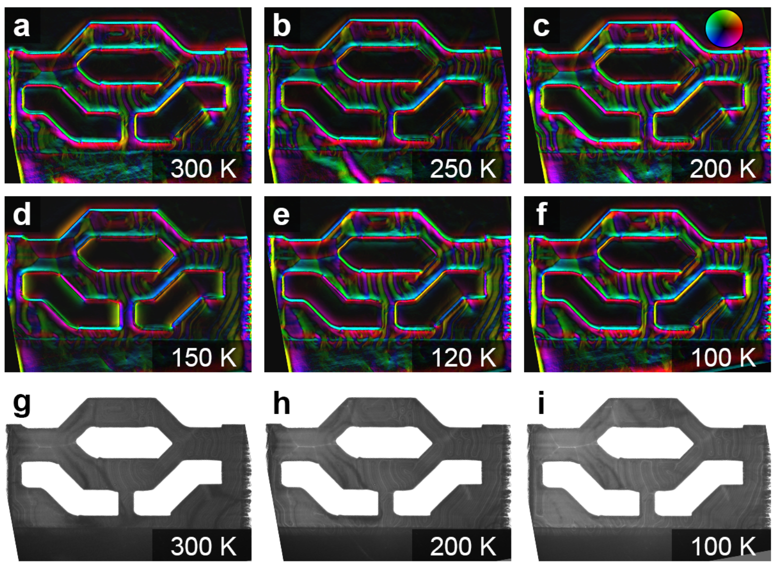

Figure B.26: Temperature dependence of the Y-selector-collector. a-f, TIE reconstructed induction maps. **g-i**, BF LTEM images.

C

Micromagnetic Simulations

Figure C.1 shows a series of micromagnetic simulations, provided by collaborator E. Lysne. The panels show a depth average along the c axis of $4069 \times 4096\,\mathrm{nm}^2$ cuboids of varying thickness. The color encodes the in-plane (ab plane) magnetization according to the color wheel in panel k, whereas the brightness represents the out of plane component (c axis) of the magnetization. Bright domains point upwards. Details for the parameters used to compute these can be found in [54, 86]. The simulated micromagnetic textures exhibit predominantly maze-like stripe domains and occasionally bubble domains. The stripe width, as well as the bubble diameter, widens with increasing thickness of the cuboids. Hence, the stripe width, respectively the periodicity, of these domain patterns is analyzed via the MATLAB script, too. The FFT is applied to the full images yielding the periodicity for the respective thickness. The green data points in figure 5.8a show the periodicity derived from simulations scaled by a factor of 1.12 to match the scaling law of the experimental data.

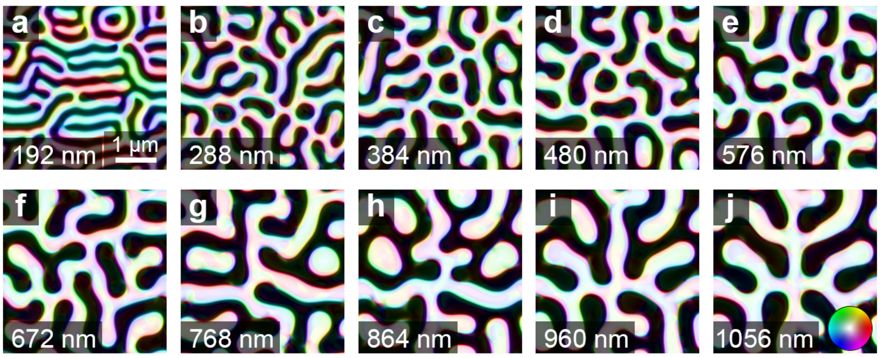

Figure C.1: Micromagnetic simulations for varying thicknesses. a-j, micromagnetic simulations for $4069 \times 4096\,\mathrm{nm}^2$ cuboids of respective thicknesses. Micromagnetic simulations provided by collaborator E. Lysne.

D

Script Based Data Analysis

Evaluation of Kittel scaling

A MATLAB script was developed for the quantitative evaluation of the stripe width in relation to the thickness. It evaluates the local periodicity $\lambda_{\mathrm{MFM}}(x, y)$ for each pixel, within a cropped region of interest, based on the magnetic texture in it's vicinity.

To run the script the MFM data is manually pre-processed: the scale of the MFM signal is cropped to non erroneous values. Subsequently the evaluation is carried out parallelized for each pixel in the following way. First, a sub-image of defined size ($N \times N$ pixels) centered around the pixel of interest is cropped from the original data. Next, the 2D fast Fourier transformation (FFT) is carried out on the sub-image, where the applied Hann window function suppresses edge effects. The obtained FFT data is then transformed to cylindrical coordinates with respect to the DC peak. subsequently radially averaged. A smooth step function is applied to suppress the DC peak for small radii and the data is fitted with a high order polynomial fit. From the fit the first maxima corresponding to the ring around the DC peak in the FFT image is determined. Subsequently, a reduced interval around this peak is reevaluated with a 3^{rd} order polynomial fit to optimize the localization of the peak. This peak corresponds to the wave number of the local periodicity of the evaluated pixel. Hence by reversing the FFT, i.e. inversion of the wave number the local periodicity $\lambda_{\mathrm{MFM}}(x, y)$ for the pixel located at the coordinates x and y is obtained.

Evidently not all pixels within an image yield reasonable, or valid values. Hence, for pixels outside the boundaries of the lamella the value in the periodicity map is artificially set to zero. Furthermore, in the border up to $N/2$ pixels from the images edges the periodicity is not calculated, because the sub-image cannot be formed from viable MFM data. This region as well as diverging results on the edges of the lamella are artificially set to zero as well.

The image size N of the sub image has a major influence on the obtained local periodicity. For small N, the obtained information is highly localized. However, the minimum size must exceed the limit given by the Nyquist theorem, i.e. contain at least two full periods in real space. Larger $N \times N$ sub-images, which contain multiple full periods, improve the quality of the FFT. But eventually increasing N defies the assumption of being representative for the localized periodicity. For this work sub-images of 128×128, 256×256 and 512×512 pixels were evaluated on an original MFM image of 1024×1024 pixels. For, $N = 512$ the spatially resolved map of the local periodicity is very smooth. However, beyond questionable local representation, it does not cover extended region of the lamella, due to the constrictions mentioned above. In contrast, for $N = 128$, severe discontinuities are observed in the spatially resolved local periodicity. Hence, a sub-image size of 256×256 pixels yields the best compromise.

In order to properly correlate the computed periodicity data to the sample thickness and evaluate the results, the corresponding thickness for every pixel is required. Therefore, form the topography image, obtained during the first pass, the plane of the substrate is determined and subtracted from the topography. The resulting height map represents the spatially resolved thickness $t(x, y)$ for every pixel. The corresponding local periodicity $\lambda_{\mathrm{MFM}}(x, y)$ is subsequently averaged for all pixels of equal thickness.

Bibliography

[1] Volker Tresp, J. Marc Overhage, Markus Bundschus, Shahrooz Rabizadeh, Peter A. Fasching, and Shipeng Yu. Going Digital: A Survey on Digitalization and Large-Scale Data Analytics in Healthcare. *Proceedings of the IEEE*, 104(11):2180–2206, nov 2016.

[2] Christoph Musik and Alexander Bogner. Book title: Digitalization & society. *Österreichische Zeitschrift für Soziologie*, 44(S1):1–14, jun 2019.

[3] Michael Rachinger, Romana Rauter, Christiana Müller, Wolfgang Vorraber, and Eva Schirgi. Digitalization and its influence on business model innovation. *Journal of Manufacturing Technology Management*, 30(8):1143–1160, dec 2019.

[4] Irina Makarova, Ksenia Shubenkova, Angelina Bagateeva, and Anton Pashkevich. Digitalization of Education as a New Destination of E-Learning. In *2018 International Symposium ELMAR*, pages 31–34. IEEE, sep 2018.

[5] Dan Wang, Zheng Xiang, and Daniel R. Fesenmaier. Smartphone Use in Everyday Life and Travel. *Journal of Travel Research*, 55(1):52–63, jan 2016.

[6] R. H. Dennard, F. H. Gaensslen, H. Yu, V. L. Rideout, E. Bassous, and A. R. LeBlanc. Design of ion-implanted MOSFET's with very small physical dimensions. *IEEE Journal of Solid-State Circuits*, 9(5):256–268, 1974.

[7] Gordon E Moore. Cramming more components onto integrated circuits, Reprinted from Electronics, volume 38, number 8, April 19, 1965, pp.114 ff. *IEEE Solid-State Circuits Society Newsletter*, 11(3):33–35, mar 2006.

[8] H. Esmaeilzadeh, E. Blem, R. S. Amant, K. Sankaralingam, and D. Burger. Dark silicon and the end of multicore scaling. In *2011 38th Annual International Symposium on Computer Architecture (ISCA)*, pages 365–376, 2011.

[9] Shinji Okazaki. Resolution limits of optical lithography. *Journal of Vacuum Science & Technology B: Microelectronics and Nanometer Structures*, 9(6):2829, nov 1991.

[10] Takashi Ito and Shinji Okazaki. Pushing the limits of lithography. *Nature*, 406(6799):1027–1031, aug 2000.

[11] Donis Flagello. Benefits and limitations of immersion lithography. *Journal of Micro/Nanolithography, MEMS, and MOEMS*, 3(1):104, jan 2004.

[12] Pieter F. Moonen, Iryna Yakimets, and Jurriaan Huskens. Fabrication of Transistors on Flexible Substrates: from Mass-Printing to High-Resolution Alternative Lithography Strategies. *Advanced Materials*, 24(41):5526–5541, nov 2012.

[13] John E Bjorkholm. EUV lithography—the successor to optical lithography. *Intel Technology Journal*, 3:98, 1998.

[14] Vivek Bakshi, editor. *EUV Lithography.* SPIE, dec 2008.

[15] Alberto Pirati, Rudy Peeters, Daniel Smith, Sjoerd Lok, Martijn van Noordenburg, Roderik van Es, Eric Verhoeven, Henk Meijer, Arthur Minnaert, Jan-Willem van der Horst, Hans Meiling, Joerg Mallmann, Christian Wagner, Judon Stoeldraijer, Geert Fisser, Jo Finders, Carmen Zoldesi, Uwe Stamm, Herman Boom, David Brandt, Daniel Brown, Igor Fomenkov, and Michael Purvis. EUV lithography performance for manufacturing: status and outlook. page 97760A, mar 2016.

[16] Sieu D. Ha and Shriram Ramanathan. Adaptive oxide electronics: A review. *Journal of Applied Physics*, 110(7):071101, oct 2011.

[17] H. Y. Hwang, Y. Iwasa, M. Kawasaki, B. Keimer, N. Nagaosa, and Y. Tokura. Emergent phenomena at oxide interfaces. *Nature Materials*, 11(2):103–113, feb 2012.

[18] Frances Hellman, Axel Hoffmann, Yaroslav Tserkovnyak, Geoffrey S. D. Beach, Eric E. Fullerton, Chris Leighton, Allan H. MacDonald, Daniel C. Ralph, Dario A. Arena, Hermann A. Dürr, Peter Fischer, Julie Grollier, Joseph P. Heremans, Tomas Jungwirth, Alexey V. Kimel, Bert Koopmans, Ilya N. Krivorotov, Steven J. May, Amanda K. Petford-Long, James M. Rondinelli, Nitin Samarth, Ivan K. Schuller, Andrei N. Slavin, Mark D. Stiles, Oleg Tchernyshyov, André Thiaville, and Barry L. Zink. Interface-induced phenomena in magnetism. *Reviews of Modern Physics*, 89(2):025006, jun 2017.

[19] Donald M. Evans, Vincent Garcia, Dennis Meier, and Manuel Bibes. Domains and domain walls in multiferroics. *Physical Sciences Reviews*, 5(9), apr 2020.

[20] Dennis Meier and Sverre M. Selbach. Ferroelectric domain walls for nanotechnology. *Nature Reviews Materials*, oct 2021.

[21] S. A. Wolf, D. D. Awschalom, R. A. Buhrman, J. M. Daughton, S. von Molnár, M. L. Roukes, A. Y. Chtchelkanova, and D. M. Treger. Spintronics: A Spin-Based Electronics Vision for the Future. *Science*, 294(5546):1488–1495, mar 2001.

[22] Igor Žutić, Jaroslav Fabian, and S Das Sarma. Spintronics: Fundamentals and applications. *Reviews of Modern Physics*, 76(2):323–410, mar 2004.

[23] Jongyeon Kim, Ayan Paul, Paul A Crowell, Steven J Koester, Sachin S Sapatnekar, Jian-Ping Wang, and Chris H Kim. Spin-Based Computing: Device Concepts, Current Status, and a Case Study on a High-Performance Microprocessor. *Proceedings of the IEEE*, 103(1):106–130, 2015.

[24] A. N. Bogdanov and D. A. Yablonskii. Thermodynamically stable "vortices" in magneticallyordered crystals. The mixed state of magnets. *Journal of Experimental and Theoretical Physics*, 68(1):3, 1989.

[25] S. Muhlbauer, B Binz, F Jonietz, C Pfleiderer, A Rosch, A Neubauer, R Georgii, and P. Boni. Skyrmion Lattice in a Chiral Magnet. *Science*, 323(5916):915–919, feb 2009.

[26] F. Jonietz, S. Mühlbauer, C. Pfleiderer, A. Neubauer, W. Münzer, A. Bauer, T. Adams, R. Georgii, P. Böni, R. A. Duine, K. Everschor, M. Garst, and A. Rosch. Spin Transfer Torques in MnSi at Ultralow Current Densities. *Science*, 330(6011):1648–1651, jan 2010.

[27] X. Z. Yu, N. Kanazawa, W. Z. Zhang, T. Nagai, T. Hara, K. Kimoto, Y. Matsui, Y. Onose, and Y. Tokura. Skyrmion flow near room temperature in an ultralow current density. *Nature Communications*, 3(1):988, jun 2012.

[28] Albert Fert, Nicolas Reyren, and Vincent Cros. Magnetic skyrmions: advances in physics and potential applications. *Nature Reviews Materials*, 2(7):1–15, mar 2017.

[29] Shijiang Luo and Long You. Skyrmion devices for memory and logic applications. *APL Materials*, 9(5):050901, may 2021.

[30] Xichao Zhang, Motohiko Ezawa, and Yan Zhou. Magnetic skyrmion logic gates: conversion, duplication and merging of skyrmions. *Scientific Reports*, 5(1):9400, nov 2015.

[31] Xuanyao Fong, Yusung Kim, Rangharajan Venkatesan, Sri Harsha Choday, Anand Raghunathan, and Kaushik Roy. Spin-Transfer Torque Memories: Devices, Circuits, and Systems. *Proceedings of the IEEE*, 104(7):1449–1488, jul 2016.

[32] Nuo Xu, Pai-Yu Chen, Jing Wang, Woosung Choi, Keun-Ho Lee, Eun Seung Jung, and Shimeng Yu. Review of physics-based compact models for emerging nonvolatile memories. *Journal of Computational Electronics*, 16(4):1257–1269, dec 2017.

[33] Fusheng Ma, Yan Zhou, H. B. Braun, and W. S. Lew. Skyrmion-Based Dynamic Magnonic Crystal. *Nano Letters*, 15(6):4029–4036, jun 2015.

[34] Mario Carpentieri, Riccardo Tomasello, Roberto Zivieri, and Giovanni Finocchio. Topological, non-topological and instanton droplets driven by spin-transfer torque in materials with perpendicular magnetic anisotropy and Dzyaloshinskii–Moriya Interaction. *Scientific Reports*, 5(1):16184, dec 2015.

[35] G. Finocchio, M. Ricci, R. Tomasello, A. Giordano, M. Lanuzza, V. Puliafito, P. Burrascano, B. Azzerboni, and M. Carpentieri. Skyrmion based microwave detectors and harvesting. *Applied Physics Letters*, 107(26):262401, dec 2015.

[36] W. Münzer, A. Neubauer, T. Adams, S. Mühlbauer, C. Franz, F. Jonietz, R. Georgii, P. Böni, B. Pedersen, M. Schmidt, A. Rosch, and C. Pfleiderer. Skyrmion lattice in the doped semiconductor $Fe_{1-x}Co_xSi$. *Physical Review B*, 81(4):41203, jan 2010.

[37] X. Z. Yu, Y. Onose, N. Kanazawa, J. H. Park, J. H. Han, Y. Matsui, N. Nagaosa, and Y. Tokura. Real-space observation of a two-dimensional skyrmion crystal. *Nature*, 465(7300):901–904, jun 2010.

[38] X. Z. Yu, N. Kanazawa, Y. Onose, K. Kimoto, W. Z. Zhang, S. Ishiwata, Y. Matsui, and Y. Tokura. Near room-temperature formation of a skyrmion crystal in thin-films of the helimagnet FeGe. *Nature Materials*, 10(2):106–109, feb 2011.

[39] Stefan Heinze, Kirsten von Bergmann, Matthias Menzel, Jens Brede, André Kubetzka, Roland Wiesendanger, Gustav Bihlmayer, and Stefan Blügel. Spontaneous atomic-scale magnetic skyrmion lattice in two dimensions. *Nature Physics*, 7(9):713–718, nov 2011.

[40] Wanjun Jiang, Pramey Upadhyaya, Wei Zhang, Guoqiang Yu, M. Benjamin Jungfleisch, Frank Y. Fradin, John E. Pearson, Yaroslav Tserkovnyak, Kang L. Wang, Olle Heinonen, Suzanne G. E. te Velthuis, and Axel Hoffmann. Blowing magnetic skyrmion bubbles. *Science*, 349(6245):283–286, jan 2015.

[41] C. Moreau-Luchaire, C. Moutafis, N. Reyren, J. Sampaio, C. a. F. Vaz, N. Van Horne, K. Bouzehouane, K. Garcia, C. Deranlot, P. Warnicke, P. Wohlhüter, J.-M. George, M. Weigand, J. Raabe, V. Cros, and A. Fert. Additive interfacial chiral interaction in multilayers for stabilization of small individual skyrmions at room temperature. *Nature Nanotechnology*, 11(5):444–448, jan 2016.

[42] Olivier Boulle, Jan Vogel, Hongxin Yang, Stefania Pizzini, Dayane de Souza Chaves, Andrea Locatelli, Tevfik Onur Menteş, Alessandro Sala, Liliana D Buda-Prejbeanu, Olivier Klein, Mohamed Belmeguenai, Yves Roussigné, Andrey Stashkevich, Salim Mourad Chérif, Lucia Aballe, Michael Foerster, Mairbek Chshiev, Stéphane Auffret, Ioan Mihai Miron, and Gilles Gaudin. Room-temperature chiral magnetic skyrmions in ultrathin magnetic nanostructures. *Nature Nanotechnology*, 11(5):449–454, jan 2016.

[43] Seonghoon Woo, Kai Litzius, Benjamin Krüger, Mi-Young Im, Lucas Caretta, Kornel Richter, Maxwell Mann, Andrea Krone, Robert M Reeve, Markus Weigand, Parnika Agrawal, Ivan Lemesh, Mohamad-Assaad Mawass, Peter Fischer, Mathias Kläui, and Geoffrey S D Beach. Observation of room-temperature magnetic skyrmions and their current-driven dynamics in ultrathin metallic ferromagnets. *Nature Materials*, 15(5):501–506, jan 2016.

[44] Anjan Soumyanarayanan, M. Raju, A. L. Gonzalez Oyarce, Anthony K. C. Tan, Mi-Young Im, A. P. Petrović, Pin Ho, K. H. Khoo, M. Tran, C. K. Gan, F. Ernult, and C. Panagopoulos. Tunable room-temperature magnetic skyrmions in Ir/Fe/Co/Pt multilayers. *Nature Materials*, 16(9):898–904, sep 2017.

[45] Guoqiang Yu, Pramey Upadhyaya, Xiang Li, Wenyuan Li, Se Kwon Kim, Yabin Fan, Kin L. Wong, Yaroslav Tserkovnyak, Pedram Khalili Amiri, and Kang L. Wang. Room-Temperature Creation and Spin–Orbit Torque Manipulation of Skyrmions in Thin Films with Engineered Asymmetry. *Nano Letters*, 16(3):1981–1988, mar 2016.

[46] X. Z. Yu, W. Koshibae, Y. Tokunaga, K. Shibata, Y. Taguchi, N. Nagaosa, and Y. Tokura. Transformation between meron and skyrmion topological spin textures in a chiral magnet. *Nature*, 564(7734):95–98, nov 2018.

[47] Yao Guang, Iuliia Bykova, Yizhou Liu, Guoqiang Yu, Eberhard Goering, Markus Weigand, Joachim Gräfe, Se Kwon Kim, Junwei Zhang, Hong Zhang, Zhengren Yan, Caihua Wan, Jiafeng Feng, Xiao Wang, Chenyang Guo, Hongxiang Wei, Yong Peng, Yaroslav Tserkovnyak, Xiufeng Han, and Gisela Schütz. Creating zero-field skyrmions in exchange-biased multilayers through X-ray illumination. *Nature Communications*, 11(1):949, dec 2020.

[48] K. Gaurav Rana, A. Finco, F. Fabre, S. Chouaieb, A. Haykal, L. D. Buda-Prejbeanu, O. Fruchart, S. Le Denmat, P. David, M. Belmeguenai, T. Denneulin, R. E. Dunin-Borkowski, G. Gaudin, V. Jacques, and O. Boulle. Room-Temperature Skyrmions at Zero Field in Exchange-Biased Ultrathin Films. *Physical Review Applied*, 13(4):044079, apr 2020.

[49] I. Kézsmárki, S. Bordács, P. Milde, E. Neuber, L. M. Eng, J. S. White, H. M. Rønnow, C. D. Dewhurst, M. Mochizuki, K. Yanai, H. Nakamura, D. Ehlers, V. Tsurkan, and A. Loidl. Néel-type skyrmion lattice with confined orientation in the polar magnetic semiconductor GaV_4S_8. *Nature Materials*, 14(11):1116–1122, nov 2015.

[50] Ádám Butykai, Sándor Bordács, István Kézsmárki, Vladimir Tsurkan, Alois Loidl, Jonathan Döring, Erik Neuber, Peter Milde, Susanne C. Kehr, and Lukas M. Eng. Characteristics of ferroelectric-ferroelastic domains in Néel-type skyrmion host GaV4S8. *Scientific Reports*, 7(1):44663, apr 2017.

[51] S. Bordács, A. Butykai, B. G. Szigeti, J. S. White, R. Cubitt, A. O. Leonov, S. Widmann, D. Ehlers, H.-A. Krug von Nidda, V. Tsurkan, A. Loidl, and I. Kézsmárki. Equilibrium Skyrmion Lattice Ground State in a Polar Easy-plane Magnet. *Scientific Reports*, 7(1):7584, dec 2017.

[52] Zhipeng Hou, Weijun Ren, Bei Ding, Guizhou Xu, Yue Wang, Bing Yang, Qiang Zhang, Ying Zhang, Enke Liu, Feng Xu, Wenhong Wang, Guangheng Wu, Xixiang Zhang, Baogen Shen, and Zhidong Zhang. Observation of Various and Spontaneous Magnetic Skyrmionic Bubbles at

Room Temperature in a Frustrated Kagome Magnet with Uniaxial Magnetic Anisotropy. *Advanced Materials*, 29(29):1–8, 2017.

[53] Zhipeng Hou, Qiang Zhang, Guizhou Xu, Chen Gong, Bei Ding, Yue Wang, Hang Li, Enke Liu, Feng Xu, Hongwei Zhang, Yuan Yao, Guangheng Wu, Xi-xiang Zhang, and Wenhong Wang. Creation of Single Chain of Nanoscale Skyrmion Bubbles with Record-High Temperature Stability in a Geometrically Confined Nanostripe. *Nano Letters*, 18(2):1274–1279, feb 2018.

[54] Markus Altthaler, Erik Lysne, Erik Roede, Lilian Prodan, Vladimir Tsurkan, Mohamed A. Kassem, Hiroyuki Nakamura, Stephan Krohns, István Kézsmárki, and Dennis Meier. Magnetic and geometric control of spin textures in the itinerant kagome magnet Fe_3Sn_2. *Physical Review Research*, 3(4):043191, dec 2021.

[55] Robert G. Garrett. Natural Distribution and Abundance of Elements. In *Essentials of Medical Geology*, pages 35–57. Springer Netherlands, Dordrecht, 2013.

[56] W. F. Ehret and D. H. Gurinsky. The Thermal Diagram of the System Iron—Tin. *Journal of the American Chemical Society*, 65(6):1226–1230, oct 1943.

[57] K. Yosida. Note on the Magnetic Properties of the FeSn System. *Progress of Theoretical Physics*, 6(3):356–365, jun 1951.

[58] Sumio Ichiba, Hiroshi Sakai, and Hisao Negita. The Mössbauer Effect in Fe_3Sn_z. *Bulletin of the Chemical Society of Japan*, 41(11):2791–2792, nov 1968.

[59] L. A. Fenner, A. A. Dee, and A. S. Wills. Non-collinearity and spin frustration in the itinerant kagome ferromagnet Fe_3Sn_2. *Journal of Physics: Condensed Matter*, 21(45):452202, mar 2009.

[60] D. Boldrin and A. S. Wills. Anomalous Hall Effect in Geometrically Frustrated Magnets. *Advances in Condensed Matter Physics*, 2012:1–12, jul 2012.

[61] Linda Ye, Mingu Kang, Junwei Liu, Felix von Cube, Christina R. Wicker, Takehito Suzuki, Chris Jozwiak, Aaron Bostwick, Eli Rotenberg, David C. Bell, Liang Fu, Riccardo Comin, and Joseph G. Checkelsky. Massive Dirac fermions in a ferromagnetic kagome metal. *Nature*, 555(7698):638–642, mar 2018.

[62] Neeraj Kumar, Y Soh, Yihao Wang, and Y Xiong. Magnetotransport as a diagnostic of spin reorientation: Kagome ferromagnet as a case study. *Physical Review B*, 100(21):214420, mar 2019.

[63] Kevin Heritage, Ben Bryant, Laura A. Fenner, Andrew S. Wills, Gabriel Aeppli, and Yeong-Ah Soh. Images of a First-Order Spin-Reorientation Phase Transition in a Metallic Kagome Ferromagnet. *Advanced Functional Materials*, 30(36):1909163, sep 2020.

[64] Alex Hubert and Rudolf Schäfer. *Magnetic Domains.* Springer Berlin Heidelberg, Berlin, Heidelberg, 1998.

[65] Li Shu-hua. Origine de la Boussole II. Aimant et Boussole. *Isis*, 45(2):175–196, jul 1954.

[66] E. du Trémolet de Lacheisserie, Damien Gignoux, and Michel Schlenker, editors. *Magnetism - Materials and Applications — — Springer.*

[67] Barbara M. Kreutz. Mediterranean Contributions to the Medieval Mariner's Compass. *Technology and Culture*, 14(3):367, jul 1973.

[68] Christine Blondel and Abdelmadjid Benseghir. The key role of Oersted's and Ampère's 1820 electromagnetic experiments in the construction of the concept of electric current. *American Journal of Physics*, 85(5):369–380, may 2017.

[69] Albert S. Schwarz. *Topology for Physicists*, volume 308 of *Grundlehren der mathematischen Wissenschaften.* Springer Berlin Heidelberg, Berlin, Heidelberg, 1994.

[70] Sinéad M. Griffin and Nicola A. Spaldin. On the relationship between topological and geometric defects. *Journal of Physics: Condensed Matter*, 29(34):343001, oct 2017.

[71] R.C. O'Handley. Magnetic Materials. In *Encyclopedia of Physical Science and Technology*, chapter Magnetic M, pages 919–944. Elsevier, 2003.

[72] J. Raabe, R. Pulwey, R. Sattler, T. Schweinböck, J. Zweck, and D. Weiss. Magnetization pattern of ferromagnetic nanodisks. *Journal of Applied Physics*, 88(7):4437, 2000.

[73] T. Shinjo, T. Okuno, R. Hassdorf, † K. Shigeto, and T. Ono. Magnetic Vortex Core Observation in Circular Dots of Permalloy. *Science*, 289(5481):930–932, aug 2000.

[74] Christian Pfleiderer. Surfaces get hairy. *Nature Physics*, 7(9):673–674, sep 2011.

[75] Kannan M. Krishnan. *Fundamentals and Applications of Magnetic Materials.* Oxford University Press, aug 2016.

[76] E. du Trémolet de Lacheisserie, Damien Gignoux, and Michel Schlenker, editors. *Magnetism - Materials and Application.* Springer, New York, 1 edition, 2005.

[77] Stephen Blundell. *Magnetism in condensed matter.* Repr. edition, 2006.

[78] Yoshiro Kakehashi. *Modern Theory of Magnetism in Metals and Alloys*, volume 175 of *Springer Series in Solid-State Sciences.* Springer Berlin Heidelberg, Berlin, Heidelberg, 1. aufl., edition, jan 2013.

[79] Yakov M. Shnir. *Magnetic Monopoles.* Springer Berlin Heidelberg, Berlin, Heidelberg, 2005.

[80] Q. N. Meier, M. Fechner, T. Nozaki, M. Sahashi, Z. Salman, T. Prokscha, A. Suter, P. Schoenherr, M. Lilienblum, P. Borisov, I. E. Dzyaloshinskii, M. Fiebig, H. Luetkens, and N. A. Spaldin. Search for the Magnetic Monopole at a Magnetoelectric Surface. *Physical Review X*, 9(1):011011, jan 2019.

[81] Charles Kittel. *Einführung in die Festkörperphysik*. Oldenbourg-Verlag, München, 14 edition, 2006.

[82] Jürgen Kübler. *Theory of Itinerant Electron Magnetism*. Oxford University Press, Oxford, 2000.

[83] Stephen Blundell. *Magnetism in Condensed Matter*. Oxford University Press, Oxford, 1 edition edition, 2001.

[84] Wolfgang Nolting and Anupuru Ramakanth. *Quantum Theory of Magnetism*. Springer Berlin Heidelberg, Berlin, Heidelberg, 2009.

[85] Arne Vansteenkiste, Jonathan Leliaert, Mykola Dvornik, Mathias Helsen, Felipe Garcia-Sanchez, and Bartel Van Waeyenberge. The design and verification of MuMax3. *AIP Advances*, 4(10):107133, mar 2014.

[86] Erik Lysne. *Novel Topological Spin Solitons for Spintronics Applications*. Doctoral thesis, Norwegian University of Science and Technology, 2021.

[87] David J. Griffiths. *Introduction to quantum mechanics*. Prentice Hall, Englewood Cliffs, N.J, 1995.

[88] J. A. Osborn, editor. *Proceedings of the Seventh Conference on Magnetism and Magnetic Materials*. Springer US, Boston, MA, 1962.

[89] I. Dzyaloshinsky. A thermodynamic theory of “weak” ferromagnetism of antiferromagnetics. *Journal of Physics and Chemistry of Solids*, 4(4):241–255, aug 1958.

[90] Tôru Moriya. Anisotropic Superexchange Interaction and Weak Ferromagnetism. *Physical Review*, 120(1):91–98, oct 1960.

[91] A. N. Bogdanov and U. B. Rößler. Chiral symmetry breaking in magnetic thin films and multilayers. *Physical Review Letters*, 87(3):37203–1–37203–4, 2001.

[92] Xiuzhen Yu, Yusuke Tokunaga, Yasujiro Taguchi, and Yoshinori Tokura. Variation of Topology in Magnetic Bubbles in a Colossal Magnetoresistive Manganite. *Advanced Materials*, 29(3):1603958, oct 2017.

[93] Charles Kittel. Physical Theory of Ferromagnetic Domains. *Reviews of Modern Physics*, 21(4):541–583, oct 1949.

[94] J. A. Cape and G. W. Lehman. Magnetic Domain Structures in Thin Uniaxial Plates with Perpendicular Easy Axis. *Journal of Applied Physics*, 42(13):5732–5756, dec 1971.

[95] C. Kooy and U. Enz. Experimental and Theoretical Study of the Domain Configuration in Thin Layers of $BaFe_{12}O_{19}$. *Philips Research Rep.*, 15:7–29, 1960.

[96] T. Garel and S. Doniach. Phase transitions with spontaneous modulation-the dipolar Ising ferromagnet. *Physical Review B*, 26(1):325–329, jul 1982.

[97] W. F. Druyvesteyn and J. W .F. Dorleijn. Calculations on some periodic magnetic domain structures; consequences for bubble devices. *Philips Research Rep.*, 26(1):11–28, 1971.

[98] Charles Kittel. Theory of the Structure of Ferromagnetic Domains in Films and Small Particles. *Physical Review*, 70(11-12):965–971, dec 1946.

[99] S. Prosandeev, S. Lisenkov, and L. Bellaiche. Kittel Law in $BiFeO_3$ Ultrathin Films: A First-Principles-Based Study. *Physical Review Letters*, 105(14):147603, jan 2010.

[100] Nicholas Manton and Paul Sutcliffe. *Topological Solitons*. Cambridge University Press, jun 2004.

[101] Achim Rosch. Moving with the current. *Nature Nanotechnology*, 8(3):160–161, jul 2013.

[102] Jiadong Zang, Vincent Cros, and Axel Hoffmann. *Topology in Magnetism*, volume 192. Springer International Publishing AG, Springer International Publishing, Springer, Cham, 2018.

[103] Usama Al Khawaja and Henk Stoof. Skyrmions in a ferromagnetic Bose–Einstein condensate. *Nature*, 411(6840):918–920, jan 2001.

[104] L. S. Leslie, A. Hansen, K. C. Wright, B. M. Deutsch, and N. P. Bigelow. Creation and Detection of Skyrmions in a Bose-Einstein Condensate. 250401(December):18–21, 2009.

[105] S. L. Sondhi, A. Karlhede, S. A. Kivelson, and E. H. Rezayi. Skyrmions and the crossover from the integer to fractional quantum Hall effect at small Zeeman energies. *Physical Review B*, 47(24):16419–16426, jan 1993.

[106] S. E. Barrett, G. Dabbagh, L. N. Pfeiffer, K. W. West, and R. Tycko. Optically Pumped NMR Evidence for Finite-Size Skyrmions in GaAs Quantum Wells near Landau Level Filling v = 1. *Physical Review Letters*, 74(25):5112–5115, 1995.

[107] A. N. Bogdanov, U. K. Rößler, and A. A. Shestakov. Skyrmions in nematic liquid crystals ¨. *Physical Review E*, 67(1):016602, 2003.

[108] Paul J. Ackerman, Rahul P. Trivedi, Bohdan Senyuk, Jao Van De Lagemaat, and Ivan I. Smalyukh. Two-dimensional skyrmions and other solitonic structures in confinement-frustrated chiral nematics. *Physical Review E*, 012505(1):012505, 2014.

[109] Helmut Eschrig. *Topology and Geometry for Physics*, volume 822 of *Lecture Notes in Physics*. Springer Berlin Heidelberg, Berlin, Heidelberg, 2011.

[110] N. D. Mermin. The topological theory of defects in ordered media. *Reviews of Modern Physics*, 51(3):591–648, jul 1979.

[111] Hans-Benjamin Braun. Topological effects in nanomagnetism: from superparamagnetism to chiral quantum solitons. *Advances in Physics*, 61(1):1–116, feb 2012.

[112] Peggy Schönherr. *Topological Structures in Magnetic and Electric Materials*. Doctoral thesis, ETH Zürich, 2018.

[113] Naoto Nagaosa and Yoshinori Tokura. Topological properties and dynamics of magnetic skyrmions. *Nature Nanotechnology*, 8(12):899–911, jul 2013.

[114] Börge Göbel, Ingrid Mertig, and Oleg A Tretiakov. Beyond skyrmions: Review and perspectives of alternative magnetic quasiparticles. *Physics Reports*, 895:1–28, feb 2021.

[115] Ajaya K. Nayak, Vivek Kumar, Tianping Ma, Peter Werner, Eckhard Pippel, Roshnee Sahoo, Françoise Damay, Ulrich K. Rößler, Claudia Felser, and Stuart S.P. Parkin. Magnetic antiskyrmions above room temperature in tetragonal Heusler materials. *Nature*, 548(7669):561–566, 2017.

[116] James C. Loudon, Alison C. Twitchett-Harrison, David Cortés-Ortuño, Max T. Birch, Luke A. Turnbull, Aleš Štefančič, Feodor Y. Ogrin, Erick O. Burgos-Parra, Nicholas Bukin, Angus Laurenson, Horia Popescu, Marijan Beg, Ondrej Hovorka, Hans Fangohr, Paul A. Midgley, Geetha Balakrishnan, and Peter D. Hatton. Do Images of Biskyrmions Show Type-II Bubbles? *Advanced Materials*, 31(16):1806598, apr 2019.

[117] M. T. Birch, D. Cortés-Ortuño, L. A. Turnbull, M. N. Wilson, F. Groß, N. Träger, A. Laurenson, N. Bukin, S. H. Moody, M. Weigand, G. Schütz, H. Popescu, R. Fan, P. Steadman, J. a. T. Verezhak, G. Balakrishnan, J. C. Loudon, A. C. Twitchett-Harrison, O. Hovorka, H. Fangohr, F. Y. Ogrin, J. Gräfe, and P. D. Hatton. Real-space imaging of confined magnetic skyrmion tubes. *Nature Communications*, 11(1):1726, nov 2020.

[118] Filipp N. Rybakov, Aleksandr B. Borisov, Stefan Blügel, and Nikolai S. Kiselev. New Type of Stable Particlelike States in Chiral Magnets. *Physical Review Letters*, 115(11):117201, nov 2015.

[119] Adam S. Ahmed, James Rowland, Bryan D. Esser, Sarah R. Dunsiger, David W. McComb, Mohit Randeria, and Roland K. Kawakami. Chiral bobbers and skyrmions in epitaxial FeGe/Si(111) films. *Physical Review Materials*, 2(4):41401, nov 2018.

[120] X. S. Wang, A Qaiumzadeh, and A Brataas. Current-Driven Dynamics of Magnetic Hopfions. *Physical Review Letters*, 123(14):147203, sep 2019.

[121] N. S. Kiselev, A. N. Bogdanov, R. Schäfer, and U. K. Rößler. Chiral skyrmions in thin magnetic films: new objects for magnetic storage technologies? *Journal of Physics D: Applied Physics*, 44(39):392001, jan 2011.

[122] Shawn D. Pollard, Joseph A. Garlow, Jiawei Yu, Zhen Wang, Yimei Zhu, and Hyunsoo Yang. Observation of stable Néel skyrmions in cobalt/palladium multilayers with Lorentz transmission electron microscopy. *Nature Communications*, 8(1):14761, nov 2017.

[123] Anne Bernand-Mantel, Lorenzo Camosi, Alexis Wartelle, Nicolas Rougemaille, Michaël Darques, and Laurent Ranno. The skyrmion-bubble transition in a ferromagnetic thin film. *SciPost Physics*, 4(5):27, jul 2018.

[124] A. Dussaux, P. Schoenherr, K. Koumpouras, J. Chico, K. Chang, L. Lorenzelli, N. Kanazawa, Y. Tokura, M. Garst, A. Bergman, C. L. Degen, and D. Meier. Local dynamics of topological magnetic defects in the itinerant helimagnet FeGe. *Nature Communications*, 7(1):12430, apr 2016.

[125] H. Wilhelm, M. Baenitz, M. Schmidt, C. Naylor, R. Lortz, U. K. Rößler, A. A. Leonov, and A. N. Bogdanov. Confinement of chiral magnetic modulations in the precursor region of FeGe. *Journal of Physics: Condensed Matter*, 24(29):294204, apr 2012.

[126] Marijan Beg, Rebecca Carey, Weiwei Wang, David Cortés-Ortuño, Mark Vousden, Marc-Antonio Bisotti, Maximilian Albert, Dmitri Chernyshenko, Ondrej Hovorka, Robert L Stamps, and Hans Fangohr. Ground state search, hysteretic behaviour and reversal mechanism of skyrmionic textures in confined helimagnetic nanostructures. *Scientific Reports*, 5(1):17137, apr 2015.

[127] Per Bak and M. Høgh Jensen. Theory of helical magnetic structures and phase transitions in MnSi and FeGe. *Journal of Physics C: Solid State Physics*, 13(31):L881–L885, nov 1980.

[128] Tsuyoshi Okubo, Sungki Chung, and Hikaru Kawamura. Multiple-q States and the Skyrmion Lattice of the Triangular-Lattice Heisenberg Antiferromagnet under Magnetic Fields. *Physical Review Letters*, 108(1):17206, mar 2012.

[129] A. Bogdanov and A. Hubert. Thermodynamically stable magnetic vortex states in magnetic crystals. *Journal of Magnetism and Magnetic Materials*, 138(3):255–269, jan 1994.

[130] U. K. Rößler, A. N. Bogdanov, and C. Pfleiderer. Spontaneous skyrmion ground states in magnetic metals. *Nature*, 442(7104):797–801, oct 2006.

[131] Su Do Yi, Shigeki Onoda, Naoto Nagaosa, and Jung Hoon Han. Skyrmions and anomalous Hall effect in a Dzyaloshinskii-Moriya spiral magnet. *Physical Review B*, 80(5):054416, aug 2009.

[132] D. Solenov, D. Mozyrsky, and I. Martin. Chirality Waves in Two-Dimensional Magnets. *Physical Review Letters*, 108(9):096403, feb 2012.

[133] S. Mühlbauer, B. Binz, F. Jonietz, C. Pfleiderer, A. Rosch, A. Neubauer, R. Grotgii, and P. Böni. Corrections and Clarifications. *Science*, 323(5916):915–919, sep 2011.

[134] R. O. Kuzian and S.-L. Drechsler. Exact one- and two-particle excitation spectra of acute-angle helimagnets above their saturation magnetic field. *Physical Review B*, 75(2):24401, jan 2007.

[135] A. O. Leonov, T. L. Monchesky, N. Romming, A. Kubetzka, A. N. Bogdanov, and R. Wiesendanger. The properties of isolated chiral skyrmions in thin magnetic films. *New Journal of Physics*, 18(6):65003, jan 2016.

[136] Andrei B. Bogatyrëv and Konstantin L. Metlov. What makes magnetic skyrmions different from magnetic bubbles? *Journal of Magnetism and Magnetic Materials*, 465:743–746, jan 2018.

[137] Xichao Zhang, Yan Zhou, Kyung Mee Song, Tae-Eon Park, Jing Xia, Motohiko Ezawa, Xiaoxi Liu, Weisheng Zhao, Guoping Zhao, and Seonghoon Woo. Skyrmion-electronics: writing, deleting, reading and processing magnetic skyrmions toward spintronic applications. *Journal of Physics: Condensed Matter*, 32(14):143001, nov 2020.

[138] Markus Hoffmann, Bernd Zimmermann, Gideon P Müller, Daniel Schürhoff, Nikolai S Kiselev, Christof Melcher, and Stefan Blügel. Antiskyrmions stabilized at interfaces by anisotropic Dzyaloshinskii-Moriya interactions. *Nature Communications*, 8(1):308, mar 2017.

[139] Lorenzo Camosi, Stanislas Rohart, Olivier Fruchart, Stefania Pizzini, Mohamed Belmeguenai, Yves Roussigné, Andreï Stashkevich, Salim Mourad Cherif, Laurent Ranno, Maurizio de Santis, and Jan Vogel. Anisotropic Dzyaloshinskii-Moriya interaction in ultrathin epitaxial Au/Co/W(110). *Physical Review B*, 95(21):214422, jun 2017.

[140] Michael Heigl, Sabri Koraltan, Marek Vaňatka, Robert Kraft, Claas Abert, Christoph Vogler, Anna Semisalova, Ping Che, Aladin Ullrich, Timo Schmidt, Julian Hintermayr, Dirk Grundler, Michael Farle, Michal Urbánek, Dieter Suess, and Manfred Albrecht. Dipolar-stabilized first and second-order antiskyrmions in ferrimagnetic multilayers. *Nature Communications*, 12(1):2611, dec 2021.

[141] Wataru Koshibae and Naoto Nagaosa. Creation of skyrmions and antiskyrmions by local heating. *Nature Communications*, 5(1):5148, jan 2014.

[142] Soong-Geun Je, Pierre Vallobra, Titiksha Srivastava, and Juan-Carlos Rojas-Sa. Creation of Magnetic Skyrmion Bubble Lattices by Ultrafast Laser in Ultrathin Films. *Nano Lett.*, page 10, 2018.

[143] Niklas Romming, Christian Hanneken, Matthias Menzel, Jessica E Bickel, Boris Wolter, Kirsten von Bergmann, André Kubetzka, and Roland Wiesendanger. Writing and Deleting Single Magnetic Skyrmions. *Science*, 341(6146):636–639, jan 2013.

[144] Andrea De Lucia, Kai Litzius, Benjamin Krüger, Oleg A Tretiakov, and Mathias Kläui. Multiscale simulations of topological transformations in magnetic-skyrmion spin structures. *Physical Review B*, 96(2):20405, jan 2017.

[145] Seonghoon Woo, Kyung Mee Song, Xichao Zhang, Motohiko Ezawa, Yan Zhou, Xiaoxi Liu, Markus Weigand, Simone Finizio, Jörg Raabe, Min-Chul Park, Ki-Young Lee, Jun Woo Choi, Byoung-Chul Min, Hyun Cheol Koo, and Joonyeon Chang. Deterministic creation and deletion of a single magnetic skyrmion observed by direct time-resolved X-ray microscopy. *Nature Electronics*, 1(5):288–296, nov 2018.

[146] Karin Everschor-Sitte, Jairo Sinova, and Artem Abanov. Painting and erasing skyrmions. *Nature Electronics*, 1(5):266–267, nov 2018.

[147] Naoto Nagaosa and Yoshinori Tokura. Topological properties and dynamics of magnetic skyrmions. *Nature Nanotechnology*, 8(12):899–911, dec 2013.

[148] Bei Ding, Zefang Li, Guizhou Xu, Hang Li, Zhipeng Hou, Enke Liu, Xuekui Xi, Feng Xu, Yuan Yao, and Wenhong Wang. Observation of Magnetic Skyrmion Bubbles in a van der Waals Ferromagnet Fe_3GeTe_2. *Nano Letters*, 20(2):868–873, jan 2020.

[149] Charudatta Phatak, Olle Heinonen, Marc De Graef, and Amanda Petford-Long. Nanoscale Skyrmions in a Nonchiral Metallic Multiferroic: Ni_2MnGa. *Nano Letters*, 16(7):4141–4148, jul 2016.

[150] Yufan Li, N. Kanazawa, X. Z. Yu, A. Tsukazaki, M. Kawasaki, M. Ichikawa, X. F. Jin, F. Kagawa, and Y. Tokura. Robust Formation of Skyrmions and Topological Hall Effect Anomaly in Epitaxial Thin Films of MnSi. *Physical Review Letters*, 110(11):117202, jan 2013.

[151] Pin-Jui Hsu, André Kubetzka, Aurore Finco, Niklas Romming, Kirsten von Bergmann, and Roland Wiesendanger. Electric-field-driven switching of individual magnetic skyrmions. *Nature Nanotechnology*, 12(2):123–126, jan 2017.

[152] Wanjun Jiang, Xichao Zhang, Guoqiang Yu, Wei Zhang, Xiao Wang, M Benjamin Jungfleisch, John E Pearson, Xuemei Cheng, Olle Heinonen, Kang L Wang, Yan Zhou, Axel Hoffmann, and Suzanne G E te Velthuis. Direct observation of the skyrmion Hall effect. *Nature Physics*, 13(2):162–169, oct 2017.

[153] P. Milde, D. Köhler, J. Seidel, L. M. Eng, A. Bauer, A. Chacon, J. Kindervater, S. Mühlbauer, C. Pfleiderer, S. Buhrandt, C. Schütte, and A. Rosch. Unwinding of a Skyrmion Lattice by Magnetic Monopoles. *Science*, 340(6136):1076–1080, nov 2013.

[154] Arianna Casiraghi, Héctor Corte-León, Mehran Vafaee, Felipe Garcia-Sanchez, Gianfranco Durin, Massimo Pasquale, Gerhard Jakob, Mathias Kläui, and Olga Kazakova. Individual skyrmion manipulation by local magnetic field gradients. *Communications Physics*, 2(1):1–9, jan 2019.

[155] C. Back, V. Cros, H. Ebert, K. Everschor-Sitte, A. Fert, M Garst, Tianping Ma, S. Mankovsky, T. L. Monchesky, M. Mostovoy, N. Nagaosa, S. S. P. Parkin, C. Pfleiderer, N. Reyren, A. Rosch, Y. Taguchi, Y Tokura, K. von Bergmann, and Jiadong Zang. The 2020 skyrmionics roadmap. *Journal of Physics D: Applied Physics*, 53(36):363001, feb 2020.

[156] P. Bruno, V. K. Dugaev, and M. Taillefumier. Topological Hall Effect and Berry Phase in Magnetic Nanostructures. *Physical Review Letters*, 93(9):96806, jan 2004.

[157] A. Neubauer, C. Pfleiderer, B. Binz, A. Rosch, R. Ritz, P. G. Niklowitz, and P. Böni. Topological Hall Effect in the *A* Phase of MnSi. *Physical Review Letters*, 102(18):186602, jan 2009.

[158] N. Kanazawa, Y. Onose, T. Arima, D. Okuyama, K. Ohoyama, S. Wakimoto, K. Kakurai, S. Ishiwata, and Y. Tokura. Large Topological Hall Effect in a Short-Period Helimagnet MnGe. *Physical Review Letters*, 106(15):156603, jan 2011.

[159] Börge Göbel, Collins Ashu Akosa, Gen Tatara, and Ingrid Mertig. Topological Hall signatures of magnetic hopfions. *Physical Review Research*, 2(1):13315, jan 2020.

[160] Christian Hanneken, Fabian Otte, André Kubetzka, Bertrand Dupé, Niklas Romming, Kirsten von Bergmann, Roland Wiesendanger, and Stefan Heinze. Electrical detection of magnetic skyrmions by tunnelling non-collinear magnetoresistance. *Nature Nanotechnology*, 10(12):1039–1042, jan 2015.

[161] Haifeng Du, Dong Liang, Chiming Jin, Lingyao Kong, Matthew J Stolt, Wei Ning, Jiyong Yang, Ying Xing, Jian Wang, Renchao Che, Jiadong Zang, Song Jin, Yuheng Zhang, and Mingliang Tian. Electrical probing of field-driven cascading quantized transitions of skyrmion cluster states in MnSi nanowires. *Nature Communications*, 6(1):7637, jan 2015.

[162] Gong Chen. Skyrmion Hall effect. *Nature Physics*, 13(2):112–113, jan 2017.

[163] Albert Fert, Vincent Cros, and João Sampaio. Skyrmions on the track. *Nature Nanotechnology*, 8(3):152–156, mar 2013.

[164] T. Schulz, R. Ritz, A. Bauer, M. Halder, M. Wagner, C. Franz, C. Pfleiderer, K. Everschor, M. Garst, and A. Rosch. Emergent electrodynamics of skyrmions in a chiral magnet. *Nature Physics*, 8(4):301–304, oct 2012.

[165] Masamitsu Hayashi, Luc Thomas, Charles Rettner, Rai Moriya, Yaroslaw B. Bazaliy, and Stuart S. P. Parkin. Current Driven Domain Wall Velocities Exceeding the Spin Angular Momentum Transfer Rate in Permalloy Nanowires. *Physical Review Letters*, 98(3):037204, jan 2007.

[166] S. Parkin, Xin Jiang, C. Kaiser, A. Panchula, K. Roche, and M. Samant. Magnetically engineered spintronic sensors and memory. *Proceedings of the IEEE*, 91(5):661–680, may 2003.

[167] Kwang-Su Ryu, Luc Thomas, See-Hun Yang, and Stuart Parkin. Chiral spin torque at magnetic domain walls. *Nature Nanotechnology*, 8(7):527–533, jul 2013.

[168] A. A. Thiele. Steady-State Motion of Magnetic Domains. *Physical Review Letters*, 30(6):230–233, nov 1973.

[169] Karin Everschor, Markus Garst, Benedikt Binz, Florian Jonietz, Sebastian Mühlbauer, Christian Pfleiderer, and Achim Rosch. Rotating skyrmion lattices by spin torques and field or temperature gradients. *Physical Review B*, 86(5):54432, nov 2012.

[170] Junichi Iwasaki, Masahito Mochizuki, and Naoto Nagaosa. Universal current-velocity relation of skyrmion motion in chiral magnets. *Nature Communications*, 4(1):1463, jan 2013.

[171] Kai Litzius, Ivan Lemesh, Benjamin Krüger, Pedram Bassirian, Lucas Caretta, Kornel Richter, Felix Büttner, Koji Sato, Oleg A Tretiakov, Johannes Förster, Robert M Reeve, Markus Weigand, Iuliia Bykova, Hermann Stoll, Gisela Schütz, Geoffrey S D Beach, and Mathias Kläui. Skyrmion Hall effect revealed by direct time-resolved X-ray microscopy. *Nature Physics*, 13(2):170–175, jan 2017.

[172] Stuart S.P. Parkin, Masamitsu Hayashi, and Luc Thomas. Magnetic Domain-Wall Racetrack Memory. *Science*, 320(5873):190–194, jan 2008.

[173] Stuart Parkin and See-Hun Yang. Memory on the racetrack. *Nature Nanotechnology*, 10(3):195–198, mar 2015.

[174] Shilei Zhang, Alexander A. Baker, Stavros Komineas, and Thorsten Hesjedal. Topological computation based on direct magnetic logic communication. *Scientific Reports*, 5(1):15773, jan 2015.

[175] Fehmi S. Yasin, Licong Peng, Rina Takagi, Naoya Kanazawa, Shinichiro Seki, Yoshinori Tokura, and Xiuzhen Yu. Bloch Lines Constituting Antiskyrmions Captured via Differential Phase Contrast. *Advanced Materials*, 32(46):2004206, nov 2020.

[176] K. Kurushima, K. Tanaka, H. Nakajima, M. Mochizuki, and S. Mori. Microscopic magnetization distribution of Bloch lines in a uniaxial magnet. *Journal of Applied Physics*, 125(5):053902, feb 2019.

[177] Mi-Young Im, Hee-Sung Han, Min-Seung Jung, Young-Sang Yu, Sooseok Lee, Seongsoo Yoon, Weilun Chao, Peter Fischer, Jung-Il Hong, and Ki-Suk Lee. Dynamics of the Bloch point in an asymmetric permalloy disk. *Nature Communications*, 10(1):593, dec 2019.

[178] E. Feldtkeller. Mikromagnetisch stetige und unstetige Magnetisierungskonfigurationen. *Zeitschrift für Angewandte Physik*, 1965.

[179] W. Döring. Point Singularities in Micromagnetism. *Journal of Applied Physics*, 39(2):1006–1007, feb 1968.

[180] Marijan Beg, Ryan A. Pepper, David Cortés-Ortuño, Bilal Atie, Marc-Antonio Bisotti, Gary Downing, Thomas Kluyver, Ondrej Hovorka, and Hans Fangohr. Stable and manipulable Bloch point. *Scientific Reports*, 9(1):7959, dec 2019.

[181] P.R. Kotiuga. The algebraic topology of Bloch points. *IEEE Transactions on Magnetics*, 25(5):3476–3478, 1989.

[182] André Thiaville, José Miguel García, Rok Dittrich, Jacques Miltat, and Thomas Schrefl. Micromagnetic study of Bloch-point-mediated vortex core reversal. *Physical Review B*, 67(9):094410, mar 2003.

[183] S. Da Col, S. Jamet, N. Rougemaille, A. Locatelli, T. O. Mentes, B. Santos Burgos, R. Afid, M. Darques, L. Cagnon, J. C. Toussaint, and O. Fruchart. Observation of Bloch-point domain walls in cylindrical magnetic nanowires. *Physical Review B*, 89(18):180405, may 2014.

[184] Mi-Young Im, Peter Fischer, Keisuke Yamada, Tomonori Sato, Shinya Kasai, Yoshinobu Nakatani, and Teruo Ono. Symmetry breaking in the formation of magnetic vortex states in a permalloy nanodisk. *Nature Communications*, 3(1):983, jan 2012.

[185] A. Wartelle, B. Trapp, M. Staňo, C. Thirion, S. Bochmann, J. Bachmann, M. Foerster, L. Aballe, T. O. Menteş, A. Locatelli, A. Sala, L. Cagnon, J.-C. Toussaint, and O. Fruchart. Bloch-point-mediated topological transformations of magnetic domain walls in cylindrical nanowires. *Physical Review B*, 99(2):024433, jan 2019.

[186] Claire Donnelly, Manuel Guizar-Sicairos, Valerio Scagnoli, Sebastian Gliga, Mirko Holler, Jörg Raabe, and Laura J. Heyderman. Three-dimensional magnetization structures revealed with X-ray vector nanotomography. *Nature*, 547(7663):328–331, jul 2017.

[187] Dimitris Plantzos. Crystals and Lenses in the Graeco-Roman World. *American Journal of Archaeology*, 101(3):451, jul 1997.

[188] Beyond the diffraction limit. *Nature Photonics*, 3(7):361–361, jul 2009.

[189] G. Binnig, H. Rohrer, Ch. Gerber, and E. Weibel. Surface Studies by Scanning Tunneling Microscopy. *Physical Review Letters*, 49(1):57–61, jul 1982.

[190] G. Binnig and H. Rohrer. Scanning tunneling microscopy. *Surface Science*, 126(1-3):236–244, mar 1983.

[191] G. Binnig, C. F. Quate, and Ch. Gerber. Atomic Force Microscope. *Physical Review Letters*, 56(9):930–933, mar 1986.

[192] F. J. Giessibl. Subatomic Features on the Silicon (111)-(7x7) Surface Observed by Atomic Force Microscopy. *Science*, 289(5478):422–425, jul 2000.

[193] Ricardo Garcia and Rubén Pérez. Dynamic atomic force microscopy methods. *Surface Science Reports*, 47(6):197–301, oct 2002.

[194] Nader Jalili and Karthik Laxminarayana. A review of atomic force microscopy imaging systems: application to molecular metrology and biological sciences. *Mechatronics*, 14(8):907–945, oct 2004.

[195] Daniel J. Müller and Yves F. Dufrêne. Atomic force microscopy as a multifunctional molecular toolbox in nanobiotechnology. *Nature Nanotechnology*, 3(5):261–269, may 2008.

[196] L. Gross, F. Mohn, N. Moll, P. Liljeroth, and G. Meyer. The Chemical Structure of a Molecule Resolved by Atomic Force Microscopy. *Science*, 325(5944):1110–1114, aug 2009.

[197] Franz J. Giessibl. Advances in atomic force microscopy. *Rev. Mod. Phys.*, 75(3):35, 2003.

[198] Yongho Seo and Wonho Jhe. Atomic force microscopy and spectroscopy. *Reports on Progress in Physics*, 71(1):016101, jan 2008.

[199] Y. Martin, C. C. Williams, and H. K. Wickramasinghe. Atomic force microscope–force mapping and profiling on a sub 100-Å scale. *Journal of Applied Physics*, 61(10):4723–4729, nov 1987.

[200] Q. Zhong, D. Inniss, K. Kjoller, and V.B. Elings. Fractured polymer/silica fiber surface studied by tapping mode atomic force microscopy. *Surface Science*, 290(1-2):L688–L692, jun 1993.

[201] T. R. Albrecht, P. Grütter, D. Horne, and D. Rugar. Frequency modulation detection using high-Q cantilevers for enhanced force microscope sensitivity. *Journal of Applied Physics*, 69(2):668–673, nov 1991.

[202] Constant A. J. Putman, Kees O. Van der Werf, Bart G. De Grooth, Niek F. Van Hulst, and Jan Greve. Tapping mode atomic force microscopy in liquid. *Applied Physics Letters*, 64(18):2454–2456, may 1994.

[203] Antonio Aliano, Giancarlo Cicero, Hossein Nili, Nicolas G. Green, Pablo García-Sánchez, Antonio Ramos, Andreas Lenshof, Thomas Laurell, Aisha Qi, Peggy Chan, Leslie Yeo, James Friend, Mikael Evander, Thomas Laurell, Andreas Lenshof, Thomas Laurell, Jian Chen, Jean Christophe Lacroix, Pascal Martin, Hyacinthe Randriamahazaka, W. Jon. P. Barnes, Bart W. Hoogenboom, Kenji Fukuzawa, Hendrik Hölscher, Hendrik Hölscher, Alessia Bottos, Elena Astanina, Luca Primo, Federico Bussolino, Xuefeng Gao, Vinh-Nguyen Phan, Nam-Trung Nguyen, Chun Yang, Patrick Abgrall, Friedrich G. Barth, Pablo Gurman, Yitzhak Rosen, Orlando Auciello, C. J. Kähler, C. Cierpka, M. Rossi, Bharat Bhushan, Manuel L. B. Palacio, and Charles L. Dezelah. AFM in Liquids. In *Encyclopedia of Nanotechnology*, pages 83–89. Springer Netherlands, Dordrecht, 2012.

[204] Joska Broekmaat, Alexander Brinkman, Dave H. A. Blank, and Guus Rijnders. High temperature surface imaging using atomic force microscopy. *Applied Physics Letters*, 92(4):043102, jan 2008.

[205] L. Rossi, J. W. Gerritsen, L. Nelemans, A. A. Khajetoorians, and B. Bryant. An ultra-compact low temperature scanning probe microscope for magnetic fields above 30 T. *Review of Scientific Instruments*, 89(11):113706, nov 2018.

[206] Gerhard Meyer and Nabil M. Amer. Novel optical approach to atomic force microscopy. *Applied Physics Letters*, 53(12):1045–1047, sep 1988.

[207] D. Rugar, H. J. Mamin, and P. Guethner. Improved fiber-optic interferometer for atomic force microscopy. *Applied Physics Letters*, 55(25):2588–2590, dec 1989.

[208] S. D. R. Wilson and A. Hulme. The effect of bubbles attached to an electrode on electrical resistance and dissolved gas concentration. *Proceedings of the Royal Society of London. A. Mathematical and Physical Sciences*, 387(1792):133–146, may 1983.

[209] Ernst Meyer, Hans Josef Hug, and Roland Bennewitz. *Scanning Probe Microscopy*. Advanced Texts in Physics. Springer Berlin Heidelberg, Berlin, Heidelberg, 2004.

[210] Peter Eaton and Paul West. *Atomic Force Microscopy*. Oxford University Press, mar 2010.

[211] F. J. Giessibl. Atomic Resolution of the Silicon (111)-(7x7) Surface by Atomic Force Microscopy. *Science*, 267(5194):68–71, jan 1995.

[212] S. Kitamura and M. Iwatsuki. Observation og Silicon Surfaces Using Ultrahigh-Vacuum Noncontact Atomic Force Microscopy. *Jpn. J. Appl. Phys.*, 35:668–671, 1996.

[213] Roland Guerre, Ute Drechsler, and Daniel Jubin et Michel Despont. Low-cost AFM cantilever manufacturing technology. *Journal of Micromechanics and Microengineering*, 18(11):115013, nov 2008.

[214] Barry R. Masters. Single-Molecule Cellular Biophysics. *Journal of Biomedical Optics*, 18(8):089901, aug 2013.

[215] Yongda Yan, Zhenjiang Hu, Xueshen Zhao, Tao Sun, Shen Dong, and Xiaodong Li. Top-Down Nanomechanical Machining of Three-Dimensional Nanostructures by Atomic Force Microscopy. *Small*, 6(6):724–728, mar 2010.

[216] P. Niedermann, W. Hänni, D. Morel, A. Perret, N. Skinner, P.-F. Indermühle, and N.-F. de Rooij Not Available. CVD diamond probes for nanotechnology. *Applied Physics A: Materials Science and Processing*, 66(7):S31–S34, mar 1998.

[217] Masaaki Futamoto, Tatsuya Hagami, Shinji Ishihara, Kazuki Soneta, and Mitsuru Ohtake. Improvement of Magnetic Force Microscope Resolution and Application to High-Density Recording Media. *IEEE Transactions on Magnetics*, 49(6):2748–2754, jun 2013.

[218] M. Precner, J. Fedor, J. Tóbik, J. Šoltýs, and V. Cambel. High Resolution Tips for Switching Magnetization MFM. *Acta Physica Polonica A*, 126(1):386–387, jul 2014.

[219] Gernot Friedbacher and Harald Fuchs. Classification of Scanning Probe Microscopies. *Pure and Applied Chemistry*, 71(7):1337–1357, jul 1999.

[220] S. J. O'Shea. Conducting atomic force microscopy study of silicon dioxide breakdown. *Journal of Vacuum Science & Technology B: Microelectronics and Nanometer Structures*, 13(5):1945, oct 1995.

[221] C. Shafai, D. J. Thomson, M. Simard-Normandin, G. Mattiussi, and P. J. Scanlon. Delineation of semiconductor doping by scanning resistance microscopy. *Applied Physics Letters*, 64(3):342–344, jan 1994.

[222] P. De Wolf, J. Snauwaert, T. Clarysse, W. Vandervorst, and L. Hellemans. Characterization of a point-contact on silicon using force microscopy-supported resistance measurements. *Applied Physics Letters*, 66(12):1530–1532, mar 1995.

[223] Alexei Gruverman, Orlando Auciello, and Hiroshi Tokumoto. Imaging and controlof domain structures in ferroelectric thin filsm via scanning force microscopy. *Annual Review of Materials Science*, 28(1):101–123, oct 1998.

[224] Sergei V. Kalinin, Brian J. Rodriguez, Stephen Jesse, Junsoo Shin, Arthur P. Baddorf, Pradyumna Gupta, Himanshu Jain, David B. Williams, and Alexei Gruverman. Vector Piezoresponse Force Microscopy. *Microscopy and Microanalysis*, 12(03):206–220, jun 2006.

[225] M. Nonnenmacher, M. P. O'Boyle, and H. K. Wickramasinghe. Kelvin probe force microscopy. *Applied Physics Letters*, 58(2921):4, 1991.

[226] Yves Martin, David W. Abraham, and H. Kumar Wickramasinghe. High-resolution capacitance measurement and potentiometry by force microscopy. *Applied Physics Letters*, 52(13):1103–1105, mar 1988.

[227] Paul Girard. Electrostatic force microscopy: principles and some applications to semiconductors. *Nanotechnology*, 12(4):485–490, oct 2001.

[228] B. Cappella and G. Dietler. Force-distance curves by atomic force microscopy. *Surface Science Reports*, 34(1-3):1–104, jan 1999.

[229] Chun Li, Yoshio Bando, and Dmitri Golberg. Current Imaging and Electromigration-Induced Splitting of GaN Nanowires As Revealed by Conductive Atomic Force Microscopy. *ACS Nano*, 4(4):2422–2428, apr 2010.

[230] Xueyun Wang, Danni Yang, Hui-Min Zhang, Chuangye Song, Jing Wang, Guotai Tan, Renkui Zheng, Shuai Dong, Sang-Wook Cheong, and Jinxing Zhang. Anisotropic resistance switching in hexagonal manganites. *Physical Review B*, 99(5):054106, feb 2019.

[231] G.A. Schwartz, C. Riedel, R. Arinero, Ph. Tordjeman, A. Alegría, and J. Colmenero. Broadband nanodielectric spectroscopy by means of amplitude modulation electrostatic force microscopy (AM-EFM). *Ultramicroscopy*, 111(8):1366–1369, jul 2011.

[232] Y. Martin and H. K. Wickramasinghe. Magnetic imaging by "force microscopy" with 1000 Å resolution. *Applied Physics Letters*, 50(20):1455–1457, may 1987.

[233] J. J. Sáenz, N. García, P. Grütter, E. Meyer, H. Heinzelmann, R. Wiesendanger, L. Rosenthaler, H. R. Hidber, and H.-J. Güntherodt. Observation of magnetic forces by the atomic force microscope. *Journal of Applied Physics*, 62(10):4293–4295, nov 1987.

[234] H. D. Arnold and G. W. Elmen. Permalloy, A New Magnetic Material of Very High Permeability. *Bell System Technical Journal*, 2(3):101–111, jul 1923.

[235] Jason W Li, Jason P Cleveland, and Roger Proksch. Bimodal magnetic force microscopy: Separation of short and long range forces. *Applied Physics Letters*, 94(16):163118, nov 2009.

[236] Lukas Stühn, Julia Auernhammer, and Christian Dietz. pH-depended protein shell dis- and reassembly of ferritin nanoparticles revealed by atomic force microscopy. *Scientific Reports*, 9(1):17755, dec 2019.

[237] O. Kazakova, R. Puttock, C. Barton, H. Corte-León, M. Jaafar, V. Neu, and A. Asenjo. Frontiers of magnetic force microscopy. *Journal of Applied Physics*, 125(6):60901, jul 2019.

[238] Miriam Jaafar, Oscar Iglesias-Freire, Luis Serrano-Ramón, Manuel Ricardo Ibarra, Jose Maria de Teresa, and Agustina Asenjo. Distinguishing magnetic and electrostatic interactions by a Kelvin probe force microscopy–magnetic force microscopy combination. *Beilstein Journal of Nanotechnology*, 2:552–560, nov 2011.

[239] Vladimír Cambel, Dagmar Gregušová, Peter Eliáš, Ján Fedor, Ivan Kostič, Ján Maňka, and Peter Ballo. Switching Magnetization Magnetic Force Microscopy — An Alternative to Conventional Lift-Mode MFM. *Journal of Electrical Engineering*, 62(1):37–43, nov 2011.

[240] W. Rave, D. Eckert, R. Schafer, B. Gebel, and K.-H. Muller. Interaction domains in isotropic, fine-grained $Sm_2Fe_{17}N_3$ permanent magnets. *IEEE Transactions on Magnetics*, 32(5):4362–4364, 1996.

[241] David B. Williams and C. Barry Carter. *Transmission Electron Microscopy*. Springer US, Boston, MA, 2009.

[242] O. Scherzer. Über einige Fehler von Elektronenlinsen. *Zeitschrift für Physik*, 101(9-10):593–603, sep 1936.

[243] Joseph I. Goldstein, Dale E. Newbury, Patrick Echlin, David C. Joy, Charles E. Lyman, Eric Lifshin, Linda Sawyer, and Joseph R. Michael. *Scanning Electron Microscopy and X-ray Microanalysis*. Springer US, Boston, MA, 2003.

[244] Lucio Ayres Caldas, Fabiana Avila Carneiro, Luiza Mendonça Higa, Fábio Luiz Monteiro, Gustavo Peixoto da Silva, Luciana Jesus da Costa, Edison Luiz Durigon, Amilcar Tanuri, and Wanderley de Souza. Ultrastructural analysis of SARS-CoV-2 interactions with the host cell via high resolution scanning electron microscopy. *Scientific Reports*, 10(1):16099, dec 2020.

[245] M.E. Taylor. Scanning Electron Microscopy in Forensic Science. *Journal of the Forensic Science Society*, 13(4):269–280, oct 1973.

[246] Lucille A. Giannuzzi and Fred A. Stevie, editors. *Introduction to Focused Ion Beams*. Springer US, Boston, MA, 2005.

[247] Nan Yao, editor. *Focused Ion Beam Systems*. Cambridge University Press, Cambridge, 2007.

[248] Kaname Yoshida, Johannes Biskupek, Hiroki Kurata, and Ute Kaiser. Critical conditions for atomic resolution imaging of molecular crystals by aberration-corrected HRTEM. *Ultramicroscopy*, 159:73–80, dec 2015.

[249] Ian MacLaren, Thomas A. Macgregor, Christopher S. Allen, and Angus I. Kirkland. Detectors—The ongoing revolution in scanning transmission electron microscopy and why this important to material characterization. *APL Materials*, 8(11):110901, nov 2020.

[250] Wolfgang Demtröder. *Experimentalphysik 2*. Springer-Lehrbuch. Springer Berlin Heidelberg, Berlin, Heidelberg, 2013.

[251] Duc-The Ngo and Luise Theil Kuhn. In situ transmission electron microscopy for magnetic nanostructures. *Advances in Natural Sciences: Nanoscience and Nanotechnology*, 7(4):045001, sep 2016.

[252] Herbert Hopster and Hans Peter Oepen, editors. *Magnetic Microscopy of Nanostructures*. NanoScience and Technology. Springer Berlin Heidelberg, Berlin, Heidelberg, 2005.

[253] D. Paganin and K. A. Nugent. Noninterferometric Phase Imaging with Partially Coherent Light. *Physical Review Letters*, 80(12):2586–2589, mar 1998.

[254] Damien McGrouther, Maria-Jose Benites, Sam McFadzean, and Stephen Mc Vitie. No TitleDevelopment of Aberration Corrected Differential Phase Contrast (DPC) STEM. *JEOLnews*, 49(1):2–10, 2014.

[255] T. Kida, L. A. Fenner, A. A. Dee, I. Terasaki, M. Hagiwara, and A. S. Wills. The giant anomalous Hall effect in the ferromagnet Fe_3Sn_2—a frustrated kagome metal. *Journal of Physics: Condensed Matter*, 23(11):112205, mar 2011.

[256] Jia-Xin Yin, Songtian S. Zhang, Hang Li, Kun Jiang, Guoqing Chang, Bingjing Zhang, Biao Lian, Cheng Xiang, Ilya Belopolski, Hao Zheng, Tyler A. Cochran, Su-Yang Xu, Guang Bian, Kai Liu, Tay-Rong Chang, Hsin Lin, Zhong-Yi Lu, Ziqiang Wang, Shuang Jia, Wenhong Wang, and M. Zahid Hasan. Giant and anisotropic many-body spin–orbit tunability in a strongly correlated kagome magnet. *Nature*, 562(7725):91–95, oct 2018.

[257] Qi Wang, Shanshan Sun, Xiao Zhang, Fei Pang, and Hechang Lei. Anomalous Hall effect of ferromagnetic Fe_3Sn_2 single crystal with geometrically frustrated kagome lattice. *Physical Review B*, 94(7):75135, jul 2016.

[258] Christopher D O'Neill, Andrew S Wills, and Andrew D Huxley. Possible topological contribution to the anomalous Hall effect of the noncollinear ferromagnet Fe_3Sn_2. *Physical Review B*, 100(17):174420, jul 2019.

[259] G. Trumpy, E. Both, C. Djéga-Mariadassou, and P. Lecocq. Mössbauer-Effect Studies of Iron-Tin Alloys. *Physical Review B*, 2(9):3477–3490, jul 1970.

[260] G. Le Caer, B. Malaman, and B. Roques. Mossbauer effect study of Fe_3Sn_2. *Journal of Physics F: Metal Physics*, 8(2):323–336, mar 1978.

[261] B Malaman, D Fruchart, and G Le Caer. Magnetic properties of Fe_3Sn_2. II. Neutron diffraction study (and Mossbauer effect). *Journal of Physics F: Metal Physics*, 8(11):2389–2399, mar 1978.

[262] G. Le Caer, B. Malaman, L. Haggstrom, and T. Ericsson. Magnetic properties of Fe3Sn2. III. A119Sn Mossbauer study. *Journal of Physics F: Metal Physics*, 9(9):1905–1919, mar 1979.

[263] Kevin Heritage, Ben Bryant, Laura A. Fenner, Andrew S. Wills, Gabriel Aeppli, and Yeong Ah Soh. Images of a First-Order Spin-Reorientation Phase Transition in a Metallic Kagome Ferromagnet. *Advanced Functional Materials*, 30(36):1–12, 2020.

[264] Manuel Pereiro, Dmitry Yudin, Jonathan Chico, Corina Etz, Olle Eriksson, and Anders Bergman. Topological excitations in a kagome magnet. *Nature Communications*, 5(1):4815, dec 2014.

[265] Zhipeng Hou, Qiang Zhang, Guizhou Xu, Senfu Zhang, Chen Gong, Bei Ding, Hang Li, Feng Xu, Yuan Yao, Enke Liu, Guangheng Wu, Xi-xiang Zhang, and Wenhong Wang. Manipulating the Topology of Nanoscale Skyrmion Bubbles by Spatially Geometric Confinement. *ACS Nano*, 13(1):922–929, jan 2019.

[266] Zhipeng Hou, Qiang Zhang, Xichao Zhang, Guizhou Xu, Jing Xia, Bei Ding, Hang Li, Senfu Zhang, Nitin M. Batra, Pedro M. F. J. Costa, Enke Liu, Guangheng Wu, Motohiko Ezawa, Xiaoxi Liu, Yan Zhou, Xixiang Zhang, and Wenhong Wang. Current-Induced Helicity Reversal of a Single Skyrmionic Bubble Chain in a Nanostructured Frustrated Magnet. *Advanced Materials*, 32(1):1904815, jan 2020.

[267] Yuan Taur, D A Buchanan, Wei Chen, D J Frank, K E Ismail, Shih-Hsien Lo, G A Sai-Halasz, R G Viswanathan, H.-C Wann, S J Wind, and Hon-Sum Wong. CMOS scaling into the nanometer regime. *Proceedings of the IEEE*, 85(4):486–504, 1997.

[268] Aleksander B. Mosberg, Erik D. Roede, Donald M. Evans, Theodor S. Holstad, Edith Bourret, Zewu Yan, Antonius T. J. van Helvoort, and Dennis Meier. FIB lift-out of conducting ferroelectric domain walls in hexagonal manganites. *Applied Physics Letters*, 115(12):122901, sep 2019.

[269] Kevin Heritage. *Macroscopic and microscopic investigation of spin reorientation of iron tin*. PhD thesis, jul 2015.

[270] V. Baltz, A. Manchon, M. Tsoi, T. Moriyama, T. Ono, and Y. Tserkovnyak. Antiferromagnetic spintronics. *Reviews of Modern Physics*, 90(1):015005, feb 2018.

[271] Jin Tang, Yaodong Wu, Lingyao Kong, Weiwei Wang, Yutao Chen, Yihao Wang, Y Soh, Yimin Xiong, Mingliang Tian, and Haifeng Du. Two-dimensional characterization of three-dimensional magnetic bubbles in Fe_3Sn_2 nanostructures. *National Science Review*, aug 2020.

[272] Myung-Geun Han, Joseph A. Garlow, Yu Liu, Huiqin Zhang, Jun Li, Donald DiMarzio, Mark W. Knight, Cedomir Petrovic, Deep Jariwala, and Yimei Zhu. Topological Magnetic-Spin Textures in Two-Dimensional van der Waals $Cr_2Ge_2Te_6$. *Nano Letters*, 19(11):7859–7865, nov 2019.

[273] Y. Tokunaga, X. Z. Yu, J. S. White, H. M. Rønnow, D. Morikawa, Y. Taguchi, and Y. Tokura. A new class of chiral materials hosting magnetic skyrmions beyond room temperature. *Nature Communications*, 6(1):7638, nov 2015.

[274] S. McVitie, S. Hughes, K. Fallon, S. McFadzean, D. McGrouther, M. Krajnak, W. Legrand, D. Maccariello, S. Collin, K. Garcia, N. Reyren, V. Cros, A. Fert, K. Zeissler, and C. H. Marrows. A transmission electron microscope study of Néel skyrmion magnetic textures in multilayer thin film systems with large interfacial chiral interaction. *Scientific Reports*, 8(1):5703, dec 2018.

[275] Arne Vansteenkiste, Jonathan Leliaert, Mykola Dvornik, Mathias Helsen, Felipe Garcia-Sanchez, and Bartel Van Waeyenberge. The design and verification of MuMax3. *AIP Advances*, 4(10):107133, oct 2014.

[276] Arthur R.C. McCray, Timothy Cote, Yue Li, Amanda K. Petford-Long, and Charudatta Phatak. Understanding Complex Magnetic Spin Textures with Simulation-Assisted Lorentz Transmission Electron Microscopy. *Physical Review Applied*, 15(4):044025, apr 2021.

[277] Jin Tang, Yaodong Wu, Lingyao Kong, Weiwei Wang, Yutao Chen, Yihao Wang, Y Soh, Yimin Xiong, Mingliang Tian, and Haifeng Du. Two-dimensional characterization of three-dimensional magnetic bubbles in Fe3Sn2 nanostructures. *National Science Review*, 8(6), jun 2021.

[278] Erik Lyne, Dennis Meier, Erik Roede, Markus Altthaler, and István Kézsmárki. Circular magnetic racetrack memory with switchable skyrmionic helicity and accelerator track, 2021.

[279] Siying Huang, Chao Zhou, Gong Chen, Hongyi Shen, Andreas K. Schmid, Kai Liu, and Yizheng Wu. Stabilization and current-induced motion of antiskyrmion in the presence of anisotropic Dzyaloshinskii-Moriya interaction. *Physical Review B*, 96(14):144412, oct 2017.

[280] R. Tomasello, E. Martinez, R. Zivieri, L. Torres, M. Carpentieri, and G. Finocchio. A strategy for the design of skyrmion racetrack memories. *Scientific Reports*, 4(1):6784, may 2015.

[281] R. Brearton, L. A. Turnbull, J. A. T. Verezhak, G. Balakrishnan, P. D. Hatton, G. van der Laan, and T. Hesjedal. Deriving the skyrmion Hall angle from skyrmion lattice dynamics. *Nature Communications*, 12(1):2723, dec 2021.

[282] Xiaoyan Yao, Jun Chen, and Shuai Dong. Controlling the helicity of magnetic skyrmions by electrical field in frustrated magnets. *New Journal of Physics*, 22(8):083032, aug 2020.

[283] J. C. Slonczewski. Current-driven excitation of magnetic multilayers. *Journal of Magnetism and Magnetic Materials*, 159(1-2):L1–L7, feb 1996.

[284] L. Berger. Possible existence of a Josephson effect in ferromagnets. *Physical Review B*, 33(3):1572–1578, feb 1986.

[285] L. Berger. Exchange interaction between electric current and magnetic domain wall containing Bloch lines. *Journal of Applied Physics*, 63(5):1663–1669, feb 1988.

[286] Z. Li and S. Zhang. Domain-Wall Dynamics and Spin-Wave Excitations with Spin-Transfer Torques. *Physical Review Letters*, 92(20):207203, feb 2004.

[287] S Zhang and Z Li. Roles of Nonequilibrium Conduction Electrons on the Magnetization Dynamics of Ferromagnets. *Physical Review Letters*, 93(12):127204, jun 2004.

[288] Jinjun Ding, Xiaofei Yang, and Tao Zhu. Manipulating current induced motion of magnetic skyrmions in the magnetic nanotrack. *Journal of Physics D: Applied Physics*, 48(11):115004, mar 2015.

List of Figures

List of Tables

Acknowledgements

No academic achievement is done by one person alone - Hence, I'd like to thank my colleagues, friends, and family, who made the work leading to this thesis possible. In particular:

Prof. Dr. István Kézsmárki for giving me the opportunity to pursue a PhD with an interesting topic in a joint way both in Augsburg and Trondheim. As my supervisor, you found a perfect balance between giving me the freedom to develop my own ideas and guiding me in the right directions when needed.

Prof. Dr. Dennis Meier for acting as my co-supervisor and facilitating my extended research visits at NTNU. Thank you for welcoming me into your team and the continuous support throughout my PhD.

Priv.-Doz. Dr. Stephan Krohns for acting as my co-supervisor, bringing structure into both my PhD and the AFM group. Thank you for always being available when problem arose and finding creative solutions.

Dr. Erik Lysne for being my closest collaborator. Your seminal contributions to our topic lead to great joint progress and paved the way to successfully finish this work.

Lukas Puntigam, **Dr. Donald Evans**, **Maximilian Winkler**, **Lima Zhou**, **Arthur Schulz**, and **Dr. Mamoun Hemmida** for their scientific and social contributions. You made lunch, coffee breaks and "Spazieren gehen" highlights of my work days and (very) late shifts bearable.

Dr. Vladimir Tsurkan and **Dr. Lilian Prodan** for providing high quality single crystals. Thank you for all the additional information on the systems and your help preparing samples. **Priv.-Doz. Dr. Hans-Albrecht Krug von Nidda** for your support, whenever magnetism overexerted me.

Erik Roede, **Dr. Mariia Stepanova**, **Dr. Theodor Holstad**, **Payel Chatterjee**, **Longfei He**, **Kasper Hunnestad** and **Dr. Jan Schultheiß**, as well as all members of the **FACET group** for their scientific and experimental input. Thank you for many great memories during my visits to NTNU.

Dr. Peggy Schönherr, **Dr. András Kovács**, **Dr. Aladin Ullrich** for the in-depth introductions to the experimental techniques. **Dr. Attila Kákay** for the introduction to micromagnetic simulations. Thank you for your hospitality during my research visits.

Thomas Wiedenmann, **Dana Vieweg**, and **Klaus Wiedenmann** for your support setting up, maintaining, and running the laboratories I used on a daily basis.

Birgitta Eisenschmid for your help, so I could focus on the scientific work instead of administrative affairs. **Anny Skroblies** for teaching me how to circumnavigate the biggest obstacles in administration.

Manuela and **Karl Altthaler**, my parents, and **Michael Altthaler**, my brother, for supporting me in challenging times up to and throughout my PhD, as well as challenging me not to settle for good enough. You allowed me to focus on my PhD, whenever needed and reminded me of the things that matter the most. Thank you for supporting me throughout this long journey!

Dr. Solveig Aamlid, my girlfriend, for being the most supportive person throughout these last months. You listened, advised, and motivated me every day. Thank you!

Finally, this thesis is dedicated to my grandfather **Anton Winter**, who sadly never got the opportunities I had.